UNIVERSIDADE FEDERAL DE PERNAMBUCO
CENTRO DE TECNOLOGIA E GEOCIÊNCIAS
DEPARTAMENTO DE ENGENHARIA ELÉTRICA
PROGRAMA DE PÓS-GRADUAÇÃO EM ENGENHARIA QUÍMICA

TIAGO JOSÉ MARQUES FRAGA

DEVELOPMENT OF NANOSORBENTS DERIVED FROM FUNCTIONALIZED n-LAYERED GRAPHENE NANOSHEETS FOR DYE REMOVAL

Recife
2020

TIAGO JOSÉ MARQUES FRAGA

DEVELOPMENT OF NANOSORBENTS DERIVED FROM FUNCTIONALIZED n-LAYERED GRAPHENE NANOSHEETS FOR DYE REMOVAL

Doctoral thesis, presented to the Program of Post-Graduation in Chemical Engineering of Federal University of Pernambuco, as partial requirement for the achievement of the title of Doctor in Chemical Engineering.

Concentration area: Engineering of Chemical and Biochemical Processes

Advisor: Prof. Dr. Mauricio Alves da Motta Sobrinho.
Co-supervisors: Prof. Dr. Marcos Gomes Ghislandi.
Prof. Dr. Marilda Nascimento Carvalho.

Recife

2020

Catalogação na fonte
Bibliotecária Margareth Malta, CRB-4 / 1198

F811d Fraga, Tiago José Marques.
Development of nanosorbents derived from functionalized n-layered graphene nanosheets for dye removal / Tiago José Marques Fraga - 2020.
228 folhas, il., gráfs., tabs.

Orientador: Prof. Dr. Mauricio Alves da Motta Sobrinho.
Coorientador: Prof. Dr. Marcos Gomes Ghislandi.
Coorientador: Prof. Dr. Marilda Nascimento Carvalho.
Tese (Doutorado) – Universidade Federal de Pernambuco. CTG. Programa de Pós-Graduação em Engenharia Química, 2020.
Inclui Referências e Apêndices.
Texto em Inglês.

1. Engenharia Química. 2. Grafeno. 3. Nanomateriais 2D. 4. Funcionalização. 5. Adsorção. 6. Efluentes têxteis. 7. Interações intermoleculares. I. Motta Sobrinho, Mauricio Alves da (Orientador). II. Ghislandi, Marcos Gomes (Coorientador). III. Carvalho, Marilda Nascimento (Coorientador). IV. Título.

UFPE

660.2 CDD (22. ed.) BCTG/2020-67

TIAGO JOSÉ MARQUES FRAGA

DEVELOPMENT OF NANOSORBENTS DERIVED FROM FUNCTIONALIZED n-LAYERED GRAPHENE NANOSHEETS FOR DYE REMOVAL

Doctoral thesis, presented to the Program of Post-Graduation in Chemical Engineering of Federal University of Pernambuco, as partial requirement for the achievement of the title of Doctor in Chemical Engineering.

Approved on: 16/12/2020.

EXAMINING BOARD

_____

Prof. Dr. Maurício Alves da Motta Sobrinho (Advisor)
Universidade Federal de Pernambuco

_____

Prof. Dr. Marcos Gomes Ghislandi (Co-supervisor)
Universidade Federal Rural de Pernambuco

_____

Profa. Dra. Marilda Nascimento Carvalho (Co-supervisor)
Universidade Federal de Pernambuco

_____

Prof. Dr. César Augusto Moraes de Abreu (Appraiser)
Universidade Federal de Pernambuco

_____

Profa. Dra. Marta Maria Menezes Bezerra Duarte (Appraiser)
Universidade Federal de Pernambuco

_____

Profa. Dra. Diana Cristina Silva de Azevedo (External Appraiser)
Universidade Federal de Pernambuco

_____

Prof. Dr. Everton Skoronski (External Appraiser)
Universidade Estadual de Santa Catarina

_____

Prof. Dr. Guilhermino José Macêdo Fechine (External Appraiser)
Universidade Presbiteriana Mackenzie

_____

Prof. Dr. Manuel Fernando Ribeiro Pereira (External Appraiser)
Universidade do Porto

“Every generation has a legend. Every journey has a first step. Every saga has a beginning”

Luke Skywalker, Star Wars Episode IX, adapted (Lucasfilm Ltd., 2019).

I dedicate this work to all the people who were motivated and inspired to contribute with a little of their capacity and knowledge to its improvement; something that is under construction, but which has to find its final destination. And when I get there, my hope is that it will be a little light for those who will come after all of us, who, like me, will work to make science flourish in the soil of our country.

Secondly, I dedicate this work to those who have always been present behind the scenes of my life: my family! You have been the bulwark in times of difficulty, fatigue and demotivation. My desire is that we should always be together, even when we are no longer part of this world, we will meet in a place established by the Father.

To the Almighty God, the Father, Son and Holy Spirit, all due glory and honor! Forever and ever, Amen!

Dedico este trabalho a todas as pessoas que foram motivadas e inspiradas a contribuir com um pouco de sua capacidade e conhecimento para o aprimoramento deste; algo que se encontra em construção, mas que há de encontrar o seu destino final. E quando chegar lá, minha esperança é a de que possa ser um pouco de luz para aqueles que virão após todos nós, que, assim como eu, trabalharão para que a ciência floresça no solo deste nosso país.

Em segundo lugar, dedico este trabalho àqueles que sempre estiveram presente nos bastidores da minha vida: a minha família! Vocês tem sido o baluarte nos momentos de dificuldade, cansaço e desmotivação. Meu desejo é que estejamos sempre juntos, mesmo quando não fizermos mais parte deste mundo, haveremos de nos encontrar num lugar estabelecido pelo Pai.

Ao Todo poderoso Deus, Pai, Filho e Espírito Santo, toda a devida glória e honra! Para todo o sempre, Amém!

ACKNOWLEDGEMENTS

It is impossible to forget the acknowledgement of my eternal gratitude to my God, the Almighty Lord, the creator and the founder of my faith: Jesus Christ. Thank you Father God, The Son and The Holly Spirit for all your mercy, grace and love.

I also would like to thank the emocional support and love provided by my wife and "right hand", Daysianne M. S. Marques Fraga, who did not only help me with kind advices, incentives and prays, but also with considerations in some of my published works. I will be always thankful and proud for all joyful experiences we have been having during all these years. Thank you, my dear, my love, my life!

I kindly thank all support provided by my family members, my grandma Edna G. Marques, you stood by me in the toughest moments and you paid a price no one would be able to pay in those times. Thank you my hero, my mother, "General Edna"! I also aknowledge the love, friendship and partnership of my brothers and sisters Vitor, Ana Cecília, Maria Luiza, Mariana Martha, Apolo and Ana Laura. I especially aknowledge my little brother Vitor G. Fraga for all lessons in law, Constitution, politics and other subjects. Great times we had! I also thank my father Marcone Fraga for the advices, support and very productive conversations about the life, politics, law, economy, etc, etc, etc. Thank you old man! I also thank my mother for our many conversations and funny moments which I will never forget.

I would also like to acknowledge all support, guideness, advices and help provided by my tutor and mentor, Prof. Dr. Maurício A. da Motta Sobrinho, without that it would not be possible to finish this work. Prof. da Motta Sobrinho and his expertise in many subjects of environmental and chemical engineering has guided me in the ways of scientific methods and the criterious discussion in this matter. Certainly, our discussions have helped me to improve the quality of my work and to open my mind to always seek other alternatives. It has been an honor to have learned and worked with you, my friend. I am relly thankfull.

Prof. Dr. Marilda N. Carvalho, vice-coordinator of the Laboratório de Análises Minerais, Solos e Água (Lamsa) of Federal University of Pernambuco (UFPE), who has provided one of the strongest bases in my scientific career, by her patience, advices and critics towards many aspects of this and several other works. It has truly been a pleasure to have worked with you. I hope we can deliver even more results to contribute to the development of the science and education in our department, and consequently in our UFPE and our country.

I also thank Prof. Dr. Marcos G. Ghislandi for all his knowledge in the subject of materials science and engineering. Surely, without his expertise in this area, I would not reach nowhere! Thank you for all your patience and to investigate with accuracy each detail of every characterization graphics in our published works. I also acknowledge your help with the improvement of the writing of this work. Thank you a lot.

The author kindly thanks the technical support provided by the people of the Laboratório de Análises Minerais, Solos e Águas (Lamsa) of UFPE, especially thank Profª Eleonora M. Luna Freire for all incentives and advices regarding my scientific career, which I believe will be helpful to take my decisions. I'll take them with me for my entire life. I also thank the secretary of Lamsa Luiz for your patience and help with many bureaucratic subjects.

I also thank my friend Prof. Jorge V. F. Lima Cavalcanti for many advices and help with this and other works in the subject of modeling and adsorption experiments. Your expertise has helped me to improve the analytic discussion and careful evaluation of the phenomena involved in the adsorption, noticeably the part of binary adsorption.

I also thank my coelagues researchers of the Graphene Research Group, inside the Grupo de Pesquisa e Tecnologias Ambientais (GPTA) of UFPE for the familiarity, for all suggestions, advices, crytics and discussion towards many subjects of this and other many works. Personaly, I acknowledge my friends Caroline M. B. de Araújo, Prof. Dr. Romero Assis Filho, Ana Maria S. Baptisttella, Maryne P. da Silva and Bruna Figueiredo. You are very special, mindful and intellectual people, who I had the honor to work with. Thank you for the "coffees" my friends!

It is worthy to be acknowledged my coleagues and scientific initiation students of GPTA, Letticia E. de Lima, Gabriel Nascimento and Gabriel da Costa for all support and to make this work "happens". Without your hard work it would not be possible to achieve the results and to make the main findings and discussion possible. Thank you, fellas,!!

I also aknowledge the technical support provided by the Center of Advanced Researches with Graphene, Nanomaterials and Nanotechnlogies (MackGraphe) of Presbyterian Mackenzie Institute, São Paulo/SP. I am especially thankful to Prof. Guilhermino M. Fechine and Dr. Pablo Muñoz for their time and patience in receiving me and for sharing a part of their vast knowledge regarding the properties of graphene composites and characterization techniques. I will never forget the learning resulted from my "quick" benchmarking season in MackGraphe in 2018.

For all advices, support and help provided, I would like to thank M.E. Tereza Cristina da Silva, from Arconic Alumínio S/A. Moreover, it is worthy to mention your expertise in characterization techniques, especially, microscopy analyses.

I also thank my friend M.E. Thiago S. Pessôa, who I had the honor to have studied the graduation in Chemical Engineering with in UFPE. Thank you "touro bandido", for all support and partnership, for our conversations, for the experiments and discussion towards many subjects of different published works. It is worthy to be reminded the friendship and familiarity of my Doctorate coleagues and friends of the Chemical Engineering Post-Graduation Program (PPGEQ/UFPE), who I had the pleasure to work and study with: Santulla L. Carvalho, André T. Ribeiro, Sabino Neto, Aercio Feitosa, and many others, who I'm not remembering in this present moment.

I would like to summarize here some of the most illuminated minds, who I had the honor and satisfaction to be one of their students, my dearest Professors (Graduation, Master and Doctorate degrees): Maria de Los Angeles Palha, Celmy Barbosa, Cesar Abreu, Yêda Almeida, Mohand Benanchour, Luiz Stragevitch, Nelson Medeiros, Maria Fernanda Pimental, Marta Duarte, José Marcos da Silva, Glória Vinhas, José Geraldo Pacheco, Augusto Knoechelmann, Rita de Lima, Luciano Almeida, Leandro Danielski, Alexandre Schuller, Sandra Sarmento, Valdinete Lins and Olga Marques (*in memoriam*). Share the knowledge is one of the noblest actitudes which a person can deliver. You provided the stairs for me, and I could rise in the ways of life inside this profession I chose to live: the chemical engineering.

I also aknowledge my gratitude to many other friends and coleagues, whose names would not fit this section. To those who I forget to mention, feel embraced.

I kindly thank the *Fundação de Amparo à Ciência e Tecnologia do Estado de Pernambuco* (FACEPE) and all their staff for the funding of this research work (under the grant # IBPG-1917-3.06/16). I aknowledge the personel of FACEPE for their kindness, patience and for helping me with bureaucracy and other issues.

Finally, I aknowledge the *Coordenação de Aperfeiçoamento de Pessoal de Nível Superior* (CAPES) for the financial support provided for the post-graduation program in Chemical Engineering (PPGEQ/UFPE).

ABSTRACT

In this work, n-Layer Graphene Oxide (nGO) was synthetized from graphite oxidation via modified Hummers method. Afterwards, the nGO was functionalized with diethylenetriamine (DETA) and $FeCl_3$ at 180 ºC to obtain the novel n-layer amino-iron oxide-functionalized graphene oxide (nGO-NH_2-Fe_3O_4). Infrared (FTIR) and Raman spectroscopies, X-Ray Diffraction (XRD), Scanning Electron Microscopy (SEM), Atomic Force Microscopy (AFM) and Thermogravimetric Analysis (TGA) were performed to characterize both nGO and nGO-NH_2-Fe_3O_4. These materials were then evaluated as adsorbents of the cationic dye Methylene Blue (MB) and the anionic Remazol Black B (RB) and Drimaren Red (DR) through a comparative approach. Adsorption experiments were performed in batch, and studies of kinetics, equilibrium, thermodynamic and sorbent regeneration were carried out to investigate the affinity of nGO, nGO-NH_2-Fe_3O_4 and the amino-functionalized nGO supported in wood waste charcoal (nGO(NH)R/C) towards the MB, RB and DR. Analysis of the point of zero net charge (pH_{PZC}) and pH effect showed that the nGO-NH_2-Fe_3O_4 pH_{PZC} was 8.2, hence the MB adsorption was higher at pH 12.0; however, the adsorption of RB and DR was not influenced by pH changes. Kinetics studies indicated that the system reached the equilibrium state after 5 min, 90 min and 120 min for MB, RB and DR, respectively. Adsorption capacity at equilibrium (q_e) were 971.43±3.13 and 177.86±10.32 mg/g; and kinetic constant (k_S) of 0.053±0.025 and 0.0024±0.0007 g/mg/min, for MB and RB, respectively. The pseudo-second-order model was better fitted to the experimental data. Equilibrium studies showed maximum monolayer adsorption capacity (q_m) of 2319.20±269.37, 264.17±15.04 and 219.75±78.55 mg/g for MB, RB and DR, respectively; furthermore, Langmuir-Freundlich isotherm best fitted the adsorption for almost all system evaluated. Thermodynamic experiments revealed that all systems were spontaneous [Delta(Gº) < 0] and evidenced the physical nature of the adsorption of MB [Delta(Hº) –150 kJ/mol] by nGO-NH_2-Fe_3O_4, whilst the removal of RB and DR was characterized as chemisorption, with Delta(Hº) 92.83 kJ/mol and 66.43 kJ/mol respectively. Recycling experiments showed that the nGO-NH_2-Fe_3O_4 maintained the MB removal rate above 95% after ten cycles. Amino-nGO was then anchored on vegetal charcoal with the objective to ease sorbent separation from aqueous medium. Despite the relatively lower adsorptive capacity towards MB dye (q_m 52.98 mg/g) in comparison to nGO-NH_2-Fe_3O_4, nGO(NH)R/C showed a quick decantation in comparison to nGO. Phytotoxicology studies on lettuce seeds evidenced an

elevated germination and elongation when exposed to nGO-NH_2-Fe_3O_4 suspension differently from pristine material, nGO. All the results showed sorbent high adsorption capacity and outstanding regeneration capability and evidenced the employment of novel nGO-NH_2-Fe_3O_4 as a highly efficient adsorbent of textile dyes. Aiming to ease the separation of the adsorbent from the effluent after the adsorption, nGO(NH)R was supported in wood waste charcoal. Sedimentation tests showed that nGO(NH)R/C fully decanted within one day, differently from nGO, that decanted after four days. Furthermore, adsorption experiments with MB were carried out for nGO(NH)R/C and showed an equilibrium time of 20 min, maximum adsorption capacity in the monolayer of 54 mg/g and a spontaneous and exothermic behavior.

Keywords: 2D nanomaterials. Adsorption. Functionalization. Graphene. Intermolecular interactions. Textile wastewaters.

RESUMO

Neste trabalho, o óxido de grafeno em n-camadas (nOG) foi sintetizado a partir da oxidação de grafite pelo método de Hummers modificado. Posteriormente, o nOG foi funcionalizado com dietilenotriamina (DETA) e $FeCl_3$ a 180 ºC para obtenção do novo óxido de grafeno amino-Fe_3O_4-funcionalizado (nOG-NH_2-Fe_3O_4). Análises de espectroscopia no Infravermelho (FTIR) e de Raman, Difração de Raios-X (XRD), Microscopia Eletrônica de Varredura (MEV), Microscopia de Força Atômica (AFM) e Termogravimetria (ATG) foram realizadas para caracterizar o nOG e nOG-NH_2-Fe_3O_4. O nOG-NH_2-Fe_3O_4 e o nGO foram então avaliados como adsorventes do corante catiônico Azul de Metileno (AM) e dos corantes aniônicos Remazol Preto B (RB) e Drimaren Vermelho (DV) através de uma abordagem comparativa. Estudos em batelada de cinética, equilíbrio, termodinâmica e regeneração do adsorvente foram realizados para investigar a afinidade do nOG, nOG-NH_2-Fe_3O_4 e o nOG amino-funcionalizado suportado em carvão vegetal de resíduos de madeira (nOG(NH)R/C) para o AM, RB e DV. A análise do ponto de carga zero (pH_{PZC}) e o efeito da variação do pH mostraram que o pH_{PZC} do nOG-NH_2-Fe_3O_4 foi de 8,2, e a adsorção de AM foi maior em pH 12,0. A adsorção do RB não foi influenciada pela variação do pH. Estudos de cinética indicaram que o sistema atingiu o estado de equilíbrio após 5 min, 90 min e 120 min para o AM, RB e DV. A capacidade de adsorção no equilíbrio (q_e) foi de 971,43±3,13 e 177,86±10,32 mg/g; e a constante cinética (k_S) de 0,0529±0,0248 e 0,0024±0,0007 g/mg/min, para o AM e o RB, respectivamente. Além disso, o modelo de pseudo-segunda ordem foi o que melhor se ajustou aos dados experimentais. Estudos de equilíbrio mostraram capacidade máxima de adsorção na monocamada de 2319,20±269,37 e 264,17±15,04 e 219,75±78,55 mg/g para o AM, RB e DV, respectivamente; além disso, a isoterma de Langmuir-Freundlich se ajustou melhor à adsorção em praticamente todos os sistemas avaliados. Experimentos de termodinâmica revelaram que todos os sistemas foram espontâneos [Delta(G^o) < 0] e evidenciaram a natureza física da adsorção do AM pelo nOG-NH_2-Fe_3O_4 [Delta(H^o) –150 kJ/mol], enquanto a remoção de RB e DV foi caracterizado como quimissorção, com Delta(H^o) 92,83 kJ/mol e 66,43 kJ/mol respectivamente. Experimentos de reciclagem mostraram que o nOG-NH_2-Fe_3O_4 manteve a taxa de remoção de AM acima de 95% após dez ciclos. Estudos de fitotoxicologia em sementes de alface evidenciaram uma elevada germinação e alongamento quando expostas à suspensão de nOG-

NH_2-Fe_3O_4, diferentemente do material precursor, nOG. Todos os resultados mostraram elevada capacidade de adsorção e de regeneração do adsorvente, evidenciando o nOG-NH_2-Fe_3O_4 como um adsorvente de alta eficiência de corantes têxteis. Com o objetivo de facilitar a separação do adsorvente do efluente após a adsorção, o nOG(NH)R foi suportado em carvão vegetal de resíduo de madeira. Testes de sedimentação mostraram que o nOG(NH)R/C decantou em dois dias, diferentemente do nOG, que decantou após quatro dias. Além disso, experimentos de adsorção com AM foram realizados para nOG(NH)R/C e mostraram um tempo de equilíbrio de 20 min, capacidade máxima de adsorção de 54 mg/g e comportamento espontâneo e exotérmico.

Palavras-chave: Adsorção. Efluentes têxteis. Funcionalização. Grafeno. Interações intermoleculares. Nanomateriais 2D.

LIST OF FIGURES

LIST OF TABLES

LIST OF ABBREVIATIONS

AFM	atomic force microscopy
AOP	advanced oxidation process
APHA	American Public Health Association
AR27	Acid Red 27 (Red Amarant dye)
ATR	Attenuated Total Reflectance
BB41	Basic Blue 41 (dye)
BET	Brunauer, Emmett e Teller (specific surface area, or isotherm model)
BOD	biochemical oxygen demand (in mg $O_2 \cdot L^{-1}$)
BR46	Basic Red 46 (dye)
CBOD	carbonaceous biochemical oxygen demand (in $mg \cdot L^{-1}$)
CF	carbon fiber
CMG	chemically modified graphene
COD	chemical oxygen demand (in mg $O_2 \cdot L^{-1}$)
CV	Crystal Violet
CVD	chemical vapor deposition
DETA	Diethylenetriamine
DFT	Density Functional Theory
DLS	dynamic light scattering
DR	Drimaren Red
DTC-GO	dithiocarbamate functionalized graphene oxide
EDS	electron dispersive spectroscopy
FTIR	infrared spectroscopy with Fourrier transform
GHNFs	graphene embedded hydrogel nanofibers
GNP	graphite nanoplatelets
GO	graphene oxide
GQD	graphene quantum dots
G-S	gas-solid, for adsorption systems
H-bond	Hydrogen bond
HRTEM	high resolution transmission electron microsocopy

IL	ionic liquid
IL-$NH_2(Br^-)$-GO	[1-(3-aminopropyl)-3-methyl imidazoliumbromide]-functionalized graphene oxide
IPD	intraparticle diffusion (kinetic model from Webber & Morris)
L-F	Langmuir-Freundlich (isotherm model)
L-S	liquid-solid, for adsorption systems
MB	Methylene Blue
MF	microfiltration
MO	Methyl Orange
MNPs	magnetic nanoparticles
NF	nanofiltration
nGO	n-layered (multilayer) graphene oxide
nGO-NH_2-Fe_3O_4	n-layer amino-Fe_3O_4-functionalized graphene oxide
nGO(NH)R/C	n-layer amino-functionalized graphene oxide anchored in charcoal
nZVI	zero valent iron
PFO	pseudo-first-order
PIL	poly(ionic liquid)
PNO	pseudo-n^{th}-order
PPDA	poly(diallyldimethylammonium chloride)
PS	Ponceau S (dye)
PSO	pseudo-second-order
PTFE	Poly(tetrafluorine-ethylene)
PVA	poly(vinyl) alcohol
PZC	point of zero charge (or isoelectric point)
RB	Remazol Black B (Reactive Black 5)
rGO	reduced graphene oxide
RO	reverse osmosis
RR2	Reactive Red 2 (Brilliant Red 5SKH or Procion Red MX-5B dye)
SEM	Scanning electron microscopy
STM	Scanning tunneling microscopy
STS	Scanning tunneling spectroscopy

TB	Trypan Blue (dye)
TEM	transmission electron microscopy
TSS	total suspended solids (in $mg \cdot L^{-1}$)
VSM	vibrating sample magnetometer
XRD	X-ray diffraction
XPS	X-ray photoelectron spectroscopy
UF	ultrafiltration
WWC	wood waste charcoal

LIST OF SYMBOLS

a_T	binding constant at the equilibrium for Temkin isotherm (in $L \cdot mg^{-1}$ or $L \cdot mol^{-1}$)
b_T	Temkin constant (in $kJ \cdot mol^{-1}$)
C	final concentration or concentration at equilibrium state (in $mg \cdot L^{-1}$ or $mol \cdot L^{-1}$)
C_0	initial concentration (in $mg \cdot L^{-1}$ or $mol \cdot L^{-1}$)
K_{Eq}	equilibrium constant of Langmuir isotherm (in $L \cdot mg^{-1}$)
K_F	equilibrium constant of Freundlich isotherm (in $(mg \cdot g^{-1}) \cdot (mg \cdot L^{-1})^n$)
k_f	adsorption rate constant for pseudo-first-order (PFO) model (in min^{-1})
K_L	equilibrium constant for the best fitted model, in the equivalent temperature, "T" for using in van't Hoff equation (dimensionless)
K_{LF}	equilibrium constant for L-F model (in $L \cdot mg^{-1}$)
k_n	adsorption rate constant for pseudo-n^{th}-order (PNO) model (in $(g \cdot mg \cdot min^{-1})^{1-n}$)
k_s	adsorption rate constant for pseudo-second-order (PSO) model (in $g \cdot mg^{-1} \cdot min^{-1}$)
n	heterogeneity factor (for L-F isotherm) and pseudo-n^{th}-order of PNO model (kinetics)
q	adsorption capacity (in $mg \cdot g^{-1}$)
q_t	adsorption capacity in a certain time "t" (in $mg \cdot g^{-1}$)
q_m^{exp}	experimental monolayer adsorption capacity (in $mg \cdot g^{-1}$)
q_m^{calc}	calculated/modeled monolayer adsorption capacity (in $mg \cdot g^{-1}$)
q_e^{exp}	experimental adsorption capacity at equilibrium for kinetics (in $mg \cdot g^{-1}$)
q_e^{calc}	calculated/modeled adsorption capacity at equilibrium for kinetics (in $mg \cdot g^{-1}$)
R	universal constant of perfect gases (8.314 $J \cdot mol^{-1} \cdot K^{-1}$ (IS); 0.082 $atm \cdot L \cdot mol^{-1} \cdot K^{-1}$)
R^2	coefficient of determination (dimensionless)
S_{BET}	specific surface area acquired from N_2 adsorption-desorption – BET method (in $m^2 \cdot g^{-1}$)
S_{DLS}	specific surface area acquired from granulometry by DLS (in $m^2 \cdot g^{-1}$)
2D	two-dimensional (for monolayer graphene and graphene oxide)
3D	three-dimensional (for graphite and other graphene-derived nanocomposites)

GREEK LETTERS

$\delta_{(O–H)}$	variation of energy relative to the ionic bond between oxygen and hydrogen, which forms water molecules
ΔG^o	standard variation of Gibbs free energy (in $kJ \cdot mol^{-1}$)
ΔH^o	standard variation of enthalpy (in $kJ \cdot mol^{-1}$)
ΔS^o	standard variation of entropy (in $kJ \cdot K^{-1} \cdot mol^{-1}$)
λ_{max}	wavelength of the maximum absorbance in UV-Vis spectra
$\pi–\pi$	type of interactions between two chemical species with π-delocated electrons
2θ	X-Ray diffraction angle (in degree)
χ^2	chi-square factor (dimesionless)
$1/\rho$	parameter of Chan and Chu model, which describes the initial removal rate of a species in photodegradation kinetics (in min^{-1})
$1/\sigma$	parameter of Chan and Chu model, relative to the maximum oxidative capacity

SUMMARY

1 INTRODUCTION

Textile industry is one of which most generate jobs around the world. This is due to its vast productive chain, which starts with the fiber production in the field (or industry) and ends up with the cloth design and dressmaking. Moreover, the textile industry subsidizes parallel sectors, such as chemical companies, especially those which produce dyes. Based on the colour index, nearly 10,000 different textile dyes are produced annually, resulting in the production of more than 700,000 tons of dye worldwide (VELUSAMY *et al*., 2021). Regarding the textile production, it is composed by several steps: sizing, de-sizing, scouring, bleaching, mercerizing, dyeing, printing and finishing (VELUSAMY *et al*., 2021; YASEEN; SCHOLZ, 2019). Among them, the finishing process is the one which presents the most deleterious potential to environment and human health. This is because of the vast consumption of water and consequently the great volume of effluents. According to recent literature survey, it is estimated that approximately 200 L of water are applied in the production of 1 kg of textile material (YASEEN; SCHOLZ, 2019). Therefore a significant part of dyes are released in the effluents of textile finishing (YASEEN; SCHOLZ, 2019).

The effluents from the textile factories are mainly characterized as alkaline with high chemical oxygen demand (COD) and biochemical oxygen demand (BOD). COD and BOD values in the last decade varied in the range of (150–30000) $mg \cdot L^{-1}$ and (80–6000) $mg \cdot L^{-1}$ on average (SAMSAMI *et al*., 2020). When the disposal of textile wastewaters takes place without due treatment, it results in severe environmental impacts. Because of their persistence and toxicity, discarded dyes in water bodies have become a source of constant concern. Additionally, most of them are not biodegradable and reduce the penetration of light into water bodies. This fact inhibits algae photosynthesis and tends to accumulate in living organisms (VELUSAMY *et al*., 2021; HU; DENG; CHENG, 2017). The presence of aromatic rings in their structures makes dyestuffs carcinogenic and mutagenic, not only in aquatic animals, but also in humans, even at low concentrations (LAI *et al*., 2019).

The continuous monitoring of organic load and presence of carcinogenic compounds in effluents dumped in water bodies is a great challenge given the limited resources of the companies. Despite government and non-governmental organization efforts in the last decades, there was a lack of a culture oriented towards environmental preservation. This fact is observed, above all, in the regions of Pernambuco countryard, such as the municipalities of Caruaru,

Toritama and Santa Cruz do Capibaribe, where small and medium-sized laundries predominate. These companies fit into the typology of small industrial dyeing machines, which provide services to various jeans manufacturing companies, scattered throughout the municipality.

The environmental liability worsens as these effluents are released into the region's water bodies, responsible for the water supply of the municipalities mentioned. It is noteworthy that the semi-arid region of Pernambuco suffers from chronic problems of water shortages due to successive periods of drought. Together with the discharge of textile effluents into the water bodies, the lack of basic infrastructure in the region, such as drainage network and poor distribution of drinking water (FARIAS, 2012), contributes to aggravate the situation. Disorganized disposal of effluents, allied with the scarcity of rainfall, has also led to problems in water quality. These phenomena somehow increase the cost of the sanitation company responsible for supply in the region. In order to mitigate the problems of water shortage and quality, micro-enterprises responsible for laundries and dry cleaners have adpted reuse of water in their processes (CAVALCANTE, 2015). The process of removal of dyes by adsorption is an admittedly tertiary treatment, since it is usually used after processes such as filtration, aeration, biodigestion, flocculation, among others.

In this scenario, many researchers have been focusing on developing new methods, or improving the stand ones, to treat effluents from the textile industry targeting the water decontamination, management, and reuse (DOTTO; McKAY, 2020). Among the most studied processes to treat textile wastewaters are flocculation, aeration, advanced oxidation processes (AOPs), membrane filtration – ultrafiltration (UF), microfiltration (MF), nanofiltration (NF), and reverse osmosis (RO) – and adsorption. Among the physical processes, adsorption has gained attention over the decades due to its low cost and easy operation (DOTTO; McKAY, 2020). Several of these researches have as object of study highly selective materials with good adsorptive capacity. Among these, nanomaterials derived from carbon have occupied a prominent place in recent research (REYNOSA-MARTÍNEZ *et al*., 2020; YAP *et al*., 2020; ROHAIZAD *et al*., 2020).

In this regard, graphene, along with its derived nanomaterials (graphene oxide (GO), reduced graphene oxide (rGO) and their functionalized counterparts), has been studied for its remarkable properties. One of the most important characteristics of graphene to be considered is its potential for use in effluent treatment, mostly due to its large surface area (theoretically up to

2630 $m^2 \cdot g^{-1}$) (EIGLER; HIRSCH, 2014; DAI *et al*., 2012; PARK; RUOFF, 2009) and its planar geometry (DHAR *et al*., 2021; GONZÁLEZ *et al*., 2015). Furthermore, graphene and its derivatives have been recently employed in several environmental applications: photodegradation of water pollutants; constitution of solar cells panels (CHEN *et al*., 2020; RASHEMI *et al*., 2020); pollution sensing and monitoring (PIRAS; EHLERT; GRYN'OVA, 2021; GEVAERD *et al*., 2020); desalination and water purification (LI; ZHU; ZHU, 2019); and adsorption of gaseous and water pollutants (REYNOSA-MARTÍNEZ *et al*., 2020; ARAÚJO *et al*., 2020; YOUSEFI *et al*., 2019).

In the present work, we have shown that adsorbents of different types of dyes have been widely used in the capture of these toxic and carcinogenic substances (DHAR *et al.*, 2021; GE *et al*., 2016; WANG *et al*., 2014). With the objective to enhance the sorbent selectivity, amino-functionalization of graphene and GO was chosen to promote modifications on their surface characteristics by the introduction of selected functional groups. Such modifications originate materials classified as chemically modified graphenes (CMGs) (WANG *et al*., 2018a). According to Georgakilas *et al*. (2016) and Eigler and Hirsch (2014), the interactions may be through covalent bonds or weak bonds occurring between the lamellae of the graphene and the ligand compound. These functional nanomaterials show enhanced adsorptive properties in comparison to pristine graphene, such as higher adsorptive capacity, quicker adsorption kinetics, easy separation and greater regenerability, according to previous reports (ROHAIZAD *et al*., 2020; DAS *et al*., 2018). Therefore, functionalization is one of the best ways to improve the performance of graphene and GO as adsorbents of various industrial pollutants, and even in other applications.

2 NOVELTY AND ORIGINALITY

Studies which refer to the adsorption of different class of dyes by precursor materials of graphene [e.g. graphite powder, expanded graphite and graphite nanoplateletes (GNP)] have been previously conducted by other researchers and their results can be found in the literature (DE OLIVEIRA *et al*., 2019; CARVALHO *et al*., 2016). The precursor process of simultaneous functionalization with amino groups and iron (III) oxide on the surface of GO nanosheets was developed by Zhao *et al*., (2016) and was the reference for what have been developed in this work. However, their process was carried out in a closed stainless steel reactor, with an aggressive temperature of 200 ºC. Moreover, this adsorbent was applied in the removal of chromium (VI) ions from aqueous solutions. Distinctively, the functionalization process of the GO layered nanosheets performed in this work was carried out in an open system, which allows the reflux of the monoethyleneglycol, and with a milder temperature, around 150–180 ºC, aiming the reduction of energy cost. Finally, the new amino-Fe_3O_4-functionalized multilayered graphene oxide, developed in this work, was applied in the adsorption of the cationic Methylene Blue (MB) and the reactive anionic dyes Remazol Black B (RB) and Drimaren Red (DR).

A second innovation is the application of the amino-functionalized multilayer GO nanosheets with iron oxide (III) (initially termed nGO-NH_2-Fe_3O_4) in the removal of reactive textile dyes. This approach difers from most of articles found in the literature, which investigated functionalized nanocarbons for the adsorption of metallic ions and Methylene Blue. As an example, Wang *et al*. (2018a) have made an interesting survey on the use of amino-functionalized nGO as adsorbent of several pollutants in aqueous medium. In the study, eight species of dyes were reported; however, most of the amino-functionalized GO nanocomposites have been used to adsorb Methylene Blue (with adsorbance capacity ranging from 95.00 to 819.00 $mg \cdot g^{-1}$); yet, below the results obtained by nGO-NH_2-Fe_3O_4 for Methylene Blue removal reported in this work. Several similar processes of amino-functionalization found in the literature, such as the one developed by Goscianska, Fathy and Aboelenyn (2017), are reported with the objective of functionalizing mesoporous charcoal. The authors employed it in the adsorption of direct dye Solophenyl Red 3BL. However, there are not enough reports on nGO-NH_2-Fe_3O_4 used as reactive dye adsorbents, which are responsible for 10 to 50% of the species present in textile effluents (KYZAS *et al*., 2018). Amino-functionalization was chosen due to its feasibility and strong potential to increase the availability of delocalized π-electrons over amino-functionalized

nGO. These π-electrons has the potential to ease π–π stacking interactions between nGO and the large structures of reactive dyes, which mainly show azo (N=N) and benzyl groups in their structures. Additionally, the amines can form strong bonds with some groups of dyes, such as sulfonic ($–SO_3^-$), and H-bonds with hydroxyl and halogens, also present in these molecules.

A third innovative feature was the process of grafting the multilayer nGO(NH)R on(into) wood waste charcoal, which occurred along with the functionalization synthesis itself. This novel adsorbent was named in this work nGO(NH)R/C. Such concern arises from the fact that the process of separation of graphene or GO/nGO nanosheets from the liquid medium is a great challenge due to the high hydrophilic character of the GO (PARK; RUOFF, 2009). In order to separate adsorbents based on nanocarbons, centrifugation at high rotational speeds, for long periods of time (over 10 min), vacuum filtration in teflon membranes, or even magnetic separation, is usually employed when grafting onto fibers or iron meshes (ZHAO *et al*., 2016, GE *et al*., 2016). With the supporting of nGO(NH)R on wood waste charcoal, an adsorbent of easy separation was obtained, which could be carry out by simple filtration (in which paper filters may be used), rapid centrifugation, or even decanting. The decrease in spin time, or spin speed, is a reduction in the cost of energy during this step.

Additionally, it is not common find published works in the literature which deals with adsorptive process involving real textile effluents. Then finally, nGO-NH_2-Fe_3O_4 and nGO(NH)R/C were tested in the treatment of raw textile effluent, with the monitoring of core-properties of it: biochemical oxygen demand (BOD), chemical oxygen demand (COD), volatile and total solids, pH, concentration and colour. This work aims to contribute to clarify this theme and change the reality of local communitites of Pernambuco State contryard.

3 GENERAL OBJECTIVE

To develop a new adsorbent based on covalent functionalized multilayer GO to remove dyes used in the textile industry. Additionally, evaluate its application in treatments of real textile effluents.

3.1 SPECIFIC OBJECTIVES

a) Development of covalently functionalizedspecieis to the nGO and its anchorage on the coal, derived from the gaseification process of wood residues, aiming to improve the posterior separation process of the adsorbent;
b) Characterization of functionalized graphene through the analysis of infrared spectroscopy (FTIR), Raman spectroscopy, X-ray diffraction (XRD), atomic force microscopy (AFM), thermogravimetric analysis (TGA) and finally, point of zero charge (pH_{PZC});
c) Perform adsorption tests with functionalized nGO as adsorbent of Methylene Blue and later with dyes used in textile industry, such as the azo-reactive Remazol Black B - to perform pH effect evaluation; and kinetic, equilibrium and thermo-dynamic studies;
d) Evaluation of adsorption kinetic and equilibrium models, applied to the experimental data; hence, the parameters obtained from the modeling;
e) Investigate the equilibrium parameters for a binary mixture of the dyes MB and RB following the predicted isotherm of Langmuir for a binary system, as wells as to carry out the investigation of the effect of pH on the adsorption;
f) Perform sorption experiments with nGO-NH_2-Fe_3O_4 and nGO(NH)R/C as adsorbents of raw textile effluents, collected in laundries and cleaners of Pernambuco countryard;
g) To evaluate the recyclability of nGO-NH_2-Fe_3O_4 by adsorption/desorption experiments;
h) Carry out the economic assessment of the synthesis and operation of nGO-NH_2-Fe_3O_4;
i) Investigate the phytotoxicity of nGO-NH_2-Fe_3O_4 and its pristine materials (graphite nanoplatelets and nGO) to plants by product exposure tests.

4 STATE OF THE ART

Between many properties, carbon can form several structures with different morphologies. Between them, the sp^2 hibridized allotropes have attracted the attention due to their many applications in diverse fields, from electronics to health and environmental science. Between the carbonaceous nanomaterials, it may be included some of well-defined forms, such as large fullerenes, carbon nanotubes (CNT), nanohorns, carbon fibers (CFs), nanosheets and nanoblocks (e.g. graphite), as depicted in Figure 1. Among the carbonaceous materials, graphene has attracted a great deal of interest from researchers worldwide due to its unique structural characteristics, application versatility and high adsorption performance.

Figure 1 - Illustration of the carbon allotropes classified according to their dimensions: fullerene, carbon nanotube, nanohorn, graphene nanosheet and nanoblock

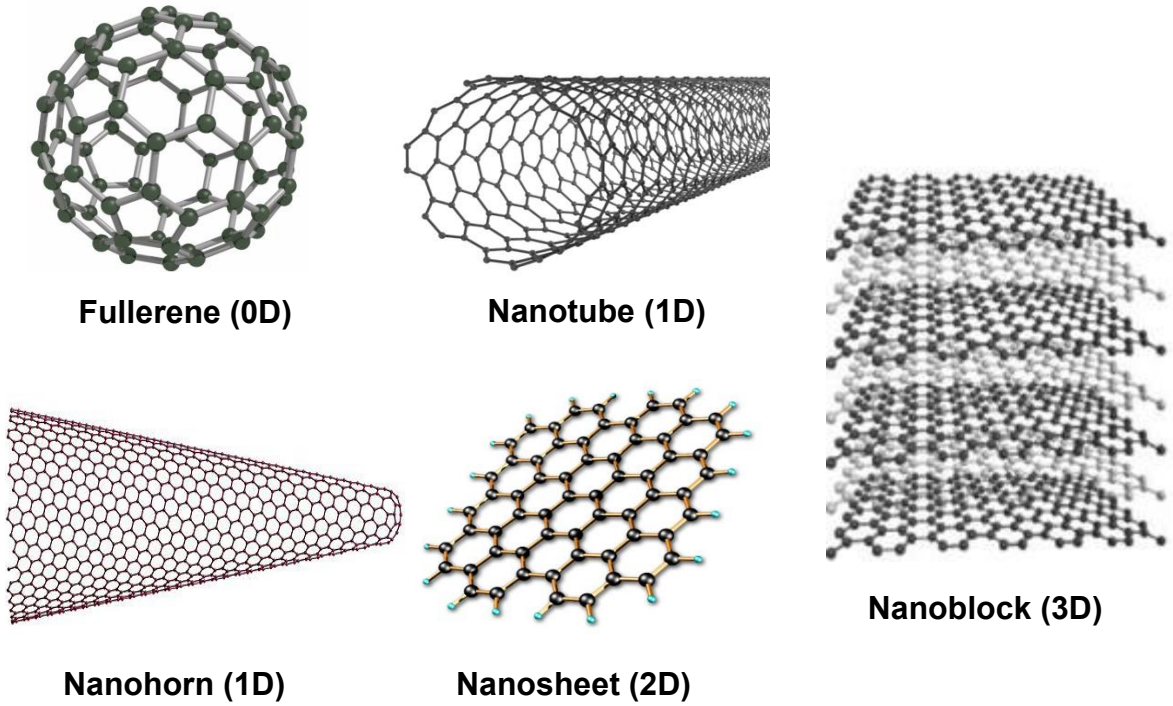

Source: the author (2020).

Idealized graphene is a two-dimensional (2D) nanosheet of pure carbon allotrope formed by hexagonal honeycomb lattice structures (similar to a benzene ring) with a hybridized sp^2

electronic configuration with molecular weight of 10^6–10^7 g·mol^{-1} (EIGLER; HIRSCH, 2014; PARK; RUOFF, 2009), as depicted in Figure 1. It is said "idealized", since any heteroatom and deffects would be found in its carbonaceous lattice; in contrast, "real" graphene posess some impurities in their structures, mostly oxygen compounds and oxides (EIGLER; HIRSCH, 2014). Moreover, 2D graphene differs from Graphene Oxides (GO), since these nanomaterials are remarked by their oxygenated functional moieties and defects in their structure, which change many of their sp^2 carbons into a sp^3 configuration, as a result of the oxidation of graphite in the presence of strong acids and oxidants (PARK; RUOFF, 2009).

Graphene is also renowned by its great mechanical properties, such as great flexibility and resistence; in this regard, graphene exhibited a tensile strength of 1916 MPa and Young's modulus of 233 GPa (GAO *et al*., 2020). Graphene and a relevant part of its derivates also posess outstanding electrochemical properties, such as electric mobility of ~ 5000.0 cm^2·V^{-1}·s^{-1}, in SiO_2 substrate, which might reach ~ 200,000.0 cm^2·V^{-1}·s^{-1} without substrate coverage (KLIMOV *et al*., 2012). Transparency is another distinguished property that allows CVD-graphene to be coated in diverse substrates: copper, polymer, gold and silicon, as examples (LIU *et al*., 2017; RAFIEE *et al*., 2012). Such properties allow the application of graphene in electronic devices, conductors, sensors and in sensitive screens.

Functionalization of graphene, on the other hand, consists in adding specific functional groups to graphene plane and edges, which would enhance some of its properties. Additionally, the functionalization path must be chosen according to the properties to be reached, and for that, a broad variety of functional groups may be applied: amines, amides, nitro, thio-compounds, halogen-derivatives, among others. In this sense, it is important to highlight that the oxidation of graphite itself is considered an oxygen-type functionalization method. Some of the many functionalization routes are discussed in details in Section 4.2.

4.1 GRAPHENE OVER THE TIME

Carbon “small” structures have attracted the attention of the chemists over the time. Thus, the chemical protocols used to synthetize graphite oxide from graphite powder by the addition of strong acids in a humid way late from more than a century. Between them, the most widespread methods are Brodie’s, Staudenmaier’s and, more recently, the Hummers’ (HUMMERS; OFFEMANN, 1958; STAUDENMAIER, 1898; BRODIE, 1860). However, these graphite oxide syntheses must be followed by mechanic exfoliation in order to obtain graphene oxide (GO) nanosheets. Nevertheless, most of exfoliation processes do not vouch satisfactory performance in the acquirement of monolayer/few-layered GO (Figure 2). Since Hummers’ method, developed in the late 50’s, many researchers have been working to improve it. Hummers’ methodology has been updated through the use of different types of reactants, varying their amounts, changing the reaction time and even optimizing some of the method’s conditions.

With respect to monolayer graphene (Figure 1), a pioneer mechanical method by which single nanosheets of graphene were obtained with a certain degree of purity was performed by Novoselov *et al*. (2004), who used *Scotch*-type tape to separate the graphene layers from the graphite crystals. Their endeavor leaded Novoselov and Geim to be awarded with the Nobel Prize for Physics in 2010. As a result of their research, classical methods of obtaining graphene and GO have been improved through the use of new routes such as controlled oxidation (MAHMOUDI *et al*., 2019; ARAÚJO *et al*., 2018; ZHU *et al*., 2010a), chemical reduction (ALAYANDE *et al*., 2019; DE SILVA *et al*., 2017), Chemical Vapor Deposition – CVD (LEE *et al*., 2021; SITEK *et al*., 2020; CHOI *et al*., 2019; LEVCHENKO *et al*., 2016; WU *et al*., 2013), electrochemical deposition/reduction (GEVAERD *et al*., 2020; ASSIS FILHO *et al*., 2020; DANILOV *et al*., 2019), ultrasonic exfoliation (GU *et al*., 2019; NAVIK *et al*., 2018), among others. In Figure 2, it is depicted the chemical routes to obtain GO, reduced-GO (rGO) and functionalized GO from graphite.

Figure 2 - Schematic representation of the chemical route to oxidize, reduce and functionalize the graphene from graphite.

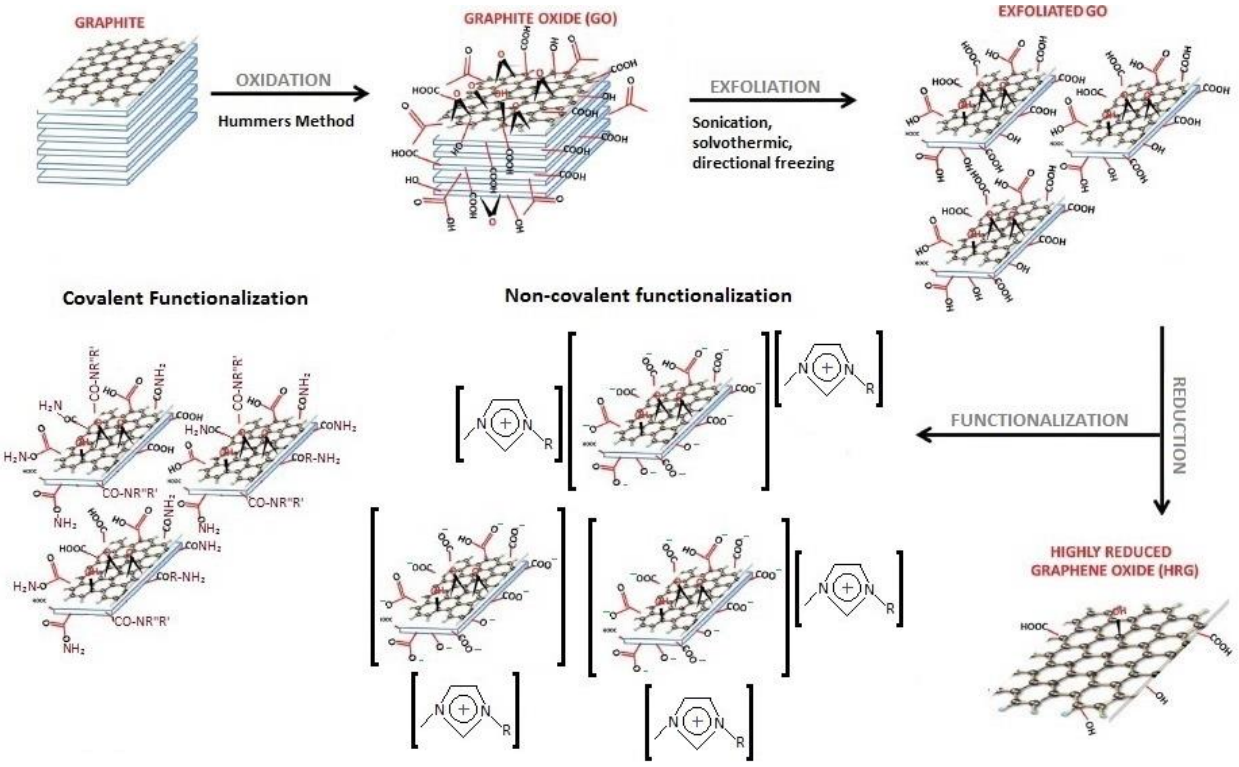

Source: adapted from FRAGA *et al*. (2019a), with permission from SciELO, Creative Commons 2021.

Recently, the ISO TS 80004/2017 was edited with the objective to better standardize the parameters of quality for 2D carbon nanomaterials. By this standard, graphene is considered, as a matter of nomenclature, as nanosheets and nanoblocks with a maximum stacking of 10 nanolayers (ISO, 2017), which can be detected through Atomic Force Microscopy (AFM) or Electron Transmission Microscopy (TEM). Previous works have reported the measurement of average thickness of a single 2D GO nanosheet by assessments of AFM profiles and Raman spectroscopy, which was approximately between 0.4–1.7 nm, taking into account the presence of impurities (SHEARER *et al*. 2016; EIGLER *et al*. 2014).

It is important to highlight the literature works which deal with the use of graphene, GO, and their derived nanomaterials for specific applications in the most varied fields of environmental science. Between them, it merits to be cited some recent investigations regarding to:

a) nanocomposites for flexible photocells, solar panels, smart batteries and other devices for energy generation and storage (CHEN *et al*., 2020; HASHEMI; RAMAKRISHNA; ABERLE, 2020; MUKHERJEE *et al*., 2020; WANG *et al*., 2020);

b) water desalination and the development of membranes for filtration technology – UF, NF and RO (CHEN *et al*., 2021; LEE *et al*., 2021; LI; ZHU; ZHU, 2019);

c) antimicrobial surfaces against bacteria, virus, fungi, among others (MOREIRA *et al*., 2021; VALENZUELA *et al*., 2020; ALAYANDE *et al*., 2019);

d) sewage monitoring, sanitization and bactericidal treatment (CHEN *et al*., 2018; NGUYEN; CASTRO-WALLACE; RODRIGUES, 2017);

e) capture of atmospheric pollutants and greenhouse gases by gas-solid (G-S) adsorption and gas-liquid absorption (ZEESHAN *et al*., 2021; GOHARIBAJESTANI; YÜRÜM; YÜRÜM, 2019; SZCZESNIAK *et al*., 2018), as well as the catalytic convertion of CO_2 into synthetic fuels (WANG *et al*., 2019a) and the sensing of gaseous pollutants (PIRAS; EHLERT; GRYN'OVA, 2021; KIM *et al*., 2020; PURBIA *et al*., 2020);

f) adsorption of heavy metals and metallic ions from aqueous media (REYNOSA-MARTÍNEZ *et al*., 2020; YAP *et al*., 2020; WANG *et al*., 2019b; GAO *et al*., 2017);

g) adsorption of dyes in batch/continuous flux from aqueous solution and, in few reports, the treatment of raw textile wastewater (ARAÚJO *et al*., 2020; LUZ-ASSUNCIÓN *et al*., 2020; KYZAS *et al*., 2018);

h) photodegradation of dyes from synthetic and real textile wastewaters (BAPTISTTELLA *et al*., 2021; DA SILVA *et al*., 2021; MOZTAHIDA; LEE, 2020; YAO *et al*., 2019; WANG *et al*., 2019c; RAMALINGAM *et al*., 2018), among others.

4.2 FUNCTIONALIZATION OF GRAPHENE AND GRAPHENE OXIDE

In principle, functionalization of graphene takes place by chemical reactions on both sides of graphene plane, such as cycloaddition, radical additions, substitutions and rearrangements, such as nucleophilic addition. Other functionalization routes might be achieved by weak interactions between graphene/GO basal plane and ionic ligands. Many of these modifications are accompanied by the hybridization of carbon of sp^2 to sp^3 (EIGLER; HIRSCH, 2014; CHUA; PUMERA, 2013; ENGLERT *et al*., 2011).

One of the main advantages of graphene functionalization is the high selectivity towards specific chemical species (BUENO *et al*., 2017); this is a key factor when seeking to maximize interactions between adsorbent and adsorbate. Other advantages of graphene functionalization, cited by Perreault, de Faria and Elimelech (2015), are the increasing specific surface area; good colloidal stability; and the presence of functional groups in its structure. According to the authors, these properties give graphene and GO the ability to generate interactions of electrostatic nature, or even complexation with organic substances present in liquid phase. Differently from GO, some functionalized-GO and functionalized-reduced-GO exhibit a highly hydrophobic character (YOUSEFI *et al*., 2019), which make them easily separable from adsorbate, eliminating the need of nanometric filters.

As disadvantages, it is mentioned limitations in the choice of covalent/non-covalent route, which vary according to the need of application of the newly developed adsorbent, as well as their operational conditions. If, by one hand, functionalization gives to graphene-based adsorbents a high specificity towards specific compounds, on the other hand, it makes them limited in their use against adsorbates of different nature. Long period of reaction is usually necessary in order to attain the maximum functionalization degree of graphenic surface; this is pointed by some authors as a drawback (SAINSBURY *et al*., 2016). High investments in equipment and cost of synthesis in terms of reactants price, energy consumprion and purification processes can also be pointed as nother disadvantage (MAHMOUD; STOLLE; STELTER, 2018). Furhtermore, most covalent functionalizations are physically irreversible, hence reactants and graphene structures become irrecoverable (FENG *et al*., 2013).

Another issue regarding the protocols of functionalized graphene by chemical modifications is the collateral impacts derived from the processes. Given this, researchers tend to be cautious with energy consumption, formation of by-products during the synthesis, final destination of their nanocomposites, among others. Despite some studies reported graphene itself as non-toxic for mammalian cells in low concentration (PATTAMMATTEL *et al*., 2017; YANG *et al*., 2013), GO and functionalized graphene may release by-products in form of gases, chemicals and ionic species during their synthesis reaction and washing. Since their toxicity and harm to human health and the ecosystem are not yet entirely known, their disposal in the environment may be treated as a liability (HU; ZHOU, 2013; YANG *et al*., 2013).

4.2.1 Covalent versus non-covalent functionalization

Covalent functionalization of graphene is characterized by the presence of functional groups bound to the basal plane structure by intense intermolecular forces, with high binding energy, typical of covalent bonds, which usually changes the sp^2 hybridization of its G networks, resulting in the formation of defects and loss of electronic properties (PUNETHA *et al*., 2017; GEORGAKILAS *et al*., 2016; ARAUJO; TERRONES; DRESSELHAUS, 2012; ENGLERT *et al*., 2011). Characteristic functional moieties of these processes are the carbonyl, hydroxyl and carboxyl groups (resulting from the oxidation of graphite itself by Hummers Method or its modification) (HUMMERS; OFFEMANN, 1958); phenyl amines (e.g. melamine, in Figure 3a and b), amides, nitro, sulfoxides, sulfones, sulfonamides, among others. In some covalent routes, a functionalizing group, such as thionyl, can replace the hydroxyl groups that form on the graphene surface after oxidation (CAI; CASANOVA, 2016).

Thio organic compounds, such as thioacetate have been used to functionalize GO through the attack of the nucleophilic thiol to the nearest electrophilic carbon of the epoxide ring, or to the adjacent C=C bond, provoking the opening of the epoxide ring. The nucleophilic attack takes place under mild conditions (~50 ºC, 5h), and the novel thiol-functionalized-GO exhibited high selectivity for gold nanoparticles (THOMAS *et al*., 2014). Similarly, primary amines also have the ability to provoke a nucleophilic attack to epoxide rings in aqueous media, producing β-amino alchools with satisfactory yield, according to early investigations (CHUA; PUMERA, 2014; AZIZI; SAIDI, 2005). Sainsbury *et al*. (2016) studied the functionalization of graphene through carbene and found that the covalent bonding of the dibromocarbene groups resulted in the re-hybridization of the carbon atoms through the formation of cyclopropyl groups, whose degree of defect in the covalent functional group was confirmed by the spectroscopy of Raman. Figure 3a shows the covalent functionalization pathway of GO, used by Song *et al*. (2017) in which, it was used melamine and dimethylsulfoxide as ligand compounds. It is possible to understand the way in which the spaces between layers of graphene sheets are occupied by the functionalizing agent (melamine).

The mechanism of covalent amino-functionalization reported by Song *et al*. (2017) is depicted in detail by Figure 3b, which shows the activity of melamine ($C_3H_6N_6$) in a similar route to the protocol used in this thesis. From this protocol, the electronic pair of nitrogen in on of the three primary amines in melamine molecule provokes the nucleophilic attack to the adjacent

carbons of carboxyl and hydroxyl groups, forming a covalent bond (N–C) of amine and amide groups.

Even with the use of an IL or a PIL species, ionic compounds by nature (CHO *et al*., 2011), it is also possible to functionalize graphene nanomaterials by forming covalent bonds (Figure 3c). It depends of the reactivity of the functional groups in the ligand and the conditions of reactional medium (LAI *et al*., 2019). This is what was observed by Bhunia *et al*., (2012), who employed 1-(3-aminopropyl)-3-methyl imidazoliumbromide (IL-$NH_2(Br^-)$) IL to synthesize the IL-$NH_2(Br^-)$-GO, which mechanism is described in Figure 3c. Despite the ionic pole in the molecules of 1-(3-aminopropyl)-3-methyl imidazoliumbromide, the primary amine provoked a nucleophilic attack on the carbons of GO structure, as reported by the authors. Similarly, Zambare *et al*. (2017) observed, by analysis of X-ray photoelectron spectroscopy (XPS), the formation of amide bonds (401.6 eV) and C=O bonds (288.2 eV) between amino-methylimidazolium IL and carbonile groups of GO, resulting in the formation of amide centers over the entire structure.

Figure 3 – a) obtention of the functionalized graphene-amine oxide through the covalent route by the addition dimethyl sulfoxide and melamine; b) covalent amino-functionalization of GO at 150 ºC by Melamine; c) covalent functionalization of GO by the amine group of 1-(3-aminopropyl)-3-methyl imidazoliumbromide (IL-NH_2(Br^-)).

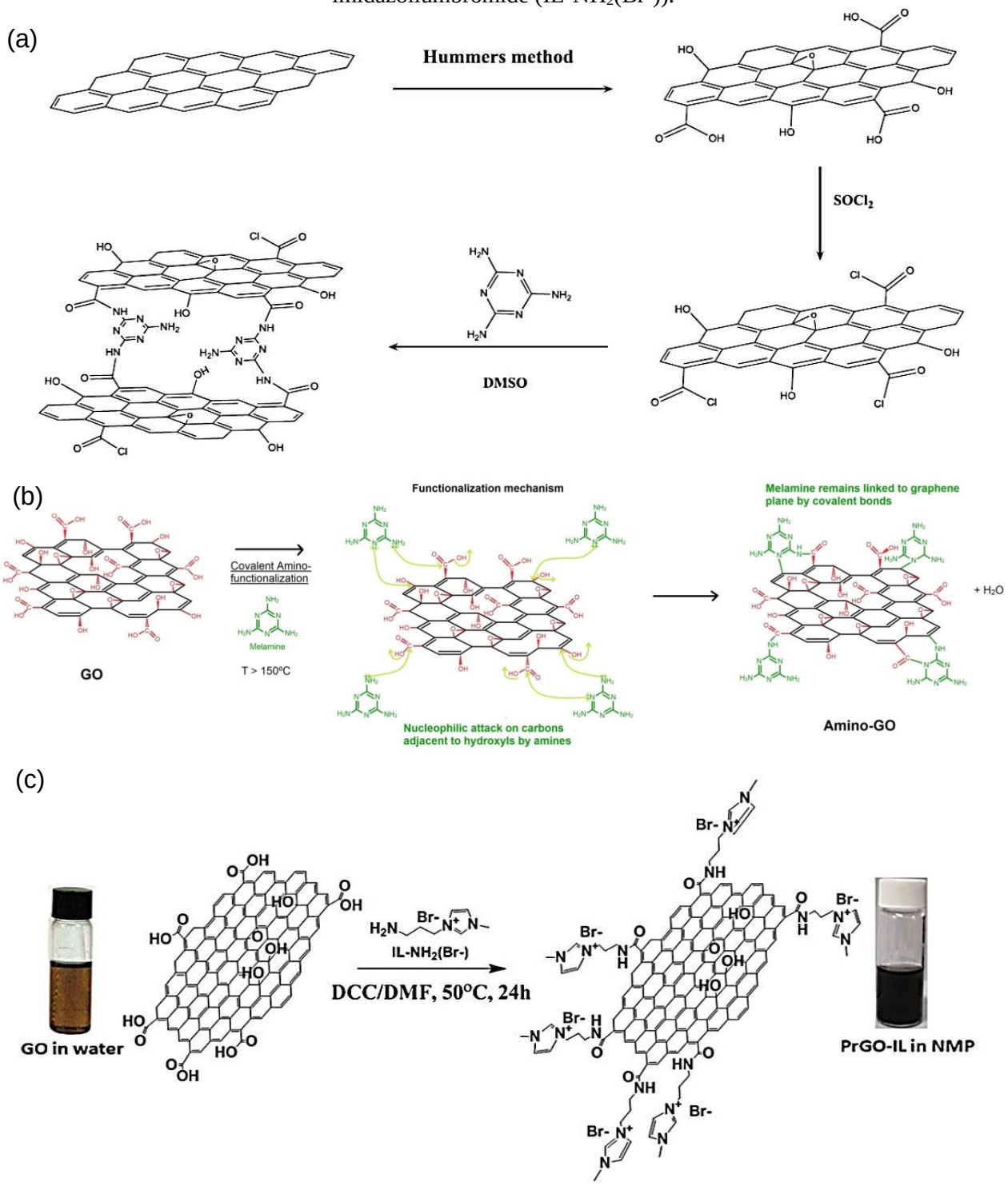

Source: a) reproduced from Song *et al*. (2017), with permission from Elsevier, Copyright 2020; b) reproduced from Fraga *et al*. (2020a), with permission from Elsevier, Copyright 2020; c) reproduced from Bhunia *et al*. (2012), with permission from the Royal Society of Chemistry, Copyright 2020.

Graphene or GO can also be functionalized through non-covalent routes, which generates the presence of functional groups based on weak interactions between them and the structure of the graphene, such as the π–π interactions, van der Waals forces, H-bonds and electron donor-receptor interactions (PUNETHA *et al*., 2017; EIGLER; HIRSCH, 2014). Generally, ionic, metallic or organometallic compounds, as well as metallic oxides, such as Mn^{2+}, CuO_2^{2-}, Fe_3O_4, α-Fe_3O_4, $MnFe_3O_4^{2+}$, among others, are employed in non-covalent functionalization of graphene, as depicted in Figure 4. In this sense, non-covalent functionalization is a necessary path to anchor metallic nanoparticles in graphenic plane. Moreover, most of works in the current literature report the use of bottom-up methods, such hydrothermal (DAS *et al*., 2018), solvothermal (AHMAD *et al*., 2021; ZHAO; LIU; HUANG, 2021) and precipitation/co-precipitation (BAPTISTTELLA *et al*., 2021), for anchoring metallic oxides over graphene frameworks (Figure 4b).

Sol-gel reaction is another bottom-up technique to successfully attach metallic oxides over graphene plane (NAZARI; SALEM, 2019). Sol-gel reaction consists in the producting a colloidal solution (sol) from metallic salts (or monomers, for polymeric matrices) and then concentrates it until it becomes a precursor for an integrated network (gel). According several reports, graphene/GO/rGO charges are introduced concomitantly prior the formation of gel phase.

There are plenty reports in recent literature which investigated the effects of the anchoring of non metallic nanoparticles in graphene basal planes; among them, it deserves to be highlighted silica nanoparticles (SiO_2, Si_xO_y) (CZEPA *et al*., 2020; SITEK *et al*., 2020), nanoclays (SENTHILNATHAN *et al*., 2020; DAS; MAI; DUAN, 2019), boron nitrides (RODRIGUEZ *et al*., 2021) and others. Furthermore, several routes for the anchorage of nanoparticles on graphene are associated to the anchoring of the whole charge and its dispersion over polymeric matrices (DAS; MAI; DUAN, 2019; JIANG *et al*., 2017).

Ionic liquids (IL) and poly-ionic liquids (PIL), such as polyvinylimidazole, polyvinylpyrrolidone, triphenylenes and pyrene derivatives, have been chosen by many researchers to functionalize graphene. It is mostly due to IL/PIL strong polarity, beyond their thermal, chemical and electrochemical stability and other adjustable physicochemical properties (YANG *et al*., 2019; PARVIZ *et al*., 2012; CHO *et al*., 2011). Usually, IL's and PIL's stay attached to graphene surface via weak dipole-dipole and ionic electron donor-receptor attractions (YANG *et al*., 2019). Moreover, interactions of cation-π nature are also reported, from which positively charged molecules of IL's are attracted by the negative pole formed the resonance of

delocalized π-electrons of the basal plane of GO, as depicted in Figure 4a. However, there are studies reporting the contributions of covalent link between certain reactive functional moieties in IL molecules and oxygenated functional groups of GO (ZAMBARE *et al*., 2017; BHUNIA *et al*., 2012), as previously discussed (see Figure 3c). Nevertheless, IL and PIL-functionalization are remarckably known as non-covalent due to the ionic nature of these compounds (CHO *et al*., 2011). Aditionally, the molecules of dyes interact with IL-GO/PIL-GO in aqueous medium mainly by π–π and electrostatic interactions, which confer high recyclability to these sorbents (ZAMBARE *et al*., 2017; ZHAO *et al*., 2015). Published works, which deals with adsorption of water and atmospheric pollutants, report notorious adsorptive capacity of PIL-GO/PIL-graphene in comparison with their precursor materials (YANG *et al*., 2019; ZAMBARE *et al*., 2017; HUANG *et al*., 2016; TAMILARASAN; RAMAPRABHU, 2015).

Furthermore, covalent functionalization of amine groups may occur in parallel to the solvothermic process of anchoring the metallic nanoparticles in the graphite plane. One example is the synthesis of Fe_3O_4 magnetic nanoparticles (MNPs) from the oxidation of $FeCl_3{\cdot}6H_2O$ in a humid way, according to processes reported in the literature (ZHAO *et al*., 2016; AI *et al*., 2013). Authors reported their anchorage on graphenic of GO plane concomitantely with amino-functionalization. Fe_3O_4 nanoparticles might be anchored to graphenic plane of GO-NH_2-Fe_3O_4 through low intensity interactions, mainly van der Waals forces and electrostatic interactions, being therefore non-covalent functionalization (GEORGAKILAS *et al*., 2016; EIGLER; HIRSCH, 2014). Both amino-functionalization and the non-covalent anchoring of Fe_3O_4 nanoparticles in nGO are depicted in Figure 4c.

Figure 4 – a) non-covalent functionalization of GO with an ionic liquid by cation-π interaction; b) anchoring of metallic nanoparticles over GO by hydrothermal, solvothermal and precipitation routes; c) amino-functionalization of GO in parallel with the solvothermal method of anchoring of Fe_3O_4 nanoparticles in the graphenic plane of GO.

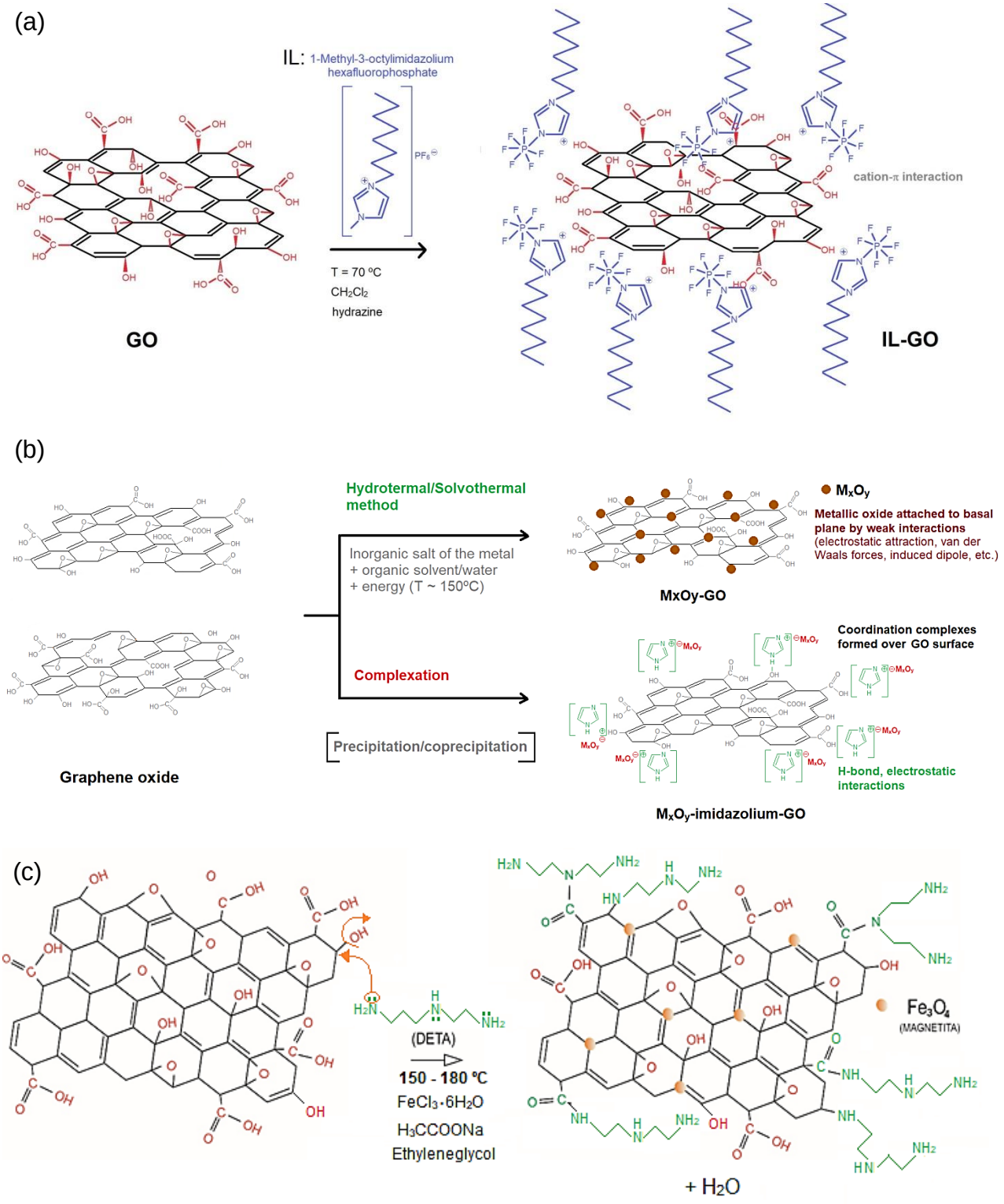

Source: the author (2020).

4.2.2 Properties of functionalized graphene

The linking of functional groups over the surface of the carbon nanocomposites guarantees properties that vary according to the type of functionalization employed. The functionalization method is determined by virtue of the application objectives of that material. Examplifying, the β-cyclodextrin-poly(1-glutamic acid) addition to the GO structure increases the adsorption capacity ($mg \cdot g^{-1}$, or $mmol \cdot g^{-1}$) of β-estradiol in aqueous alcoholic medium (JIANG *et al*., 2017), but this fact does not guarantee, by itself, that the same GO-γ-cyclodextrin-poly(1-glutamic acid) will have similar performance in adsorption of heavy metals.

The presence of functional groups linked to the graphene structure is easily detected by the infrared spectroscopy (FTIR) analysis, where new bands appear at different frequencies (cm^{-1}) compared to the previous spectrum (graphene or GO before of functionalization). As an example, Figure 5a exhibits infrared spectra of the GO before and after polyethyleneimine functionalization (SHU *et al*., 2017). In GO-polyethyleneimine (PFGA) spectrum, a band appeared in 1453 and 1653 cm^{-1} which are attributed to C-N stretching vibration and C=O stretching vibration of primary amides, both derived from polyethyleneimine. Nevertheless, GO characteristic bands remained in evidence in PFGA spectrum, such as 3000–3600 cm^{-1} (vibration stretching of hydroxyl groups); and 1731 cm^{-1} (stretching vibration of C=O bonds from carboxyl groups).

Im *et al*. (2017) impregnated graphene nanosheets with polyvinyl alcohol (PVA) and subjected it to electrical pulses to synthesize the graphene embedded hydrogel nanofibers (GHNFs), as termed by the authors. Aftewards, this novel nanocomposite was applied in the adsorption of Methylene Blue (MB) and Crystal Violet (CV) dyes in continuous flux. The electric double-layer capacitance modification conferred electrochemical affinity and high selectivity to this new composite in order to detect the presence of the MB and CV cationic dyes in systems with flow. In order to evaluate the nature of the interactions between the adsorbent and the adsorbate, the Density Functional Theory (DFT) was used through the software Gaussian 09 and ORCA 3.3. The authors verified that the physical interactions π–π were present in order to stabilize the adsorbent-adsorbate configuration in the aqueous medium, which caused changes in the impedance of the medium.

Figure 5 – a) Infrared spectra (FTIR) for GO and GO-poly(ethyleneimine) (PFGA); b) X-ray patterns (XRD) of GO and GO-poly(ethyleneimine); c) FTIR spectra for dibromocarbene-functionalized GO and GO; d) Raman spectra for dibromocarbene-functionalized GO and GO.

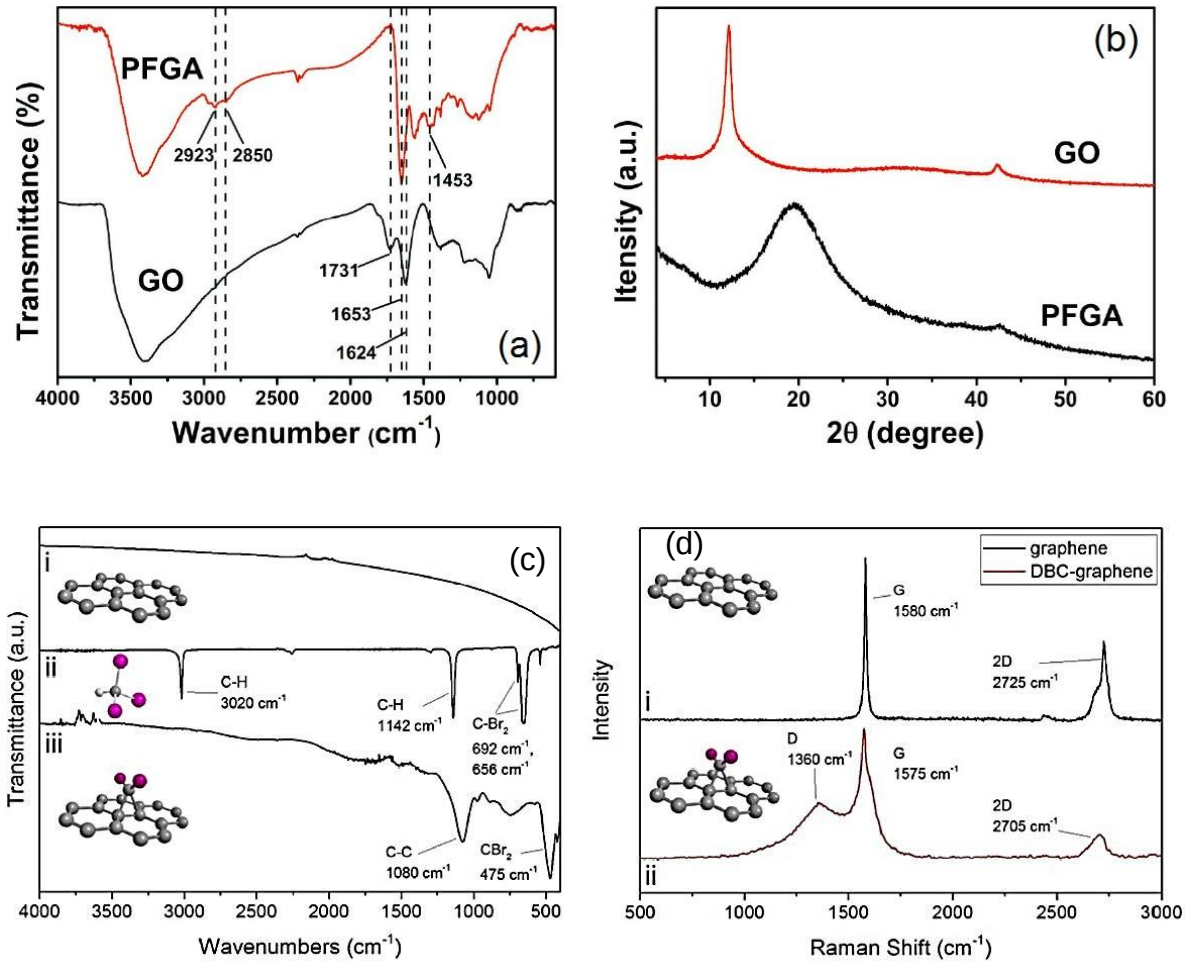

Source: (a) and (b) reproduced from Shu *et al*. (2017), with permission from Elsevier, Copyright 2020; (c) and (d) reproduced from Sainsbury et al. (2016), with permission from American Chemical Society, Copyright 2020.

X-ray diffraction (XRD) analysis has been applied to reveal the presence of metallic compounds in the graphene frameworks. For carbon nanomaterials, it is an important tool to assess changes in material crystalline structure after modifications. In addition, the interaction of X-rays with a crystalline phase results in the creation of a standard diffraction pattern (LAI *et al*., 2019). Figure 5b shows two X-ray spectra for GO before and after polyethyleneimine functionalization, where it is possible to check the peak displacement at 2θ from 15º to 20º. This corresponds to a decrease in the space between layers (from 7.3Å to 4.5Å) and is attributed by Shu *et al*. (2017) to the disordered accumulation of GO-polyethyleneimine (PFGA) sheets to

form 3D networks. When oxidized, graphite XRD patterns exhibite a change in the positioning of the peak in 2θ 25.5º to nearly 11.0º, which is related to the shift of the (002) peak at 25.5º to lower angles, due to the addition of oxygenated groups to the sample, increasing the graphitic interlayer distance. However, it is important to mention that this peak at 10–11º (Figure 5b) is characteristic of graphite oxide, or at least, multi-layer graphene oxide, exhibiting an increased interlayer distance of around 0.8 nm.

Graphene nanosheets have outstanded photocatalytic and electrocatalyct activities because of their low band-gap energy, which facilitates the electrons transference from the valence band to conductive band under external stimulus (e.g. light radiation, or electric current), resulting in the generation of free radicals from oxidant species (CHUA; PUMERA, 2018). This feature allows the employment of graphene nanomaterials in photocatalytic processes with great efficiency (MOZTAHIDA; LEE, 2020).

Specific metallic oxides (e.g. Fe_3O_4, ZnO, CuO and TiO_2), when aggregated to GO nanosheets, are responsible for confer photocatalytic activity to them, as many of these nanocomposites are employed in heterogeneous photo-Fenton degradation of water pollutants (BAPTISTTELLA *et al*., 2021; NAZARI; SALEM, 2019; WANG et al., 2019c; YAO *et al*., 2019). Another property of Fe_xO_y-functionalized-graphene which deserves to be highlighted is the magnetic density, especially when magnetite, ferrite, or other Fe_xO_y-derivative are anchored in GO. Consequently, Fe_xO_y-GO might be easily separated from aqueous media by a simple magnet (BAPSTITTELLA *et al*., 2021; WANG *et al*., 2019b; KHURANA *et al*., 2018; LV *et al*., 2014).

With the objective of enhance the catalytic properties, the covalent functionalization of graphene with dibromocarbene and its influence in interlayer band-gap and electronic properties were studied by Sainsbury *et al*. (2016). Bromocarbene groups were detected by FTIR spectroscopy, by the appearance of characteristic peaks from bromoform spectrum, which exhibited three bands: at 3020 cm^{-1} and 1142 cm^{-1}, due to C–H stretching and bending vibrations, respectively; C–Br stretch vibration was evident at 656 cm^{-1} with a bounce at 692 cm^{-1} (Figure 5c). Moreover, Raman spectra exhibited shifts in G and 2D bands from 1580 to 1575 cm^{-1} and from 2725 to 2705 cm^{-1}, respectively, after functionalization (Figure 5d). This is an indicative of both mechanical strain in the lattice and a doping effect of the dibromocarbene ligands located at the edges of graphenic plane. Therefore, according to the authors, such changes are due to the

formation of cyclopropyl groups and rehybridization of carbon atoms tangential of the lattice plane. Still, according to the authors, radical dibromocarbene functionalization potentialized graphene wide-area by thermolyis/photolysis of radical precursors as well as plasma processing, which might allow its application in scale-up technologies.

Finally, it is deserved to be mentioned some advances of the anchoring non-metallic structures over graphene framework, as silica (SiO_2, Si_xO_y networks), nanoclays and some boron nitride derivatives (RODRIGUEZ *et al*., 2021). Beyond others, heat dispersion and mechanical stability are some of the most remarkable features of Si_xO_y-graphene. Due to their great mechanical stability, nanoclays-graphene and Si_xO_y-graphene composites can be used as column packing material, for fixed-bed adsorption and for solid phase extraction (CZEPA et al., 2020).

Graphite oxidation process and subsequent functionalization, causes alterations in its morphological properties, such as the increase in the thickness between the layers and the appearance of "voids" in its structure, due to the changes in the sp^2 hybridization (LAI *et al*., 2019; EIGLER; HIRSCH, 2014). Alterations of this nature tend to facilitate the diffusion of the adsorbate molecules between the adsorbent layers, or even increase the availability of adsorbent active sites. On the other hand, some functional groups cause re-stacking of mono (or few layers) graphene, which can be undesirable in some aspects, since some functional groups become unavailable for adsorbate interactions. Such morphological changes are detected by transmission electron microscopy (TEM) and are better explained in conjunction with other analyses, such as BET, XRD and Raman spectroscopy. AFM, TEM and high-resolution transmission electron microscopy (HRTEM) are powerful tools by which high resolution images can be obtained and generate numerous statistical data that make it possible to calculate the thickness between layers. According to Huber *et al*. (2019), AFM technique, beyond the acquisition of surface images with powerful resolution, it allows imaging of organic molecules with intramolecular resolution. AFM was applied by the authors to evidence the transition between physisorption to chemisorption state of the adsorption of CO_2 by copper and iron adatoms. Figure 6 (a and b) exhibits TEM images of GO functionalized with ionic liquids and with poly-ionic liquids, in which the presence of aggregated poly-ionic liquid is verified in GO nanolayers (TAMILARASAN; RAMANPRABHU, 2015). Figure 6c shows the AFM image of graphene on SiO_2 substrate, after the deposition of GO and its chemical reduction (EIGLER *et al*., 2014). The thickness profiles of

a monolayer and bilayer region are also depicted. AFM image of reduced “almost intact” graphene oxide (ai-GO) with its profile is shown in Figure 6d.

Gao *et al*. (2020), Xiong *et al*. (2017) and Huang *et al*. (2017), among other works, reported that the process of graphene functionalization may lead to increases or decreases in its specific surface area (measured in $m^2 \cdot g^{-1}$). These changes were verified through the BET and Dynamic light scattering (DLS) techniques, usually associated to TEM and AFM microscopy. However, they did not reflect negatively on the adsorption efficiency of these adsorbents. Perreault, de Faria and Elimelech (2015) reported elevations in the surface area and an increase of the active sites, after the anchoring of MNPs in the graphene nanosheets. Disminishing of graphene surface area after functionalization is related to the aggregation of graphene nanosheets (XIONG *et al*., 2017; HUANG *et al*., 2017). However, the intercalation of oxygenated groups between graphene nanosheets of exfoliated graphite was responsible to increase of its BET surface area more than 200 times in comparison to its pristine graphite (GAO *et al*., 2020).

Figure 6 - TEM photographs of: a) Poly(ionic liquids) functionalized graphene oxide (PILs-GO); b) Poly(vinylimidazole) functionalized GO; c) AFM image of GO on SiO_2 substrate with the monolayer and bilayer profiles; d) AFM image and thickness profile of reduced ai-GO.

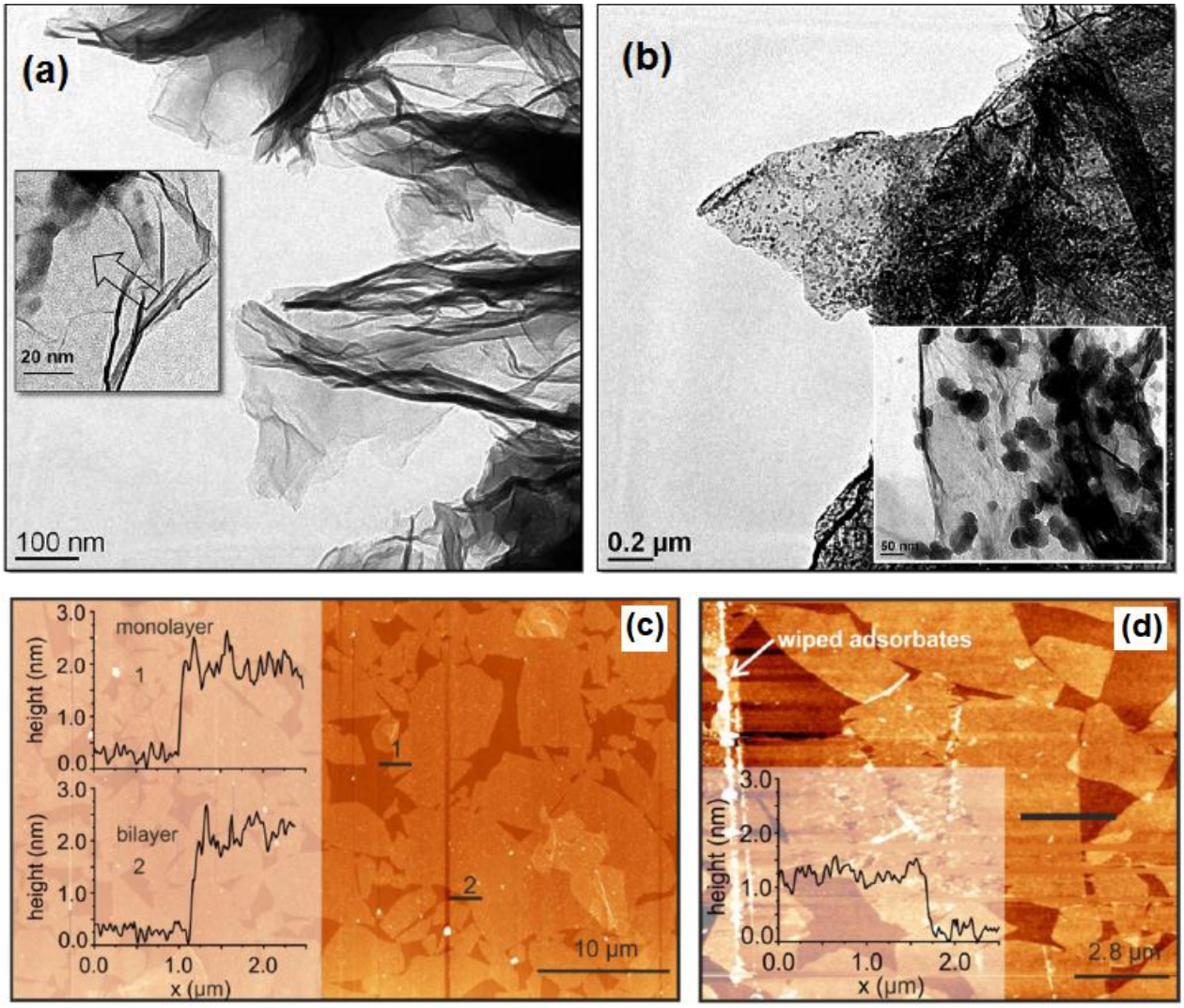

Source: a) and b) reproduced from Tamilarasan and Ramanprabhu (2015), with permission from the Royal Society of Chemistry, Copyright 2020; c) and d) adapted from Eigler *et al*. (2014), with permission from American Chemical Society, Copyright 2020.

4.2.3 Nature of interactions between functionalized graphene and other chemical species

Georgakilas *et al*. (2016) described several aggregate systems involving graphene and functionalized GO, as well as the nature of the interactive forces which drive them. Among these systems, the π–π interactions, which, according to the author, necessarily depend on two factors: the occurrence of π-electron systems present in the two interacting species, and the molecular

geometry of these species. Figure 7a shows a system in which molecules containing aromatic rings are engaged in π–π stacking interactions with GO structure.

Electrostatic attractions occur when the sorbente and sorbate have opposite charges, this type of interaction is very frequent in systems functionalized graphene/GO – metallic ions (or ionic dyes). Kumar and Jiang (2017) observed that the adsorption of the ions $H_2AsO_4^-$ and $HAsO_4^{2-}$ is very favorable at low pH. Under natural conditions, the adsorbent GO-β-cyclodextrin-Fe_3O_4 has a large amount of hydroxyl and carboxyl groups distributed over its surface, making it negatively charged. When the pH decreases, the adsorbent becomes positively charged (GO-OH^- to GO-OH^{2+}; Fe-OH^- to Fe-OH^{2+}), which favors electrostatic interaction with As (V) ions.

Covalent bonds is one of the most common way to functional groups interacts with GO plane. In this sense, very strong interactions may derive from the chemical attack of an organic compound (nucleophile) to oxygenated groups distributed over GO surface and edges. These interactions are provoked by intense dipole-dipole relationship and the "new" groups stay attached to graphene by new covalent bonds. These modifications are usually irreversible, according to studies reported in the literature (PARK; RUOFF, 2009). In this sense, the amino-functionalization carried out at high temperatures is classified as a covalent, since the interactions between amines and the basal plane of graphene/GO are of strong energy and derive from the nucleophilic attack of hydroxyl groups by the amines (CZEPA *et al*., 2020; CAI; CASANOVA, 2016). Figure 7b shows the interactions between methylimidazole (IL) and GO to form the covalently-functionalized mimGO. Covalent bonds are also the main reported interaction for chemisorption process, which happens in the adsorption of metallic ions. Examples can be cited, such as the complexation of Cr(VI) in the surface of amino-functionalized GO (WANG *et al*., 2018; ZHAO *et al*., 2016), and the high energy interactions involving reactive dyes (KYZAS *et al*., 2015), such the adsorption of Reactive Black 5 by amino-functionalized GO, as exhaustively reported in this thesis.

Another type of interactions that frequently occur in systems involving functionalized graphene is Van der Waals forces, which arise between the hexagonal arrangement of carbon atoms and the structures of dyes containing aromatic rings. These are dipole moments, caused by the displacement of partial charges along the electronic clouds of large molecules. These interactions are characterized by low energy intensity, of the order of 2–4 $kJ \cdot mol^{-1}$ (SCHEUFELE *et al*., 2016). Moreover, it is reported that one of the possible causes for 2D

carbonaceous nanomaterials exhibit high hydrophobicity in aquous medium is the strong Van der Waals forces between layers, which increases the tendence of aggregation (CZEPA *et al*., 2020).

It is reported by several works in the literature that hydrophilic interactions occurs in high intensity between GO and polar solvents, and it is a consequence of the activity of oxygenated groups (mainly hydroxyl, epoxide, carboxyl and ketone) distributed over GO surface (PARK; RUOFF, 2009; WANG *et al*., 2009). The presence of these functional groups, on the other hand, decreases the surface hydrophobicity, and increases the dispersion of GO in water. Additionally, oxygenated groups might lower GO adsorption efficiency of some kind of organic contaminants by forming water clusters over its surface (ERSAN *et al*., 2017). Nevertheless, this phenomenom is not sufficiently reported when non-functionalized GO is employed as nanosorbet of dyes. On the contrary, exfoliated GO has been satisfactorily applied as efficient sorbent for Methylene Blue (481–504 $mg \cdot g^{-1}$) (TU *et al*., 2019; ARAÚJO *et al*., 2018), Safranin (98 $mg \cdot g^{-1}$) (BANERJEE *et al*., 2015), Direct Red 23 (58 $mg \cdot g^{-1}$) and Acid Orange 8 (68 $mg \cdot g^{-1}$) (KONICKI *et al*., 2017), Methyl Orange (55.56 $mg \cdot g^{-1}$) (TU *et al*., 2019), among others. Therefore, this is a theme which needs in-depth investigation. The decrease of graphene hydrophilicity and, consequently, their easy separation from polar solvents is a reason to choose the addition of non-oxygenated functional groups on graphene and GO surface.

In addition to van der Waals forces, chemical bonds, electrostatic and $\pi-\pi$ interactions, it can be cited the hydrogen bonds (H-bonds), which may be formed between the hydroxyl and carboxyl groups of GO surface and specific functional groups contained in the reactants, such as polymers (WANG *et al*., 2014). An example of these interactions are those between the GO and poly(diallyldimethylammonium chloride) (PPDA) structures, depicted in Figure 7c.

Figure 7 – a) π–π stacking interactions between benzene groups and the hexagon arrangements of carbon atoms of GO; b) electrostatic interactions between methylimidazole (mim) and GO in the preparation of mimGO sponge; c) Hydrogen forces and electrostatic interactions actuating between hydroxyl and carboxyl groups over GO surface and PPDA.

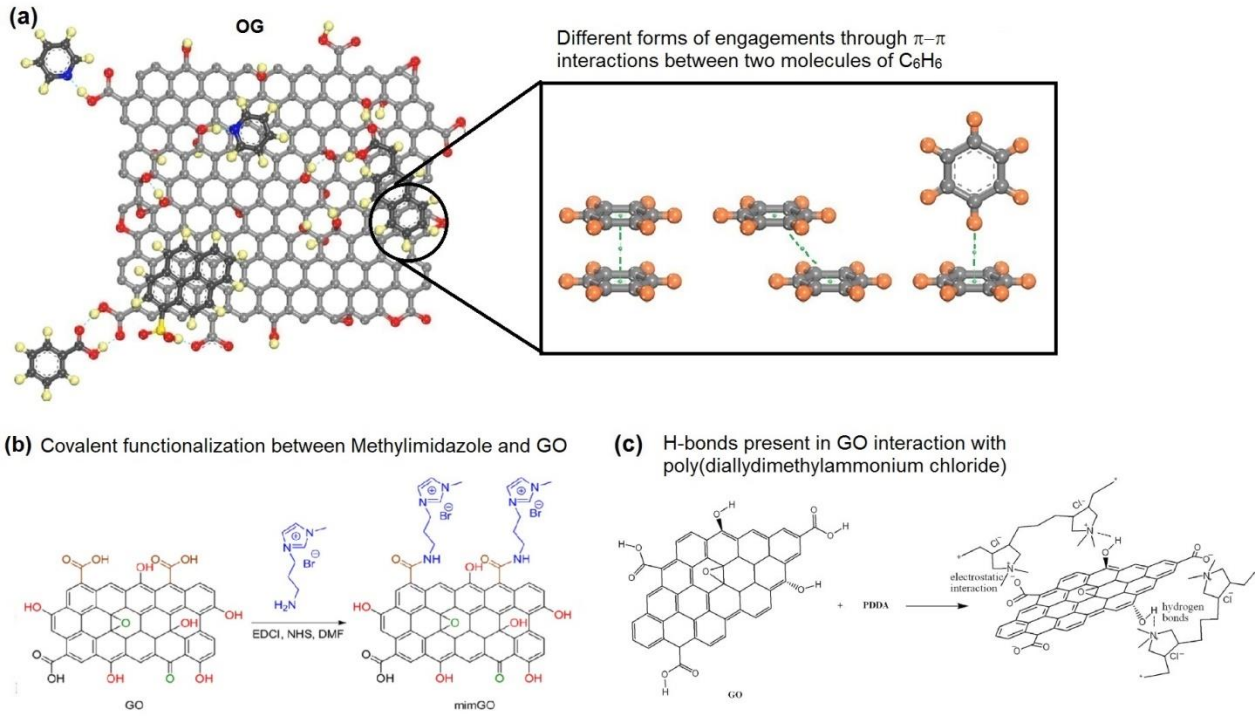

Source: adapted from Georgakilas *et al.* (2016) [a]; Zambare *et al*. (2017) *apud* Lai *et al*. (2019) [b]; Wang *et al.* (2014) [c], with permission from American Chemical Society and Elsevier, Copyright 2020.

4.3 ADSORPTION OF DYES ONTO FUNCTIONALIZED GRAPHENE

4.3.1 Classification of textile dyes

Dyes and pigments are used in various industrial segments, such as food, painting, plastics and, to a greater extent, textile industries. The dyes, called textiles, are classified according to several factors, such as solubility, structure and molecular weight, fiber type and fiber adherence (GREGORY, 1990). It is in accordance to this last characteristic that they derive their most known denominations: reactive, direct, dispersed, acid and basic (GUARATINI; ZANONI, 2000).

Reactive dyes are those most used in the dyeing process, since they contain an electrophilic (reactive and chromophore) group capable of forming covalent bonds with the hydroxyl groups of the cellulosic fibers; with amino, hydroxyl and thiol groups of the protein fibers; and also with the amino groups of the polyamides (GUARATINI; ZANONI, 2000). Generally, these reactive groups are the azo (characterized by the double bond formed between Nitrogen atoms, N=N), diazo and anthraquinone, and this functional group are responsible for giving the color to the dye. Auxhochrom groups, on the other hand, are responsible to confer the intensity of the color, make the dyes soluble in water and confer substantivity to the dye on the fiber (ease the fixation of the dye on the fiber). These groups may vary from amino, hydroxyl, carboxyl and sulphonic (HORROCKS; ANAND, 2000). This group includes the dyes of the Remazol™ (*Dystar Group*), Drimaren™ (*Clariant do Brasil S/A*) and Everzol™ (*Everlight Taiwan*) family.

The second type of dye most used in the textile industry is that of direct dyes, which are characterized as water soluble compounds able to dye cellulose fibers through van der Waals interactions (GUARATINI; ZANONI, 2000). Dispersed dyes are more commonly employed in polyester fibers by means of hot dyeing processes; are insoluble in water, but form very stable dispersions in organic solvents.

4.3.2 The employment of functionalized graphene as adsorbent of dyestuffs

Oxygenated compounds-functionalized graphenes, or simply GO's, have been used to remove anionic dyes with satisfactory adsorption capacity and efficiency. Furthermore, high density of oxygen-containing functional groups on GO nanosheets can enhance the adsorption of dyes, due to the abundance of active sites on its surface according some authors (SARKAR; BORA; DOLUI, 2014; KUO; WU; WU, 2008).

Luz-Assunción *et al*. (2020) carried out a comparative assessment of the adsorption of Reactive Red 2 (RR2) dye by the "oxygen-functionalized" GO and graphene quantum dots (GQDs). C/O ratio, acquired from EDS analysis, evidenced the degree of oxidation of GO, as GQDs exhibited C/O 7.85, whilst GO exhibited C/O 3.13. Authors reported a RR2 removal efficiency of 33.0 $mg \cdot g^{-1}$ (after 8 h) for GQDs and 18.5 $mg \cdot g^{-1}$ for GO (within 7 h). To achieve these results, kinetics experiments were carried out with 50 mL of RR2 solution 30 $mg \cdot L^{-1}$ and adsorbent dosage of 0.75 $g \cdot L^{-1}$, at pH values of 2.0 (for GO) and 5.0 (for GQDs) and environmental temperature (25 ºC). According to the authors, the best performance of GQDs is explained by greater number of active sites available for the adsorption due to its greater surface area (120 $m^2 \cdot g^{-1}$ for GQDs and 34 $m^2 \cdot g^{-1}$ for GO, measured by BET technique).

Despite this discussion make sense, the work lacks an in-depth investigation towards the effect of oxygenated functional groups in the interactions between sorbent and sorbate, which clearly influence the adsorption. Moreover, the effects of temperature were completely neglected in their research, from which it could be estimated the nature of RR2 adsorption (chemisorption or physisorption), as well as the predicted mechanisms involved. Finally, it is consensus that the great surface area of graphene nanomaterials can only be reached under concentrations sufficiently low and BET method is not adequate to represent graphene in aqueous medium due to re-stacking of graphene nanosheets (ZHOU *et al*., 2015; EIGLER; HIRSCH, 2014).

Differently, Araújo *et al*. (2018) reported a maximum adsorption capacity (q_m^{exp}) of GO in the adsorption of the cationic Methylene Blue dye: ~ 530 $mg \cdot g^{-1}$. Equilibrium experiments were carried out with 0.01 g of GO per 25 mL of MB solution, C_0 varied from 50–500 $mg \cdot L^{-1}$, at 300 rpm, 25 ºC and pH 5.5. q_m^{exp} value is above the average reported in other works found in current literature for MB adsorption onto GO in similar conditions. Moreover, the authors investigated the influence of oxidation variables on the adsorption of MB by a 2^3 factorial design in another work (ARAÚJO *et al*., 2019). From that, it was observed that the oxidant species ($KMnO_4$ and

$Na_2CO_3 \cdot 1.5H_2O_2$) in modified Hummers Method and the reaction temperature (35 and 45 ºC) influenced the adsorption of MB. It was obtained 99% of MB removal (50 $mg \cdot L^{-1}$) in the condition 1.0 g of graphite powder + 3.0 g of $KMnO_4$ + 25 mL of H_2SO_4 at 45 ºC. This is because the high oxidation degree generated more oxygen groups over GO structure and consequently enhanced the adsorption.

The application of graphene functionalized with poly-ionic liquids as adsorbent of anionic dyes was evaluated by Zhao *et al*. (2015), which employed polyvinylimidazole-1 as a methylene blue adsorbent. Tamilarasan and Ramanprabhu (2015), on the other hand, used polyimidazole-functionalized graphene to capture CO_2. Despite the excellent performance of the adsorbent, the major challenge in the functionalization of graphene (or GO) with poly-ionic liquids is the need to use an inert atmosphere during the functionalization reaction. This is necessary to avoid the early oxidation of the reactants, which makes the process more expensive. Thus, high adsorption capacities were reported in the literature in the L-S and G-S processes: Zhao *et al*. (2015) reported 1910 $mg \cdot g^{-1}$ in the adsorption equilibrium of Methylene Blue (10.0 mL of MB solution, C_0 within 100–500 $mg \cdot L^{-1}$, 5.0 mg of r-GO-PIL, contact time: 30 h); Tamilarasan and Ramanprabhu (2015) reported an experimental maximum adsorption capacity in the monolayer (q_m^{exp}) of 695 $\mu mol \cdot g^{-1}$ in CO_2 adsorption (absolute pressure ~ 100 kPa and 283 K). Langmuir model was used with good fit in both works.

Im *et al*. (2017) developed a novel composite from graphene functionalized with phenyl groups supported on nanofibers of hydrogel polymers (GHNFs) to adsorb Methylene Blue (MB) and Crystal Violet (CV). Adsorption capacities of 0.43 and 0.33 $mmol \cdot g^{-1} \cdot s^{-1}$ were obtained for MB and CV, respectively; the process occurred in a continuous system with a flow rate of 1.50 $mL \cdot s^{-1}$ (0.05 g of GHNFs per 50 mL of 0.5 $mmol \cdot L^{-1}$ dye solution).

The amino-functionalization process of GO was employed by Shu *et al*. (2017) through the rapid reaction of polyethyleneimine with the GO. Infrared spectroscopy analysis showed the presence of C–N bonds in the obtained airgel, with stretches at 2852 cm^{-1}, 2923 cm^{-1} and 1453 cm^{-1}. The aerogel was evaluated as an adsorbent of the anionic dyes Methyl Orange (MO) and Red Amaranth (termed Acid Red 27, AR27). The following values of the maximum adsorption capacity were obtained: 3059.20 $mg \cdot g^{-1}$ and 2043.70 $mg \cdot g^{-1}$ for MO and AR27, respectively (2.0 mg of PFGA, 60 mL of dye solution; pH 2 for MO and pH < 10 for MB). According to the authors, such results are the highest values for q_m until then reported for these dyes.

Covalent functionalization of GO with organic functional groups containing sulphur (thiocompounds) are also reported in the literature. Gao *et al*. (2017), for example, studied the adsorption efficiency of dithiocarbamate functionalized graphene (DTC-GO) to adsorb Pb^{2+} ions in aqueous solution. It was obtained a maximum adsorption capacity of 132.01 $mg \cdot g^{-1}$ (5.0 mg of DTC-GO, 20 mL of Pb^{2+} solution, C_0 ranged from 20 to 100 $mg \cdot L^{-1}$, pH at 5.3). Furthermore, the Langmuir's isotherm model showed the best fit to the adsorption process. Mahmoodi *et al*. (2017) also employed DTC-GO to remove Basic Blue 41 (BB41) and Basic Red 46 (BR46) with satisfactory adsorption capacity: 128.50 and 111.00 $mg \cdot g^{-1}$ for BB41 and BR46, respectively (0.04 g of DTC-GO for 250 mL of 20 $mg \cdot L^{-1}$ dye solution at room temperature, 25 ºC; contact time 60 min). FTIR spectra showed the appearance of new peaks at 616, 1070 and 1423 cm^{-1} which were assigned to the C–S vibration, C=S vibration and C–N (in N–C=S) from dithiocarbamate groups (ZHANG *et al*., 2008). The presence of dithiocarbamate groups on the graphene surface is responsible for the enhancement of its adsorption capacity.

Non-covalent functionalization of GO was investigated by Bayantong *et al*., (2021), who synthesized the nanocomposite metal-ferrite anchored on GO (MFe_2O_4@GO, in which M = Cu, Co or Ni) and applied it in the removal of MB dye. Equilibrium experiments were carried out and the maximum "modeled" adsorption capacity (q_m^{calc}) was acquired for MFe_2O_4@GO: 25.81 $mg \cdot g^{-1}$ (M = Cu), 50.15 $mg \cdot g^{-1}$ (M = Co) and 76.34 $mg \cdot g^{-1}$ (M = Ni). Experiments performed under the following conditions: 5.0 mg of MFe_2O_4@GO (foam type nanocomposite) for 10 mL of MB solution, pH 6.15, 120 rpm and 25 ºC. Unfortunately, authors did not provide the graphics with the isotherms q *versus* C in order to evaluate the experimental maximum adsorption capacity (q_m^{exp}). However, from kinetics experiments it was obtained exeperimental maximum adsorption capacity at equilibrium (q_e^{exp}) as follows: 12.4 $mg \cdot g^{-1}$ (M = Ni, 45 min); 11.5 $mg \cdot g^{-1}$ (M = Co, 60 min); 11.3 $mg \cdot g^{-1}$ (M = Cu, 60 min).

According to the authors, the high porosity of the adsorbents and their specific surface area (BET method) in association with strong electrostatic interactions (solution pH > pH_{PZC}) were the main drive of the adsorption of MB. This was confirmed by analyses of BET and SEM-EDS and thermodynamic assays: ΔH^o +15.16 $kJ \cdot mol^{-1}$ ($NiFe_2O_4$@GO), ΔH^o +12.04 $kJ \cdot mol^{-1}$ ($CuFe_2O_4$@GO) and ΔH^o +12.66 $kJ \cdot mol^{-1}$ ($CoFe_2O_4$@GO). Morphological assessment evidenced the formation of composites with great rugosity and several blocked structures.

4.3.3 Functionalized graphene supported in micro-macro matrices

Functional groups attached in graphene plane and edges promote a link between graphene and other types of supports. Some researchers have applied functionalized graphene-decorated polymers to compose ultrafiltration and separation membranes (POTHAYA *et al*., 2019; MA *et al*., 2019); others, have successfully anchored graphene-metallic oxide nanomaterials on the surface of charcoals and vegetal fibers aiming to ease the separation of the sorbent from adsorbate solution (SHANG *et al*., 2019; SHANG *et al*., 2016; GE *et al*., 2016).

Graphene-polymer based nanocomposites are also object of study of many authors, and have been investigated in the composition of membranes for MF, UF, NF and RO (SUTER; SINCLAIR; COVENEY, 2020; COHEN-TANUGI *et al*., 2016; WERBER; OSUJI; ELIMELECH, 2016), as well as adsorbents (YAP *et al*., 2020; WANG *et al*., 2019b). For adsorption purposes, it can be highlighted the fabrication of hydrogels from poly(diallyldimethylammonium chloride)/graphene oxide (PDDA/GO) (Figure 7c). PPDA/GO has been used as adsorbents for anionic dyes Ponceau S (PS) and Trypan Blue (TB) with satisfactory efficiency (WANG *et al*., 2014). Due to the strong π–π stacking and anion-cation interactions, there were high removal efficiencies for both PS and TB. The maximum adsorption capacity obtained was 37.85 $mg \cdot g^{-1}$ and 48.54 $mg \cdot g^{-1}$, for PS and TB respectively. Polymer-graphene frameworks have also been developed with metallic compounds grafted in their matrices for antimicrobial surfaces (VALENZUELA *et al*., 2020; MOREIRA *et al*., 2020).

Remarkably, the graphene-polymer association has brought many breakthroughs regarding the enhanced selectivity and rejection rate in these membranes (CHEN *et al*., 2021). However, the achievement of a satisfactory dispersion of the charge (graphene and functionalized graphene nanofillers) over polymeric matrices poses as a challenge for researchers who develop such nanocomposites (IVANOVA *et al*., 2020; MEDEIROS *et al*., 2020). This is because of the aggregation of graphene charges might causes blank points over the membranes, decreasing their selectivenes and, consequently, their removal efficiency (SUTER; SINCLAIR; COVENEY, 2020). More papers which deal with functionalized-graphene anchoring in synthetic polymeric matrices can be found in comparison to carbons and natural fibers. However, this thesis focused on the natural and biomass derived matrixes, since wood wastes were employed as biomass for producing charcoal as support for the amino-functionalized multilayer graphene oxide [nGO(NH)R], as discussed in Sections 6.3 and 7.11.

Ge *et al*. (2016) used the process of anchoring the functionalized GO with citric acid (CA) in corn fibers (CF), called under the nomenclature GO-CA-CF, to remove Methylene Blue. This process gave the adsorbent a better ease of separation, since the magnetic separation of the GO-CA-CF from the Methylene Blue solution after the adsorption process was employed; the efficiency and practicality of this separation process was verified by Cazetta *et al*. (2016) and Zhao *et al*., (2016). After the equilibrium and kinetic tests, the GO-CA-CF had a maximum adsorption capacity of 315.50 $mg \cdot g^{-1}$, reaching steady state after 20 min. In this sense, the pseudo-second order model was the best fit for the experimental data, with a good coefficient of determination (R^2, 0.991).

The anchoring of graphene-derived nanocomposites over micro-macro matrices is pointed as one way to facilitate the sorbent separation after the adsorptive process beyond the enhancement of sorbents capacity. Following this trend, Shang *et al*. (2016) successfully anchored GO on water hyacinth biochar and applied it in the adsorption of Cr(VI) ions. Additionally, the increase in the adsorption efficiency of biochars was another motivation to produce the GO-decorated water hyacinth biochar. And it was evidenced in the increase of nearly 170% in monolayer adsorption capacity of GO-water hyacinth biochar in comparison with some pure and modified biochars (Saw dust activated carbon, rice husk carbon, iron-doped ordered mesoporous carbon, among others). Three years later, other researchers anchored EDTA + zero valent iron (nZVI) nanoparticles on GO and grafted it in biochar obtained from residues of Mongolian milkvetch plants (*Astragalus membranaceus*) (SHANG *et al*., 2019). This novel engineered nanocomposite ws then applied to remove Cr(VI) by adsorption, and a significant adsorption capacity of 490 $mg \cdot g^{-1}$ had been reached. Therefore, this result is 3.25 times the maximum adsorption capacity acquired by GO-water hyacinth biochar, 150 $mg \cdot g^{-1}$ (SHANG *et al*., 2016). Moreover, according to the authors, EDTA had a strong influence on Cr(VI) adsorption, while NO_3^- showed a detrimental behavior on Cr(VI) scavenging. The adsorption mechanisms cited were electrostatic interactions, co-precipitation and Cr(VI) reduction, however, a deeper discussion towards this subject was not provided.

As evidenced by a thorough survey in the literature, there is a lack of substantial works regarding the supporting of graphene nanomaterials on biochars and their use as adsorbent of dyes. In this sense, this is another knowledge gap that this work aims to surpress.

5 ADSORPTION FUNDAMENTALS

Adsorption is the unit operation in which takes place the adhesion of atoms, ions or molecules from a gas, liquid or dissolved solid (named “adsorbate”) to a surface of a solid (termed “adsorbent”). In synthesis, the species migrate from the fluid to the solid phase. The adsorption theory states that adhesion results from molecular contact between two materials and the interface forces that maintain the adsorbate attached to the adsorbent active sites. From this principle, adsorption is widely applied for separation and purification of fluid mixtures, catalytic reactions and the removal of pollutants from water and wastewater. Within this last field, adsorption techniques are used as high-quality treatment processes for the removal of dissolved pollutants, such as pharmaceuticals, dyes, metallic ions, pesticides and other water pollutants, most of them from industrial wastewater. Finally, adsorption assays might be carried out in continuous or batch mode; it can also be carried out in a CSTR type vassel, or in a continuous flux column, as depicted in Figure 8. In this work, all experiments were carried out in batch.

Figure 8 – Configurations of adsorption assays.

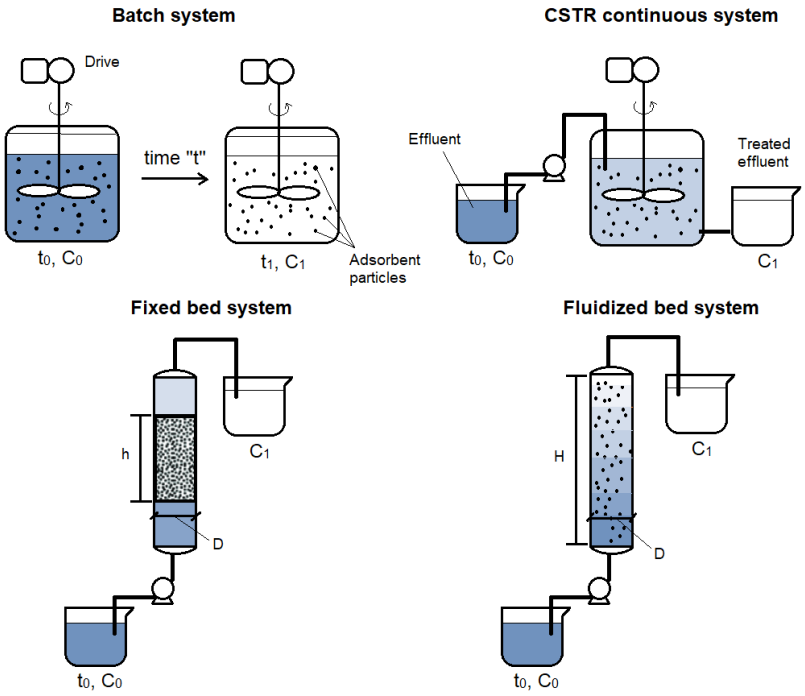

Source: the author (2020)

5.1 ADSORPTION CAPACITY AND EFFICIENCY

According to Perry, Green and Maloney (1999), the amount of solute adsorbed in solid phase (called adsorption capacity, q) can be given in terms of moles, milligrams or volume of adsorbate per unit mass or volume of adsorbent. In liquid phase, the units commonly employed for this variable are $mol \cdot g^{-1}$ and $mg \cdot g^{-1}$.

The adsorbate mass adsorbed at equilibrium is calculated according to Equation 1, meaning an overall mass balance between the two fluid and solid phases in a closed system where the solvent is inert and there is no significant change in fluid volume through the adsorption:

$$q = \frac{(C_0 - C) \cdot V}{m} \quad (1)$$

where q is the adsorption capacity (in $mg \cdot g^{-1}$); V is the volume of the solution (in L); m is the adsorbent mass (in g).

The percentage of sorbate removal, or efficiency of the adsorption [R(%)], is presented by Equation 2:

$$R(\%) = \frac{(C_0 - C)}{C_0} \times 100 \quad (2)$$

where R(%) is the removal efficiency (in %); C_0 is the initial concentration of the solution (in $mg \cdot L^{-1}$); C is the concentration of adsorbate after the adsorption process (in $mg \cdot L^{-1}$).

5.2 ADSORPTION ISOTHERMS

Two widely used adsorption isotherms in the literature to describe the behavior of adsorptive processes between the liquid-solid (L-S) phases are the Langmuir and Freundlich isotherms, or the combination of both models. However, alternative models such as the Dubinin-Haduskevitch, BET and Temkin isotherms might also employed with good adjustments to experimental data.

5.2.1 Adsorption isotherms and methods of experimental data fitting

Among the most diverse forms of adjustment of the models to the experimental data, there are numerous published works that report the use of the linear regression method to fit the models to the experimental data (GANESAN; LOUIS; DAMODARAN, 2018; KHURANA *et al*., 2018; OTHMAN *et al*., 2018). However, according to authors who studied the influences of the adjustment methods on the experimental results and their phenomenological conclusions, the cited method does not represent the adsorption process, since there are situations in which it is necessary to eliminate a certain number of experimental points to obtain the ideal adjustment of these to the model, beyond the propagation of errors related to data fluctuation (PICCIN *et al*., 2017). This results in obtaining a "false" coefficient of determination (R^2) and, consequently, directs the researcher to false conclusions about the process. However, the adjustment through non-linear methods or solvers from software such as Matlab™, Maple™, Origin™ or even Microsoft Excel™ are widely recommended by authors who have deepened this theme, since the errors resulting from the adjustment by the equation itself are minimized (PICCIN *et al*., 2017, McKAY *et al*., 2014, FOO, HAMEED, 2010).

Similar issues arise when kinetic data is assessed, which mostly the pseudo-second-order (PSO) model would be mistakenly chosen by many researchers as the “most representative” of their kinetic, since it would be more “accurate” in terms of R^2 (SIMONIN, 2016). Therefore, for equilibrium, kinetic and thermodynamic modeling it was employed the method of “non-linear” fitting in this work. Following this methodology, the statistical tool nonlinear chi-square factor (χ^2) was adopted to evaluate the variation of experimental data, since it indicates the difference between experimental/observed and the modeled/expected covariance (FOO; HAMEED, 2010; HO; CHIU; WANG, 2005).

As reported in the literature, specialized in this theme (PICCIN *et al*., 2017; SIMONIN, 2016; HO; CHIU; WANG, 2005), the quality of the model fitting was assessed in this work by the coefficient of determination (R^2), given by Equation 3, and the chi-square factor (χ^2), given by Equation 5. Both parameters are statistically calculated as a function of the “*C*–dependent variable” capacity of adsorption (q, given in $mg \cdot g^{-1}$). Finally, it is important to mention that R^2 and χ^2 are calculated by the math software. In this work, it was used the Origin™ 9.0.

$$R^2 = 1 - \frac{\sum_{i=1}^{N}(q_i - \hat{q}_i)^2}{\sum_{i=1}^{N}(q_i - \langle q_i \rangle)^2} \quad (3)$$

$$\langle q \rangle = \left(\frac{1}{\mathrm{N}}\right) \sum_{i=1}^{\mathrm{N}} q_i \quad (4)$$

Where N is the number of experimental points assessed in kinetic or equilibrium experiments; ‹q_i› stands for the average value of the q_i's (i = 1, 2, … N; q is given in mg·g^{-1}); $\widehat{q_i}$ (also given in mg·g^{-1}) stands for the adsorptive capacity predicted by the model. Moreover, q is a generic term to express the parameters, which were acquired from kinetic models (pseudo-first-order, pseudo-second-order, intraparticle diffusion, among others), or isotherm models (Langmuir, Langmuir-Freundlich, among others). In this work, the q expressed in equations 3, 4 and 5 might be the adsorption capacity at kinetic equilibrium (q_e), or the monolayer adsorption capacity (q_m) and clearly depends on the fitted model.

$$\chi^2 = \sum_{i=1}^{\mathrm{N}} \frac{(q_i - \widehat{q_i})^2}{\widehat{q_i}} \quad (5)$$

In which $\widehat{q_i}$ is the equilibrium capacity obtained by calculating from the model (in mg·g^{-1}), and q_i is experimental data of the adsorption capacity (in mg·g^{-1}), which can be q_e or q_m, depending on the modeling.

Finally, if R^2 is closer to 1, it is an indicative of a good fit; on the contrary, how closer to 0 R^2 remains, it is an indicative of a not satisfactory fit. Moreover, $R^2 < 0$ is also possible, since a very bad fit would be achieved using nonlinear regression (SIMONIN, 2016). If the modeled data are similar to the experimental ones, χ^2 will be a small number; if they are different, χ^2 will be a large number (HO; CHIU; WANG, 2005).

5.2.2 Types of adsorption isotherms

Depending on the behavior of the adsorption isotherm of the system, it can be classified as: irreversible; favorable, linear or unfavorable. The adsorption isotherms show the equilibrium relationship between the concentration in the fluid phase and the concentration in the adsorbent particles at a given temperature. Their behavior can be described mathematically by the separation factor (R_L) (McCABE; SMITH; HARRIOT, 2004) and graphically, depending on the aspect of their concavity, as described in Figure 9. According to the criterion of the separation factor, an isotherm is irreversible when $R_L = 1$, linear when $0 < R_L < 1$, and unfavorable when R_L

> 1 (McCABE; SMITH; HARRIOT, 2004; CHAILEK *et al*., 2018). Values of R_L are given by Equation 6:

$$R_L = \frac{1}{1+K_{Eq}C_0} \tag{6}$$

Where K_{Eq} is the equilibrium constant of Langmuir (in $L \cdot g^{-1}$), given by Equation 7; and C_0 is the highest initial concentration used in equilibrium studies (in $mg \cdot L^{-1}$).

Figure 9 – Examples of sorption isotherms as a function of Separation factor (R_L), representing several types of system: favorable, linear, non-favorable.

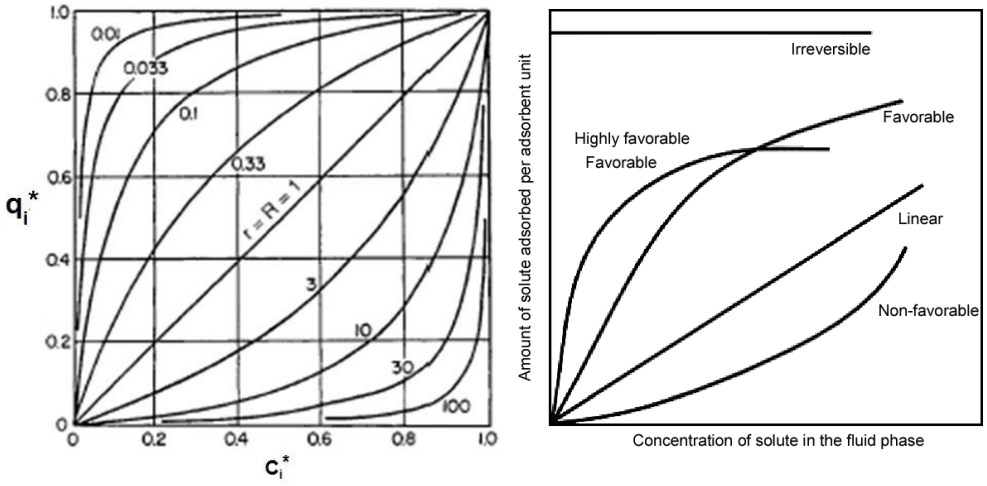

Source: reproduced from Perry, Green and Maloney (1999); McCabe, Smith and Harriot (2004).

Most adsorbents are highly porous, and adsorption occurs primarily at the pore walls or at specific sites within the particles. Due to the pores being generally very small, the area of inner surface is of order of magnitude larger than the external area, often being 500 to 10,000 $m^2 \cdot g^{-1}$ (McCABE; SMITH; HARRIOT, 2004).

The separation occurs because of differences in molecular weight, shape or polarity, which can hold some molecules more strongly on the surface than others or because the pores are so small to hold larger molecules (RUTHVEN, 1984; McCABE; SMITH; HARRIOT, 2004).

5.2.3 Langmuir model

The classical isotherm used for a flat and homogeneous surface, and the most popular of the nonlinear isotherms, is the Langmuir model (PERRY; GREEN; MALONEY, 1999). Langmuir's theory assumes that the forces acting on adsorption are similar in nature to those involving chemical combination – a pseudo-reaction. It is implicitly considered that the system is ideal; the molecules are adsorbed and adhere to the surface of the adsorbent at defined and localized sites, with homogeneous surface monolayer adsorption. Resistances to mass transfer, the diffusion of the species in the solvent and the convection are neglected (RUTHVEN, 1984; WANG *et al*., 2014; GE *et al*., 2016).

Despite the inexistence of linear behavior required for application in the Henry Law region, this isotherm is often applied to correlate heterogeneous adsorbent data over a wide range of concentrations (RUTHVEN, 1984).

Langmuir isotherm is presented according Equation 7.

$$\frac{q}{q_m} = \frac{K_{Eq} C}{1 + K_{Eq} C} \tag{7}$$

where q_m is the maximum adsorption capacity or the saturation capacity in monolayer by adsorption at the surface of the solid at equilibrium (in $mg \cdot g^{-1}$); K_{Eq} the equilibrium constant (in $L \cdot mg^{-1}$); C the adsorbate concentration; and q the adsorption capacity at equilibrium, for that determined concentration (in $mg \cdot L^{-1}$).

5.2.4 Freundlich model

The classical Freundlich isotherm indicates the occurrence of an exponential distribution of adsorption energies (PERRY; GREEN; MALONEY, 1999) and describes heterogeneous adsorption mechanisms with different degrees of affinity of adsorbent active sites (HUANG; YAN, 2018). The Freundlich isotherm is presented in Equation 8.

$$q = K_F C^{1/n} \quad (8)$$

being q and C the same meanings already defined for Langmuir isotherm; K_F (commonly referred in the literature as "Freundlich's Constant" and is given in terms of $mg \cdot g^{-1} \cdot (mg \cdot L)^n$ and n are constants that relate, respectively, to the adsorption capacity distribution of the active sites and that of the adsorbent, and $n > 1$ (ROUQUEROL; ROUQUEROL; SING, 1999).

5.2.3 Langmuir-Freundlich model

The model that combines the two most applied isotherms for adsorption studies for solid-liquid systems is the Langmuir-Freundlich (L-F) isotherm, which is given by Equation 9. The L-F model can be applied to systems involving mixtures as well as for compounds of similar molecular size and nature, however that present some degree of heterogeneity in the adsorptive process (CARVALHO *et al*., 2012; TURIEL; PEREZ-CONDE; MARTIN-ESTEBAN, 2003).

$$\frac{q}{q_m} = \frac{K_{LF} C^n}{1 + K_{LF} C^n} \quad (9)$$

where q is the adsorption capacity at equilibrium for a given initial concentration (in $mg \cdot g^{-1}$); C, the concentration at equilibrium (in $mg \cdot L^{-1}$); K_{LF}, the equilibrium constant, obtained by the process of fitting L-F model to the experimental data [in $(L \cdot mg^{-1})^n$]; q_m, the maximum adsorption capacity (in $mg \cdot g^{-1}$); and finally, n is the heterogeneity factor, associated with the number of layers of adsorption (RUTHVEN, 1984).

5.2.4 Temkin Model

Temkin isotherm model is applied assuming adsorption heat of sorbate decreases linearly with increasing adsorption capacity (HUANG; YAN, 2018; FOO; HAMEED, 2010), and is widely applied to describe chemisorption processes on heterogeneous surfaces, according to Ge *et al*. (2016). Temkin isotherm is shown in Equation 10:

$$q = \frac{RT}{b_T} \ln(a_T C) \quad (10)$$

where a_T is the binding constant at the equilibrium (in $L \cdot mg^{-1}$ or $L \cdot mol^{-1}$); b_T is the Temkin constant (in $kJ \cdot mol^{-1}$); R is the universal constant of the ideal gases (8.314 $J \cdot K^{-1} \cdot mol^{-1}$); and T is the temperature in which the experiment is performed (in K).

5.2.5 BET model for liquid-solid adsorption

Brunauer-Emmet-Teller (BET) isotherm is one of the classical models which best represents the adsorption of a certain compound in a gas-solid (G-S) system with the formation of multiple layers (RUTHVEN, 1984; ROUQUEROL; ROUQUEROL; SING, 1999; BRUNAUER; EMMETT; TELLER, 1938). Nevertheless, BET isotherm can be simplified to application in L-S systems, as Ebadi, Mohammadzadeh and Khudiev (2009) empirical model for BET isotherm has demonstrated. BET for L-S system considers that adsorbate can be adsorbed with the formation of multiple layers. In this case, it is assumed the distribution of adsorbed molecules occurs randomly (EBADI; MOHAMMADZADEH; KHUDIEV, 2009; OLIVEIRA *et al*., 2019). A non-linear version of BET model is given by Equation 11.

$$q = q_m \frac{K_s C}{(1 - K_l C)(1 - K_l C + K_s C)} \quad (11)$$

As it can be seen, Equation 11 exhibits three degrees of freedom (K_s, K_l and q_m); in which q_m the monolayer maximum adsorption capacity ($mg \cdot g^{-1}$); K_l the equilibrium constant of adsorption for the upper layers, and Ks the equilibrium constant for the first layer (EBADI; MOHAMMADZADEH; KHUDIEV, 2009).

5.2.6 Adsorption equilibrium of a binary mixture

Regarding multicomponent systems, the isotherm of Langmuir can be extended to each compound of the mixture (RUTHVEN 1984; ALLEN; McKAY; POTTER, 2004). For a binary mixture of dyes, A and B, the predictive model of Langmuir isotherm for the adsorption of A and B are given for the Equations 12 and 13, respectively.

$$\frac{q}{q_m^A} = \frac{K_L^A C_A}{1 + a_0^A C_A + a_0^B C_B} \tag{12}$$

$$\frac{q}{q_m^B} = \frac{K_L^B C_B}{1 + a_0^A C_A + a_0^B C_B} \tag{13}$$

In which C_A and C_B are the equilibrium concentration for the components "A" and "B", respectively ($mg \cdot L^{-1}$); the singles components set parameters (a_0^A and a_0^B) were acquired from Langmuir model fitted in the single A and B adsorption; K_L^A and K_L^B are the equilibrium constants for binary system for the components A and B respectively ($L \cdot mg^{-1}$); while q_m^A and q_m^B are the maximum adsorption capacity for A and B ($mg \cdot g^{-1}$).

5.3 MODELS OF ADSORPTION KINETICS

The study of adsorption kinetics is important in describing the adsorption process as it explains how fast the process occurs and also provides information on the factors affecting or controlling the adsorption rate. Various models can be used to analyze the kinetics of the adsorption process. The pseudo-first-order (PFO) and pseudo-second-order (PSO) kinetic equations of Lagergren (1898) and Ho and McKay (1999), respectively, are the most widely used for the adsorption of solutes from a liquid phase. However, for the examination of the controlling mechanisms of adsorption process, such as chemical reaction, diffusion control and bulk mass transfer, several kinetics models are used to test the experimental data. Among them are the Weber and Morris', which are known as intraparticle diffusion (IPD) model (WEBER; MORRIS, 1965); the Elovich model; and others.

In order to analyze the adsorption rate, the kinetic data was modeled using the integral equations of the Largergren's PFO and Ho's PSO models, provided by Equations 15 and 17 (TAHIR; BHATTI; IQBAL, 2016). The main parameters that can be reached from these phenomenological modeling are: the sorption capacity at equilibrium state (q_e, given in $mg \cdot g^{-1}$), kinetic constant rate for PFO (k_f, given in min^{-1}) and the kinetic constant rate for PSO (k_s, given in $g \cdot mg^{-1} \cdot min^{-1}$).

The Lagergren pseudo-first-order adsorption model follows the mass balance expressed in Equation 14 (LAGERGREN, 1898):

$$\frac{dq}{dt} = k_f (q_e - q_t) \tag{14}$$

Solving the ordinary differential equation, it is obtained the model given by Equation 15, which is PFO model in its non-linear form:

$$q_t = q_e (1 - e^{-k_f t}) \tag{15}$$

Ho pseudo-second-order model in its differential form is given by Equation 16 (HO; McKAY, 1999):

$$\frac{dq}{dt} = k_f (q_e - q_t)^2 \tag{16}$$

Integrating the Equation 16, it is possible to achieve the Equation 17, which is Ho PSO model written in its non-linear form:

$$q_t = \frac{k_S q_e^2 t}{(1 + k_s q_e t)} \tag{17}$$

According to the literature which deals with the fundaments of adsorption, some errors are embed in linear regression methods, which leads to achievement of "false" coefficients of determination (R^2) (PICCIN *et al.*, 2017; McKAY *et al.*, 2014, FOO, HAMEED, 2010), as thoroughly described in Section 5.2.1. This is the main reason for the avoidance of the use of

linear regression; therefore, in this work was employed the non-linear regression of the experimental data, which could be carried out by specific tools in math softwares.

5.3.1 Pseudo-n^{th}-order model

Although they are widely used in adsorption kinetic modeling, PFO and PSO are not the most reliable models when one wants to define a pseudo-order of an adsorptive process, since its order factor (n) might be placed between 1 and 2. Therefore, three parameters pseudo-n^{th}-order (PNO) model has been applied to experimental data by researchers in order to evaluate the kinetic parameters with more precision (TSENG *et al*., 2014). Non-linear form of PNO model can be expressed by Equation 18.

$$\frac{q_t}{q_e} = 1 - \frac{1}{\left[1 + (n-1) q_e^{n-1} k_n t\right]^{1/(n-1)}} \tag{18}$$

In which q_t is the adsorption capacity in the time t ($mg \cdot g^{-1}$); q_e is the adsorption capacity at the equilibrium state ($mg \cdot g^{-1}$); k_n is the the PNO rate constant ($mgn^{-1} \cdot g^{1-n} \cdot min^{-1}$); n is the pseudo-order factor of the adsorption (TSENG *et al*., 2014).

5.3.2 Intraparticle diffusion model

Intraparticle diffusion (IPD) model was developed by Weber and Morris (1965) and is given by the Equation 19. This model is usually employed to describe the adsorption by diffusion inside the pores of the adsorbent, neglecting the external mass transfer resistances to the adsorbent particles (SIMONIN, 2016).

$$q_t = k_{ID} t^{1/2} + k_0 \tag{19}$$

where k_{ID} is the intraparticle diffusion rate coefficient (in $L \cdot mol^{-1}$); while k_0 is a constant related to the resistance to the diffusion (in $mg \cdot g^{-1}$).

When experimental kinetic data are fitted by IPD model, it suggests that adsorption cannot be a function of boundary layer thickness or external mass transfer. Otherwise, it can be described as a mechanism governed by the resistance to mass transfer within the pores of the adsorbent (DIRAKI *et al*. 2018).

5.3.3 Elovich model

Elovich model assumes that real solid surfaces are energetically heterogeneous and the adsorption kinetics at low coverage is not influenced by the interactions between adsorbed species and desorption phenomenon is neglected. The non-linear form of Elovich model is given by Equation 20.

$$q_t = \frac{1}{\beta}\ln(1+\alpha\beta t) \tag{20}$$

where α is the initial adsorption rate ($mg \cdot g^{-1} \cdot min^{-1}$) and β represents the extent of surface coverage ($mg \cdot g^{-1}$).

5.4 ADSORPTION THERMODYNAMICS

The thermodynamic approach to the equilibrium study is quite generalized and can be applied to adsorption processes, as well as to any other equilibrium of different phases (RUTHVEN, 1984). The standard state functions are: enthalpy change (ΔH^o, $kJ \cdot mol^{-1}$), free energy variation of Gibbs (ΔG^o, $kJ \cdot mol^{-1}$) and variation of entropy (ΔS^o, $kJ \cdot mol^{-1} \cdot K^{-1}$). Through the values of these parameters it is possible to determine whether the process is favorable, endothermic or exothermic. According to the adsorption enthalpy values, it is possible to determine the nature of the interactions between the adsorbate and the adsorbent.

5.4.1 Henry's Law applied to adsorptive process

In the application of Henry's Law for the adsorption process to be used as the object of study of this work, some hypotheses should be assumed, without which the proposed models would be very limited (RUTHVEN, 1984):

i) adsorption occurs in a low coverage system, where all effects of adsorbent surface interaction between the adsorbed molecules and those present in the vicinity can be neglected;
(ii) process is physically adsorptive, which means there is no dissociation of the species present in the adsorbate (chemisorption) and consequently no changes in the molecular state occur;
iii) for a better understanding of the model, the surface of the adsorbent is considered uniform;
(iv) concentrations studied are low enough to assume that all the molecules in the liquid phase are sufficiently isolated from their neighborhood, to the point of disregarding the resistance forces resulting from the interaction between the molecules;
v) finally, linear equilibrium relation between the fluid and the adsorbed phase is assumed.

In the hypotheses listed above, Henry's Law applied to a given L-S adsorption process is given by Equation 21:

$$q = K_A C \tag{21}$$

where: q is the adsorption capacity (in $mg \cdot g^{-1}$ or $mol \cdot g^{-1}$); K_A is the Henry constant applied to equilibrium in the L-S adsorptive process (in $L \cdot g^{-1}$); and C is the adsorbate concentration in the liquid phase (in $mg \cdot L^{-1}$ or $mol \cdot L^{-1}$).

The adsorbed concentration at the surface of the solid phase (n_s) is given by Equation 22:

$$n_S = \frac{K_A C}{s_e} \tag{22}$$

where s_e is the specific surface area of the adsorbent (in $m^2 \cdot g^{-1}$); and n_s is given in $mg \cdot m^{-2}$, or $mol \cdot m^{-2}$.

5.4.2 Enthalpy, Entropy and Free Energy of adsorption

It is common to find in the majority of the papers which reports thermodynamic studies of the adsorption in batch the calculations of state functions for adsorption (free energy of Gibbs, ΔG^o; enthalpy of adsorption, ΔH^o; and the entropy of adsorption, ΔS^o). These parameters are employed to base the discussion over the energies associated to the adsorption, the mechanisms of adsorption and the sorbent-sorbate interface characteristics. However, these data should be used with a satisfactory sorbent characterization; otherwise such discussion would be merely speculative. In this work, these thermodynamic state functions were calculated by Equation 26 (adsorption enthalpy and entropy changes) and Equation 27 (Gibbs free energy change for adsorption) (PERRY; GREEN; MALONEY, 1999; RUTHVEN, 1984).

Another way to obtain the adsorption enthalpy change ($\Delta H°$) is solving the ordinary differential equation of the isosteric heat of adsorption, given by Clausius-Clapeyron equation (Equation 23) for two states of equilibrium constant (*K*), given at two different temperatures (SAHA; CHOWDHURY, 2011).

$$\frac{d\ln K}{dT} = \frac{\Delta H^o}{RT^2} \tag{23}$$

Solving the differential equation for two temperature states (T_1 and T_2) and the respective equilibrium constants evaluated at these temperatures (K_1 and K_2), it is achieved the Van't Hoff equation applied to the isosteric method (THOMAS; SPITZER, 2021; 2017; ROUQUEROL; ROUQUEROL; SING, 1999), mathematically described by Equation 24:

$$\Delta H^o = -R\left[\frac{T_2 T_1}{(T_2 - T_1)}\right]\ln\left(\frac{K_2}{K_1}\right). \tag{24}$$

where: R is the universal constant of the perfect gases, given in 8.314 $J{\cdot}K^{-1}{\cdot}mol^{-1}$; T_1 and T_2 are the temperatures at which the process is conducted; K_1 and K_2 the equilibrium adsorption constants according to the Langmuir model obtained for the temperatures T_1 and T_2 respectively (PERRY; GREEN; MALONEY, 1999).

Moreover, K_i is given by the Henry's equation for the adsorption, represented by Equation 25:

$$K_i = K_{Ai} \cdot q_{mi} \text{ (in which i = 1, 2, 3,...)} \quad (25)$$

However, when integrating the Equation 23 for a given generic temperature (T), it is obtained the Van't Hoff equation written in its general form (Equation 26), much used by several works found in the literature. From this equation, the adsorption enthalpy change (ΔH °) and the adsorption entropy change (ΔSº) can be easily calculated by the graph ln (K_L) *versus* 1/T, "the Arrhenius plot", when it is presented as a straight line (SAHA; CHOWDHURY, 2011). Through the intercept with ordenate axis, it is possible to calculate the ΔSº; on the other hand, through the angular coefficient, it is possible to calculate ΔHº (KHURANA *et al*., 2018; GANESAN; LOUIS; DAMODARAN, 2018).

$$\ln(K_L^0) = \frac{\Delta S^o}{R} - \frac{\Delta H^o}{R}\left(\frac{1}{T}\right) \quad (26)$$

The change of Free energy of adsorption (ΔGº) is given by Equation 27.

$$\Delta G^o = -RT \ln K_L^0 \quad (27)$$

Additionally, K_L^0 is given by Equation 28 in order to make it dimensionless, so it can be employed in Van't Hoff equation, according to more recent published work about this controversial theme in the literature (LIMA *et al*., 2019; CHANG; THOMAN JR, 2014):

$$K_L^0 = \frac{(1000 \cdot Sorbate\_molecular\_weight) \cdot K_L \cdot C}{\gamma} \quad (28)$$

where K_L is the equilibrium constant modeled by non-linear fitting for experiments conducted under a given temperature; it depends on the isotherm model which best fitted the equilibrium data: Langmuir, L-F, Sips, among others (LIMA *et al*., 2019); C^0 is the standard concentration of

adsorbate (1.0 $mg \cdot L^{-1}$); γ is the coefficient of activity of the adsorbate in liquid phase, which can be considered as 1 (dimensionless).

Finally, the entropy change of adsorption (ΔSº) is also mathematically given by Equation 29.

$$\Delta S^{o} = \frac{\Delta H^{o} - \Delta G^{o}}{T} \quad (29)$$

According to Rouquerol, Rouquerol and Sing (1999) and Ruthven (1984), negative values of ΔG° indicate that the adsorption of the dyes in the adsorbent occurs in a spontaneous way. Positive values of ΔH° indicate the endothermic nature of the process, while negative values indicate that the process is exothermic in nature. Physical adsorption processes will always be exothermic (ROUQUEROL; ROUQUEROL; SING, 1999); however, the energy involved is less than the condensation heat of the solvent.

In general, the intermolecular interaction energies involved in the process of physosorption are very low in relation to the interactions of a chemical nature, which govern chemosorption, being, therefore, a process of reversible nature (ROUQUEROL; ROUQUEROL; SING, 1999). According to Scheufele *et al*. (2016), the bands of the energies relative to the nature of the adsorbent-adsorbate interactions follow the following order: covalent bonds (200–460 $kJ \cdot mol^{-1}$)> Electrostatic forces (6–80 $kJ \cdot mol^{-1}$) > Hydrogen bonds (4–13 $kJ \cdot mol^{-1}$) > Van der Waals forces (2–4 $kJ \cdot mol^{-1}$).

6 MATERIALS AND METHODS

In the following sections, it is presented the methodology employed to produce and characterize the nanocomposites used as nanosorbents of the MB, RB and DR dyes. In this regard, the nanocomposites assessed in this work were accordingly named n-layer graphene oxide (nGO), amino-Fe_3O_4-functionalized n-layer graphene oxide (nGO-NH_2-Fe_3O_4) and amino-functionalized n-layer graphene oxide supported on wood waste charcoal (nGO(NH)R/C). Information such as the chemical route, reactions, and variables, as well as material preparation and the conditions under which the analyses were carried out, are also discussed. After the characterization methodology, the adsorption sections are systematically presented in a way from which is possible to acquire information about the adsorbates (molecular weight and structure, maximum absorbance wavelength, among others) and the conditions in which the adsorption of MB, RB and DR were performed. These were assessed by preliminary experiments: point of zero charge and the influence of pH over the adsorption of each dye. Following these, the methodology of specific adsorption experiments, such as kinetics, equilibrium, thermodynamic and regeneration are addressed with details. The treatment of raw textile wastewater by coagulation and adsorption onto nGO-NH_2-Fe_3O_4 is carefully described. Finally, phytotoxicity assays of graphite nanoplatelets (GNP), nGO and nGO-NH_2-Fe_3O_4 was assessed through the exposure of American lettuce seeds (*Lactucca sativa l*) on these materials.

6.1 SYNTHESIS OF N-LAYER GRAPHENE OXIDE (MODIFIED HUMMERS METHOD)

The graphene oxide synthesis, obtained from the graphite, was carried out through the process known as Modified Hummers Method, which derives from the method developed by Hummers and Offeman in the mid-1950s for graphite oxidation (HUMMERS; OFFEMAN, 1958). 1.0 g of graphite powder (99% A.P., *Merck*) was weighed in a precision scale model FA2104N (*Bioprecisa*) and added together with 28 mL of concentrated sulfuric acid (H_2SO_4, 98% A.P., *VETEC Sigma-Aldrich*). H_2SO_4 was previously stored in a freezer under 5 °C prior to the mixture with graphite powder. Then, the becker was placed in a magnetic agitator Q26122 (*Quimis*) under stirring at 300–350 rpm. The temperature was kept below 12 °C until the complete homogenization of the mixture. The temperature control during the graphite dilution

phase in H_2SO_4 was carried out rigorously through ice bath. Then potasse permanganate ($KMnO_4$, 99% A.P., *Dinâmica*) was added slowly to the sample. After $KMnO_4$ addition, the temperature rose to 32 °C and the system was maintained under these conditions for a period of 6h. After the oxidation reaction of the graphite, 35 mL of hydrogene peroxide (H_2O_2, 37% A.P., *Dinâmica Química*) was added to finish the reaction. Graphite oxide sample sample was washed with 50 mL of solution of 25% of hydrochloric acid (diluted from HCl, 98% A.P., *Dinâmica Química*) and then it was subjected to successive washes with distilled water until the pH of the suspension reached 2.8–3.5. After the washing steps, the suspension of graphite oxide was diluted in distilled water from 1:4. Finally, to acquire nGO suspension, the graphite oxide suspension was submitted to ultrasonic exfoliation in a tank bath (working volume 1.9 L) with coupled transducer model P30H (*Elma*), operating at 37 kHz, 400–480 W and room temperature, 25 ºC, for 4 hours.

6.2 FUNCTIONALIZATION OF NGO WITH AMINE AND FE_3O_4 NANOPARTICLES

To obtain the amino-functionalized nGO with anchored Fe_3O_4 nanoparticles. An aliquot of nearly 370 mL of nGO in aquous suspension (~ 0.0027 $g \cdot mL^{-1}$) was separated and mixed with 250 mL of monoethylene glycol (HOH_2CCH_2OH, 99% A.P., *NEON Química*). The mixture was placed in a magnetic heater model Q26122 (*Quimis*) under vigorous steering (300–350 rpm) to evaporate the water from nGO suspension and subsequently reach the temperature of 180 °C. Then, 0.5 g of iron chloride hexahydrate ($FeCl_3 \cdot 6H_2O$, 99% A.P., *Dinâmica*) and 3.0 g of anhydrous sodium acetate (CH_3COONa, 99% A.P., *Sigma-Aldrich*) were added to the sample. Finally, 35 mL of diethylenetriamine (DETA, 99% A.P., *Sigma-Aldrich*) was added to the mixture after it reached 180 ºC. The solvothermic method of anchoring Fe_3O_4 nanoparticles occurred concurrently with the functionalization reaction of the amino groups of nGO (AI *et al*., 2011). The functionalization reaction took place in batch mode, in a 600 mL closed loop reflux flask, with vigorous stirring speed (300–350 rpm) for 6 hours and temperature strictly controlled at 180 ºC. After the reaction, the mixture was cooled to room temperature (25–30 ºC). After cooled, the sample was washed with 150 mL of ethanol (absolute, 99% A.P., *NEON Química*) and then successive washes with distilled water were carried out. The suspension was then decanted and the supernatant removed. The amino-Fe_3O_4-functionalized nGO suspension was

then stocked to perform UV-Vis scanning and subsequent characterization analyzes, as well as for use in the adsorptive process.

6.3 SUPPORTING OF NGO(NH)R ON WOOD WASTE CHARCOAL

Vegetal charcoal was produced in a bed co-current, open top, downdraft biomass gasifier, connected to a spark lighter, with a prime power rating of 2.25 kW. The engine was coupled to a Toyama generator (Figure 10). The gasifier is installed in the Laboratory of Activated Charcoal (LCA), Department of Mechanical Engineering, Federal University of Paraíba (UFPB). Wood wastes from furnitures of public schools located at João Pessoa city were supplied as biomass for the gasifier. After the gasification process, the charcoal was collected at the bottom of the gasifier and then it was crushed and sieved to 200 mesh. The same charcoal, derived from wood wastes, produced in the same gasifier and by the same methods was studied as adsorbent of the reactive dye Indosol Black NF1200 by Kelm *et al*. (2019). Moreover, Pessôa *et al*. (2019) studied the adsorptive properties of the biochar produced from wastes of açaí cores; similarly, this biochar was product of the gasification process. Therefore, detailed information regarding the process of gasification of wood waste charcoal, as well as wastes from açaí cores, can be found in published papers (KELM *et al*., 2019; PESSÔA *et al*., 2019).

Figure 10 – Scheme of the gasifier used to produce synthesis gas and charcoals from biomass.

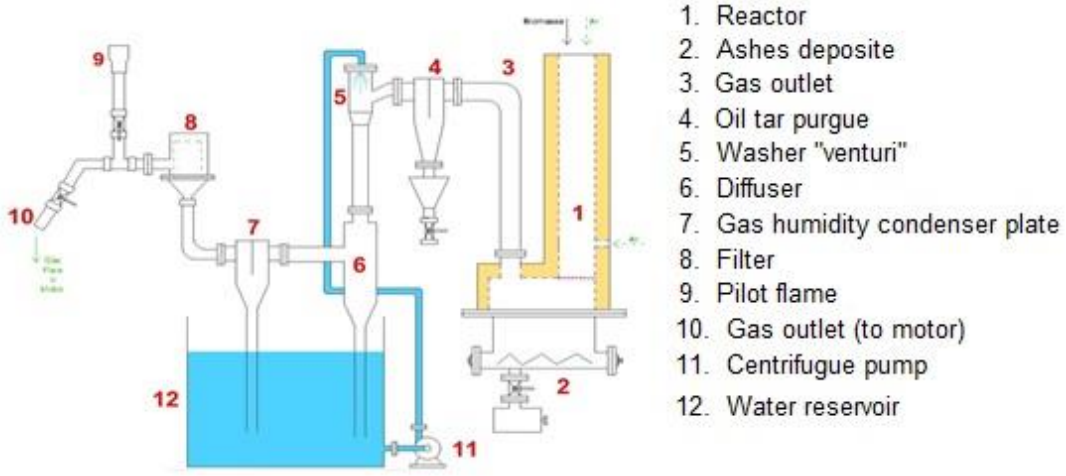

Source: reproduced from Pessôa *et al*. (2019), with permission from Elsevier, Copyright 2020.

Aiming the anchorage of amino-functionalized graphene on vegetal charcoal, it was added aliquots of 1.0 g and 2.0 g of vegetal charcoal during the functionalization step, with 1.0 g of nGO in 250 mL of ethyleneglycol. 35.0 mL of DETA was then added to the mixture at 180 ºC and 350 rpm, for 6 h. The supporting of nGO(NH)R in charcoal took place simultaneously as amino-functionalization reaction (Figure 11). The proportions of nGO(NH)R per charcoal were established for 1:1 and 1:2 (in mass) in orther to investigate its influence in the adsorption. Consequently, both materials were respectively termed nGO(NH)R/C (1:1 w/w) and nGO(NH)R/C (1:2 w/w) in this thesis. After functionalization, the samples were washed with 150 mL of ethanol (absolute, 99% A.P., *NEON Química*) and subsequently washed with distilled water until the pH stabilization. Furtehrly, nGO(NH)R/C samples were dried in an oven at 75 ºC and small aliquots were separated for characterization. Oxygenated groups of nGO/nGO(NH)R can act as anchoring sited for supporting these molecules on biomass fibers (WANG *et al*., 2018b); similarly, these functional moieties play the same role in face of charcoal surfaces and their active sites.

Figure 11 – Schematic representation of amino-functionalization of nGO and nGO(NH)R supporting onto wood waste charcoal.

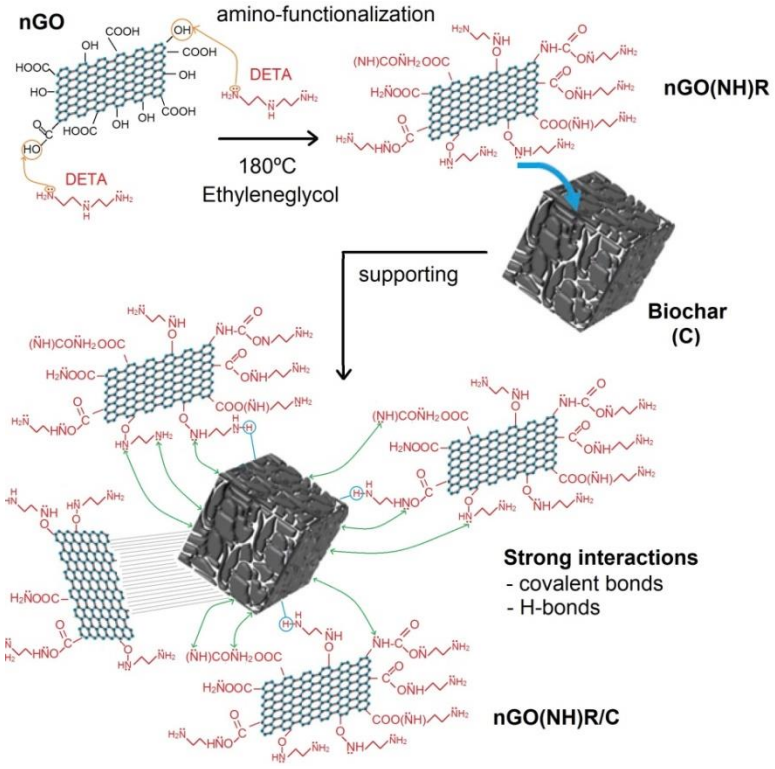

Source: the author (2019).

6.4 CHARACTERIZATION TECHNIQUES

Among the most varied techniques to characterize functionalized graphene samples, one of the most important is infrared spectroscopy with Fourrier Trasform (FTIR), since it is intended to reveal which functional groups were aggregated to the surface of graphene, GO and rGO after functionalization reactions. This analysis becomes crucial when high defect densities are observed in the basal plane, because under such circumstances, the degree of functionalization of the sample can not be detected only by Raman spectroscopy (EIGLER; HIRSCH, 2014). FTIR analyzes for the samples of nGO, nGO-NH_2-Fe_3O_4 and nGO(NH)R/C (1.0 and 2.0 g) were performed using Shimadzu model IRTracer-100 (*Shimadzu*) coupled with an Attenuated Total Reflectance (ATR) crystal. FTIR analyses were also carried out in a spectrometer model Tensor 27 (*Brüker*), with transmittance through KBr tablets (only for samples nGO and nGO-NH_2-Fe_3O_4 before and after adsorption of MB and RB). All analyses were conducted under ambient air moisture controlled below 54%. Eventual deviations in the spectra were correct through data baseline tool of Origin^{TM} 9.0.

Scanning electron microscopy (SEM) was performed in a microscope model VEGA3 (*Tescan*). Aliquots of nGO and nGO-NH_2-Fe_3O_4 suspension (with concentration of 3.1 and 5.7 $mg \cdot mL^{-1}$, respectively) were dried in a stove at 75 ºC and then were kept under vacuum control to avoid water adsorption from environmental moisture. The materials were deposited on the surface of a carbon conductive tape in order to allow the electron conduction from the field emission cannon through the samples. After that, the samples were deposited in *stubbs* and were covered with gold under vacuum atmosphere. The microscope system is assembled inside a vacuum chamber. Moreover, the samples spots were focused by two confocal and one objective lens, which could be adsjusted to 500–20000x. Energy dispersive spectroscopy (EDS) was carried out in a EDS spectrometer model AztecLive (*Oxford*) for the sample of nGO-NH_2-Fe_3O_4, prepeared under similar conditions described above, although without covering with gold in order to avoid further interferences in the action of electron beam.

Atomic Force Microscopy (AFM) was employed to evidence the roughness, thickness and other morphological nano-characteristics of nGO and nGO-NH_2-Fe_3O_4. AFM analysis was performed in an atomic force microscope model Icon Dimension (*Brüker*), equipped with RTESPA. nGO and nGO-NH_2-Fe_3O_4 suspension were diluted in deionized water to 1:1000.

Subsequently, the samples were dried and then deposited on fresh mica substrate prior to accomplish the images capturing. A number of 30 flake profiles were counted and analyzed by Gwyddion™ software, which also generated all thickness and roughness profiles.

Raman spectroscopy was performed in order to evaluate the behavior of the the characteristic graphitic bands. The analysis occurred in the baseline plane of nGO/functionalized nGO, performed by a Raman spectroscope model Alpha 300 (*Witec*). The samples were irradiated with a red laser of 633 nm. In each sample, at least ten individual spectra were measured at random points; each spectrum was obtained with accumulations of 30 s using a lens of 100x and a grid of 600 mm/line.

X-ray diffraction (XRD) was performed through an X-ray diffractometer model Ultima (*Rigaku*). The samples were dried at 75 ºC and then collected to a vacuum dissecator to avoid adsorption of moisture. The samples were deposited on the diffractometer holder, in which diffraction angle (2θ) ranged from 5 to 90º.

UV-Vis spectra of nGO and nGO-NH_2-Fe_3O_4 were obtained through spectral scanning in an UV-Vis spectrophotometer, model Aquamat™ Thermo Genius 10S (*ThermoFisher*). Wavelength ranged from 200 to 1000 nm. nGO and nGO-NH_2-Fe_3O_4 aqueous suspensions were diluted to 1:100 to avoid interferences and variations in the absorbance peaks.

Thermal stability of graphite powder, graphite oxide, nGO and nGO-NH_2-Fe_3O_4 were characterized using thermogravimetric analysis (TGA). All measurements were conducted in a thermogravimetric analyzer model STA 449F3 Jupiter (*Netzsch*), under atmosphere of synthetic air (80% of N_2 and 20% of O_2) with flux of 50 $mL \cdot min^{-1}$, over a temperature range of 30–1000 °C and with heating ramp rate of 3.0 $K \cdot min^{-1}$.

Finally, the specific surface area (in $m^2 \cdot g^{-1}$), pore volume ($cm^3 \cdot g^{-1}$) and average pore size (in nm) of wood waste charcoal and nGO(NH)R/C (1:1 and 1:2 w/w) were acquired by BET method of adsorption-desorption of N_2 at 77.3 K in a surface area analyzer Quantachrome (*NOVA Scientific*). Additionally, the particle size distribution and specific surface area of the samples of nGO, nGO-NH_2-Fe_3O_4 and nGO(NH)R/C in aquous suspension was analyzed in a dynamic light scattering (DLS) granulometer model Mastersizer 2000 (*Malvern*) with particle size range 0.02–2000.00 nm.

6.4.1 Point of zero charge

The point of zero charge (or isoelectric point, according to some reported works, pH_{PZC}) was performed through the salt addition method (MAHMOOD *et al*., 2011) carried out in 12 points of pH, with the pH varying between 2 and 12. 20.0 mL of aqueous suspensions of nGO and nGO-NH_2-Fe_3O_4 (~ 0.08–0.12 g) were added to Erlenmeyer flasks with 20.0 mL of aqueous solution of NaCl 0.1 mol·L^{-1} at 25 °C. The pH of each sample was measured in the bench phameter model Q400as (*Quimis*) and adjusted with solutions of HCl 6.0 and 0.1 mol·L^{-1} and NaOH 6.0 and 0.1 mol·L^{-1}. All samples were then placed in an incubator with orbital agitaton model MA-420 (*Marconi*) and the contact time of the adsorbent with the solution at the set pH was 24 hours; the stirring speed was set at 300 rpm.

6.5 DYES – PREPARATION OF SOLUTIONS AND CHARACTERIZATION

MB and RB were respectively purchased from *Neon Química Ltd*. and *Dystar do Brasil S/A*. DR was supplied by *Clariant do Brasil S/A*. Stock solutions (1000 mg·L^{-1}) of all dyes were prepeared and the UV-Vis sacanning of their diluted solutions (10, 20, 50 and 100 mg·L^{-1}) was carried out in an UV-Vis spectrophotometer Aquamat™ Thermo Genius 10S (*ThermoFisher*). The powder samples of RB and DR were dried and stocked in Eppendorff tubes free of moisture. Finally, FTIR spectra for the reactive dyes (RB and DR) were acquired in order to investigate the characteristic bands of each dye, which furtherly appeared in FTIR spectra of nGO-NH_2-Fe_3O_4 after regeneration protocol for RB and DR adsorption. Powder samples of RB and DR were analysed through deposition in ATR crystal in an infrared spectroscope model IRTracer-100 (*Shimadzu*). Wavenumbers ranged from 500–4000 cm^{-1}.

6.6 ADSORPTION IN BATCH

Stock solutions of the dyestuffs to be evaluated were prepared, whose concentration were determined according to the performed experiment. Aliquots of 25 mL of dye solution were transferred to 125 mL erlenmeyers. The erlenmeyers were deposited on the shaker table model

Q225M (*Quimis*) under set agitation velocity. All experiments were performed with constant agitation (300 rpm) under environmental conditions (25 °C, 1.0 atm). The pH of the dye solution was individually adjusted in agreement with the analysis of pH effect for each dye, as furtherly discussed in Section 7.3. After adsorption, the adsorbent and the adsorbate were separated by filtration in a Teflon filter mesh 45 μm. Residual concentrations of dyes in solution (*C*) were determined by absorbance measuring at the corresponding λ_{max} in an UV-Vis spectrophotometer model Aquamat^{TM} Thermo Genius 10S (*ThermoFisher*). All experiments were performed in duplicate, while *C* was calculated by the arithmetic mean between the two measures. Using the final concentration data, adsorption efficiency (*R*(%), in %) and adsorption capacity (*q*, given in $mg \cdot g^{-1}$) were finally calculated according to Equations 2 and 1, respectively. Most operational conditions were set in agreement with early reports (ARAÚJO *et al*., 2018; 2019) and followed the methodology of previous researches (FRAGA *et al*., 2020b; KELM *et al*., 2019; PESSÔA *et al*., 2019) from the research group *Grupo de Processos e Tecnologias Ambientais* (GPTA) at UFPE.

Depending on the solubility of nGO and nGO-NH_2-Fe_3O_4 in water, and consequent difficulty in the filtration process, separation of the adsorbent from the adsorbate could be performed by centrifugation at a constant rate of 4500–5000 rpm in a centrifugue model Q222E (*Quimis*) during an interval of 5–7 min.

Adsorbent dosage of nGO and nGO-NH-Fe_3O_4 samples (concentration, in $mg \cdot mL^{-1}$) was measured by gravimetry by adding 1.0 mL to previously heated and wheighted Petry dishes. The dishes were placed in a stove heated at 70 ºC until the water is completely vaporated. The dishes were then wheighted and the difference between the measures was the mass of nGO/nGO-NH-Fe_3O_4 present on the dishes. Finally, the concentrations of nGO/ nGO-NH-Fe_3O_4 suspensions were calculated.

6.7 EFFECT OF PH OVER THE ADSORPTION

Tests of pH effect in the adsorption were carried out by evaluating the adsorption capacity in the pH range of 2.0 to 12.0. Aliquots of 1.0 mL of nGO-NH_2-Fe_3O_4 suspension were contacted

with 25.0 mL of dye solution, and stirred at 300 rpm for determined contact time – 20 min for the adsorption of MB; 90 min for RB; and 120 min for DR. The pH's of dye solutions after the experiments were measured in the bench phameter model Q400as (*Quimis*). The pHs of dye solutions were adjusted with solutions of HCl 6.0 and 0.1 $mol \cdot L^{-1}$ and NaOH 6.0 and 0.1 $mol \cdot L^{-1}$. After the adsorptive process, the adsorbent was separated from the adsorbate by filtration on 45 μm poly(tetrafluorine-ethylene) (PTFE) filters and the final concentrations of the samples were measured in the UV-Vis spectrophotometer Thermo Genius 10S (*ThermoFisher*).

6.8 EXPERIMENTS OF ADSORPTION KINETICS

For the kinetic study, the aliquots of 25 mL of adsorbate solution, with pre-established initial concentration (C_0, 100 $mg \cdot L^{-1}$), were mixed with 1.0 mL aliquots of adsorbent (nGO or nGO-NH_2-Fe_3O_4 suspension, with concentration ranging from 5.7–6.0 $mg \cdot mL^{-1}$). The samples were placed in an orbital agitator model Q225M (*Quimis*) under stirring speed of 300 rpm. The contact time in this step varied from 1 to 120 min. The experiments were carried out under 298 K, 1.0 atm and natural solution pH. To obtain adsorption kinetic parameters (adsorption kinetic constant, *k*), the data were modeled using the non-linear equations of Lagergren's pseudo-first-order model (PFO) and the Ho's pseudo-second-order model (PSO) according to Equations 15 and 17. The models of pseudo-n^{th}-order (PNO) and the intraparticle diffusion (IPD) were also evaluated by non-linear fitting in Origin™ 9.0. In this sense, the model that best fit the experimental data (which has the highest coefficient of determination (R^2) was adopted as the representative of the kinetics of the process.

6.9 EXPERIMENTS OF ADSORPTION EQUILIBRIUM

The equilibrium experiments were performed to determine the isotherm that best represents the adsorption behavior, as well as the adsorption parameters, such as the maximum adsorption capacity (q_m), the equilibrium constant (K_{Eq}) and the heterogeneity factor (*n*). All the tests were carried out in batch under the following conditions: adsorbent dosages, 1.0 mL of nGO and nGO-NH_2-Fe_3O_4 (~ 5.7 $mg \cdot mL^{-1}$) and 0.1g of nGO(NH)R/C; 25 mL of dye solution at

specific pH (11.0 for MB and neutral pH 5.8–7.0 for RB), temperature of 298 K and stirring velocity of 300 rpm. The contact time was established in adsorption kinetics experiments - applied at the time when the system reached the equilibrium state. The adsorbate concentration ranged from 10 to 500 $mg \cdot L^{-1}$ in order to achieve the highest possible saturation of nGO and nGO-NH_3-Fe_3O_4 sorbents. The method of non-linear fitting was used to fit each isotherm models to experimental data and consequently to obtain the adsorption parameters. The models were adjusted using the "non-linear curve fit" tool of the Origin^{TM} 9.0 program.

6.9.1 Equilibrium of adsorption of a binary mixture (Methylene Blue–Remazol Black B)

A binary mixture of MB and RB was prepared in the proportion of 1:1 in order to evaluate the behavior of the adsorption of each dye. Equilibrium experiments for the adsorption of the mixture of two adsorbates by the same adsorbent were carried out in the same conditions established in the equilibrium experiments for a single component adsorption (Section 6.9). Yet, the pH of MB-RB solution was established at 7.0. According to reported in the literature (ALLEN; McKAY; POTTER, 2004; ROUQUEROL; ROUQUEROL; SING, 1999), the influence of the presence of one dye on the adsorption of the other can be assessed. For that, the concentrations of each dye in the mixture, before and after the adsorption, were measured in the UV-Vis spectrophotometer. For that, each dye concentrations were assessed through its correspondent analyitcal curve (λ_{max} 659 nm for MB, and 569 nm for RB). Then, the equilibrium adsorption capacities for MB and RB (in $mg \cdot g^{-1}$) were calculated and plotted q *versus* C in order to acquire the isotherms for MB and RB in the mixture. The equilibrium data were then modeled according to the predictive model of the Langmuir isotherm, adapted for a binary mixture (Equations 12 and 13).

6.10 EXPERIMENTS OF ADSORPTION THERMODYNAMICS

Aiming to obtain the thermodynamic parameters, Enthalpy of adsorption (ΔH^o); Gibbs free energy of adsorption (ΔG^o); and adsorption entropy (ΔS^o), adsorption equilibrium tests (similar to those described in topic 4.8) were performed by varying the operating temperature of the system. However, the experiments were carried out in the range of concentration 10.0–500.0 $mg \cdot L^{-1}$, in order to obey the postulates of Henry's Law. For this, erlenmeyers of 125 mL containing the different dye solutions used in the experiments were placed in the Shaker incubator Marconi, model MA-420, preheated at the temperature established for experiments at 298 K, 318 K and 338 K. The duration of the experiment for each dye was determined according to the equilibrium time obtained in the adsorption kinetics experiment.

Thermodynamic state functions (ΔH^o, ΔG^o and ΔS^o) were obtained by applying the Equations 25 and 26; as well as the graphs ln (K_L) *versus* 1/T and their respective intercepts of the straight line with y-axis and their angular coefficients.

6.11 SORBENT REGENERATION

Adsorbent regeneration experiments were performed to evaluate losses in adsorption performance after several adsorption-desorption cycles. After adsorption of MB, RB and DR under experimental conditions described in section 6.6 (batch adsorption), nGO-NH_2-Fe_3O_4 was separated from the dye solution by centrifugation and washed three times with distilled water to remove the non-adsorbed dye. The sample was then transferred to a 25 mL bottle of distilled water in a model Shaker incubator Marconi, model MA-420, set at 65 ºC. According to some studies in the literature that reported desorption of dyes and other organic pollutants, such as pesticides and aromatic compounds, at higher temperatures than the adsorption process (CHEN *et al*., 2016; GRAJEK, 2000). In addition, desorption experiments were conducted under 300 rpm for 1 h, and neutral pH (~ 7.00).

6.12 TREATMENT OF RAW TEXTILE WASTEWATER BY ADSORPTION ONTO NGO-NH_2-FE_3O_4

6.12.1 Coagulation and sampling of raw wastewater

The raw textile wastewater was collected in the laundromat *Lavanderia Nossa Senhora do Carmo Ltd*. in the city of Caruaru, Pernambuco, Brazil. The effluent from washing and finishing processes is treated by flocculation followed by decantation in the wastewater treatment station located in the laundromat facility. After the equalization process, the flocculation was performed with 5.0 kg of $Al_2(SO_4)_3$, employed as coagulant agent, per each 60.0 m^3 of raw effluent and with the addition of NaOH (s). The wastewater flocculation took place in a tank of 129 m^3. The effluent pH in the coagulation/flocculation tank varied within 6.0–8.0 and the whole batch of effluent treatment was carried out in 4 h.

Samples of the raw and coagulated wastewater were collected from the tanks in the laundromat treatment station in the same day and time. Effluent samples were stored in plastic reservoirs of 5.0 L and kept in freezer under 5 ºC. Then the samples of raw and coagulated wastewater were submitted to adsorption onto nGO-NH_2-Fe_3O_4 by experiments in batch in the same conditions established in the Section 6.6.

6.12.2 Procedures of effluent characterization

The main parameters of wastewater characterization were assessed before and after the process of adsorption: total suspended solids (TSS), chemical oxygen demand (COD), biochemical oxygen demand (BOD), apparent color (Hazen), turbidity (NTU) and pH. Finally, these parameters were assessed in accordance to what is established in the current legislation for the quality standards of water bodies and treated effluents disposal, the Resolution CONAMA 410 (BRAZIL, 2011). Data were also compared with parameters established by the *2012 Guidelines for Water Reuse* for industrial reuse of reclaimed water (USEPA, 2012).

Apparent color of the effluent samples was measured in a photometer Spectroquant NOVA 60 (*Merck*), effluent samples were deposited on a quartz bucket. The turbidity was measured in a portable turbidimeter model Q279P (*Quimis*). pH of wastewater samples was measured in a pHameter Q400AS (*Quimis*).

The concentration of total suspended solids (TSS, in $mg \cdot L^{-1}$) was determined following the methodology reported in the technical standard SABESP NTS 013 (SABESP, 1999). From this standard, 5 mL of wastewater sample is filtered in vacuum and the filter membrane is deposited in a porcelain capsule of 125 mL. The capsule is then transferred to a muffle and calcined at 550 ºC for 30 min. After the calcination, the capsule with the solid residue is weighted and the difference of weigh is employed in the calculation of TSS concentration.

COD and BOD analyses were carried out following proper methodologies reported in APHA Standard Methods (APHA, 1999). For COD analysis, a digestion solution is prepeared with solution of potassium dicromate (K_2CrO_4) 0.40 $mol \cdot L^{-1}$. Catalytic solution is prepared with with solution of H_2SO_4 15.3 $mol \cdot L^{-1}$ and $AgSO_4$ 0.02 $mol \cdot L^{-1}$. Then, 2.0 mL of effluent sample is mixed with 1.5 mL of digestion solution plus 3.5 mL of catalytic solution and placed in a thermodiggestor model TR620 (*Merck*) set at 150 ºC during 2 h. After the digestion of the sample, the residual concentration is measured in an UV-Vis spectrophotometer Thermo Genius 10S (*ThermoFisher*). The UV-Vis calibration curve is performed prior the concentration measurements, as established in previous procedures (APHA, 1999). The "white" solution was distilled water at room temperature (~25 ºC). To perform BOD analyses, effluent samples were deposited in BOD flasks of 500 mL and placed in a respirometer model Oxitop IS6 (*WTW*), and then the samples were placed in an incubator model Q315M (*Quimis*) for 5 days.

6.13 STUDIES OF PHYTOTOXICITY

Acute toxicity studies were performed by exposing *Lactuca sativa L* seeds to GNP, nGO and nGO-NH_2-Fe_3O_4 suspension, according to a procedure adapted from Sobrero and Ronco (2004). The objective was to estimate the toxicity degree by the germination (SG) and elongation (SE) percentuals. Ten (10) seeds of American lettuce were spread on a Petri dish coated with filter paper and then it was added 2.0 mL of nGO and nGO-NH_2-Fe_3O_4 suspensions. Moreover, the toxicity of dye solutions after adsorptive process was also evaluated through this method. The assays were performed in triplicate, according to the procedure reported by the authors. The positive control was performed by adding 4.0 mL of Zn (II) solution to a third proof sample in order to compare the inhibitor power between them. The two samples and the test specimen were

packed in aluminum film and placed in the incubator at a temperature of 22 ± 2°C for a period of 120 hours.

After the incubation period, the samples were removed from the incubator and it was verified if there was development of lettuce seeds. For seeds in which growth occurred, root and stem length were measured and compared to the test specimen. For those cases where germination was greater than 90% of total seeds, the result was considered acceptable, therefore, the evaluated substance was not considered to be highly inhibitory (toxic).

For each germinated seed, the root length was measured to calculate the normalized residual percentage of germinated seeds (Equation 29) and residual percentage of elongation (Equation 30) for dye solutions and graphene suspensions (BAGUR-GONZÁLEZ *et al*., 2011). All experiments were performed in duplicity.

$$SG = \frac{Germ_{Sample(i)} - Germ_{Control}}{Germ_{Control}} \tag{29}$$

where $Germ_{sample(i)}$ is the average number of germinated seeds in saturation extract "i" (%), and $Germ_{control}$ is the average number of germinated seeds in the blank control (%).

$$SE = \frac{Elong_{Sample(i)} - Elong_{Control}}{Elong_{Control}} \tag{30}$$

where $Elong_{sample(i)}$ is the average length of the seed roots in the saturation extract "i" (cm), and $Elong_{control}$ is the length of the seed roots in the blank control (cm).

7 RESULTS AND DISCUSSION

In the following sections, the data, results and main findings subject of the investigation regarding the employment of nGO and its functionalized derivatives are summarized and discussed with depth. Stand methodology was used to investigate the properties of each material following their characterization results, which were extensively compared with works published in the literature. Then, the results and main findings acquired in the adsorption assays with MB, RB and DR dyes are summarized and discussed in the following sections. Graphics, tables and schematic representations are displayed in the following sections with their respective discussions. The experiments with real textile wastewater were also analyzed and the main effluent parameters after the treatment by coagulation plus adsorption were compared with the indicators established in current Brazilian and US legislation. A cost assessment is also reported in the final sections, in which the readers might have an understanding of the production and operational cost of nGO and nGO-NH_2-Fe_3O_4. Finally, the results of phytotoxicity assays are reported and discussed in comparison with the current literature.

7.1 MATERIALS CHARACTERIZATION

7.1.1 Infrared spectroscopy

Figure 12a shows FTIR spectra for nGO and nGO-NH_2-Fe_3O_4 acquired from ATR method. The wide band between 3427.0 and 3250.0 cm^{-1} refers to the stretching vibration of the O–H bonds of the nGO carboxylic acids and hydroxyl groups over nGO surface (ZHANG *et al*., 2015), this band was also revealed in the nGO-NH_2-Fe_3O_4 spectrum. The stretching vibrations of –NH bond is represented by narrow bands in FTIR spectra, with average intensity between 3300.0 and 3500.0 cm^{-1}, and can be attributed to the presence of amine groups on the surface of the adsorbent. However, amine N–H stretching vibration band are clearly overlapped by the band at 3200–3500 cm^{-1}, related to stretching vibrations of O–H bonds. In nGO-NH_2-Fe_3O_4 spectrum, the 580.0 cm^{-1} peak is attributed to the Fe–O bond vibration of Fe_3O_4 nanoparticles in the adsorbent, similarly to report by Guo *et al*. (2015). The peak at 1572.5 cm^{-1} is caused by the stress vibration and flexural vibration of the N–H bond, which is considered the presence of

amino groups on the surface of functionalized graphene oxide (CALIMAN *et al*., 2018; ZHAO *et al*., 2016). In addition, the intense peak at 1658.0 cm^{-1} can be attributed to amide groups as a consequence of parallel reactions during functionalization synthesis.

Figure 12 – FTIR spectra of: nGO, nGO-NH_2-Fe_3O_4 acquired by ATR method; b) nGO(NH)R/C (1.0 g and 2.0 g of charcoal) acquired by ATR method; c) nGO, nGO-NH_2-Fe_3O_4 and nGO-NH_2-Fe_3O_4 after sorbent regeneration assays of MB (10 cycles), acquired by transmittance through KBr pellet; d) nGO-NH_2-Fe_3O_4 before and after sorbent regeneration assays of RB (10 cycles) and DR (5 cycles), acquired by transmittance through KBr pellets.

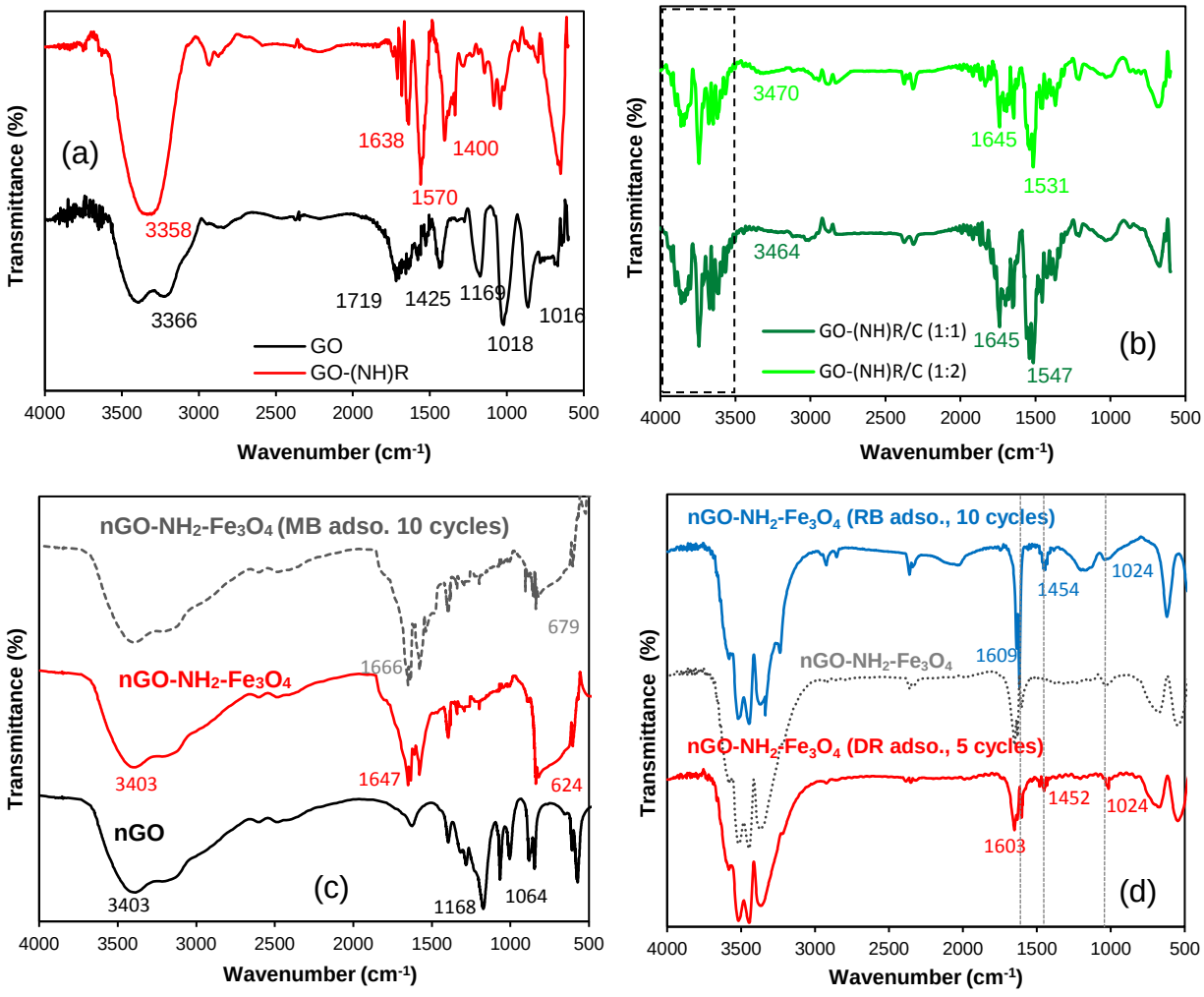

Source: a) reproduced from Fraga *et al*. (2019b), with permission from Springer-Nature, Copyright 2020; b) the author; c) adapted from Fraga *et al*. (2018), with permission from Springer-Nature, Copyright 2020; d) the author (2019).

FTIR spectra for amino-functionalized nGO anchored in wood charcoal (Figure 12b) exhibited a band between 3500 cm^{-1} and 3950 cm^{-1}, attributed to the presence of –OH groups over the nanocomposite surface and edges. However, these bands are delocated from their original wavenumber intervals (2900–3500 cm^{-1}) and exhibits strong fluctuation in comparison to nGO and nGO-NH-Fe_3O_4 spectra. This behavior needs an in-depth investigation, since it might be an influence of ATR method to acquire FTIR spectra of charcoal-based materials. Moreover, the band at 1645 cm^{-1} is attributed to amides, which are consequence of DETA amidation reaction with –COOH, –OH and epoxyl groups of nGO, which took place in parallel with amino-functionalization. There weren't any differences in the positions of the peaks and bands between both spectra, thus nGO(NH)R/C (1:1) exhibited more intense peaks in comparison to nGO(NH)R/C (1:2). This behavior might be related to a higher mass ratio nGO(NH)R/C, which consequently increase the intensity of some peaks. The presence of these characteristic peaks is a strong indicative of successful anchorage of nGO(NH)R over charcoal surface.

Infrared spectroscopy analysis was also performed for the nGO-NH_2-Fe_3O_4 samples after 10 regeneration cycles for MB and RB adsorption (Figure 12c and d) in order to evaluate the occurrence of changes in their functional groups. The samples of nGO-NH_2-Fe_3O_4 were prepared after 10 cycles of adsorption/desorption of MB and RB following the method of sorbent regeneration specified in the section 6.11. For DR, it was only performed 5 regeneration cycles. nGO-NH_2-Fe_3O_4/MB remained with the distribution of its bands along the almost unchanged spectrum. However, there is a decrease in band intensity in the range of 560–620 cm^{-1}, possibly due to the removal of some Fe_3O_4 nanoparticles due to the regeneration process, with several washes, centrifugation and desorption at 65 ºC. The band at 1022 cm^{-1} for nGO-NH_2-Fe_3O_4/RB might be attributed to –S=O– stretching vibration of sulfoxide groups (R–SO–R) present in the RB molecules (BILAL *et al*., 2018; NEOH *et al*., 2015). According to early reports which monitored the degradation of RB through FTIR asessment, reactive dyes also exhibit bands at 1450 cm^{-1} and nearly 1600 cm^{-1}, which are related to vibrational strechs of N=N bonds from the chromophore azo/diazo and benzyl groups, respectively (BILAL *et al*., 2018; NEOH *et al*., 2015). The band at 1454 cm^{-1} appeared in both nGO-NH_2-Fe_3O_4/RB and nGO-NH_2-Fe_3O_4/DR (in minor intensity) spectra, indicating the presence of azo grups in the samples. Furhtermore, the detection of sulfoxide (1022 cm^{-1}) and aromatic groups (intense band at 1609 cm^{-1}) is evidence that the RB molecules remained attached to nGO-NH_2-Fe_3O_4 surface even after several

regeneration rounds. This behavior is the opposite from what is verified for MB adsorption (Figure 12c). Moreover, it indicates that the binding energy of RB–nGO-NH_2-Fe_3O_4 interactions is considerably great to be broken by the supplied heat during sorbent regeneration (under 65 ºC and 300 rpm). Detailed information regarding the thermodynamics of adsorption and regeneration assessment is given in sections 7.7 and 7.8.

Finally, the difference in the intensity and the broadness of some bands between the spectra of nGO and nGO-NH_2-Fe_3O_4, acquired by ATR (Figure 12a) and transmittance through KBr pellets (Figure 12c and d) might be attributed to the method of sample preparation and the analysis themselves. Moreover, in KBr transmission, a greater amount of water from environment moisture was adsorbed in the sample, which was consequently reflected in the band relative of the stretching vibration of O–H bonds. This band was broader for KBr transmission (2860–3780 cm^{-1}) in comparison to ATR spectra (2990–3650 cm^{-1}).

7.1.2 Scanning Electron Microscopy with Energy-Dispersive Spectroscopy

The morphological structures of nGO and nGO-NH_2-Fe_3O_4 are depicted in Figure 13. It is possible to visualize the overlap of some folded layers and wrinkles between them. In addition, some clear aggregation points, with a much larger overall roughness, can be seen on the surface of nGO-NH_2-Fe_3O_4 (Figure 13d, e and f), compared to the nGO sample (Figure 13a, b and c). The larger wrinklages in nGO-NH_2-Fe_3O_4 samples is due to the amino-functionalization, which promoted bonds between different functional groups from different nanosheets. This is in accordance to reported data found in the literature (PARK; RUOFF, 2009). The presence of agglomerated Fe_3O_4 nanoparticles on the samples was detected by EDS technique.

Figure 13 – SEM photographs executed for: nGO at 5 kX (a), 10 kX (b) and 20 kX (c); nGO-NH_2-Fe_3O_4 at 5 kX (d), 10 kX (e) and 20 kX (f).

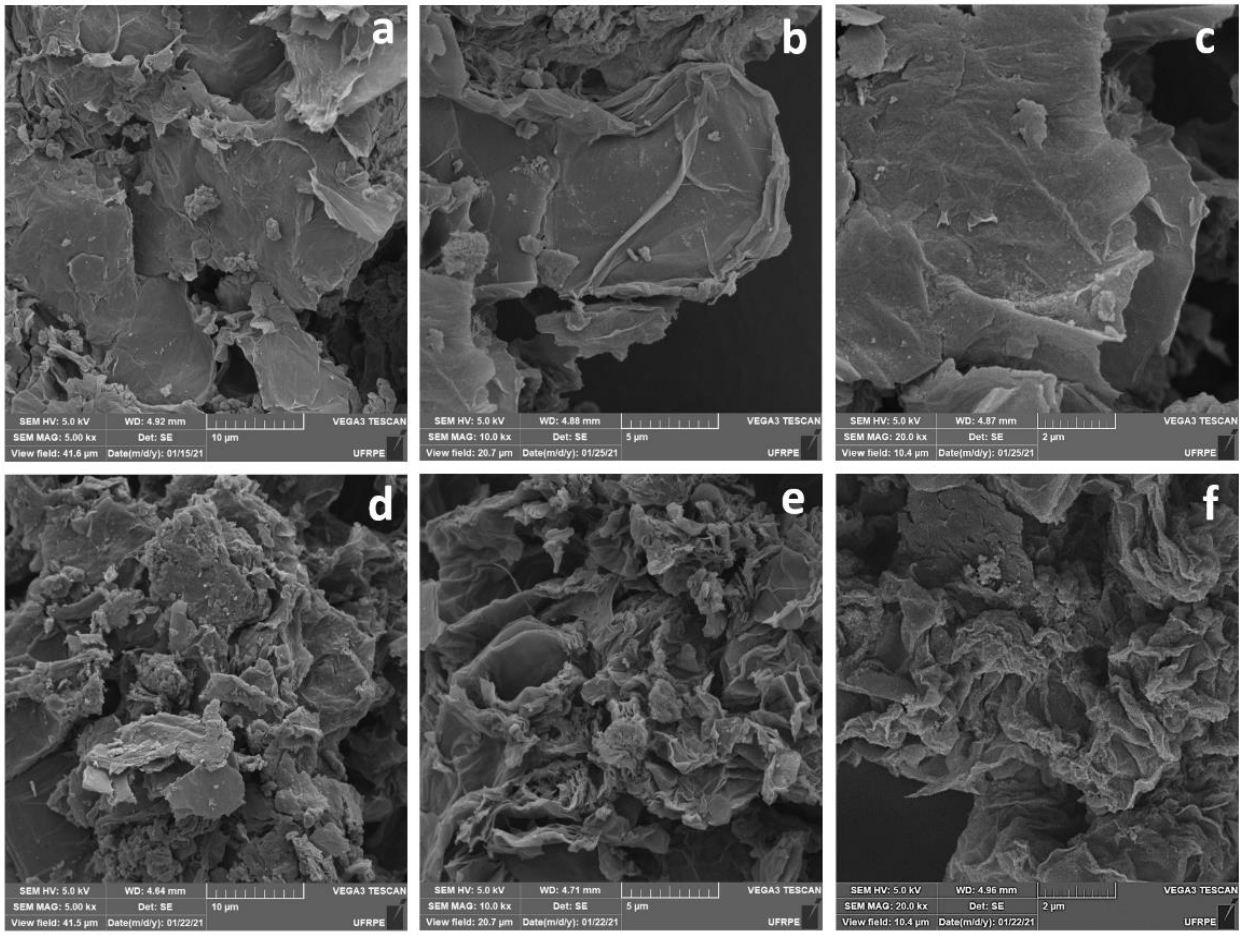

Source: the author (2020).

SEM analyses were also carried out for wood waste charcoal and from them it was possible to visualize the porous structure of charcoal grains in pure charcoal and in nGO(NH)R/C samples (Figure 14). However, most part of the pure charcoal was seen in small pieces and with impurities impregned over their structure (Figure 14a, b and c), which can be inferred that the crushing and sieving process at 100 Mesh provoked the erosion of substantial part of the grains. Impurities in charcoal samples might be explained by the different source of wood wastes, collected from various locations in João Pessoa town.

nGO(NH)R/C samples evidenced a composite structure, in which nGO(NH)R flakes were blended with charcoal grains in an disordered way (Figure 14d to i). Nevertheless, part of nGO(NH)R was also sucessfuly anchored over some charcoal grains, as can be seen in Figure 14i (covered walls of charcoal, at the bottom of the SEM picture). Moreover, SEM images also

exhibited that part of nGO(NH)R/C occupied some pores of the charcoal grains (Figure 14f). From SEM technique, as well as BET assessment of the samples of nGO(NH)R/C and pure charcoal, it is evidenced that nGO(NH)R engaged the active sites of charcoal, decreasing its specific surface area, as described with depth in the Section 7.1.9.

One possible reason for the phenomenon mentioned above can be explained by the lack of previous treatment on the surface of the charcoal, such as chemical activation (acid or basic). These pre-treatments would clean and open the pores of charcoal grains, as well as to increase their specific surface area (EL FARISSI *et al*., 2020). Moreover, depending on the chemical activation, oxygenated groups (mostly –OH, and –COOH and phenol in less quantity) can be bestowed over the charcoal surface, as reported by Pessôa *et al*. (2019) and Fan *et al*. (2010). The presence of oxygenated groups in charcoal surface would enhance the interaction between the active sites of charcoal grains and nGO(NH)R flakes, thus easing the dispersion. Therefore, the investigation of the influence of pre-chemical activation of charcoal in the quality of nGO(NH)R dispersion over charcoal surface is subject of ongoing research works and further publications. Another reason that might explain the disordered blending of nGO(NH)R with charcoal grains is the great ratio (w/w) of nGO in the functionalization-supporting method. For that, further investigation of novel anchoring protocols with shorter nGO/charcoal proportion in the middle should be performed. Finally, the employment of ultrasound in the functionalization synthesis can be assessed in order to avoid the re-stacking of nGO and nGO(NH)R nanosheets.

Figure 14 – SEM images for wood waste charcoal in 5 kX (a), 8 kX (b and c); nGO(NH)R/C (1:1 in w/w) in 5 kX (d), 8 kX (e) and 20 kX (f); nGO(NH)R/C (1:2 in w/w) in 2 kX (g), 5 kX (h) and 10 kX.

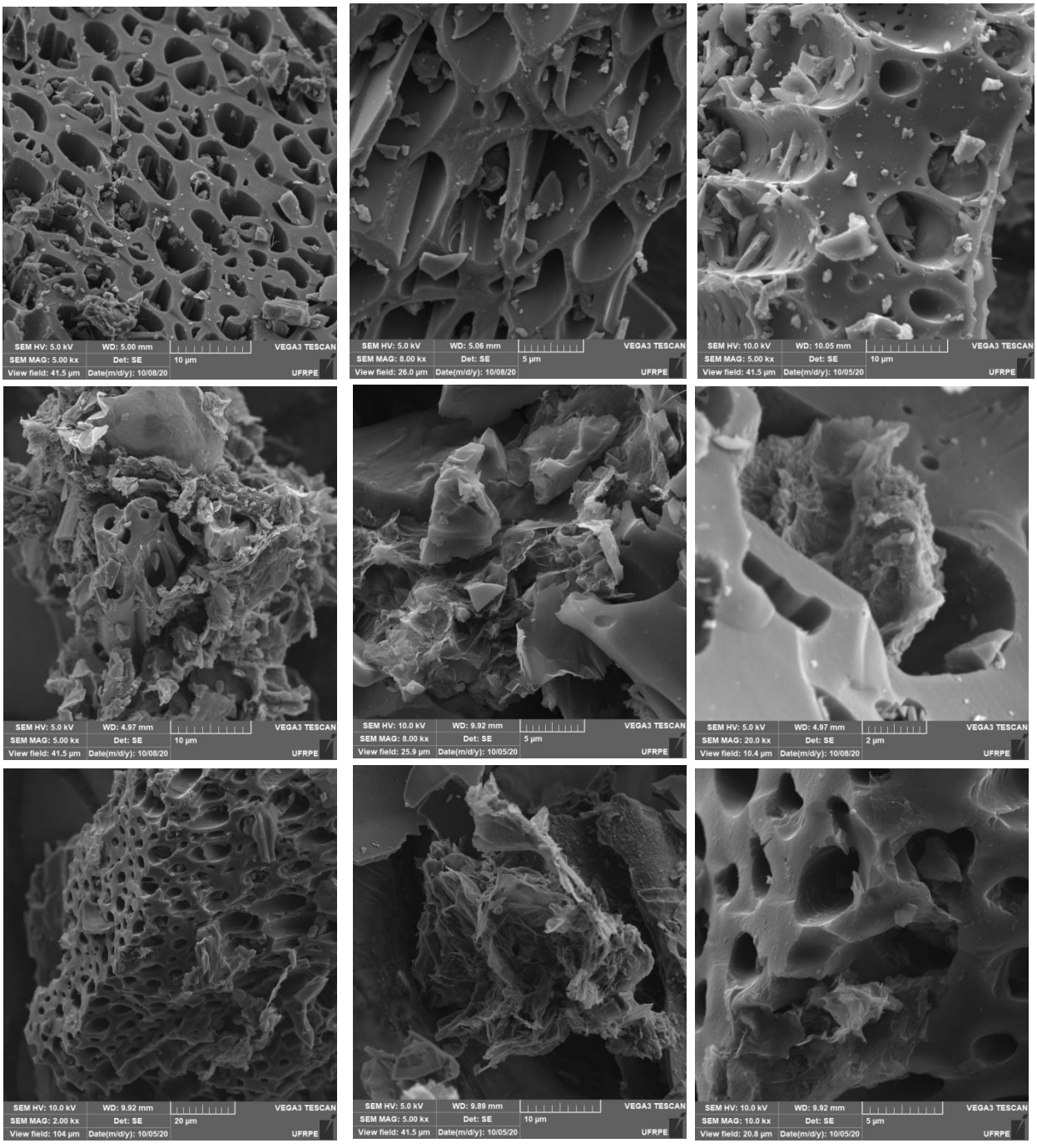

Source: the author (2020).

EDS analysis was carried out to assess the elemental content in nGO-NH_2-Fe_3O_4 sample. Five different SEM microphotographs were acquired from the SEM microscope and analysed in

the EDS spectrometer, as depicted in Figure 15a. The images were layered and specific radiation scans for iron (Fe-kα1, Figure 15c), oxygen (O-kα1, Figure 15d), carbon (C-kα1-2, Figure 15e). Moreover, the representative spectrum for EDS (Figure 15f) exhibits the bands of O (0.55 keV), C (0.25 keV) and Fe (0.7 keV, 6.4 keV and 7.05 keV). Furthermore, trace amounts of Si (1.75 keV), Al (1.98 keV) and Na (1.05 keV) were also found in the sample. This might be attributed to contamination during the preparation of the sample, though it does not influence the EDS characterization overally, neither in the intended application of nGO-NH_2-Fe_3O_4. The average elemental contents, acquired from EDS for nGO-NH_2-Fe_3O_4 evaluated in 5 different scans, are summarized in Table 1.

Table 1 – Elemental characterization of nGO-NH_2-Fe_3O_4, acquired by EDS.

Element	**Element Weight (%)**	**σ (%)**
C	57.52	1.86
O	25.50	1.40
Fe	13.56	2.20
Si	3.20	0.38
Na	0.50	0.10
Al	0.20	0.10

The summary of elemental contents of nGO-NH_2-Fe_3O_4 showed that carbon is the element with the greatest content (57.52±1.86 %) in the sample, followed by oxygen (25.50±1.40 %) and iron (13.56±2.20 %). These data evidence the anchoring of Fe_3O_4 over nGO-NH_2 graphenic plane after the parallel routes of amino and non-covalent functionalization. Low content of Fe (in mass %) in the sample is result of the functionalization path chosen, in which the amount of amines/amides over nGO structure were priorized in face of the needs to enhance the interactions with dyes molecules. This is also evidenced in the magnetization analysis (Appendix C, Figure C1), since it was observed a low coercivity and a low magnetic density in comparison to other MNPs (AI *et al*., 2011), Fe_3O_4 and nGO-Fe_3O_4 (DA SILVA *et al*., 2021),

both synthesized by hydrothermal method. Yet, the magnetic properties of the nanomaterials are not object of investigation of this thesis.

Finally, the elemental content of iron (13 %) is in total agreement with what was observed in TGA, as the nGO-NH_2-Fe_3O_4 weigth decreased to ~ 10% from 550 ºC. Moreover, the remaining Fe_3O_4 in the sample at high temperatures, might has changed its crystalline configuration, once Fe_3O_4 reduces termically under low temperatures (200–600 ºC), changing its crystalline phase to γ-Fe_3O_4 (ZHANG *et al*., 2016).

Figure 15 – a) SEM photograph of nGO-NH_2-Fe_3O_4; b) SEM layered image of nGO-NH_2-Fe_3O_4 with the detected EDS spots of the radiation; EDS radiation imaging for: Fe-kα1 (c), O-kα1 (d), C-kα1-2 (e); f) EDS spectrum of nGO-NH_2-Fe_3O_4.

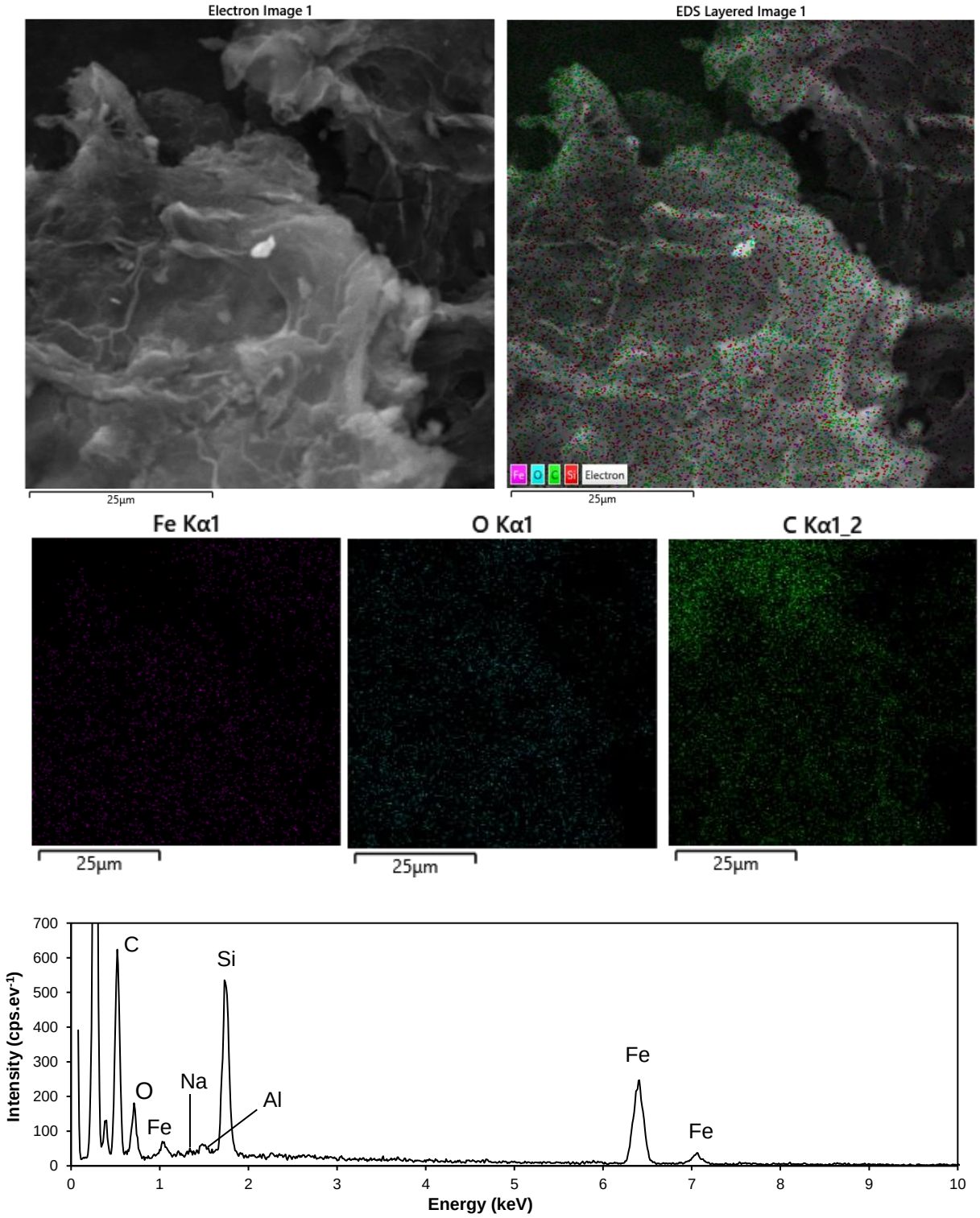

Source: the author (2020).

7.1.3 Atomic Force Microscopy

AFM photographs of nGO (Figure 16a) and nGO-NH_2-Fe_3O_4 (Figure 16b) showed several flakes of both samples scattered along the whole substrate. However, nGO-NH_2-Fe_3O_4 sample exhibited more protruding undulations in its flakes, evidencing a strong agglomeration process of nGO nanosheets after amino-functionalization. Interactive forces are responsible for nGO nanosheets re-stacking after functionalization, as depicted by AFM data.

Figure 16 – AFM images for nGO (a) and nGO-NH_2-Fe_3O_4 (b), evaluated substrate area: 623.8 μm^2 (Gwyddion™); example of AFM profile thickness (y - in nm *versus* x – in μm) for nGO (c) and nGO-NH-Fe_3O_4 (d).

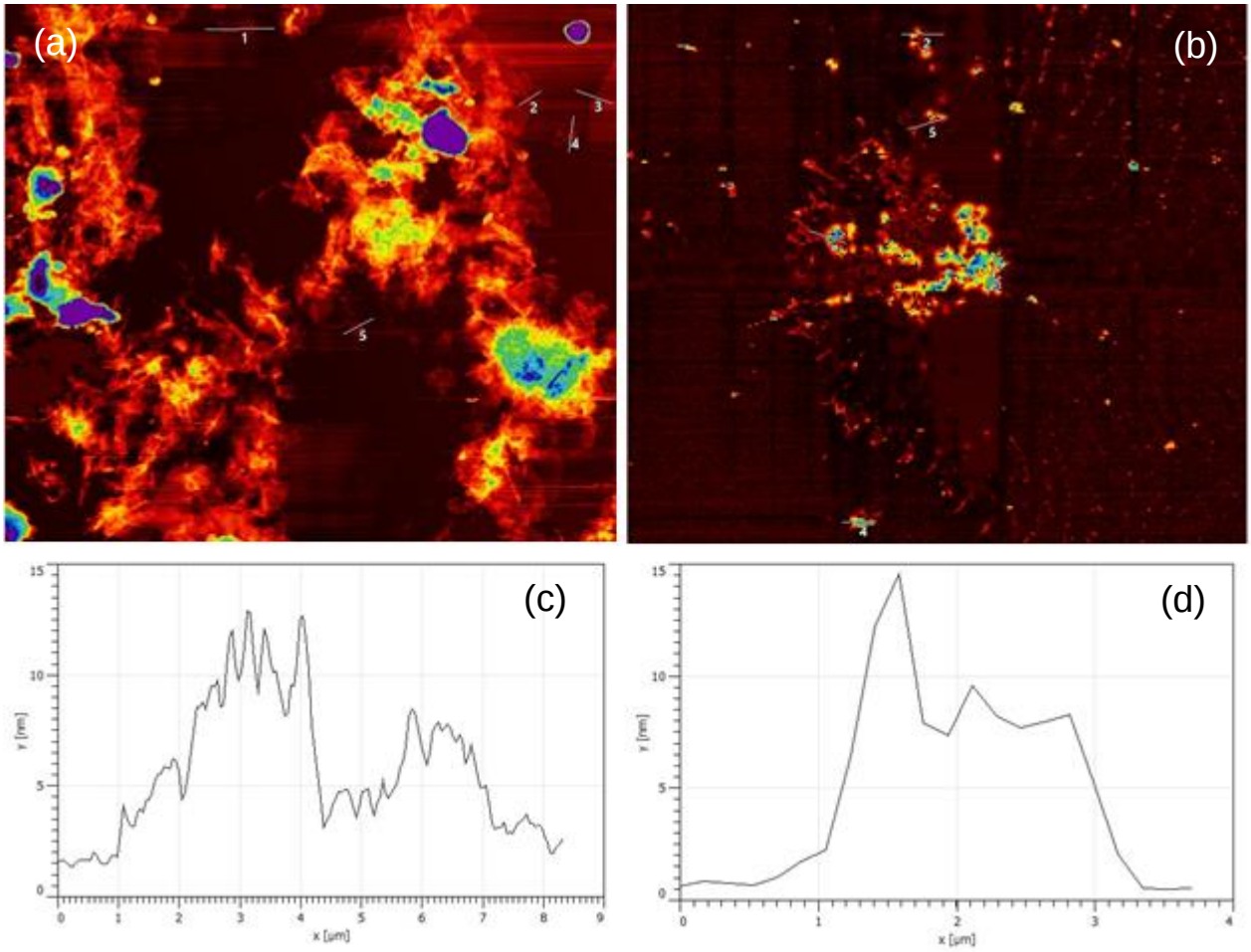

Source: adapted from Fraga *et al*. (2019b), with permission from Springer-Nature, Copyright 2020.

AFM multi-profile analysis evidenced the presence of small nanoflakes with thickness smaller than 2.0 nm in nGO sample (Figure 16c). Additionally, nGO average thickness was 5.79 nm and mean square roughness (RMS) 9.31 nm, data measured from 30 profiles. Differently, nGO-NH_2-Fe_3O_4 showed an average thickness of 8.43 nm, RMS 12.14 nm and the sample exhibited small agglomerated packs of nanoflakes that reached 41.99 nm of maximum thickness (Figure 16d). Strong agglomeration and re-stacking of nGO nanosheets are attributed to an increase in stored interactions forces, such as van der Waals and π–π stacking interactions, between nGO(NH)R layers (ENGLERT *et al.*, 2011). Average areas of nanoflakes were 9.57 μm^2 and 32.45 μm^2 for nGO and nGO-NH_2-Fe_3O_4, respectively (measurements were performed in 30 spots on a selected substrate area of 650.20 μm^2).

According to Ferrari and Basko (2013), the number of graphene layers (n) in a graphene sample can be determined by elastic light scattering (Rayleigh) spectroscopy. However, this assessment is better indicated for exfoliated samples on optimized substrates and does not provide other structural or electronic information than particle size aspects (CASIRAGHI *et al*., 2007; BLAKE *et al*., 2007). Therefore, it would be merely speculative calculate the number of layers based on the average thickness of nGO-NH_2-Fe_3O_4 reached by AFM, since the thickness of a standard single-layer of nGO-NH_2-Fe_3O_4 is not known.

From the standard measured thickness of a single GO nanosheet, which is between 0.4–1.7 nm, according to previous works (SHEARER *et al*. 2016; EIGLER *et al*. 2014), it can be remarked that nGO and nGO-NH_2-Fe_3O_4 showed an average of 6 and 9 standard single 2D stacked GO nanosheets, respectively. These results suggest that most of the flakes would fit ISO TS 80004/2017 standard number of layers (< 10) for 2D graphene nanoblocks for non-electronic applications (ISO, 2017). Nevertheless, in face of the stacking, variability and non-uniformity of their morphology, the best nomenclature for the nanocomposites studied in this work is the “n-layer graphene” [nGO and nGO-NH_2-Fe_3O_4].

7.1.4 X-ray diffraction

The samples of nGO, nGO(NH)R (Figure 17a), Fe_3O_4 and nGO-NH_2-Fe_3O_4 (Figure 17b) were characterized by XRD and compared to graphite standard (JCPDS 75-2078, 3,347 Å) (Figure 17c) and single nGO sample (Figure 17d). Furthermore, amorphous-like structure of pure wood waste charcoal is evidenced by the behavior in XRD diffractogram, acquired for its sample, as depicted in Figure 17a (grey lines).

Figure 17 – a) comparative XRD patterns of JCPDS graphite powder, nGO, nGO(NH)R and wood waste charcoal; b) comparative XRD patterns of nGO, pure Fe_3O_4 and nGO-NH_2-Fe_3O_4; c) single XRD patterns of graphite powder; d) single XRD patterns of nGO.

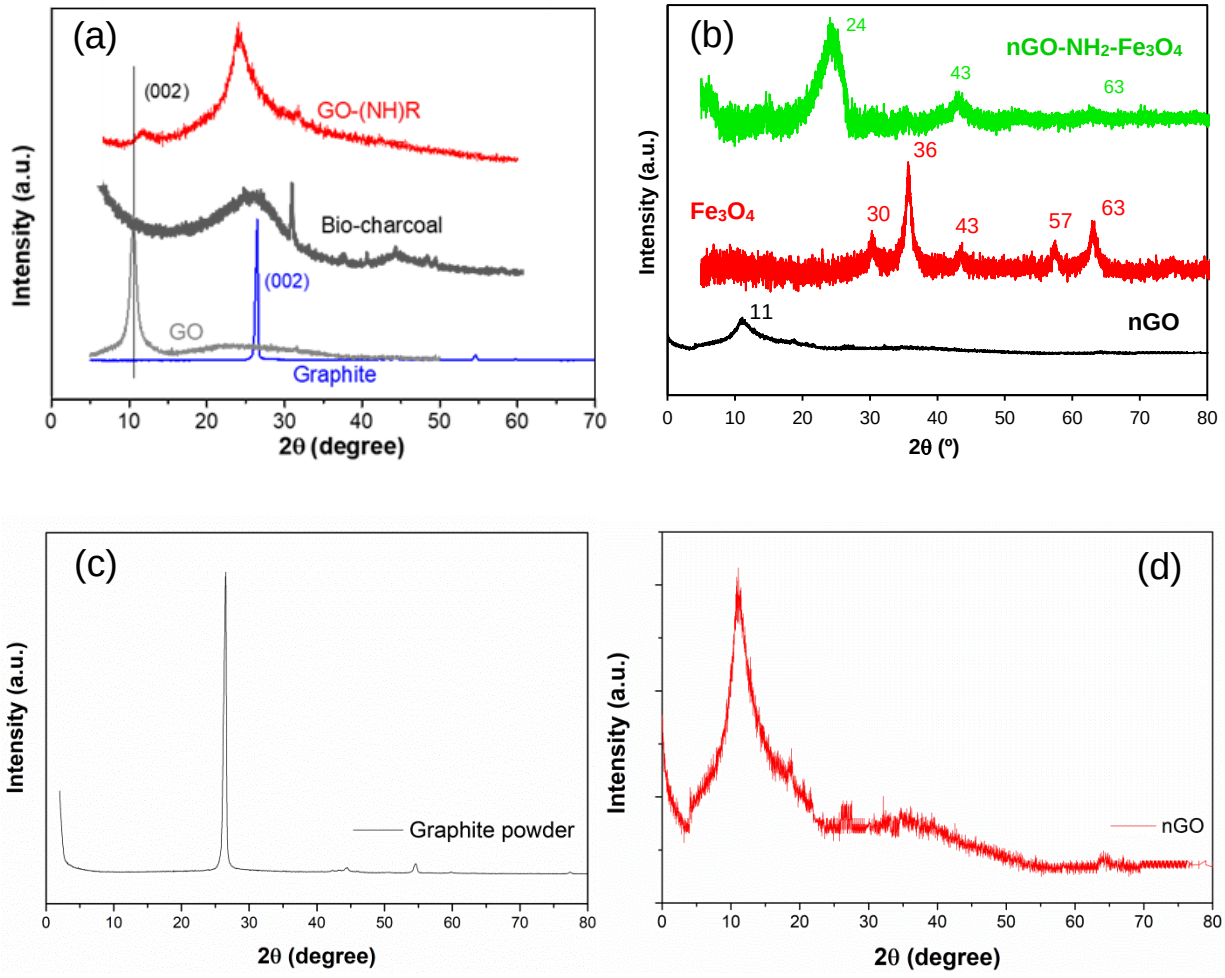

Source: the author (2018).

For the graphite, the peaks equal to 26.5° and 54.6°, the diffraction planes (002) and (004), referring to the basal planes of the graphene, were observed in addition to the plane (101) in 44.5° (Figure 17c). All these peaks are characteristic of three-dimensional crystalline graphite. The plane 002 is quite narrow and intense. The nGO(NH)R and bio-charcoal diffractograms show the same behavior (Figure 17a, red and dark-gray lines), there is an indication of an amorphous band characteristic of non-crystalline materials, such as graphene oxide of few layers; however, it is possible to note the presence of small peaks. The traces of the peak related to the plane (002) were shifted to 25.5 ° and suggest that the oxidation of the graphite structure was not enough to oxidize 100% of the layers. For nGO (Figure 17d), there is also an indication of a small peak, still related to the plane (002), which was shifted to 2θ ~ 14° and is characteristic of interplanar distances of ~ 0.8 nm, as reported previously (STEPHAN *et al*., 1994). This distance is greater than the separation of the graphene sheets (0.34 nm), so it is suggested the formation of functional groups, such as phenolics, amino, ferritic groups and hydroxyl between graphite nano-layers during their functionalization.

Additionally, it was not possible to find a clear diffraction peak around 10–11º in nGO-NH_2-Fe_3O_4, which is related to the shift of the (002) peak at 26º to lower angles due to the addition of oxygenated groups to the sample. This shift of 002 peak from 2θ 26º to 11º is consequence of the increase on the graphitic interlayer distance. However, it is important to mention that this peak at 10º is characteristic of graphite oxide, or at least, multi-layer graphene oxide, exhibiting an increased interlayer distance of around 0.88 nm (MU *et al*., 2013; ZHU *et al*., 2010b). Monolayer graphene should not show any clear diffraction peak, as the 3D crystalline structure is disrupted during exfoliation. We assume that only a re-stacking of this oxidized monolayer material could show again, broader and less intense diffractions patterns of the (002) plane. In amino-Fe_3O_4-functionalized pattern, it is also possible to notice the presence of small traces of graphite oxide at 11º.

XRD patterns of Fe_3O_4 (Figure 17b, red lines), by its turn, exhibits characteristic peaks at 36º, 43º and 57º, that corresponds to the diffraction of (311), (222), (422) and crystal planes of pure Fe_3O_4 nanoparticles with spinal structure, as reported in previous works (HABIBI, 2014). Some of these peaks also appear in small intensity in nGO-NH_2-Fe_3O_4 diffractogram (43º and 63º – Figure 17b, lines in green), which evidences the presence of Fe_3O_4 anchored over its surface. Finally, the diffractogram of nGO-NH_2-Fe_3O_4 exhibits the (002) peak at 24º–25°, which is

characteristic of functionalized or reduced GO samples, according to previous reports (SHEN *et al*., 2009; FANG *et al*., 2009).

Despite the great variations in the data, characteristic peaks of pristine Fe_3O_4 can be seen in nGO-NH_2-Fe_3O_4 pattern (2θ 43º and 63º), though in small intensity, while the peaks at 2θ 30º and 36º (311) practically desapeared. Firstly, this is due to the low mass ratio nGO:$FeCl_3$ chosen in the functionalization protocol, which resulted in a low content of Fe_3O_3 in the sample, as discussed in EDS, section 7.1.2. Furthermore, the decrease in (111), (311) and (422) peaks might be attributed to changes in the phase of Fe_3O_4, which is result of the temperature of solvothermal functionalization synthesis (up to 180 ºC). The effect of temperature and thermal reduction over the crystalline properties of Fe_3O_4 was investigated with depth by Zhang *et al*. (2016). According to the authors, oxidation of Fe_3O_4 at high temperature (above 900 ºC) quickly converts a Fe_3O_4 (111) epilayer to an α-Fe_2O_3 (001) epilayer; under low temperatures (below 600 ºC), Fe_3O_4 is reduced to γ-Fe_2O_3 (111).

7.1.5 Raman spectroscopy

Raman spectra for powdered graphite, nGO and nGO-NH_2-Fe_3O_4 are compared in Figure 18a, while nGO(NH)R spectra are depicted in Figure 18b and c. The spectra of all carbon frameworks have a set of characteristic bands; the main bands are the D band (~ 1360 cm^{-1}) and the G band (~ 1560 cm^{-1}).

Figure 18 – a) Raman spectra for samples of graphite powder, nGO and nGO-NH_2-Fe_3O_4; b) Raman spectra for the samples of nGO, nGO(NH)R, nGO(NH)R/C (1:1) and charcoal; c) Raman spectra for nGO, nGO(NH)R and nGO(NH)R/C (1:1), with evidenced G and D band.

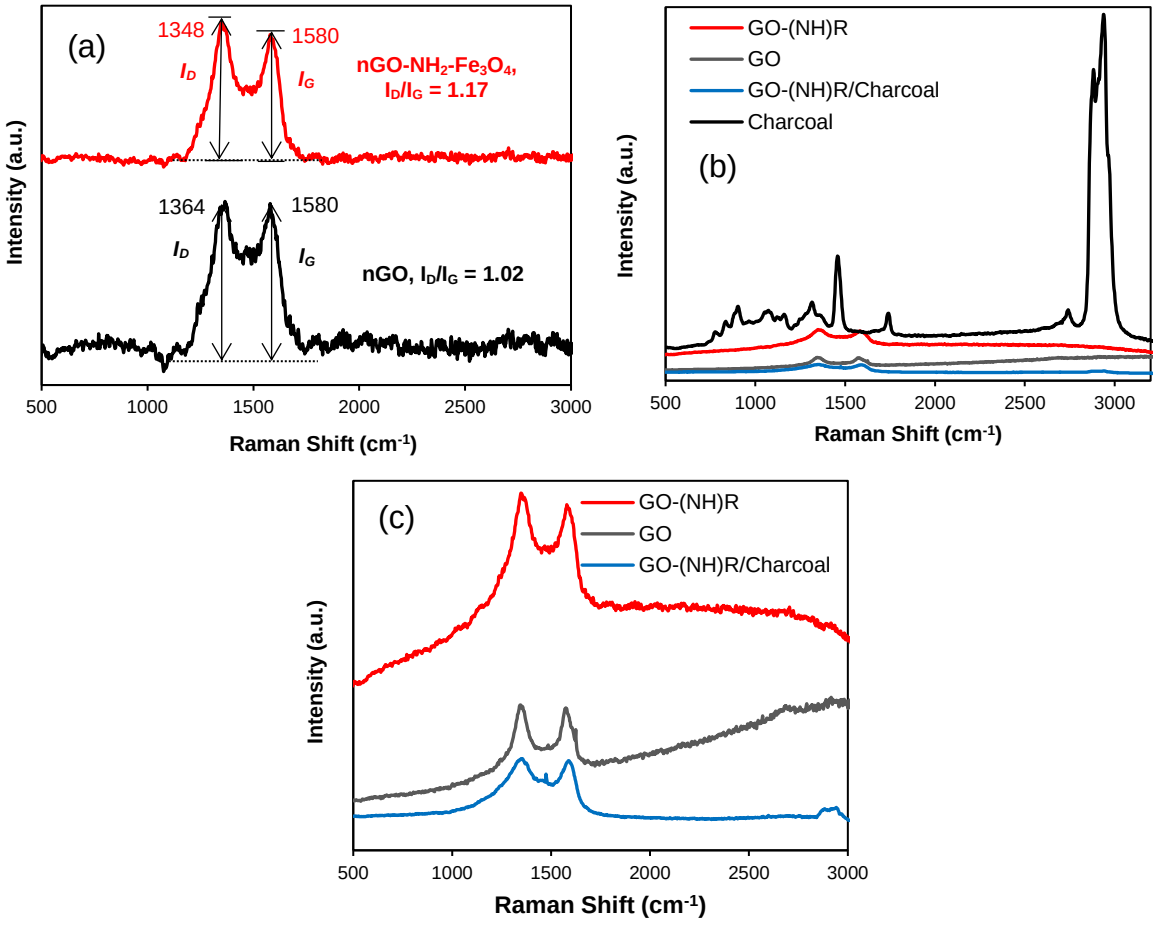

Source: (a) adapted from Fraga *et al*. (2018), with permission from Springer-Nature, Copyright 2020; (b) and (c) the author (2018).

According to Ferrari *et al*. (2006), the G band is due to the elongation movement of the sp^2 bonds between the carbon atoms of the basal 2D plane, which reflects the planar crystalline structure of the graphite/graphene materials. The band D is due to the Raman scattering in the discontinuity zone and vibrations out of plane, which reflects symmetry breaking and disordered (or defective) structures (ARAUJO; TERRONES; DRESSELHAUS, 2012; ENGLERT *et al*., 2011). Such structures include defects, boundaries of crystals, breaking of symmetry, chiralities in plane edges, etc (YOU *et al*., 2008).

The second most prominent harmonic, around 2700 cm^{-1}, is called the 2D band and reflects the stacking structure of the graphene sheets along the c (perpendicular) axis (FERRARI *et al*., 2006). According to the analysis, the two most intense characteristics of the graphite powder are, as expected, the G band at ~ 1575 cm^{-1} and the 2D band at ~ 2681 cm^{-1} (VECERA *et al*., 2017; ZHU *et al*., 2010a). For the oxidized (nGO) and functionalized (nGO-NH_2-Fe_3O_4) samples no clear 2D peak can be identified. Raman 2D band disappearance on nGO-NH_2-Fe_3O_4 spectrum clearly revealed a structure with very low integrity compared to its graphite precursor, and even to its reduced forms (ENGLERT *et al*., 2011). Chemical modifications such as oxidation/functionalization can lead to severe structural damage to the surface of these materials, introducing defects, which may include residual carboxylic acids, epoxides, amino and ferritic groups, which can disrupt the structure of the web (ARAUJO; TERRONES; DRESSELHAUS, 2012). The amplitude and high intensity of the peak of defect D (small in the graphite powder precursor) for these samples confirm this hypothesis (GHISLANDI *et al*., 2015).

Additionally, it is observed an increase in I_D/I_G rate from 1.02 to 1.17 after GO amino-Fe_3O_4-functionalization (Figure 18a). This is an evidence of a decrease in sp^2 carbon domain with the introduction of sp^3 defect sites, which are related to new Raman vibrational modes, according to Vecera *et al*. (2017). Moreover, increasing in I_D/I_G ratio is an indicative of an extent of sp^3 disorder in bonded graphitic domain (KHURANA *et al*., 2018; FERRARI; BASKO, 2013; ZHU *et al*., 2010a). Morphologically, the intensity of I_D/I_G ratio can be used to describe disorder degree arised from ripples, edges defects and chiralities, charged impurities, presence of domain boundaries, among others (ZHU *et al*., 2010a; YOU *et al*., 2008). Accentuated decrease in D peak after amino-Fe_3O_4-functionalization can also be interpretated as an indicative of structural zigzag edges formation. Strong D peaks, on contrary, are attributed to more organized armchair shaped edges (ARAUJO; TERRONES; DRESSELHAUS, 2012; YOU *et al*., 2008 *apud* ZHU *et*

al., 2010a; CASIRAGHI *et al*., 2009). However, this information must be confirmed by an in-depth evaluation of other advanced characterization techniques, such as TEM/HRTEM, scanning tunneling microscopy (STM) and spectroscopy (STS).

Raman spectra of charcoal (Figure 18b) exhibited an intense D+G band in 2900 cm^{-1} which is related to second-order spectrum. According to Manoj (2016), these harmonic evidences that in charcoal, about 6–8 stacked graphene layers might be formed, as a consequence of leaching. Nevertheless, the great intensity of this band is intriguing, since Raman spectra for charcoal are not commonly investigated, and the reported works did not evidence such strong bands around 2900 cm^{-1}. Additionally, according to Araujo, Terrones and Dresselhaus (2012), the appearance of D+G band consists in symmetries breaking spectroscopic features, provoked by defects in graphitic structure. For nGO(NH)R/C, on the other hand the band in 2900 cm^{-1} practically disappeared after the anchoring of amino-functionalized nGO. It is clear that this phenomenon is related to possible functional/morphological changes over charcoal surface due to nGO(NH)R ancoring under extreme reaction conditions (180–190 ºC and 300 rpm). Yet, changes on charcoal surface after amino-functionalization was evidenced by SEM analyses, as reported in Section 7.1.2. However, the successful anchoring and dispersion of nGO(NH)R throughout the surface and pores of charcoal grains remain unknown and deserves further deep investigation. Figure 18c shows the spectra of nGO, nGO-NH_2-Fe_3O_4 and the nGO(NH)R/C.

7.1.6 UV-Vis spectrophotometry

Figure 19 shows the UV-Vis spectra of nGO and nGO-NH_2-Fe_3O_4. The presence of a peak in λ_m 315 nm in the visible band (200–700 nm) of GO-NH_2-Fe_3O_4 spectrum, indicating the formation of Fe_3O_4 of low dimensionality (VALIZADEH; RASOULIFARD; SEYED DORRAJI, 2014; LV *et al*., 2014), which has a reddish color. This observation corroborates the analysis of X-ray diffraction, since the occurrence of a low intensity peak occurs in the region of 2θ 31º, which can be attributed to the presence of Fe_3O_4, according to data reported by Gonçalves *et al*. (2009). The authors promoted the anchoring of iron oxide nanoparticles in a carbonaceous material that revealed characteristic peaks in its XRD patterns, among them, this peak at 2θ 31º.

In addition, λ_m 230 nm was very similar to those reported for GO and graphene in the literature (GHISLANDI *et al*., 2015; LORYUENYONG *et al*., 2013).

Figure 19 – UV-Vis spectra for nGO and nGO-NH_2-Fe_3O_4 samples.

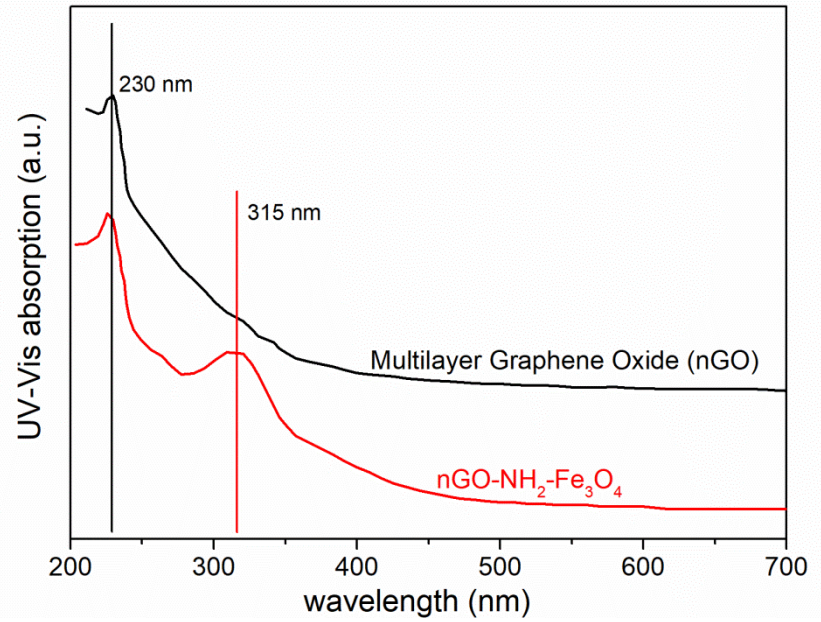

Source: the author (2019).

7.1.7 Thermogravimetric analysis

The thermic stability of graphite powder was confirmed by TGA technique, since its thermogram exhibited that its weight started to decrease after 650 ºC (Figure 20a, black line). nGO thermogram (Figure 20b, red line) showed weight decrease of 4% between 0 and 100 ºC due to the removal of water in form of moisture; similar behavior is observed in graphite oxide thermogram (Figure 20a, grey line). nGO-NH_2-Fe_3O_4 (Figure 20b, blue line), for its part, exhibited only 1% reduction. Moreover, TGA evidenced that graphite powder was sufficiently oxidized in modified Hummers method (ARAÚJO *et al*., 2018; HUMMERS; OFFEMAN, 1958), since a substantial weight decrease in graphite oxide (Figure 20a) and nGO (Figure 20b) samples is observed between 200–450 ºC. This mass loss is due to the uptake of oxygenated groups (–OOH, –OH) from graphene basal plane (MUÑOZ *et al*., 2018; SHEN *et al*., 2010; YANG *et al*., 2009) and corresponded to 30% for nGO.

Figure 20 – Thermograms of: a) graphite and graphite oxide; b) nGO and nGO-NH_2-Fe_3O_4.

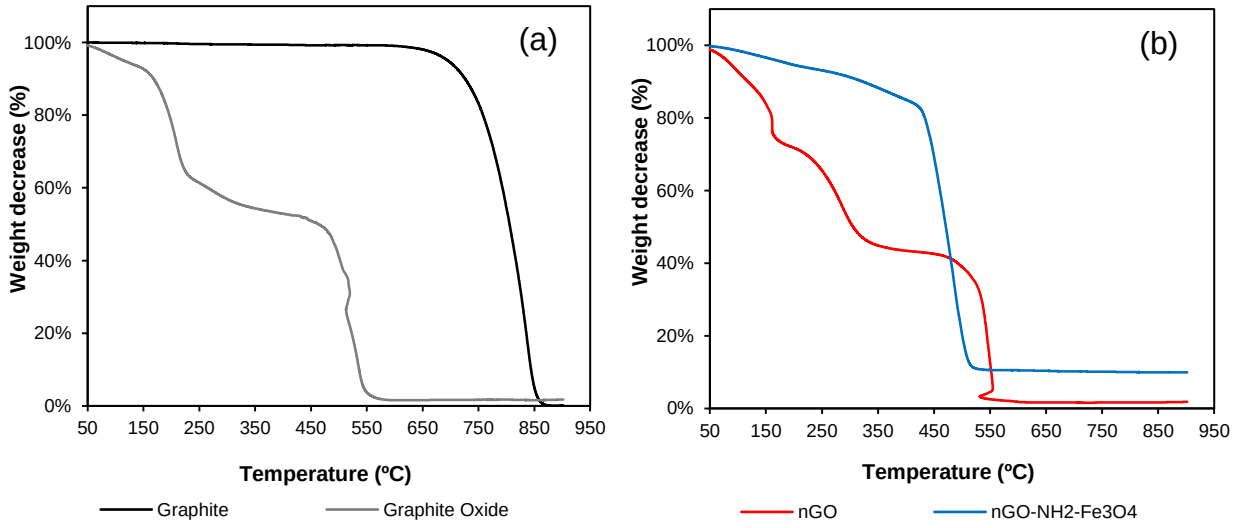

Source: the author (2019).

Moreover, according to reports found in the literature (SHEN *et al*., 2010; SHEN *et al*., 2009), oxidation product of graphite has a layered morphology with oxygenated functional moieties between layers, thereby weakening the interlayer van der Waals forces. According to Shen *et al*. (2009), oxidation of graphite disrupts the hexagonal carbon basal planes on the interior of multilayered stacks of graphite oxide, thus accelerating the uptake of oxygenated groups and consequent weight loss. However, such loss occurred in small intensity when it comes to nGO-NH_2-Fe_3O_4 sample (Figure 20b, blue line), that exhibited 11% of weight decrease at 200–450 ºC. This indicates that most oxygenated groups were reduced during amino-functionalization process. At temperatures range 50–120 ºC reactants with primary amines in their structures (DETA, ethylenediamine, dodecylamine, among others) can break the epoxide rings distributed over nGO surface; however, at higher temperatures (150–200 ºC), primary amines mainly attack the hydroxyl groups of nGO (ZHANG *et al*., 2013). The residual 10% of mass from 520 ºC in the thermogram of nGO-NH_2-Fe_3O_4 can be attributed to the remaining presence of Fe_3O_4. This behavior is not evidenced in the samples of oxygenated compounds, graphite oxide and nGO.

Finally, it is not verified significant differences between the thermograms of graphite oxide (Figure 20a) and nGO (Figure 20b) with the exception of an inflexion point near 180 ºC. Both curves exhibit intense mass decrease within 0–100 ºC, relative to the loss of moisture, and a

more proeminent mass loss between 250 to 450 ºC, attributed to the uptake of oxigenated groups, as aforementioned. It can be explained by the process of drying of nGO, which provoked a re-stacking, making this sample very similar to graphite oxide, yet with a higher degree of disorder, as verified and discussed in Raman spectroscopy section (7.1.5). However, neither the exfoliation nor the re-stacking was sufficient to increase the adsorption of water from moisture by nGO, despite it can be observed a slightly intense mass loss in its thermogram (nearly 7%) between 0–100 ºC.

7.1.8 Specific surface area and pores volume by BET method and Dynamic Light Scattering (DLS)

Specific surface area (S_{BET}) was acquired for nGO(NH)R/C (in both proportions, 1:1 and 1:2 w/w) by adsorption and desorption of N_2 and the data of textural properties of the materials are summarized in Table 2. BET technique also evidenced the mesoporous structure of the nanocomposites, with average pore size of 8.55 nm for nGO(NH)R/C (1:1 w/w) and 9.96 nm for nGO(NH)R/C (1:2 w/w) (THOMMES *et al*., 2015). Pure charcoal, on the other hand, showed a narrower mesoporous structure with pore size 2.21 nm. The substantial increase of porosity might be consequence of the aggregation of the nGO(NH)R nanosheets/nanoblocks and their blending with charcoal grains. Additionally, the decrease in S_{BET} of pure charcoal from 181.7 $m^2 \cdot g^{-1}$ to nearly 8.00 $m^2 \cdot g^{-1}$ after the amino-functionalization of nGO in parallel with the supporting process on charcoal is due to the occupation of charcoal active sites with nGO(NH)R nanoflakes.

Table 2 – Textural properties of pure wood waste charcoal and amino-functionalized nGO supported in charcoal.

Sample	S_{BET} ($m^2 \cdot g^{-1}$)	V_P ($cm^3 \cdot g^{-1}$)	d_P (nm)
Pure wood waste charcoal	181.70	$6.58 \cdot 10^{-2}$	2.21
nGO(NH)R/C (1:1 w/w)	8.34	$3.17 \cdot 10^{-3}$	8.55
nGO(NH)R/C (1:2 w/w)	8.06	$3.20 \cdot 10^{-3}$	9.96

The isotherms for N_2 adsorption by both nGO(NH)R/C and the pristine wood waste charcoal (Figure 21) showed a behavior similar to the reversible Type II model, in agreement with most recent IUPAC classification (THOMMES *et al*., 2015). According to Thomes *et al*. (2015), reversible Type II isotherms are given by the physisorption of most gases on nonporous or macroporous adsorbents. Furthermore, from Figure 21 it is also seen that all systems presented hysteresis phenomenon, thus nGO(NH)R/C in lesser intensity. Yet, according to Thommes *et al*. (2015):

> This (hysteresis in N_2 adsorption-desorption) occurs when the pore width exceeds a certain critical width, which is dependent on the adsorption system and temperature (e.g., for nitrogen and argon adsorption in cylindrical pores at 77 K and 87 K, respectively, hysteresis starts to occur for pores wider than ~ 4 nm).

Figure 21 – Isotherms of adsorption-dessorption of N_2 for the samples of wood waste charcoal (WWC) and nGO(NH)R/C (1:1 e 1:2).

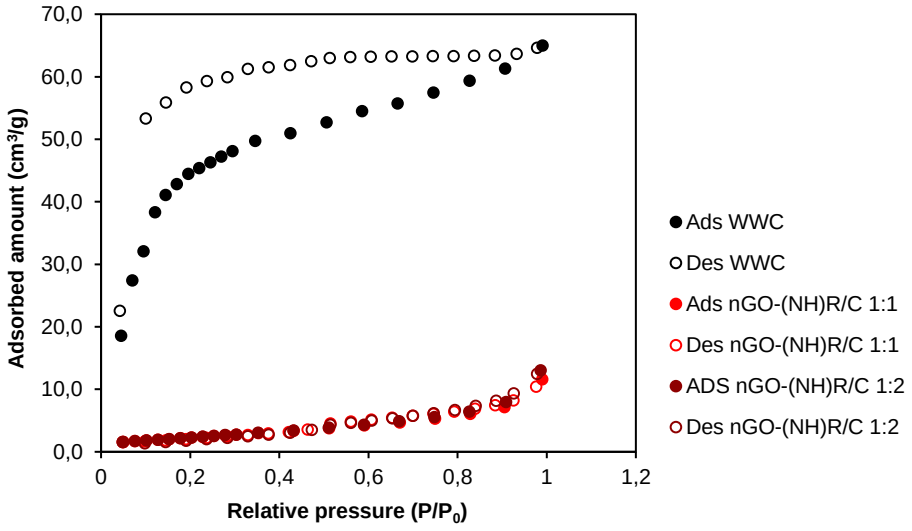

Source: the author (2020).

Granulometry analysis through dynamic light scattering (DLS) was carried out to assess the particle size distribution (Figure 22) of the samples in aqueous suspension: nGO, nGO-NH_2-Fe_3O_4 and nGO(NH)R/C (not dried in an oven). Particle size distribution data showed that at least

28.0% of nGO-NH_2-Fe_3O_4 particles are classified with diameter size between 14.3–30.2 μm, evidencing the agglomeration of nGO-NH_2-Fe_3O_4 nanoblocks. nGO sample exhibited particle size distribution in which 35.0% of its particles are classified between 15.2–34.6 mm. nGO(NH)R/C, by its turn, exhibited granulometry in which 42.2% of its particles are classified between 34.7–91.2 mm. These results were expected, since wood waste charcoal was sieved in 100 Mesh (149 μm). Moreover, granulometry profile for nGO(NH)R/C evidenced that part of charcoal grains were sliced during the amino-functionalization, which resulted in particles with shorter size, despite the agglomeration of nGO(NH)R. This took place because of high temperature (~ 180 ºC) and vigorous agitation (350 rpm), which might have broken significant part of charcoal grains.

Figure 22 – Particle size distribution and specific surface area of nGO, nGO-NH_2-Fe_3O_4 and nGO(NH)R/C. Data acquired from DLS granulometer.

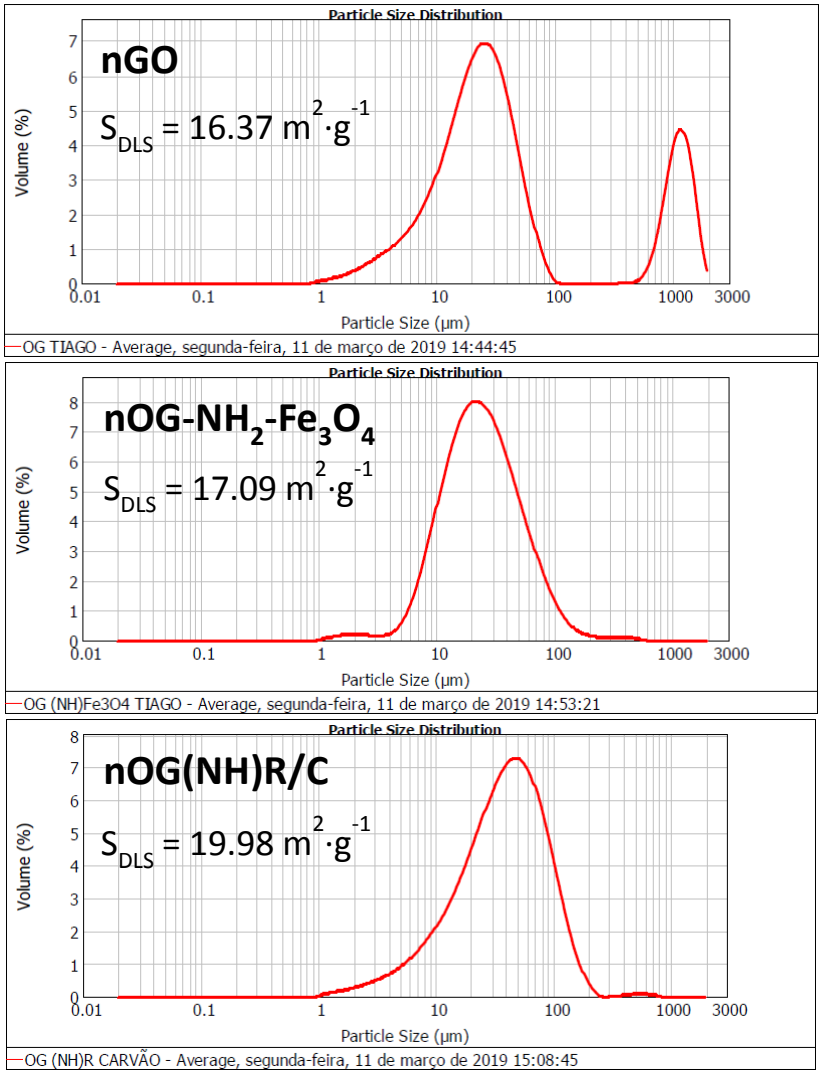

Source: the author (2019).

Specific surface area (S_{DLS}) and other textural properties were also acquired by DLS and nGO(NH)R/C showed the greatest specific surface area in aqueous suspension, nearly 20.0 $m^2 \cdot g^{-1}$. nGO and nGO-NH_2-Fe_3O_4 showed S_{DLS} 16.4 and 17.1 $m^2 \cdot g^{-1}$, respectively. Results from DLS showed great difference from BET method, since DLS is performed for suspended solids in a solvent, under the effect of a surfactant. For adsorptive processes conducted at aqueous medium, it is safe to estate that DLS technique is more representative than BET. This is because, in BET

analyses, the samples of graphene-derived nanomaterials are dried at certain temperature under vacuum prior the adsorption-desorption of N_2, which leads to a re-stacking of nanosheets. This is a totally different condition from working with graphene in aqueous medium. Finally, literature reports showed that in order to fully access the surface area of graphene nanomaterials, it is necessary to operate under very low concentrations, < 35 $\mu g \cdot mL^{-1}$, (ZHOU *et al*., 2015; EIGLER; HIRSCH, 2014).

Given this, a careful approach is necessary in order to establish the surface area of nGO and nGO-NH_2-Fe_3O_4, as some conditions are not observed in BET analysis. Once the functionalized-GO measured BET specific surface area is much lower than the GO theoretical surface area, 2630 $m^2 \cdot g^{-1}$, one might infer that the adsorbent would not be useful to remove some type of pollutants. However, an in-depth investigation towards the "surface chemistry" of this functionalized-graphene must be carried out in order to predict possible interactions with adsorbate molecules. These possible interactions (π–π stacking, H-bond, electrostatic attraction, among others) take place in the sorbent interface, not necessarily inside a porous structure; and might be as powerful as porous molecular sieving for dye adsorption.

7.1.9 Point of zero charge – pH_{PZC}

Results of eh pH of point of zero charge (pH_{PZC}) are exhibited by graphs pH_{final} *versus* $pH_{initial}$ and were acquired for nGO-NH_2-Fe_3O_4, nGO(NH)R/C (1:1 and 1:2 w/w) and the pristine nGO and wood waste charcoal. Graphs pH_{final} *versus* $pH_{initial}$ and the pH_{PZC} for each material are depicted in the Figure 23.

Figure 23 – Evaluation of the point of zero charge (pH_{PZC}) of: a) nGO; b) nGO-NH_2-Fe_3O_4; c) charcoal derived from wood wastes; d) nGO(NH)R/C (1:1 and 1:2 w/w).

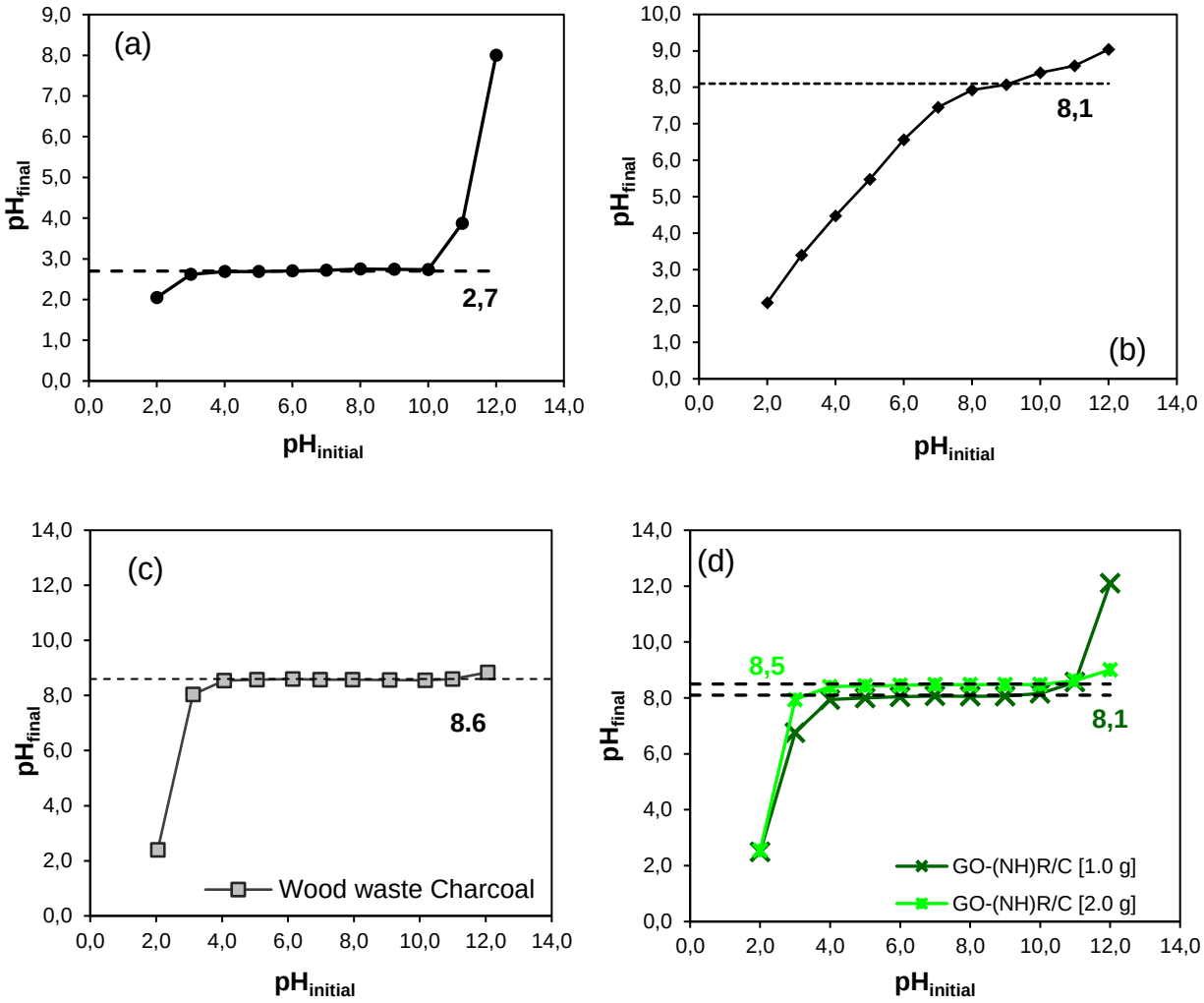

Source: the author (2018).

The point of zero charge analysis showed that the pH_{PZC} was 2.7 for nGO sample (Figure 23a); this data is in full agreement to other results reported in the literature for GO nanomaterials (ARAÚJO *et al*., 2018). On the other hand, the pH_{PZC} of nGO-NH_2-Fe_3O_4 was 8.2 (Figure 23b), which evidences that the amino-functionalization was responsible to change the positive charged nature of the adsorbent surface into an anionic character. This can be interpreted as a consequence of the disappearance of most carboxyl groups of nGO, which is responsible for the cationic behavior of GO in aqueous medium and the insertion of amines in nGO structure. pH_{PZC}

acquired for nGO(NH)R/C (Figure 23d) exhibited same pattern of nGO-NH_2-Fe_3O_4, which evidences that the supporting of nGO(NH)R structures over charcoal was not sufficient to change the charge distribution pattern of the amino-functionalized nGO. Finally, the pH_{PZC} of pure wood waste charcoal was 8.6 (Figure 23c), nearly to the value achieved by Kelm *et al*. (2019), which was 9.8. The influence of pH on the adsorptive process and its relation with pH_{PZC} is thoroughly discussed in the Section 7.3.

The pattern of the curve pH_{final} *versus* $pH_{initial}$ of the amino-functionalized nGO anchored in wood waste charcoal [nGO(NH)R/C] (Figure 23d) exhibited similar behavior of pure wood waste charcoal (Figure 23c); however, the pH_{PZC} was nearly the same of nGO-NH_2-Fe_3O_4, (8.1 for 1.0 g of charcoal, and 8.5 for 2.0 g of charcoal) which evidences the successful anchoring of nGO(NH)R on wood waste charcoal surface. It is clear that, how great the proportion of charcoal, the higher was the pH_{final}, and consequently the pH_{PZC}. In this sense, it was expected a difference on the value of pH_{PZC} in comparison of pure wood waste charcoal, since the amines, amides and other oxygenated groups (derived from nGO) can generate changes in the balance of charges of the sorbent surface and active sites.

7.2 CHARACTERISTIC OF DYES

The molecular structures of the reactive MB, RB and DR are given in Figure 24. Moreover, from UV-Vis spectra (Figure 25a, c and e), the wavelength values at which a maximum absorbance peak was observed were obtained from the scanning of 200 to 1100 nm. The following wavelengths (λ_{max}) were observed: 659 nm for MB (molecular weight 319.85 $g \cdot mol^{-1}$), 569 nm for RB (molecular weight 991.79 $g \cdot mol^{-1}$) and 540 nm for DR (molecular weight 584.93 $g \cdot mol^{-1}$).

Figure 24 – Molecular structures of the dyes Methylene Blue (MB), Remazol Black B (RB) and Drimaren Red (DR).

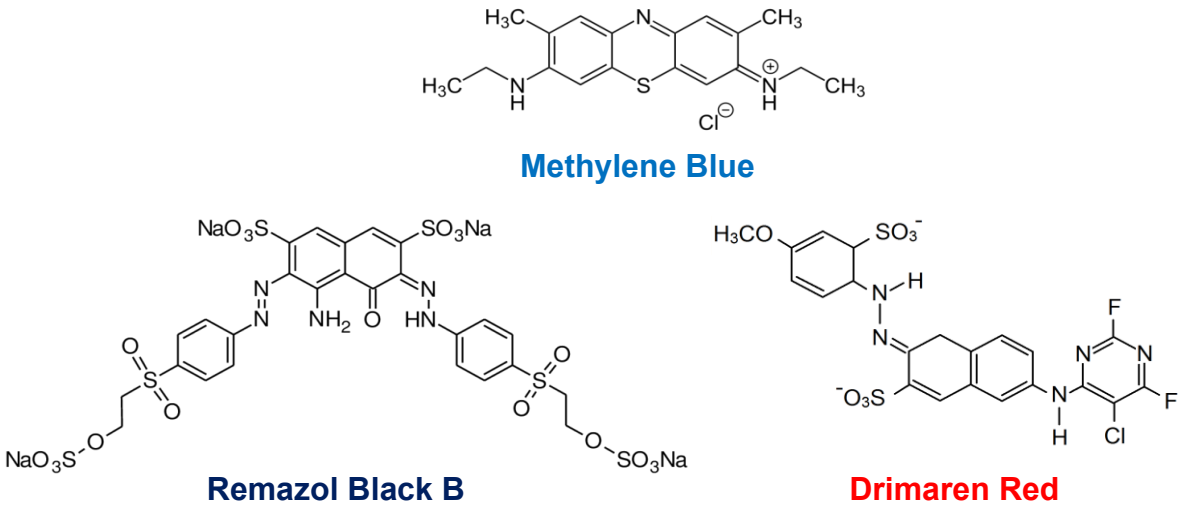

Source: the author (2020).

FTIR spectra of RB and DR (Figure 25b, c and d) exhibit characteristic bands for reactive azo dyes. The band at ~1022 cm^{-1} is attributed to stretching vibration of R–SO–R bonds and evidences the sulfoxide nature of these dyes (NEOH *et al.*, 2015). The band at 1450 cm^{-1} is attributed to –N=N– stretch vibration of azo groups, while the bands at 1600 cm^{-1} are related to –C=C– stretching vibration of benzyl groups (BILAL *et al.*, 2018; NEOH *et al.*, 2015). These data, along with dyes molecular structures are key information to unravel the interactions between dyes and nGO-NH_2-Fe_3O_4 (and nGO) discussed with depth in the following sections.

Figure 25 – UV-Vis spectra of MB (a), RB (c), DR (e), acquired at different concentrations; FTIR spectra of MB (b), RB (d) and DR (f); (d and f): analyses carried out through ATR crystal, with powdered dyes samples.

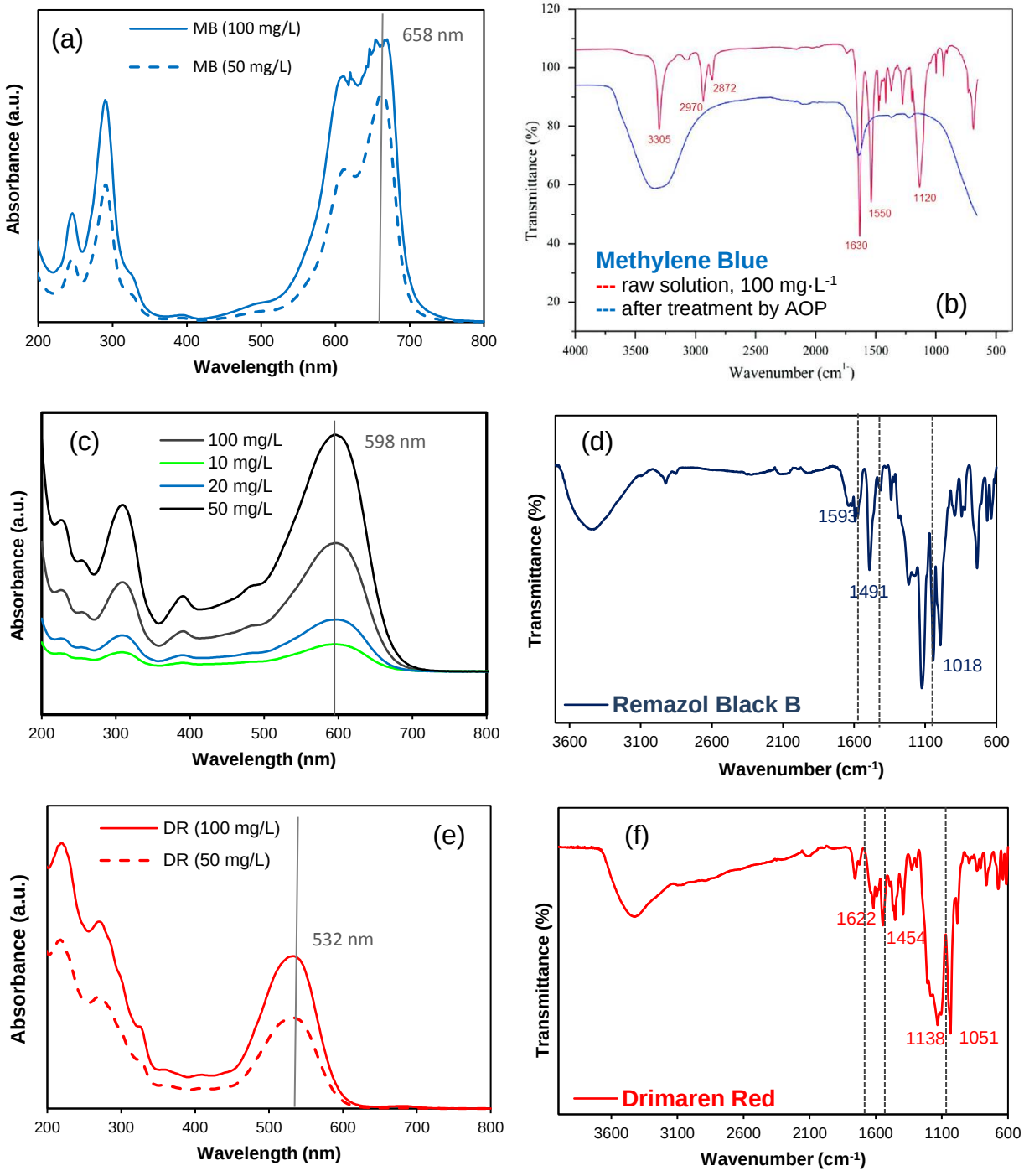

Source: a) and c–f): the author (2020); b) adapted from Barışçı, Turkay and Dimoglo (2016), Creative Commons 2021.

7.3 EVALUATION OF PH EFFECTS AND SORBENT-SORBATE INTERACTIONS

The effect of pH on the adsorption process is evaluated by adsorbing the dye in several pH ranges of its solution. When it was tested the adsorption of MB with pH solution below the point of zero charge of nGO-NH_2-Fe_3O_4 (pH_{PZC} 8.1), the adsorption capacity did not show satisfactory results. However, in the pH range above the pH_{PZC}, greater results were obtained for adsorption capacity, 60–105 $mg \cdot g^{-1}$ (Figure 26a). This behavior is due to the increase of the negative charge distribution on the surface of the nGO-NH_2-Fe_3O_4, which favor the electrostatic interactions between sorbent and sorbate, increasing the adsorption of the cationic dye MB. This behavior is observed for the adsorption of MB by pure wood waste charcoal (Figure 26c). The opposite effect is observed when operating with the MB solution pH below the acidity range.

pH influence study showed that the anionic DR was better adsorbed at pH range 4.0 – 8.0, naturally below pH_{PZC} (Figure 26b, red cross points). When adsorbate solution pH is higher than pH_{PZC} ($pH > pH_{PZC}$), nGO-NH_2-Fe_3O_4 surface becomes negatively charged due to the deprotonation of carboxyl and hydroxyl groups and this favor the adsorption of cationic dyes (PERREAULT; DE FARIA; ELIMELECH, 2015).

Intriguing results of pH effect showed that the adsorption of the RB is not influenced by pH changes, in comparison to the results presented by MB. This can be explained by the size of the electron cloud over RB molecule, a reactive diazo dye with four aromatic rings and a double N=N bond (diazo) in its structure (HORROCKS; ANAND, 2000), as previously depicted in Figure 24.

Figure 26 – a) effect of pH change over the sorption capacity of nGO and nGO-NH_2-Fe_3O_4 at MB and RB removal; b) effect of pH change over the sorption capacity of nGO-NH_2-Fe_3O_4 towards DR removal; c) effect of pH change over the sorption capacity of nGO(NH)R (anchored in 1.0 g of wood waste charcoal) and pure charcoal towards the adsorption of MB (adsorbent dosage: 0.1 g in both experiments). Experiments performed under 25 ºC, 25 mL of dye solution with concentration 20 mg·L^{-1} and stirring velocity 300 rpm; contact time: 20 min for MB, 90 min for RB and DR.

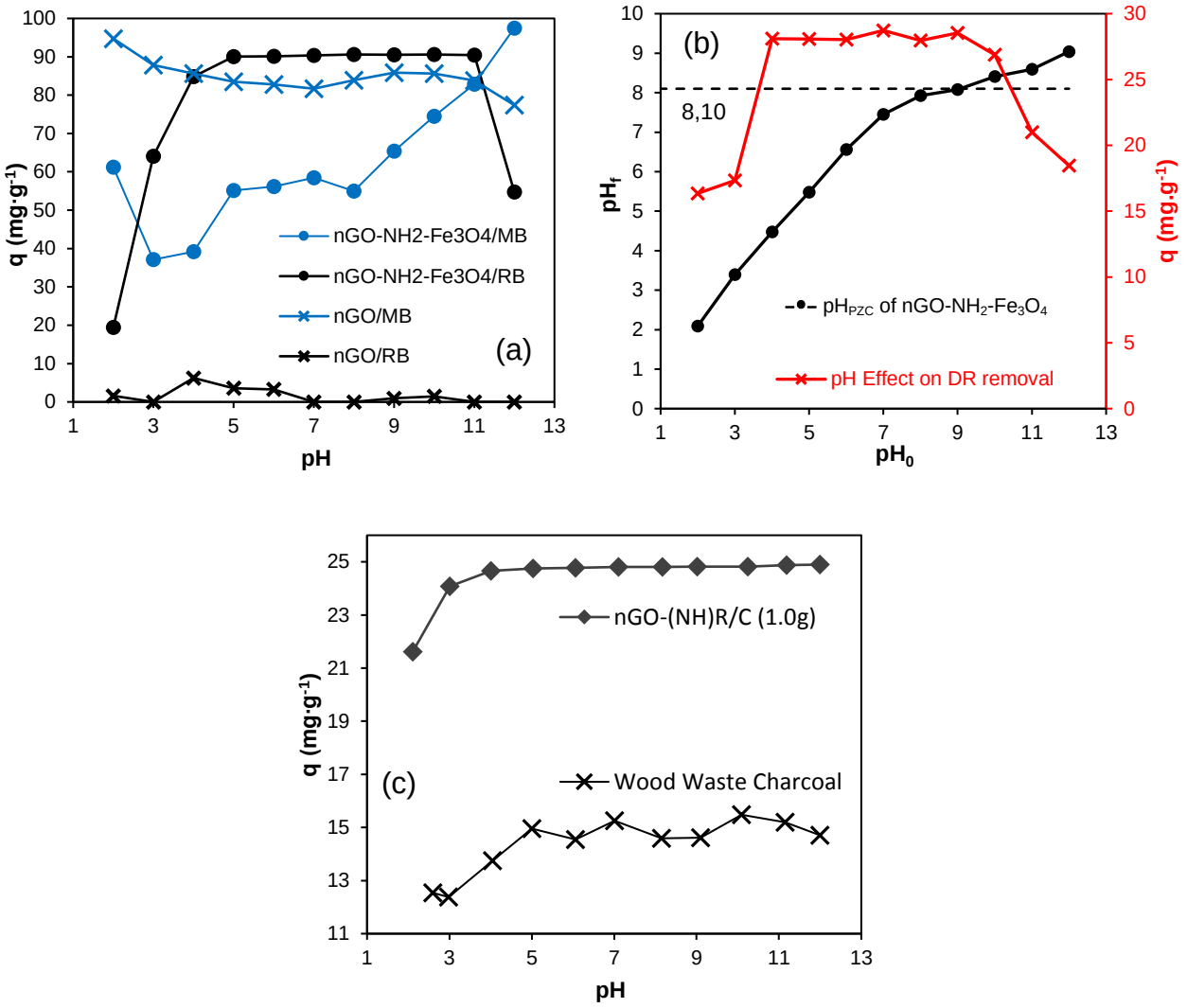

Source: the author (2018).

Molecular structures of RB and DR make them more susceptible to interactions of π–π stacking nature than to electrostatic interactions, as depicted in Figure 27. It is very likely that both interactions occur in parallel, as well as others of weaker nature, such as hydrogen bonds (H-bonds) and van der Waals forces (LAI *et al*., 2019; GEORGAKILAS *et al*., 2016). However, the contribution of π–π stacking interactions for the capture of RB and DR molecules is

considerably larger. The very low values of the adsorption capacity presented by the RB in the pH ranges of 2.0–3.0 might be due to the dye degradation process, since there was a significant change in the color of RB solution, changing from blue marine to brilliant brown.

Data reported in the literature show that the functionalization of graphene or graphene oxide with amino derivatives contributes to increase the electronic cloud caused by the large carbonaceous structure (CALIMAN *et al*., 2018; EIGLER; HIRSCH, 2014). This is because the presence of the electronic pairs of the atom of nitrogen atoms contributes to increase the resonance of π-electrons throughout the structure of the amino-functionalized graphene (PURVIA *et al*., 2020; CALIMAN *et al*., 2018). This phenomenon contributes to intensify interactions of π–π stacking nature and is one of the reasons for the great increase in the maximum adsorption capacity of nGO-NH_2-Fe_3O_4 (in the removal of MB and RB) in comparison to nGO.

H-bonds can also be formed during the adsorption of RB due to the disposal of hydroxyl groups in both sorbate and the nGO and nGO-NH_2-Fe_3O_4, as shown in Figure 27. Moreover, some species of dyes possess halogens in their molecular structures, which contribute to form H-bonds.

Additionally, the reactive RB and DR, possess chromophore (azo groups), auxhochromes and fixing groups distributed over their molecular structures (sulfonic groups) (GUARATINI; ZANONI, 2000; HORROKS; ANAND, 2000). In the interactions between these dyes and nGO-NH_2-Fe_3O_4 there are great possibilities of forming covalent bonds between amines and chromophores (sulfuric or sulfonic groups) (KYZAS *et al*., 2015). This nature of interactions leads to a chemisorptive process, since strong dipole-dipole interactions, notably associated with high energy levels, is associated to that type of adsorption (HUBER *et al*., 2019). Finally, in agreement with what was stated by Ruthven (1984) and Rouquerol, Rouquerol and Sing (1999), the adsorption of RB and DR by nGO-NH_2-Fe_3O_4 can be considered as of chemical nature in face of its adsorption behavior: long equilibrium time, up to 120 min (Figure 28c, d and e); endothermic behavior, ΔH^o +92.83 kJ·mol^{-1} (RB) and +66.43 kJ·mol^{-1} (DR) [as described in Table 5, Section 7.5.2]; low regeneration rate by temperature-assisted desorption (as further depicted in Figure 32); the detection of characteristic bands of dye in FTIR spectra of post-adsorption samples. In this sense, it can be inferable that covalent bonds might have formed between hydroxyl and sulphonic groups of RB/DR molecules and the amines, amides and other

remaining oxygenated groups ditributted over nGO-NH_2-Fe_3O_4 surface.

Figure 27 – Schematic representation of different types of interactions between nGO-NH_2-Fe_3O_4 and the dyes MB, RB and DR.

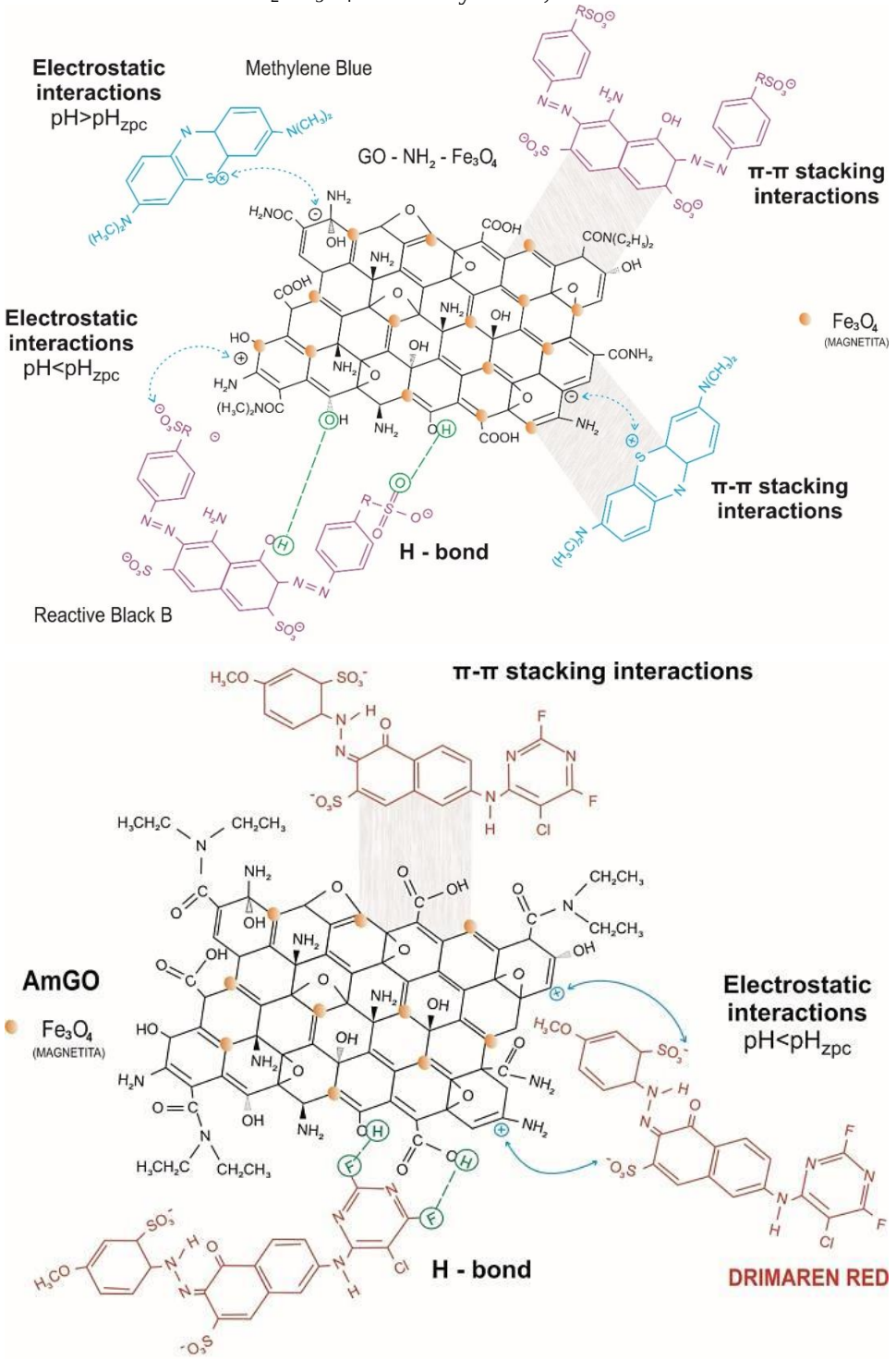

Source: adapted from Fraga *et al*. (2019b) and Fraga *et al*. (2020c), with permission from Springer-Nature, Copyright 2020.

7.4 ADSORPTION KINETICS

7.4.1 Adsorption kinetics – Methylene Blue, Remazol Black B and Drimaren Red

Figure 28 shows the adsorption kinetics curves for the removal of MB, RB and DR by adsorption through nGO and nGO-NH_2-Fe_3O_4. The kinetic models evaluated according to Equations 14, 16, 17, 18 and 19 and their parameters are presented in Table 3. All experiments were performed with MB and RB solution at pH 12.0 and 5.7, respectivelly (natural pH of the RB solution, 5.7–6.0), while the the experiments were carried out under pH 7.0 for DR. It was verified that the adsorption of the MB reached higher values of sorption capacity than the RB for the two adsorbents evaluated; however, nGO-NH_2-Fe_3O_4 obtained better results compared to nGO for the two dyes. A more in-depth approach to adsorption kinetics is presented through the kinetic modeling curves (Figure 28, graphics inside the boxes), which is possible to verify the adjustments of the models through the "non-linear fit" tool of the Origin^{TM} 9.0.

Furthermore, kinetic data showed a fast adsorption of MB through both nanosorbents, in which the equilibrium state was reached after 5 min. Moreover, the experimental adsorption capacity (q_e^{exp}) was 973.27 mg·g^{-1} for the adsorption of MB by nGO-NH_2-Fe_3O_4 and 498.35 mg·g^{-1} for nGO. Differently from MB, RB kinetics was considerably slow for nGO and nGO-NH_2-Fe_3O_4, in which the equilibrium state was reached after 60 min and 90 min, respectively (Figure 28b and d). According to the classical literature, quick adsorption is an indicative of the physical nature of the adsorption (ROUQUEROL; RUQUEROL; SING, 1999; RUTHVEN, 1984). However, such conclusion must not rely only in the behavior and modeling of kinetic data. Thus, it also must be based in an in-depth investigation over the thermodynamic data, the mechanisms of adsorption and the possible interactions between adsorbate and sorbent, which are discussed in the sections 7.3 and 7.7.

Figure 28 – Kinetic data for adsorption of: a) MB by nGO; b) RB by nGO; c) MB by nGO-NH_2-Fe_3O_4; d) RB by nGO-NH_2-Fe_3O_4; e) DR by nGO-NH_2-Fe_3O_4; (between charts, are PFO, PSO and IPD models, fitted in Origin™ 9.0 for data before reaching equilibrium state). Experimental conditions: environmental temperature, 25 ºC; 25 mL of dye solution; initial concentration 100.0 mg·L^{-1}; stirring speed of 300 rpm; adsorbent dosage: 1.0 mL of nGO and nGO-NH_2-Fe_3O_4 (0.0057 g·mL^{-1})

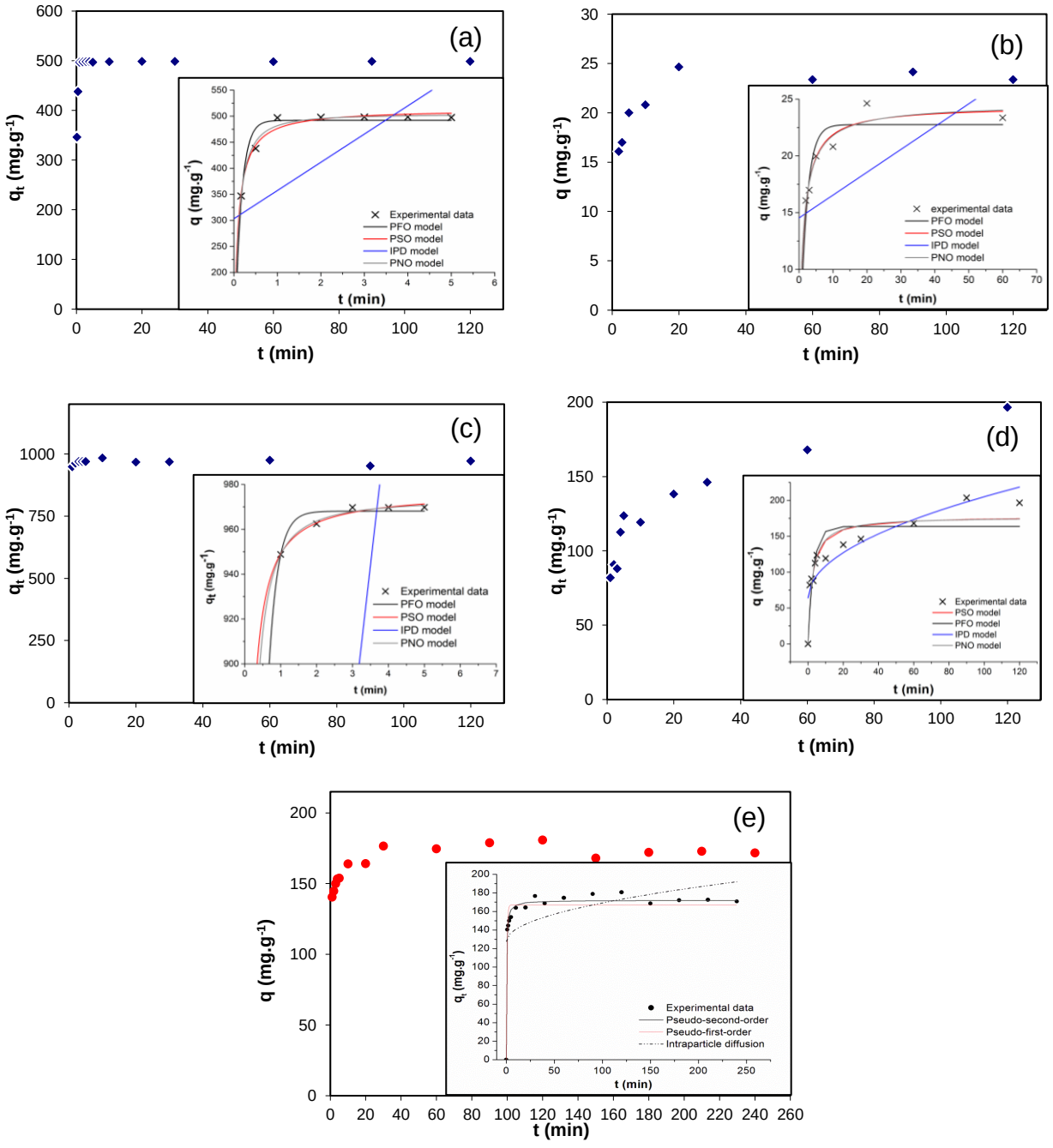

Source: adapted from Fraga *et al*. (2019b) and Fraga *et al*. (2020c), with permission from Springer-Nature, Copyright 2020.

After adjusting the experimental data according to the kinetic models it was verified that the pseudo-n^{th}-order model best fitted the adsorption of MB by nGO-NH_2-Fe_3O_4, in which the adsorption capacity evaluated at equilibrium (q_e^{calc}) and the kinetic constant of PNO (k_n) were 969.85±3.11 mg·g^{-1} and 6.57·10^{-1}±1.76 (g·mg·min^{-1})$^{1-n}$, respectively. PNO model exhibited a satisfactory coefficient of determination (R^2 0.999) and a considerable low chi-square factor (χ^2 62.66) for the system nGO-NH_2-Fe_3O_4/MB. Another indicative of the satisfactory fit was the value of the modeled adsorption capacity in equilibrium (q_e^{calc}), which was very close to the experimental adsorption capacity in equilibrium (q_e^{exp}) (SIMONIN, 2016), which was 973.27 mg·g^{-1} (Table 3). PNO model also exhibited a satisfactory fitting for the adsorption of the systems nGO-MB, nGO-RB and nGO-NH_2-Fe_3O_4-MB, in which, the respective kinetic order (n) were: 1.66±0.22, 1.95±0.52 and 1.37±0.61. With the exception of the system nGO-NH_2-Fe_3O_4/RB, PNO model showed calculated equilibrium adsorption capacities (q_e) very similar to their respective experimental values.

The pseudo-second-order (PSO) model also showed a good fit for adsorption kinetics of MB onto nGO and nGO-NH_2-Fe_3O_4 (Figure 28a and c) and presented satisfactory coefficients of determination (R^2): 0.997 and 0.999, respectively. Furthermore, the χ^2 factor (65.43) for PSO fitting of kinetic data for nGO-NH_2-Fe_3O_4/MB exhibited similar value in comparison to PNO (χ^2 62.66) and q_e^{calc} value was close to q_e^{exp}, as it was for PNO model, as observed from Table 3. For RB adsorption, otherwise, PSO did not show a satisfactory fit for the system nGO-NH_2-Fe_3O_4–RB, which is not evidenced only in the low determination coefficient (R^2 0.874), but also in the great values of standard deviances for PSO parameters. Regarding the PSO fit, the lower kinetic rate constant (k_S of order ~ 10^{-1}), indicates that the adsorption rate (for MB adsorption by nGO-NH_2-Fe_3O_4 and also for RB by both nanosorbents) decreases with the contact time (TANG *et al*., 2019). Yet, according to the several reported works, PSO best fit indicates that the rate-limiting of the adsorption is the chemisorptive process (TANG *et al*., 2019; RAMALINGAM *et al*., 2018; GANESAN; LOUIS; DAMODARAN, 2018), which involves valency forces through sharing or exchange of electrons between adsorbent and adsorbate (HO; McKAY, 1999). Moreover, the kinetic data for this dye showed great fluctuation, especially in the adsorption of RB by nGO-NH_2-Fe_3O_4, as evidenced by the greatest χ^2 (> 300) between all assessed models. This might explain the worst adjustment for all models.

Table 3 – Parameters of sorption kinetics, obtained for MB, RB and DR removal by nGO and nGO-NH_2-Fe_3O_4.

Pseudo-first-order					
	q_e^{calc} (mg·g^{-1})	k_F (min^{-1})		R^2	χ^2
nGO/MB	492.05±7.28	6.97±0.67		0.990	291.57
nGO/RB	23.16±0.60	$4.88\cdot10^{-1}\pm6.03\cdot10^{-2}$		0.970	1.79
nGO-NH_2-Fe_3O_4/MB	969.09±2.44	3.85±0.40		0.999	59.28
nGO-NH_2-Fe_3O_4/RB	163.70±11.14	$3.15\cdot10^{-1}\pm8.04\cdot10^{-2}$		0.777	686.90
nGO-NH_2-Fe_3O_4/DR	167.34±2.85	1.53±0.27		0.943	104.82
Pseudo-second-order					
	q_e^{calc} (mg·g^{-1})	k_S (g·mg^{-1}·min^{-1})		R^2	χ^2
nGO/MB	513.64±5.32	$2.48\cdot10^{-2}\pm2.57\cdot10^{-3}$		0.997	98.44
nGO/RB	24.18±0.46	$3.74\cdot10^{-2}\pm5.50\cdot10^{-3}$		0.988	0.74
nGO-NH_2-Fe_3O_4/MB	971.43±3.13	$5.29\cdot10^{-2}\pm2.48\cdot10^{-2}$		0.999	65.43
nGO-NH_2-Fe_3O_4/RB	177.86±10.32	$2.40\cdot10^{-3}\pm7.51\cdot10^{-4}$		0.874	388.12
nGO-NH_2-Fe_3O_4/DR	172.23±1.89	$1.80\cdot10^{-2}\pm2.99\cdot10^{-3}$		0.981	34.63
Pseudo-n^{th}-order					
	q_e^{calc} (mg·g^{-1})	k_n (g·mg·min^{-1})$^{1-n}$	n	R^2	χ^2
nGO/MB	503.92±7.35	$1.73\cdot10^{-1}\pm2.16\cdot10^{-1}$	1.66±0.22	0.997	87.15
nGO/RB	24.12±0.83	$4.26\cdot10^{-2}\pm5.80\cdot10^{-2}$	1.95±0.52	0.985	0.86
nGO-NH_2-Fe_3O_4/MB	969.85±3.11	$6.57\cdot10^{-1}\pm1.76$	1.37±0.61	0.999	62.66
nGO-NH_2-Fe_3O_4/RB	318.38±116.75	$1.45\cdot10^{-1}\pm3.79\cdot10^{-1}$	8.04±4.08	0.945	170.08
nGO-NH_2-Fe_3O_4/DR	219.17±32.74	$7.11\cdot10^{-1}\pm0.00$	7.46±3.87	0.997	6.87
Intraparticle diffusion					
	k_0 (mg·g^{-1})	k_{ID} (L·mg^{-1})		R^2	χ^2
nGO/MB	303.06±80.71	108.40±61.40		0.232	23187.21
nGO/RB	12.66±3.21	1.34±0.55		0.387	36.27
nGO-NH_2-Fe_3O_4/MB	767.07±123.77	28.87±23.08		0.049	74236.19
nGO-NH_2-Fe_3O_4/RB	64.04±11.29	14.11±2.10		0.780	617.31
nGO-NH_2-Fe_3O_4/DR	132.82±16.50	1.08±0.69		0.118	22.06
Experimental adsorption capacity in equilibrium					
System	**nGO-NH_2-Fe_3O_4/MB**	**nGO/MB**	**nGO-NH_2-Fe_3O_4/RB**	**nGO/RB**	**nGO-NH_2-Fe_3O_4/DR**
q_m^{exp} (mg·g^{-1})	973.27	498.35	196.94	23.61	174.40

Experimental data did not fit to intraparticle diffusion model (IPD), as non-linear determination coefficients were low ($R^2 < 0.313$ on average). This is explained by the non-porous structure of graphene nanomaterials in aqueous suspension, es evidenced in DLS and microscopy

(SEM and AFM) analyses. Similar behavior is observed for the adsorption of MB by the functionalized nGO-NH_2-Fe_3O_4. In this case, MB molecules remain parallel to the basal plane of the graphene, interacting with –OH, –NH_2 and other groups on its surface (MINITHA *et al*., 2017). In addition, the kinetics for MB adsorption onto graphene nanomaterials can be understood as a function of the boundary layer thickness and the external mass transfer coefficient (DIRAKI *et al*., 2018), rather than a possible intraparticular diffusion. This is a consequence of the 2D (or nearly 2D) shape of graphene nanomaterials, from which the porosity can be neglected.

The mathematical modeling of Elovich model only converged for the kinetics data of DR adsorption by nGO-NH_2-Fe_3O_4. This model showed satisfactory fit for DR removal, with R^2 0.996 and χ^2 0.07, despite not being the most representative. Furthermore, Elovich parameters were $\alpha = 1.15 \cdot 10^{-1} \pm 6.69 \cdot 10^{-3}$ mg·g^{-1}·min^{-1} and $\beta = 8.73 \cdot 10^{7} \pm 8.96 \cdot 10^{7}$ g·mg^{-1}. The kinetic of DR removal by nGO was not investigated.

The adsorption of DR by nGO-NH_2-Fe_3O_4 reached the equilibrium state within 90 min (Figure 28e). Pseudo-n-order model better fitted the experimental kinetic data in comparison to the other two models evaluated (R^2 0.997), with k_n 0.71±0.002 mg^{1-n}·g^{1-n}·min^{-1} and calculated sorption capacity at equilibrium (q_e^{calc}) 219.17±32.74 mg·g^{-1} (Table 3). The great value of the heterogeneity factor (n = 7.46±3.87) suggests a highly heterogeneous interface, which is in agreement with the mechanism of adsorption in multilayer, as predicted by BET isotherm, adapted for L-S systems as described by Ebadi, Mohammadzadeh and Khudiev (2009).

In a mesoporous/macroporous material, sorption mechanisms may occur in basically three steps: first, the external film diffusion takes place, in which adsorbate molecules reach the surface of sorbent particles; secondly, intraparticle diffusion, in which sorbate molecules move within particles pores; and finally adsorption, when the transferred molecules reach the active sites inside particle pores (SENTHIL KUMAR; VARJANI; SUGANYA, 2018). However, for 2D nanomaterials, or few-layered nanomaterials, such as nGO and nGO-NH_2-Fe_3O_4, the intraparticle diffusion is practically inexistent, since the pollutant molecules approximate the surface of the nanosorbent and engage in interactive forces, which depends on the functional groups over their structures (WANG *et al*., 2018a). Following the previously mentioned phenomenon, Weber and Morris intraparticle diffusion model did not show a satisfactory fitting, since a low determination coefficient was achieved ($R^2 < 0.780$). These results suggest that the adsorption occurs in nGO-

NH_2-Fe_3O_4 surface, in which there are only external resistances to mass transfer, as a rate limiting factor for adsorption mechanism (YU *et al*., 2018).

Once nGO-NH_2-Fe_3O_4 is reached by the dye molecules, they are stacked onto its surface by π−π stacking interactions (Figure 27); this occurs as a consequence of nGO-NH_2-Fe_3O_4 electronic configuration, which displays several delocalized π−electrons within the remained sp^2 carbon honeycomb lattice structure (WANG *et al*., 2018), and DR great molecular structure (with three aromatic rings, one azo-bond, N=N, and five electronic pair of nitrogen atoms). Nevertheless, electron receptor-donor interactions may occur depending on the operational conditions. Examplifying, when solution pH is kept below pH_{PZC} (8.10), electrostatic interactions are strongly favored, due to nGO-NH_2-Fe_3O_4 staying positively charged, which attracts negatively charged DR molecules (KYZAS *et al*., 2018; WANG *et al*., 2018). H-bonds, on the other hand, may be formed due to interactions between halogen elements present in DR molecular structure and H elements bonded to carboxyl, hydroxyl and amine groups over nGO-NH_2-Fe_3O_4 surface (PERREAULT; DE FARIA; ELIMELECH, 2015). Section 7.3 reports detailed information regarding the sorbent-sorbate interactions.

7.5 ADSORPTION EQUILIBRIUM

7.5.1 Adsorption equilibrium for Methylene Blue and Remazol Black B

The adsorption isotherms described in Figure 29 showed that the removal of MB and RB have descending concavities, characterizing a favorable behavior (McCABE; HARRIOT; SMITH, 2005). It was also observed that experimental data for MB adsorption by nGO (Figure 29a) were fit to all isotherms satisfactorily, which is reflected in the overlap of the curves. Furthermore, the other systems showed different fitting of the isotherm models.

Figure 29 – Equilibrium experimental data and sorption isotherms according to Langmuir, Freundlich, Temkin and L-F models for the adsorption of MB by nGO (a), RB by nGO (b), MB by nGO-NH_2-Fe_3O_4 (c) and of RB by nGO-NH_2-Fe_3O_4 (d). Experiments performed under the following conditions: 25 ºC, 25 mL of dye solution, pH 8.0 (for MB–nGO), pH 12.0 (for MB–nGO-NH_2-Fe_3O_4) and pH 5.7 (for RB at nGO and nGO-NH_2-Fe_3O_4), 300 rpm.

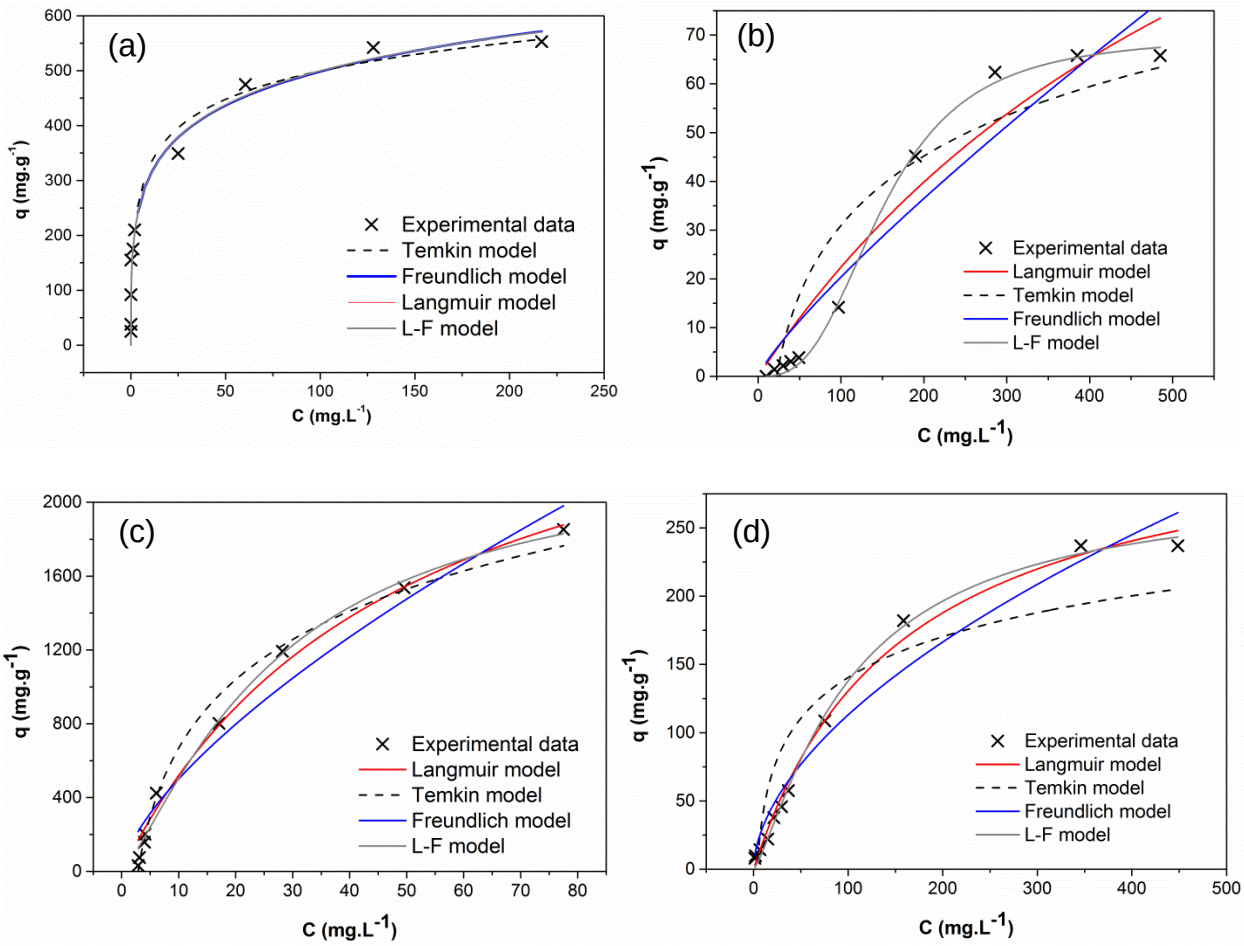

Source: the author (2020).

Positive concavities are observed in all equilibrium isotherms, despite the slight inflexion observed in the initial points of the system nGO/RB (Figure 29b). From that it is observed that the experimental maximum adsorption capacity (q_m^{exp}) were 1852.95 mg·g^{-1} (nGO-NH_2-Fe_3O_4/MB), 553.21 mg·g^{-1} (nGO/MB), 237.04 mg·g^{-1} (nGO-NH_2-Fe_3O_4/RB) and 65.79 mg·g^{-1} (nGO/RB). Graphically, it is also observed that the experimental data are well adjusted to the model curves, which is evidenced by the statistical parameters for the modeling of each isotherm in Origin^{TM} 9.0.

Mathematical modeling showed that the experimental data showed best fit to Langmuir isotherm (Equation 7) in comparison with other models and showed a satisfactory coefficient of determination, 0.957, in average. Incidentally, according to Ruthven (1984), Langmuir model is better representative for monolayer adsorption and homogeneous adsorption systems. The calculated maximum adsorption capacity in monolayer (q_m^{calc}) and the sorption equilibrium constant (K_{Eq}) for MB removal in nGO-NH_2-Fe_3O_4 were 3063.62±345.27 $mg \cdot g^{-1}$ and $2.04 \cdot 10^{-2} \pm 4.41 \cdot 10^{-3}$ $L \cdot mg^{-1}$, respectively. According to a comparative study (Table 5), the maximum adsorption capacity of MB by nGO-NH_2-Fe_3O_4 is six time the MB adsorption through nGO (graphically described in Figure 29a) and GO (ARAÚJO *et al*., 2018) and considerably higher than other adsorbents derived of nanocarbons found in the literature for the adsorption of dyes (DE OLIVEIRA *et al*., 2019; GANESAN; LOUIS; DAMODARAN, 2018; ZHAO *et al*., 2017; CARVALHO *et al*., 2016). Detailed information regarding the comparative study of adsorption performance of several graphene-based nanosorbents is presented in the Section 7.10.

Table 4 summarizes all parameters of the models tested and their respective values of R^2 and Chi-square factor (χ^2) in order to verify if these models were representative of the adsorptive process of MB and RB by nGO and nGO-NH_2-Fe_3O_4. The main parameters n, q_m, K_{Eq} obtained after the equilibrium tests and later adjustments of the Langmuir and Freundlich models, as well as the Temkin, a_T and b_T parameters, obtained through the nonlinear adjustment in Origin™ 9.0 (non-linear curve fit tool) are summarized on it.

Table 4 – Summary of parameters of equilibrium for the sorption of MB and RB by nGO and nGO-NH_2-Fe_3O_4.

Langmuir					
adsorbent/adsorbate	q_m^{calc} **(mg·g^{-1})**	K_{Eq} **(L·mg^{-1})**	R_L	**R^2**	**χ^2**
nGO-NH_2-Fe_3O_4/MB	3063.62±345.27	$2.04\cdot10^{-2}\pm4.41\cdot10^{-3}$	0.089	0.985	7162.71
nGO/MB	717.30±46.75	$6.81\cdot10^{-3}\pm1.09\cdot10^{-3}$	0.227	0.985	591.09
nGO-NH_2-Fe_3O_4/RB	320.90±20.92	$6.81\cdot10^{-3}\pm1.09\cdot10^{-3}$	0.227	0.985	118.29
nGO/RB	179.37±85.06	$1.43\cdot10^{-3}\pm1.01\cdot10^{-3}$	0.583	0.939	52.89
Freundlich					
adsorbent/adsorbate	K_f **(mg·g^{-1})·(mg·L^{-1})^n**	***n***		**R^2**	**χ^2**
nGO-NH_2-Fe_3O_4/MB	106.49±30.26	1.49±0.16		0.956	20493.77
nGO/MB	20.63±7.74	1.84±0.23		0.937	738.28
nGO-NH_2-Fe_3O_4/RB	9.23±3.46	1.84±0.23		0.938	494.24
nGO/RB	$4.29\cdot10^{-1}\pm3.68\cdot10^{-1}$	1.19±0.21		0.917	72.14
Temkin					
adsorbent/adsorbate	a_T **(L·mg^{-1})**	b_T **(kJ·mol^{-1})**		**R^2**	**χ^2**
nGO-NH_2-Fe_3O_4/MB	$3.48\cdot10^{-1}\pm2.28\cdot10^{-2}$	4.63±0.17		0.989	5049.00
nGO/MB	$1.02\cdot10^{-1}\pm1.98\cdot10^{-2}$	18.47±1.64		0.980	745.36
nGO-NH_2-Fe_3O_4/RB	$1.02\cdot10^{-1}\pm1.98\cdot10^{-2}$	41.14±3.68		0.940	473.62
nGO/RB	$4.52\cdot10^{-2}$	120.70		0.859	122.77
Langmuir-Freundlich					
	q_m^{calc} **(mg·g^{-1})**	K_{LF}	***n***	**R^2**	**χ^2**
nGO-NH_2-Fe_3O_4/MB	2319.20±269.37	$1.49\cdot10^{-2}\pm4.62\cdot10^{-3}$	$1.27\pm1.56\cdot10^{-1}$	0.990	5242.12
nGO/MB	590.16±33.51	$2.26\cdot10^{-3}\pm1.11\cdot10^{-3}$	$1.35\pm1.38\cdot10^{-1}$	0.992	299.80
nGO-NH_2-Fe_3O_4/RB	264.17±15.04	$2.28\cdot10^{-3}\pm1.11\cdot10^{-3}$	$1.34\pm1.38\cdot10^{-1}$	0.992	60.00
nGO/RB	69.79±1.80	$4.89\cdot10^{-7}\pm6.94\cdot10^{-7}$	$2.89\pm2.89\cdot10^{-1}$	0.997	2.60
Experimental adsorption capacity in the monolayer					
System	nGO-NH_2-Fe_3O_4/MB	nGO/MB	nGO-NH_2-Fe_3O_4/RB		nGO/RB
q_m^{exp} **(mg·g^{-1})**	1852.95	553.21	237.04		65.79

In addition, the Temkin model (Equation 10) was also tested for MB adsorption by both nanosorbents and its constants, obtained for the equilibrium process: a_T $3.48\cdot10^{-1}\pm2.28\cdot10^{-2}$ L·mg^{-1} (for nGO-NH_2-Fe_3O_4) and $1.02\cdot10^{-1}\pm1.98\cdot10^{-2}$ (for nGO); b_T 4.63±0.17 kJ·mol^{-1} (for nGO-NH_2-Fe_3O_4) and 18.47±1.64 kJ·mol^{-1} (nGO). Relatively low values of b_T is an indicative of Temkin isotherm can be applied to explain the equilibrium data as a function of the adsorption heat

(kJ·mol^{-1}) and, consequently, of sorbent-sorbate interactions (ARAÚJO *et al*., 2018; DAS *et al*., 2018; WANJERI *et al*., 2018, LINGAMDINNE *et al*., 2018). Many works which deals with this subject have reported similar values for Temkin constants: a_T 0.684 L·mg^{-1} and b_T 62.4 kJ·mol^{-1} for the adsorption of Rhodamine B onto GO (DAS *et al*., 2018); a_T 16.11 L·mg^{-1} and b_T 2.25 kJ·mol^{-1} for the adsorption of Crystal Violet onto poly(vinyl alcohol)-graphene (CHAILEK *et al*., 2018); and a_T 1.84·10^{-2} L·mg^{-1} and b_T 8.18·10^{-2} kJ·mol^{-1} for the adsorption of Eriochrome Black T by the magnetic GO-Fe_3O_4 (KHURANA *et al*., 2018).

L-F model was employed to the experimental data with satisfactory fit for all systems, and exhibited great non-linear determination coefficient ($R^2 > 0.99$) and small χ^2 (< 1000, on average). This was already expected, since L-F isotherm is a three-parameter model, which tends to show a best fit in comparison to double-parameter models, such Langmuir and freundlich. Furthermore, L-F showed q_m^{calc} 590.16±33.51 mg·g^{-1} for MB adsorption by nGO, near to q_m^{calc} acquired from Langmuir isotherm 717.30±46.75 mg·g^{-1} (R^2 0.985, χ^2 591.09). Additionally, q_m^{calc} for L-F model was 23% greater than q_m^{exp} value (553.21 mg·g^{-1}), as expressed in Table 4. This is another parameter to evidence that data of nGO/MB system was the worst fit for L-F isotherm.

The adsorption of RB by nGO (Figure 29b), by its turn, was best represented by L-F model, in which the greatest R^2 was achieved (0.997) and a considerably low χ^2 (2.60) in comparison to the other models. nGO–RB system showed the highest heterogeneity factor (*n*) for L-F model, 2.89±0.29, which evidences a highly diversity of free energies and might be associated to multiple biding sites of a heterogeneous interface (LUPUL *et al*., 2015; KOOPAL *et al*., 1994). Maximum modeled adsorption capacities in the monolayer (q_m^{calc}), achieved by L-F model were: 2319.20±269.37 mg·g^{-1} for nGO-NH_2-Fe_3O_4–MB (Figure 29c); 264.17±15.04 mg·g^{-1} for nGO-NH_2-Fe_3O_4–RB (Figure 29d); and 69.79±1.80 mg·g^{-1} for nGO–RB, as described in Table 4. Finally, L-F model showed a good fit of nGO-NH_2-Fe_3O_4–MB equilibrium data, from which q_m^{calc} was closer to the experimental q_m^{exp} (1852.95 mg·g^{-1}) in comparison to Langmuir isotherm. The heterogeneity factor (*n*) for this system was 1.27±0.16, which can be considered as a relatively heterogeneous interface of adsorption.

7.5.2 Adsorption equilibrium for Drimaren Red

As aforementioned, the equilibrium experimental data for the adsorption of DR by nGO-NH_2-Fe_3O_4 was analyzed and fitted to four adsorption isotherms. Figure 30 exhibits the results regarding the non-linear fittings to Langmuir, Freundlich, Temkin and L-S adapted BET model. Table 5 presents the data for the non-linear adjustments to the proposed models. As it can be seen in Table 5, equilibrium data was poorly adjusted to Langmuir (Figure 30a), Freundlich (Figure 30b) and Temkin (Figure 30c) isotherms, as the correlation coefficients (R^2) were all below 0.87, and the χ^2 values were also very high, ranging from 10,000 to 45,150. A satisfactory adjustment, however, was observed for the simplified BET model, applied to L-S systems (EBADI; MOHAMMADZADEH; KHUDIEV, 2009). In this situation, the R^2 value was near 0.95, and χ^2 was at least less than a half compared to those from other models.

Table 5 - Parameters of Langmuir, Freundlich, Temkin and BET isotherms for the adsorption of DR by nGO-NH_2-Fe_3O_4; mathematical modeling performed through non-linear fitting tool of Origin™ 9.0.

Langmuir				
q_m (mg·g^{-1})	**K_L (L·mg^{-1})**		**R^2**	**χ^2**
8724.33±3721.21	$4.33 \cdot 10^{-4} \pm 2.00 \cdot 10^{-4}$		0.86	11989.87
Freundlich				
n	**K_F (mg·g^{-1})·(L·mg^{-1})^n**		**R^2**	**χ^2**
1.04± 0.40	3.79± 9.32		0.86	11860.89
Temkin				
a_T (L·mol^{-1})	**b_T (kJ·mol^{-1})**		**R^2**	**χ^2**
210.08± 329.75	54.03± 16.54		0.49	45149.61
BET (for L-S)				
q_m (mg·g^{-1})	**K_l**	**K_s**	**R^2**	**χ^2**
219.75±78.55	$2.70 \cdot 10^{-3} \pm 3.91 \cdot 10^{-4}$	36.32 ± 1.04	0.95	5222.28

In fact, considering the isotherms classification proposed by Giles, Smith and Huitson (1974), the isotherm obtained at 298 K could be classified within the subgroups 3 or 4, as first

ones can identify a plateau representing the completion of the first monolayer. Secondly, there is the rising representing the development following (or not) to the completion of the second layer. In this case, it is clearly noticeable the “S” shape of the isotherm in Figure 30d, which is also a characteristic format of BET isotherms (EBADI; MOHAMMADZADEH; KHUDIEV, 2009). Finally, calculated monolayer adsorptive capacity (q_m), acquired by BET model fit, was 219.75±78.55 $mg \cdot g^{-1}$ and the equilibrium constant (K_l) was $2.7 \cdot 10^{-3} \pm 3.91 \cdot 10^{-4}$. These data evidence that the calculated parameter is in agreement with the experimental q_e after reached the equilibrium state, 179.80 $mg \cdot g^{-1}$ (Table 5).

According to Brunauer, Emmett and Teller (1938), the adsorption of gases might occur with the formation of multiples layers over the sorbent. Assuming that the interactions between adsorbent and adsorbate are of chemical nature, the uppermost surface of the adsorbent induces dipoles in the first layer of adsorbate molecules, which in turn induce dipoles in the next layer and so on until several layers are formed up. Extrapolating this reasoning to a delimited L-S system, the solute molecules would act exactelly a gas with the formation of multiple layers, obeing the postulates of Brunauer, Emmett and Teller (1938). However, the sorbate concentration must be sufficiently lower in a way they could behave as a gas. This is what Ebadi, MOhammadzadeh and Khudiev (2009), as well as other authors who investigate L-S adsorption, assumed when they proposed their model of BET isotherm adapted for L-S systems.

Figure 30 - Langmuir (a), Freundlich (b), Temkin (c) and BET for liquids (d) non-linear fittings to the equilibrium experimental data of DR adsorption at 298 K. Experiments performed with 25 mL of DR solution, pH 6.0, 300 rpm, contact time 90 min, nGO-NH_2-Fe_3O_4 dosage: 6.2 mg·mL^{-1}; mathematical modeling performed through non-linear fitting tool of Origin™ 9.0.

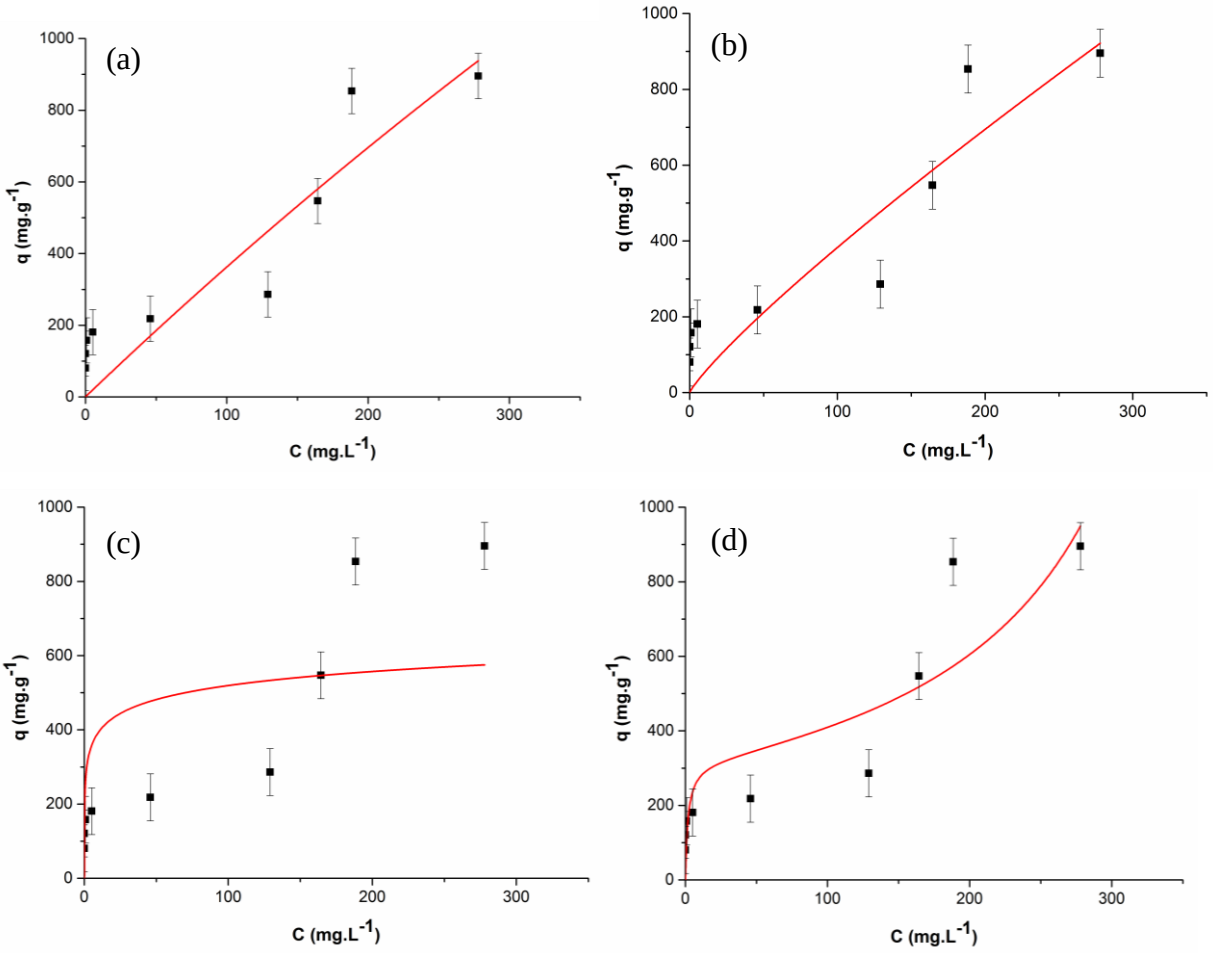

Source: reproduced from Fraga *et al*. (2020c), with permission from Springer-Nature, Copyright 2020.

7.6 BINARY ADSORPTION (METHYLENE BLUE–REMAZOL BLACK B)

Following the tendency observed in single component adsorption, the higher adsorption capacity of MB in the binary mixture MB-RB by nGO-NH_2-Fe_3O_4 was verified from pH 7–12.0, with its peak at pH 11.0 (87.61 mg·g^{-1}), whilst RB acquired higher adsorption capacity in pH 7.0 (87.57 mg·g^{-1}) [Figure 31a]. These results evidenced that interactions of electrostatic nature remain governing the interaction between MB and nGO-NH_2-Fe_3O_4 even in the presence of RB

molecules. In this regard, pH 7.0 was selected as the most representative for the operational condition of equilibrium studies performed for the binary MB-RB mixture.

Equilibrium isotherms for MB and RB in the binary MB-RB system evidenced that both curves were favorable isotherms (Figure 31b). Additionally, MB achieved the following parameters, according to Langmuir model: q_m^{MB} 2116.99±105.05 mg·g^{-1} and K_L^{MB} 4.00·10^{-2}±7.00 L·mg^{-1} (R^2 0.966); while RB reached q_m^{RB} 1017.06±305.02 mg·g^{-1} and K_L^{RB} 3.05·10^{-2}±10.23 L·mg^{-1} (R^2 0.925). By these results it is verified that the adsorption of MB and RB took place in a cooperative way, in which RB adsorption was enhanced by the presence of MB since in bicomponent system its q_m increased three times in comparison to single RB/nGO-NH_2-Fe_3O_4 system. This is explained by the effect of increasing the affinity of the nGO-NH_2-Fe_3O_4 surface for RB adsorption as a consequence of the combination of MB and RB in solution, as reported by Allen, McKay and Potter (2004). This can be product of changes in the balance of charges over the surface of nGO-NH_2-Fe_3O_4 or even as a consequence of a reorientation of the molecules of adsorbed dyes in the sorbent-sorbate interface.

Figure 31 – a) effect of pH on MB and RB removal. Experiments performed under environmental temperature, 25 ºC; 25 mL of sorbate solution; initial concentration 20.0 mg·L^{-1}; sorbent dosage: 1.0 mL of nGO and nGO-NH_2-Fe_3O_4 suspension (5.7 mg·mL^{-1}); stirring velocity of 300 rpm; binary mixture MB-RB in the proportion of 1:1; b) equilibrium experimental data and isotherm models for the adsorption of MB and RB onto nGO-NH_2-Fe_3O_4 in binary mixture system (1:1), at pH 7.0; experiments performed at the following conditions: 25 ºC, 25 mL of dye solution, adsorbent dosage 5.7 mg; stirring velocity of 300 rpm; non-linear fitting by Origin™ 9.0; c) UV-Vis spectra for solutions of RB and MB dyes.

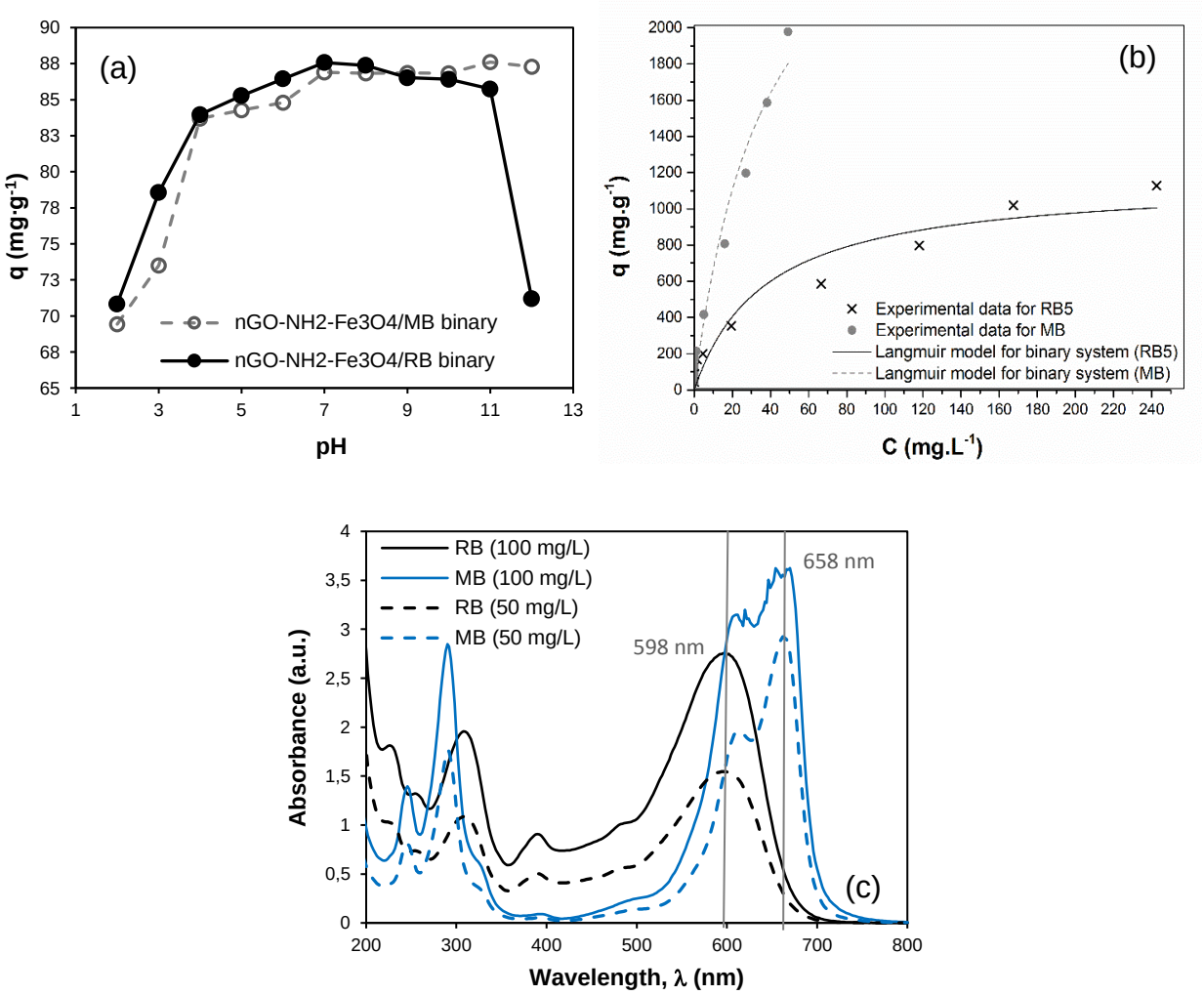

Source: (a) and (b) reproduced from Fraga *et al*. (2019b), with permission from Springer-Nature, Copyright 2020

7.7 THERMODYNAMICS OF ADSORPTION

The thermodynamic behavior of the adsorption of MB and RB in nGO-NH_2-Fe_3O_4 can be described graphically by its isothermal behavior with increasing temperature (Figure 32). For MB, adsorption capacity decreases with increasing temperature (Figure 32a), as a characteristic process of physosorption; (ROUQUEROL; ROUQUEROL; SING, 1999; RUTHVEN, 1984). However, an in-depth investigation should be conducted in agreement with kinetic and characterization data in order to obtain a precise conclusion about the adsorption mechanisms of MB and RB. In this sense, the thermodynamic parameters (ΔH^o and ΔS^o) were obtained from equilibrium isotherms at different temperatures (Table 6) by the intercept with "y-axis" and the angular coefficient of the straight line plotted by ln (*K*) *versus* 1/T (Figure 32b, d and f), obtained from van't Hoff Equation (Equation 25).

Table 6 – Thermodynamics parameters for the adsorption of MB, RB and DR by nGO-NH_2-Fe_3O_4.

	T (K)	K_L **(10^3)**	ΔG^o **(kJ·mol^{-1})**	ΔH^o **(kJ·mol^{-1})**	ΔS^o **(kJ·K^{-1}·mol^{-1})**
	298	4477.90	–37.94		
MB	318	56.22	–27.10	–150.01	$-3.78\cdot10^{-1}$
	338	3.55	–20.25		
	298	11.59	–23.19		
RB	318	244.21	–30.74	92.83	$3.91\cdot10^{-1}$
	338	948.67	–34.10		
	298	305.00	–31.91		
DR	318	3760.00	–38.51	66.43	0.33
	338	7040.00	–45.11		

Figure 32 – Isotherms obtained for the temperatures 25 ºC, 45 ºC e 65 ºC for the adsorption of MB (a), RB (c) and DR (e) by nGO-NH_2-Fe_3O_4; graphics ln (K_L) *versus* 1/T for MB (c) RB (d) and DR (f). Experiments conducted at the following conditions: dye solution volume 25 mL; pH 12.0 (MB) e 5.7 (RB); sorbent dosage 1.0 mL of nGO-NH_2-Fe_3O_4 suspension (5.70 mg·mL^{-1}); stirring velocity 300 rpm.

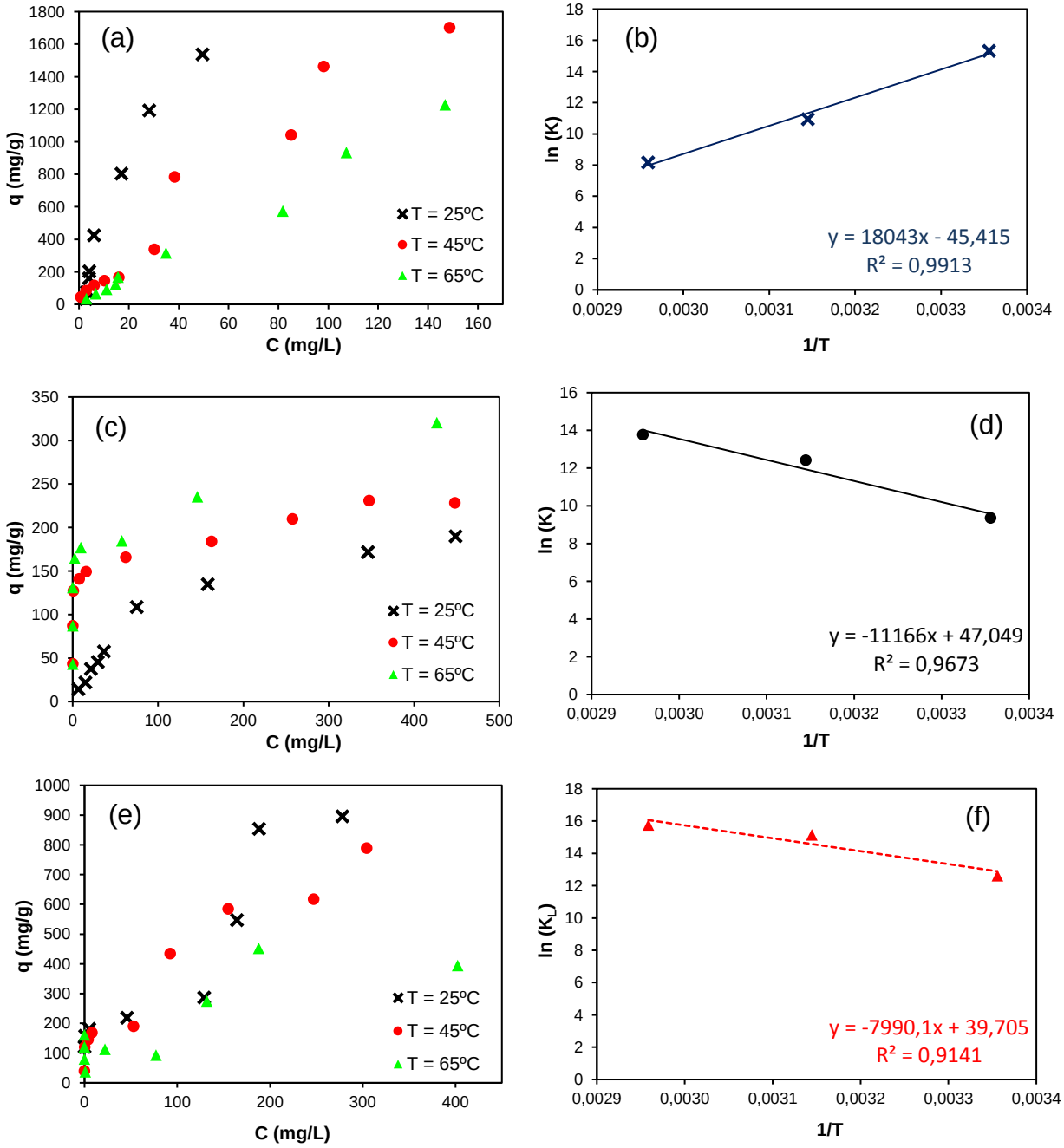

Source: (a) and (b): the author (2019); (c) and (d): reproduced from Fraga *et al.* (2019b), with permission from Springer Nature, Copyright 2020.

For the adsorption of MB, the standard enthalpy change (ΔH^o), –150.01 kJ·mol^{-1}, describes an exothermic process, which contributes to the conclusion that a process of physosorption occurred; the adsorption of RB, on the other hand, reached ΔH^o +92.83 kJ·mol^{-1}, characterizing an endothermic phenomenon, following the trend of chemisorption (ROUQUEROL; ROUQUEROL; SING, 1999; RUTHVEN, 1984). In this sense, the chemisorption energies generally follow the range of 80–200 kJ·mol^{-1}, and by thermodynamic parameters of MB and RB, it is also pertinent to conclude that the adsorption can be attributed to a physicochemical process, as reported by Saha and Chowdhury (2011). In addition, high ΔH^o values exhibited for RB adsorption can be attributed to strong interactive forces between RB and functional groups of nGO-NH_2-Fe_3O_4, such as hydrogen-bonds and covalent bonds formed by oxygen atoms from sulphonate groups (–SO_3^-) of RB (Figure 24) and functional moieties of nGO-NH_2-Fe_3O_4 (amines, amides and oxygenated groups remaining from nGO, as depicted in FTIR, Figure 12d).

Negative values for Gibbs' free energy changes (ΔG^o) showed that the adsorption of MB and RB was spontaneous. In addition, the changes in sorption entropy (ΔS^o), calculated for MB and RB, were –0.38 kJ·mol^{-1}·K^{-1}, which guarantees an enthalpy driven adsorption process; and +0.39 kJ·mol^{-1}·K^{-1} for RB adsorption, corresponding to a slight randomness at the nGO-NH_2-Fe_3O_4/RB interface and an increase in the degree of freedom of RB adsorbed onto the surface of nGO-NH_2- Fe_3O_4 (SAHA; CHOWDHURY, 2011).

$\Delta G°$ for the adsorption of DR by nGO-NH_2-Fe_3O_4 were negative for the three temperatures (Table 6): –6.28 kJ·mol^{-1} (298 K), –6.85 kJ·mol^{-1} (303 K) and –7.18 kJ·mol^{-1} (313 K), evidencing that the adsorption were spontaneous in every temperature. The enthalpy and entropy were respectively +66.43 kJ·mol^{-1} and +0.33 kJ·K^{-1}·mol^{-1} (Table 6). Similarly to RB, positive values of ΔH^o reveal the chemical behavior of the adsorption of DR by nGO-NH_2-Fe_3O_4, in which the adsorptive capacity increased with the temperature (Figure 32e). From thermodynamic, kinetics and characterization data, it is concluded that the DR stays bound to nGO-NH_2-Fe_3O_4 surface groups with strong interactive forces, nearly as a chemical bond.

Positive value of $\Delta S°$ evidences a certain degree of disorder over DR–nGO-NH_2-Fe_3O_4 interface, which might be related to the heterogeneous multilayer character of the adsorption, since BET model best fitted the experimental data. For DR, the chemisorption can also be described as a consequence of covalent bonds which might be formed between sulfonic groups

and halogens (Cl and F) of DR molecular structure (Figure 24) and the hydroxyl and amines distributed over nGO-NH_2-Fe_3O_4 surface and edges. This is also evidenced by the presence of the bands at 1024 cm^{-1}, 1452 cm^{-1} and 1609 cm^{-1} in FTIR spectrum for nGO-NH_2-Fe_3O_4 after the adsorption of DR (Figure 12d); these bands are relative to the stretching vibrations of R–SO–R, N=N and C=C bonds, from azo, sulphonate and benzene groups of DR structure, respectively (BILAL *et al*., 2018; NEOH *et al*., 2015).

7.8 REGENERATION OF NGO-NH_2-FE_3O_4

The recyclability data of nGO-NH_2-Fe_3O_4 in the adsorption of MB, RB and DR are depicted in Figure 33a, while the dye recover in each cycle is shown in Figure 33b. By adsorption/desorption tests, nGO-NH_2-Fe_3O_4 adsorption efficiency remained 95.6% after 10 cycles of MB adsorption (Figure 33). Furhtermore, there was no substantial loss in the removal efficiency of MB through the regeneration cycles. For RB, on the other hand, it was observed a greater loss in sorption efficiency over 10 cycles, remaining 79.8%.

Figure 33 – a) Regeneration of nGO-NH_2-Fe_3O_4 after MB, RB and DR adsorption; b) total recovered dye in each cycle. Desorption performed by 3 washings with distiled water, and sorbent regeneration in an incubator at 65 ºC with stirring velocity of 300 rpm during 1h.

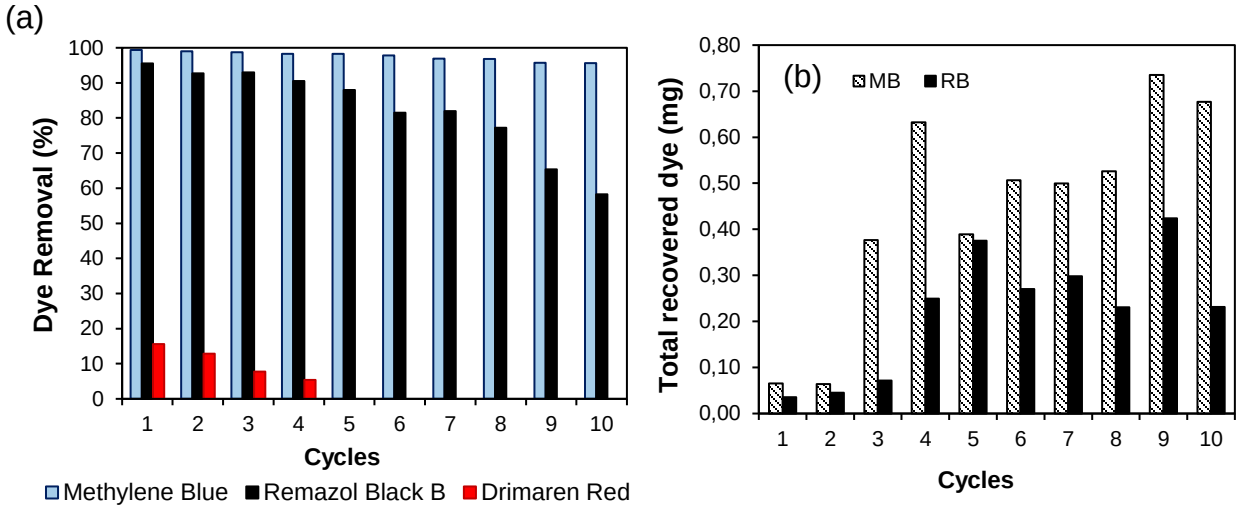

Source: the author (2019).

The recyclability of nGO-NH_2-Fe_3O_4 for the adsorption of MB was more efficient than that observed for RB adsorption. This was due to the broader molecular structure of RB, which has more aromatic rings, N=N bonds and higher "stacking" capacity through π–π interactions if compared to MB. These electronic configurations ensure RB tendency to maintain high strength interactions with nGO-NH_2-Fe_3O_4, commonly observed in chemosorption processes, which make it difficult to desorb RB in aqueous medium. Moreover, the RB chemosorption process makes it unfeasible to simply desorption by increasing the water temperature during regeneration, requiring its regeneration through chemical modification of the medium, such as changes in pH to alkaline or acid (HAN *et al*., 2017) or by washing the adsorbent with a polar solvent. Data reported in the literature show that graphene-based nanomaterials guarantee high adsorption capacity, mild operating conditions and high recyclability in relation to several pollutant species, which can be considered as one of its most ecological properties (GE *et al*., 2016). High regeneration allows the reuse of nGO-NH_2-Fe_3O_4 in the same dye removal process and its use in other types of dye adsorption, but its efficiency can decrease along the cycles depending on sorbate nature, as verified by the data of RB.

After the regeneration cycles, the concentration of the adsorbate in the effluents of washing and regeneration was measured with the objective to quantify the amount of dye which can be recovered in sorbent recycling (Figure 33b). The results of dye recovery showed an average of 0.45 mg of MB per each cycle (total of 4.47 mg in all 10 cycles); RB, on the other hand, showed an average of 0.22 mg recovered in each cycle (total of 2.23 mg in all cycles). The amount of DR recovered was irrelevant, since DR remained chemisorbed in nGO-NH_2-Fe_3O_4 active sites. These results evidenced that part of the dye can be recovered through the vaporization of water in the washing and regeneration steps along with the nGO-NH_2-Fe_3O_4, which can be reused in the adsorption processes.

7.9 TREATMENT OF RAW TEXTILE WASTEWATER BY ADSORPTION ONTO NGO-NH_2-FE_3O_4

nGO-NH_2-Fe_3O_4 was investigated as adsorbent of post-treated textile wastewater with the objective of further reuse of water in the textile washing process. For that, samples of raw textile wastewater, collected from the end of pipe in the washing process and after the coagulation tank in the laundromat, were submitted to adsorption by nGO-NH_2-Fe_3O_4. Experimental data showed significant decreases in the most significant parameters of quality for treated wastewater for industrial reuse purposes. Moreover, with the exception of apparent color (177 Hazen), all quality parameters for treated effluents were in agreement with the Brazilian legislation, CONAMA Resolution 430 (BRAZIL, 2011), as described in Table 7.

It is worthy mention that dyeing wastewater possesses a high load of metallic ions, soaps, salts and surfactants, beyond the textile dyestuffs (WANG *et al*., 2011). It is clear that all these compounds compete with dyes for the active sites of the adsorbent. This is evidenced by the relative low removal of color in comparison to the other parameters: 53.6% for the raw sample. It was also verified that the COD (in mg $O_2 \cdot L^{-1}$) decreased 55% after the coagulation and adsorption process. Nevertheless, the BOD showed values below 10 of all samples, evidencing the lower biodegradable load of the raw textile wastewater, even after the treatment by coagulation and adsorption. BOD values for the treated wastewater (flocculation + decantation + adsorption) met the requirements for industrial reuse in most of States in USA monitored by US EPA, according to the Guidelines for Water Reuse (USEPA, 2012). However, the data of turbidity did not meet the required values neither in CONAMA 430 (Brazil, 2011), nor in EPA guidelines for industrial reuse (USEPA, 2012), as described in Table 7.

These results corroborate to highlight nGO-NH_2-Fe_3O_4 high potential of application on real textile pollutants, since a large amount of a real laudromat pollutants were removed from the effluent after the adsorption. The removal of aparent color by nGO-NH_2-Fe_3O_4 (53.6%) was lower than what observed by Araújo *et al*. (2020), who investigated the treatment of raw textile wastewater by GO followed by coagulation. The authors reported a decrease of 66% in color after the adsorptive treatment. Same trend was observed for turbidity removal (%), in which the treatment of real textile wastewater by GO reached 85% (ARAÚJO *et al*., 2020), while the real effluent treated by nGO-NH_2-Fe_3O_4 reached 75% of turbidity removal. However, it is necessary to consider that in this work, the process variables were not optimized. Further investigation is

necessary to unravel the effect of significant variables (pH, adsorbent dosage, temperature) on the removal efficiency.

Table 7 – Parameters of raw textile wastewater before and after the adsorption onto nGO-NH_2-Fe_3O_4 Experiments carried out under the following conditions: nGO-NH_2-Fe_3O_4 dosage, 0.0057g; room temperature, 25 ºC; 25 mL of wastewater; 300 rpm of agitation velocity.

	Before adsorption		**After adsorption**		**Maximum limits, Legislation parameters**	
	Raw wastewater	**Coagulated wastewater**	**Raw wastewater**	**Coagulated wastewater**	**CONAMA, Brazil [1]**	**EPA, USA [2]**
Turbidity (NTU)	105.0	63.5	25.9	24.7	100.0	10.0 [4]
pH	7.67	7.25	8.72	8.67	5.0–9.0	6.0–9.0 [6]
Temperature (ºC)	25–27	25–27	25–27	25–27	70	N/A [8]
Aparent color (Hazen)	360	274	177	199	75	MR [7]
TSS ($mg \cdot L^{-1}$)	2.38	0.59	0.42	0.23	80% [3]	30.0
COD ($mg\ O_2 \cdot L^{-1}$)	607.96	380.08	640.63	269.57	N/A [8]	60.0 [5]
BOD ($mg\ O_2 \cdot L^{-1}$)	7.0	6.0	8.0	6.0	120.0	30.0
Bacterial indicators (U/100 mL)	N/A [8]	N/A [8]	N/A [8]	N/A [8]	N/A [8]	23–240

[1] maximum limit according to legal parameters for the classification of "treated wastewater", destined to release into water bodies after conventional and specialized treatments – Resolution CONAMA 430 (BRAZIL, 2011);

[2] maximum limits established for "industrial reuse", as reported in the Guidelines for Water Reuse, from US Environmental Protection Agency (USEPA, 2012);

[3] minimum removal efficiency (in %), after wastewater treatment (BRAZIL, 2011);

[4] parameter established only by the California and North Carolina States; other monitored States did not establish maximum limits for turbidity in reusable waters dor industrial purposes; the exception is the Washington State, which is more restrictive: < 5.0 NTU (USEPA, 2012);

[5] parameter of carbonaceous biochemical oxygen demand (CBOD, in $mg \cdot L^{-1}$), established by the Florida State (USEPA, 2012);

[6] pH monitored for "restricted indoor and unrestricted outdoor use" (Class R), according to USEPA (2012);

[7] MR: measure reported (only).

[8] N/A: not applicable;

TSS for the treated wastewater after coagulation + adsorption onto nGO-NH_2-Fe_3O_4 fit the Brazilian legislation, since after both processes the effluent exhibited a decrease of 90.3% in TSS and CONAMA 430 requires more than 20.0% in treatment efficiency for TSS removal (Table 7). Considering the adsorption of raw textile wastewater (without coagulation process), the treated effluent showed a decrease in TSS of 82.4%, also meeting the limits of CONAMA 430 (BRAZIL, 2011). The lower result for TSS removal after the conjugated coagulation-adsorption treatment, might be explained by the presence of organometallic precipitates (from the activity of $Al_2(SO_4)_3$ in basic pH). These precipitates then occupied the active sites of nGO-NH_2-Fe_3O_4, releasing other organic suspended substances in the aquous medium. Furthermore, TSS measured for all wastewater samples (raw, coagulated, coagulated + adsorption, among others) showed results that fit USEPA (2012) maximum limits (< 30.0 $mg \cdot L^{-1}$, in the average for most States), as described in Table 7.

The pH measured for the textile wastewater after adsorptive treatment fit the parameter established by Brazilian legislation CONAMA 430 (5.0–9.0), the same was observed for the textile effluent after the coagulation treatment (Table 7). Furthermore, pH is a parameter which does not have a maximum limit established for industrial reuse, according to USEPA guidelines. Thus, it was included the maximum limit for restricted indoor and unrestricted outdoor use (pH, 6.0–9.0) for comparative purposes (USEPA, 2012).

Once the adsorptive process was not carried out under temperatures above the room conditions (~ 25–27 ºC), it is safe to estate that this parameter (discharge temperature, in ºC) met the maximum limit (70 ºC) established by the resolution CONAMA 430 (Brazil, 2011). Moreover, the USEPA guidelines (2012) did not fix temperature limits for industrial reuse of water (USEPA, 2012).

USEPA Guidelines also establish indicators for the presence of bacteria in treated effluents for industrial reuse, which vary according to each State. In general, it is necessary to monitor the total and fecal coliforms (*E. coli* and *Enterococci*). CONAMA 430, by its turn, does not establish standards for bacteria, though it delivers the establishment of specific standards for the phosphorus parameter to competent environmental agencies (BRAZIL, 2011). In this thesis, it was not investigated the presence of bacteria, as well as other biological pathogens, in the raw and coagulated wastewater.

7.10 COMPARATIVE STUDY TOWARDS FUNCTIONALIZED GRAPHENE AS SORBENT OF SEVERAL DYESTUFFS

The performance of several adsorbents based on graphene or functionalized graphene oxide was evaluated according to the data summarized in Table 8. Reported data show that nGO-NH_2-Fe_3O_4 has a high adsorption capacity compared to other graphene-based adsorbents, especially in comparison to nGO, its precursor material. A substantial increase of more than 100% in the adsorption capacity obtained in tests with MB was obseverd. Another aspect in which the nGO-NH_2-Fe_3O_4 has a great prominence is its very high regeneration capacity, since after 10 cycles of adsorption/desorption, its efficiency remains practically unchanged. In this regard, many works which deal with graphene nanocomposites as adsorbents of textile dyes report an average of 4–6 cycles of regeneration. This tendence is also expressed in Table 8, with the exception of GO-Fe_3O_4, applied in the removal of Rhodamine B by Ganesan, Louis and Damodaran (2018).

The kinetic model which most represented the adsorption of dyes by these materials was the PSO model. This information contributes to understand the surface phenomena over the graphene-dye interface, since most of resistances to mass transfer are located in the bulk phase and boundary layer (GANESAN; LOUIS; DAMODARAN, 2018; MINITHA *et al*., 2017). Some works report the fit of IPD model (DAS *et al*., 2018), however few of them investigate the physical reason for those fitting and most of them used linear regression for their fitting and both IPD and PSO shown great determination coefficients (R^2).

As for the adsorption isotherms, there is no model that stands out in the representation of the adsorption of dyes by these materials. Furhtermore, the most representative models (Langmuir, Freundlich and Temkin) fit satisfactorily to the experimental data presented in Table 8, included others that were not reported in this study.

It is also verified from the comparative study that the predominant sorbent-sorbate interactions are the π–π stacking interactions. These are favored by the large sp^2 configuration of carbon hexagonal lattice of graphene-derived adsorbents. This favors the attraction of other molecules of great size, especially those that have large amounts of aromatic rings and double (or triple) bonds in its structure (SPYROU; RUDOLF, 2014). In this sence, reactive dyes are more likely to form π–π sconjugation with graphenic plane (Table 8). However, a considerable number of works report the role of electrostatic interactions, where they are favored by variations in the pH of the dye solutions.

The presence of oxygenated groups over GO surface (hydroxyl, carboxyl and epoxide) decreases the surface hydrophobicity, and increases its dispersion in water. This phenomenon turns its separation from adsorbate medium rather difficult. Additionally, oxygenated groups might lower GO adsorption efficiency towards some kind of dyes, as reported by Ersan *et al*. (2017). Nevertheless, the water cluster formation is not sufficiently reported when GO is employed as nanosorbent of dyes. On the contrary, as can be seen in Table 8, exfoliated GO has been satisfactorily applied as efficient sorbent for Methylene Blue (500–504 $mg \cdot g^{-1}$) (ARAÚJO *et al*., 2018), Rhodamine B (224.00 $mg \cdot g^{-1}$) (DAS *et al*., 2018), Remazol Black B (69.78 $mg \cdot g^{-1}$) (this work), among others, and no cluster formation was reported in these studies.

Table 8 – Comparative study of the adsorption of different species of dyes by amino-Fe_3O_4-functionalized nGO and outhers types of graphene-derived sorbents found in the literature.

Adsorbent	Adsorbate	q_m^{calc}, mg·g^{-1}	Isotherm model	Kinetic model	Predict mechanism	pH	Reg. cycles	References
GO	Methylene Blue	504.00	Temkin	PSO	Elect. Interactions, π–π	4.0-6.0	N/A	Araújo *et al.* (2018)
r-GO	Methylene Blue	144.90	Langmuir	PSO	Elect. Interactions	8.0-12.0	N/A	Minitha *et al.* (2017)
Fe_3O_4-GO	Methylene Blue	131.10	Langmuir	PSO	π–π	9.0-10.0	5	Ganesan, Louis and Damodaran (2018)
Ag NPs/GO	Methylene Blue	365.00	N/A	PSO	Elect. Interactions	N/A	N/A	Rohaizad *et al.* (2020)
Hemin-GO	Methylene Blue	99.20	N/A	PSO	π–π	9.0	5	Zhao *et al.* (2017)
GO	Rhodamine B	224.00	Temkin	IPD	π–π	4.0	7	Das *et al.* (2018)
Bi_2O_3-GO	Rhodamine B	320.00	Temkin	IPD	H-bond	4.0	N/A	Das *et al.* (2018)
Fe_3O_4-GO	Rhodamine B	39.65	Langmuir	PSO	π–π	3.0	8	Ganesan, Louis and Damodaran (2018)
β-cyclodextrin-Graphene	Methyl Orange	328.20	Langmuir	PSO	π–π	N/A	6	Tan and Hu (2017)
xGnP^{TM} graphite nanoplatelets	Direct Red 80	26.41	BET type II	PSO	π–π, Elect. Inter., H-bond	3.5	4	De Oliveira *et al.* (2019)
xGnP^{TM} graphite nanoplatelets	Drimaren Dark Blue	20.51	BET type IV	PSO	π–π, Elect. Inter., H-bond	3.5	4	De Oliveira *et al.* (2019)
Methylimidazole-GO	Direct Red 80	501.30	Langmuir	PSO	Elect. Interactions	12.0	4	Zambare *et al.* (2017)
nGO	Methylene Blue	717.30	L-F	PSO	Elect. Interactions, π–π	12.0	N/A	Present work
nGO	Remazol Black B	69.78	Freundlich	PSO	Elect. Interactions, π–π	5.7	N/A	Present work
nGO-NH_2-Fe_3O_4	Methylene Blue	2319.20	L-F	PSO	Elect. Interactions, π–π	12.0	10	Present work
nGO-NH_2-Fe_3O_4	Remazol Black B	264.17	L-F	PSO	covalent	5.7	5	Present work
nGO-NH_2-Fe_3O_4	Drimaren Red	219.75	BET (L-S)*	PNO	π–π	6.0	N/A	Present work

* L-S: BET model adjusted for Liquid-solid systems.

7.11 ADSORPTION OF MB BY NGO(NH)R/C

In face of the high hydrophilicity of nGO, amino-functionalized graphene oxide (nGO(NH)R) was supported in wood waste charcoal with the main objective of facilitating the sorbent separation from aqueous medium after the adsorption. For this, sedimentation assays were conducted with nGO and nGO(NH)R/C (1:1 w/w) in aqueous suspension (10.0 $mg \cdot mL^{-1}$) and it was observed that nGO(NH)R/C fully decanted within 2 days, while nGO sedimented after 4 days. Information regarding the sedimentation of nGO and nGO(NH)R/C is supplied in Appendix D.

7.11.1 Adsorption kinetics

Kinetic data showed that the adsorptive capacity at equilibrium (q_e^{exp}) of wood waste charcoal more than doubled after the anchoring of nGO(NH)R over its surface (in the proportion nGO(NH)R:charcoal of 1:1 and 1:2, in mass), as described in Table 9. These results evidence that part of the active sites of nGO(NH)R remained available for the interaction with MB molecules, which supplemented the adsorption capacity of wood waste charcoal, as verified in BET characterization data. Moreover, kinetic curves were nearly the same; experimental data acquired for 25 mL of MB solution with C_0 100.0±3.5 $mg \cdot L^{-1}$, 300 rpm and 25 ºC and 0.1 g of nGO(NH)R/C (1:1) and (1:2).

IPD model did not show a satisfactory fit for any adsorbent ($R^2 < 0.200$ and great values of χ^2). This might be explained by the fact that charcoal has a narrower mesoporous structure according to BET analysis, and the active sites are located mainly in the surface, and not inside the pores. For nGO(NH)R/C adsorbents, as the amino-functionalized GO occupied significant part of the active sites of charcoal and part of its remaining pores, which was revealed in BET N_2 adsorption/desorption isotherm, the intraparticle diffusion is not representative of the adsorption. Given this, it is observed by kinetic data, in agreement with characterization results, that the adsorption of MB took place in the surface of the adsorbent and most of the limiting step of the adsorption is related to the external diffusion, even for pure charcoal. Furherly, investigation of the supporting of graphene nanoderivatives on charcoal must be carried out with carbons of greater particle size (< 60 Mesh), which might have a well-defined porous structure.

Table 9 – kinetic parameters for the adsorption of MB by nGO(NH)R/C (1:1 in w/w) and pure wood waste charcoal.

System	PFO		PSO		PNO		IPD	
GO-NH/C (1:1)	q_e^{calc} (mg·g^{-1})	24.80±0.04	q_e^{calc} (mg·g^{-1})	24.89±0.02	q_e^{calc} (mg·g^{-1})	24.98±0.02	k_0 (mg·g^{-1})	19.49±2.99
	k_f (min^{-1})	3.99±0.30	k_s (g·mg^{-1}·min^{-1})	1.60±0.13	k_n (g·mg·min^{-1})$^{1-n}$	1.24±0.19	k_{ID}	0.78±0.55
q_e^{exp} 24.92 mg·g^{-1}					n	2.83±0.19		
	R^2	0.999	R^2	0.9999	R^2	0.9999	R^2	0.078
	χ^2	0.017	χ^2	0.002	χ^2	$3.99\cdot10^{-4}$	χ^2	43.52
GO-NH/C (1:2)	q_e^{calc} (mg·g^{-1})	25.68±0.04	q_e^{calc} (mg·g^{-1})	25.77±0.02	q_e^{calc} (mg·g^{-1})	25.86±0.02	k_0 (mg·g^{-1})	20.19±3.10
q_e^{exp} 25.81 mg·g^{-1}	k_f (min^{-1})	4.03±0.30	k_s (g·mg^{-1}·min^{-1})	1.60±0.13	k_n (g·mg·min^{-1})$^{1-n}$	1.24±0.09	k_{ID}	0.80±0.57
					n	2.83±0.19		
	R^2	0.9997	R^2	0.9999	R^2	1.0000	R^2	0.077
	χ^2	0.02	χ^2	0.002	χ^2	$3.99\cdot10^{-4}$	χ^2	46.71
Wood Waste Charcoal	q_e^{calc} (mg·g^{-1})	11.90±0.25	q_e (mg·g^{-1})	11.18±0.27	q_e^{calc} (mg·g^{-1})	13.02±9.89	k_0 (mg·g^{-1})	8.15±1.29
	k_f (min^{-1})	3.14±1.86	k_s (g·mg^{-1}·min^{-1})	0.61±0.37	k_n (g·mg·min^{-1})$^{1-n}$	$7.03\cdot10^{-5}$ ±$4.30\cdot10^{-3}$	k_{ID}	0.43±0.24
q_e^{exp} 11.40 mg·g^{-1}					n	7.86±31.81		
	R^2	0.929	R^2	0.945	R^2	0.949	R^2	0.162
	χ^2	0.68	χ^2	0.54	χ^2	0.49	χ^2	8.14

* N/A: PNO modeling was not carried out by the author for wood waste charcoal–MB.

Kinetics of adsorption of MB onto nGO(NH)R/C (1:1) showed that the equilibrium was reached within 10 min with experiemental adsorption capacity at equilibrium state (q_e^{exp}) of 25.81 mg·g^{-1}, as depicted in Figure 34a and Table 9. Beyond that, the modeling of experimental data showed the respective calculated adsorption capacities at equilibrium (q_e^{calc}): 24.80±0.04 mg·g^{-1}, 24.89±0.02 mg·g^{-1}, 24.98±0.02 mg·g^{-1} and k_0 19.49±2.99 mg·g^{-1} for PFO, PNO, PSO and IPD models (Table 9).

Figure 34 – kinetic experimental data of the adsorption of MB by: a) nGO(NH)R/C (1:1); b) pure wood waste charcoal; mathematical modeling by PFO, PSO, PNO and IPD models. Experiments carried out with 0.1g of nGO(NH)R/C, at 25 ºC, 300 rpm.

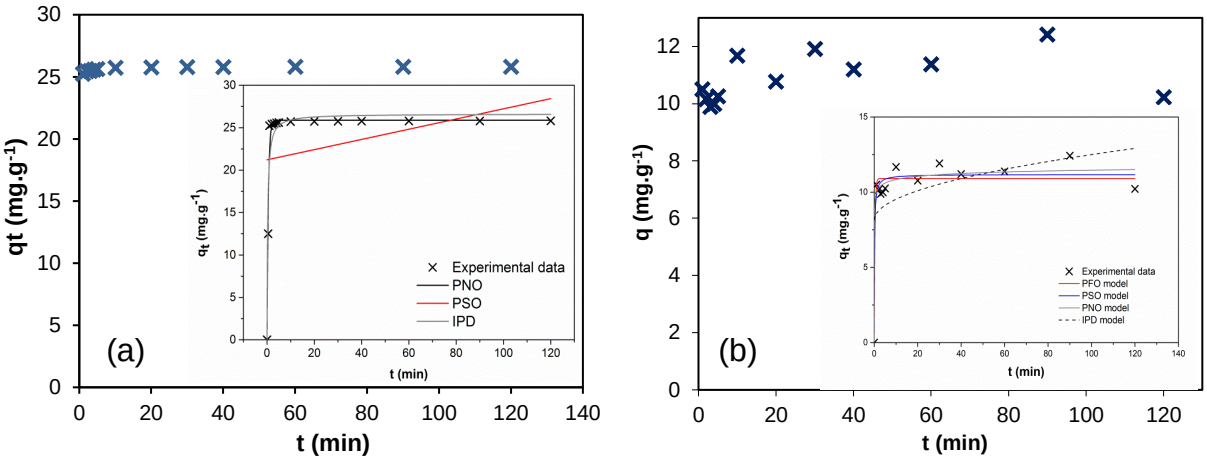

Source: the author (2019).

The pseudo-n^{th}-order constant rate was 1.24±0.09 $mg^{1-n} \cdot g^{1-n} \cdot min^{-1}$ (with kinetic order, n = 2.83±0.19), while PSO kinetic constant rate was 1.60±0.13 $g.mg^{-1} \cdot min^{-1}$. PNO model was the one which best fitted to experimental data, with great coefficient of determination (R^2 0.9999) and the lower chi-square factor (χ^2 ~ 0.004) in comparison to other models. Moreover, PNO parameter of kinetic order being nearly 2.8 suggests that PSO model could also be representative for the kintics of MB adsorption. This result explains that adsorption mechanisms could be governed by external mass transfer without intrapore resistance, in which the limiting factor is located in the bulk and film interface. Such conclusion is also corroborated by the inexpressive fitting of IPD model.

Finally, from kinetic data, it is observed that nGO(NH)R content supported on wood waste charcoal barely influenced the adsorption of MB, as expected. In this regard, the textural properties of both nanocomposites were very similar.

For the adsorption of MB by pure wood waste charcoal, the PSO model was the one which best fitted the experimental data (Figure 34b). However, an unsatisfactory correlation is

observed, since R^2 was 0.945, even with a considerable low chi-square factor (χ^2 0.54). In instance, the calculated adsorption capacity at equilibrium for PSO (q_e^{calc} 11.18±0.27 mg·g^{-1}) was nearly the same of the experimental value (q_e^{exp} 11.40 mg·g^{-1}) in comparison to the other models investigated in kinetics modeling.

7.11.2 Equilibrium of the adsorption of MB by nGO(NH)R/C

Equilibrium experiments of the adsorption of MB by nGO(NH)R/C showed that both isotherms were favorable (Figure 35, a and b). The experimental maximum adsorption capacities (q_m^{exp}) of nGO(NH)R/C in proportions 1:1 and 1:2 did not show significant difference; however, it is observed that q_m^{exp} increased 54% in comparison to pure wood waste charcoal (Figure 35c). Furthermore, L-F model and Langmuir model best fitted the adsorption with very similar coefficient of non-linear regression, as seen in Table 10. The modeled adsorption capacities in the monolayer (q_m^{calc}) respectively acquired for nGO(NH)R/C (1:1) and nGO(NH)R/C (1:2) were 48.84±3.67 and 54.07±2.74 mg·g^{-1} according to L-F model. Heterogeneity factor (n) were 1.59±0.50 and 0.86±0.17 for nGO(NH)R/C (1:1) and nGO(NH)R/C (1:2), respectively.

Despite some works report values significantly higher for modeled adsorptive capacity, mostly between 100–400 mg·g^{-1} (MEILI *et al*., 2019; JI *et al*., 2019; ISLAM *et al*., 2017), these results are in agreement to others reported in recently published works which deal with the adsorption of dyes by biochars derived from biomass. It is worthy to be summarized by their maximum monolayer adsorption capacity: 12.0 mg·g^{-1} for the adsorption of Indosol Black NF1200 by biochar derived from wood residues in gasification process (KELM *et al*., 2019); 20.6 mg·g^{-1} for the adsorption of Methylene Blue by kaolin and biochar derived from pine cone trees; data acquired for a continuous fixed-bed column system (DAWOOD; SEN; PHAN, 2019); finally, Huang, Chen and Zhang (2018) reported q_m^{calc} = 53.68 mg·g^{-1} for the adsorption of Methylene Blue by biochar produced from rabit and pig manure and calcined at 500 ºC (termed PMB_{500} by the authors).

Figure 35 – equilibrium data for the adsorption of MB by nGO(NH)R/C – 1:1 (a), nGO(NH)R/C – 1:2 (b) and pure wood waste charcoal (c); experimental data fitted by the isotherm models of Langmuir, Freundlich, Temkin and L-F.

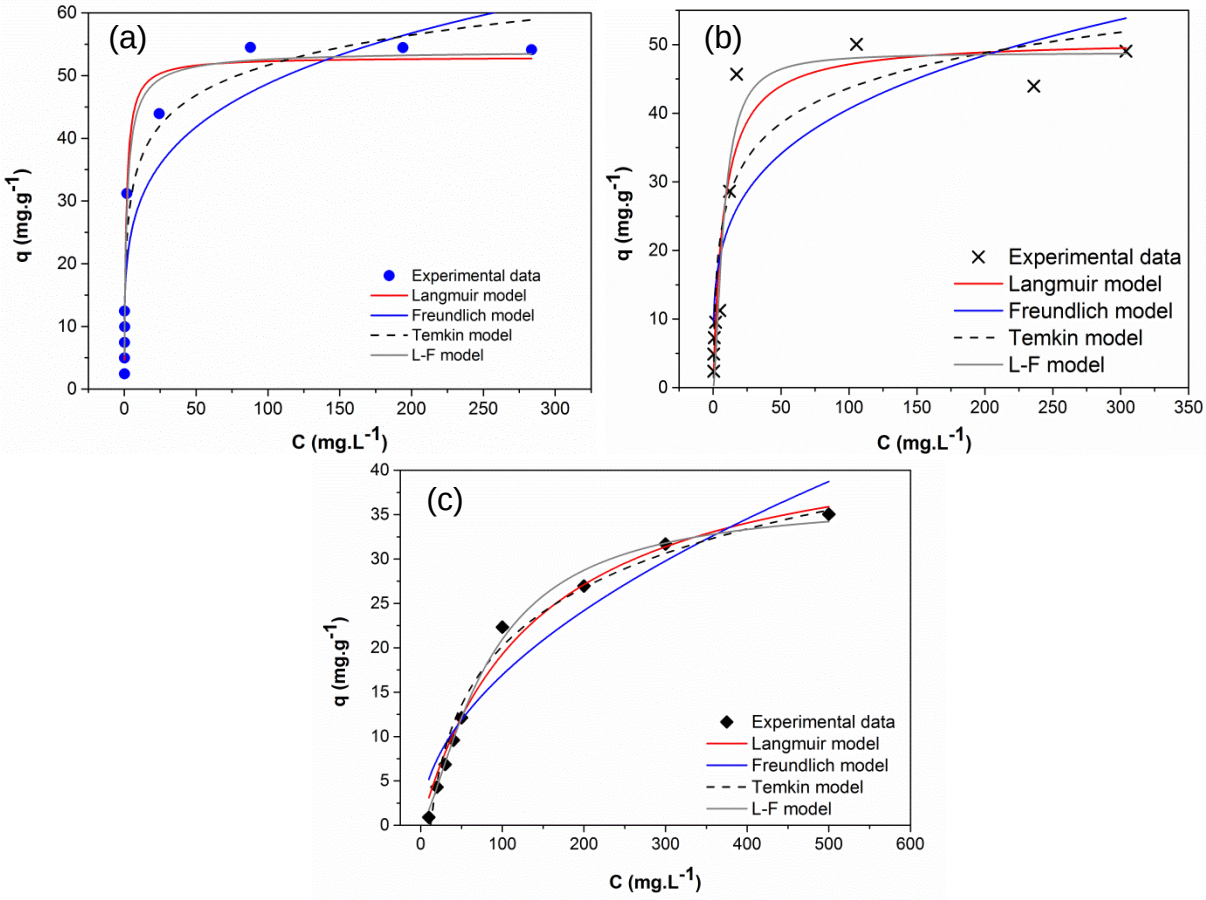

Source: the author (2019).

Table 10 – Equilibrium parameters for the adsorption of MB by nGO(NH)R/C (1:1), nGO(NH)R/C (1:2) and pure wood waste charcoal.

	Langmuir		Freundlich		Temkin		L-F	
nOG(NH)R/C (1:1)	q_m^{calc} (mg·g^{-1})	50.78±3.57	K_f (mg·g^{-1})·(mg·L)$^{-1/n}$	12.64±3.65	a_T (L·g^{-1})	3.67±2.02	q_m^{calc} (mg·g^{-1})	48.84±3.67
	K_{eq} (L·mg^{-1})	$1.29\cdot10^{-1}$ ±$3.97.10^{-2}$	n	3.94±0.94	b_T (kJ·mol^{-1})	334.93 ±44.27	K_{LF} (L·mg^{-1})	$3.89\cdot10^{-2}$ ±$4.10\cdot10^{-2}$
	R_L	0.016					n	1.59±0.50
	R^2	0.926	R^2	0.771	R^2	0.863	R^2	0.927
	χ^2	30.004	χ^2	93.072	χ^2	55.636	χ^2	29.630
nOG(NH)R/C (1:2)	q_m^{calc} (mg·g^{-1})	52.98±1.99	K_f (mg·g^{-1})·(mg·L)$^{-1/n}$	17.59±3.16	a_T (L·g^{-1})	17.37±6.14	q_m^{calc} (mg·g^{-1})	54.07±2.74
	K_{eq} (L·mg^{-1})	$7.59\cdot10^{-1}$ ±$1.61\cdot10^{-1}$	n	4.52±0.77	b_T (kJ·mol^{-1})	357.65 ±25.43	K_{LF} (L·mg^{-1})	$6.69\cdot10^{-1}$ ±$1.70\cdot10^{-1}$
	R_L	0.003					n	0.86±0.17
	R^2	0.971	R^2	0.879	R^2	0.957	R^2	0.969
	χ^2	14.336	χ^2	60.625	χ^2	21.751	χ^2	15.540
Wod waste charcoal	q_m^{calc} (mg·g^{-1})	32.55±4.42	K_f (mg·g^{-1})·(mg·L)$^{-1/n}$	6.68±2.19	a_T (L·g^{-1})	2.06±1.63	q_m^{calc} (mg·g^{-1})	57.55±90.69
	K_{eq} (L·mg^{-1})	$9.07\cdot10^{-2}$ ±$4.85\cdot10^{-2}$	n	3.50±0.82	b_T (kJ·mol^{-1})	494.01 ±102.36	K_{LF} (L·mg^{-1})	$1.09\cdot10^{-1}$ ±$1.52\cdot10^{-1}$
	R_L	0.022					n	0.44±0.41
	R^2	0.771	R^2	0.839	R^2	0.762	R^2	0.724
	χ^2	37.801	χ^2	26.576	χ^2	39.354	χ^2	41.140

	nOG(NH)R/C (1:1)	nOG(NH)R/C (1:2)	Wod waste charcoal
q_m^{exp} (mg·g^{-1})	49.55	54.35	34.70

7.11.3 Thermodynamic and recyclability nGO(NH)R/C

Recyclability experiments for the adsorption of MB by nGO(NH)R/C (1:1) and nGO(NH)R/C (1:2) showed that both sorbents kept the removal percentage after six cycles, as depicted in Figure 36a. These data are in agreement with thermodynamic assessment of the adsorption of MB onto this sorbent, from which it was achieved adsorption enthalpy (ΔH^o) of –51.41 kJ·mol^{-1} (Table 11). Energies of small intensity are pointed as a clear indicative of weak interactions between adsorbent and adsorbate, such as electrostatic and π–π stacking interactions, van der Waals forces and hydrophobic interactions (SCHEUFELLE *et al.*, 2016). Generally, adsorbents submitted to physisorption processes, with low energy of adsorption, are easily

regenerable, once its interactive bonds can be broken without significant amount of energy. In this sense, the desorption of the adsorbate in the solvent, under high temperatures might be sufficient to regenerate the adsorbent, since the opposite way of the adsorption were adopted (CHEN *et al*., 2016; GRAJEK, 2000).

Table 11 – Thermodynamic parameters for the adsorption of MB by nGO(NH)R/C (1:2).

T (K)	q_m **(mg·g^{-1})**	K_L **(10^3)**	**ΔG° (kJ·mol^{-1})**	**ΔH° (kJ·mol^{-1})**	**ΔS° (kJ·mol^{-1}·K^{-1})**
298	60.60	135.30	–29.27		
318	128.41	5.76	–21.45	–51.41	–0.08
338	108.64	12.57	–23.39		

Moreover, Gibbs' free energies (ΔG°) were –29.27 kJ·mol^{-1} (at 298 K), –21.45 kJ·mol^{-1} (318 K) and –23.39 kJ·mol^{-1} (338 K), which evidences the spontaneous character of the adsorption (ROUQUEROL; ROUQUEROL; SINGH, 1999; RUTHVEN, 1984). The negative and small value of ΔS° explains a small degree of disorder over the interface MB–nGO(NH)R/C (1:2). Thermodynamic parameters were acquired from the graphic ln (K_L) *versus* 1/T (Figure 36c), derived from the modeling of the isotherms fitted to the experimental data at different temperatures, as depicted in Figure 36b.

Figure 36 – a) recycling tests for the adsorption of MB by nGO(NH)R/C (1.0 g and 2.0 g of charcoal); b) isotherms applied for the adsorption of MB by nGO(NH)R/C (1:2) in 298K, 318K and 338K; c) plot of ln (K_L) *versus* 1/T for the adsorption of MB by nGO(NH)R/C (1:2)

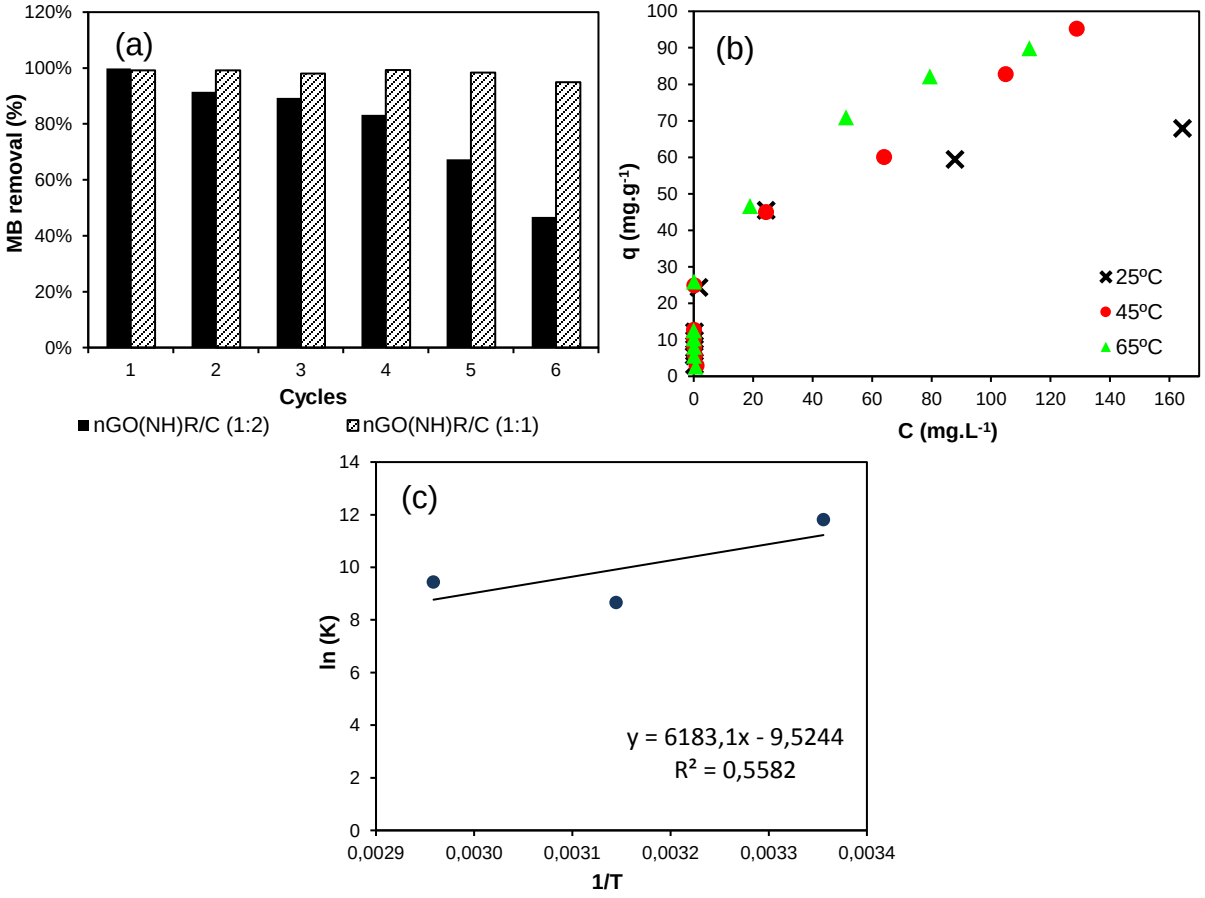

Source: the author (2019).

7.12 PHYTOTOXICITY ASSESSMENT FOR GNP, NGO AND NGO-NH_2-FE_3O_4

Figure 37 shows some samples of American lettuce (*Lactuca sativa L*), after exposition to nGO and nGO-NH_2-Fe_3O_4 suspensions in incubation at 22 ºC during 120 h, for that it is possible to observe sprouted seeds in some samples and other which did not germinate (Figure 37c). The percentage of elongation and germination of the seeds for the samples of GNP, nGO and nGO-NH_2-Fe_3O_4 are depicted in Figure 38. Moreover, the complete assessment, with parameters of SG(%) and SE(%) are described in the Tables B1, B2 and B3 in APPENDIX B section.

Figure 37 – American lettuce seeds (*Lactuca sativa L*) after exposal in: a) nGO suspension 3%; b) nGO suspension 10%; c) nGO suspension 100%; d) nGO-NH_2-Fe_3O_4 suspension 3%; e) nGO-NH_2-Fe_3O_4 suspension 10%; f) nGO-NH_2-Fe_3O_4 suspension 100%. Samples stayed in ncubator at 22 ºC during 120 h, insullated from light.

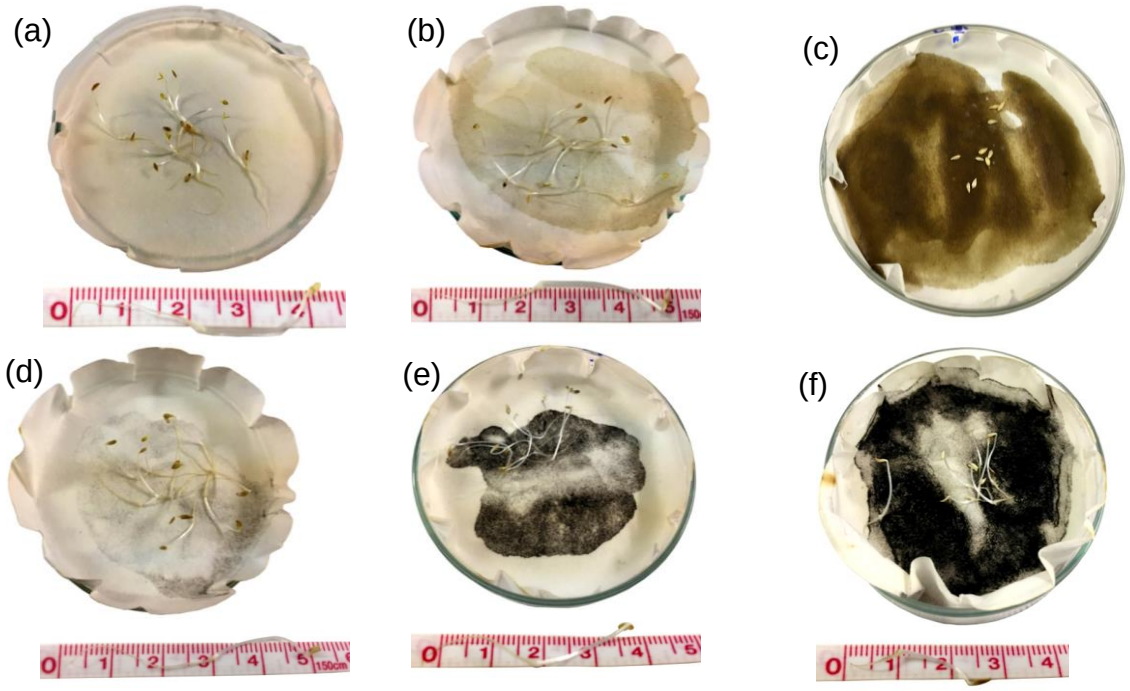

Source: reproduced from Fraga *et al*. (2020c), with permission from Springer-Nature, Copyright 2020.

Figure 38 – a) Average root elongation in diferente media: GNP, nGO and nGO-NH_2-Fe_3O_4 in the concentrations 1% - 100% v/v; b) percentage of seeds germination in diferente concentrations 1% - 100% v/v for GNP, nGO and nGO-NH_2-Fe_3O_4.

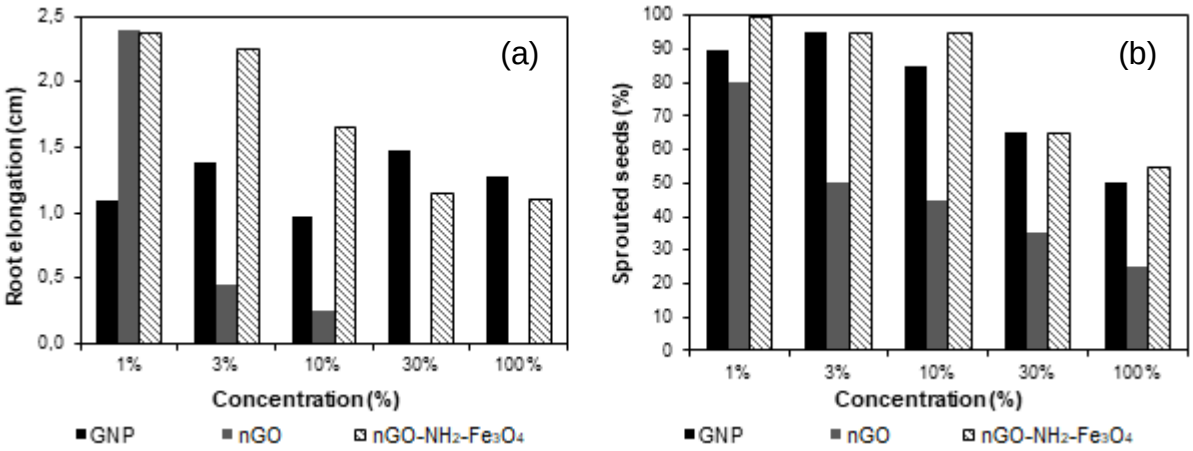

Source: the author (2019).

An accurate investigation of toxicity of commercial GNP (Table B1), nGO (Table B2) and nGO-NH_2-Fe_3O_4 (Table B3) is recommended since part of these adsorbents might be released in water bodies after the adsorption of dyes (and other compounds) from textile wastewaters. Once released together with the treated effluent, it is important to measure the inhibitory potential of nGO and nGO-NH_2-Fe_3O_4 towards fauna and flora. In this sense, acute toxicity tests were performed with seeds of *Lactuca sativa L*, and showed that nGO had a high inhibitory degree of lettuce seed development, in which none of the 10 seeds presented growth (Figure 37a). This result is in agreement with studies reported in the literature for suspensions of pure GO and after processes of treatment of industrial effluents (YANG *et al*., 2013). In addition, GO toxicity studies on *Escherichia coli*-type bacteria have shown a high degree of antibacterial activity in which there was a fall in metabolic activity of the cells from 70% to 13%, given a concentration of nGO of $8.50 \cdot 10^{-2}$ mg·mL^{-1} (HU *et al*., 2010). Other studies have also pointed to a 67.6% reduction in cell activity in *Staphylococcus aureus* bacteria (GUO *et al*., 2017). Moreover, histotlogical assays evidenced that few-layers graphene has great toxic potential in epithelial human cells, as well as in mammals' tissues and organs, such kidneys. Moreover, few-layers graphene also showed great hematoxicity in biochemical analyses (RUIZ *et al*., 2020).

nGO-NH_2-Fe_3O_4, did not present inhibitory power as the nGO, with growth of more than 95% of the seeds for the samples with concentration 3%, 10% and 30% v/v (Figure 38b). However, in seeds exposed to nGO-NH_2-Fe_3O_4, there was an average root and stem growth of 1.1 cm, thus it was 55% of the growth presented by seeds exposed only to the sample nGO-NH_2-Fe_3O_4 100% v/v. nGO exhibited a relatively low inhibitory power for sample 3% v/v; however, from 10% v/v the seed sprout decreased consistently to 50%, reaching only 25% of the seeds for the sample nGO 100% v/v (Figure 38b). These preliminary results demonstrate that nGO-NH_2-Fe_3O_4 does not have such a great inhibitory power compared to its precursor material, nGO, through which there was no development of the seeds of *Lactuca Sativa L*. Even with such results, it is necessary a study directed to native organisms from water bodies or similar environment, such as crustaceans or mammals. These experiments can be performed by *in vitro* cellular interaction tests, intravenous injection or *in vivo* ingestion (YANG *et al*., 2013) in order to fully evaluate nGO-HN_2-Fe_3O_4 toxicity. Finally, SG and SE indexes for nGO-HN_2-Fe_3O_4 were satisfactory, with the exception of one of the duplicate sample 100% v/v (SG = –0.56), as seen in Table B3 in APPENDIX B section.

GNP, in turn, exhibited a high normalized residual percentage of germinated seeds (SG) for sample with concentration 100% v/v (–0.67), being classified as highly phytotocic (BAGUR-GONZALEZ *et al*., 2011). Besides GNP presented medium toxicity for one of the samples 30% v/v, all samples of concentration below 30% v/v showed low phytotoxicity (SG > –0.25). These data are in total agreement with the results of residual percentage of elongation (SE) for GNP, which also exhibited low phytotoxicity for all samples, > –0.21 (see the Table B1, at APPENDIX B).

7.13 COST ASSESSMENT OF NANOSORBENTS SYNTHESIS AND OPERATION

In order to carry out the cost analysis as more accurate as possible, a survey of reactants and raw material cost was performed. It had been searched websites specialized in the sale of chemicals in Brazil and abroad (*Merck-Millipore*, *Sigma Aldrich*, *Synth Brazil*, among others). The survey was focused in prices for sale in large scale, since commodities products usually do not fit the analytic grade necessary to ensure nGO and nGO-NH_2-Fe_3O_4 purity. Therefore, it was chosen information regarding products sold in the largest possible volume (up to 10 L, kg). Table 12 summarizes the chemicals suppliers that were consulted in this survey. Furthermore, this survey took place during December, 2018, so the reactants prices might change according to fluctuations in local and international markets.

Table 12 – Chemical suppliers' websites

Sigma-Aldrich	https://www.sigmaaldrich.com/technical-service-home/product-catalog.html
Fisher Science	https://www.fishersci.com/us/en/home.html
Synth Brazil	https://www.lojasynth.com/reagentes-analiticosmaterias-primas/reagentes-analiticosmaterias-primas/
NEON Comercial, Brazil	http://www.neoncomercial.com.br/
Química Moderna, Brazil	http://www.quimicamoderna.net.br/?page_id=296&mycart_category=1
Submarino S/A, Brazil	https://submarino.com

Table 13 summarizes the cost evaluation per each reactant employed in the synthesis of nGO and nGO-NH_2-Fe_3O_4, while the Table 14 describes the effect of the sorbent reuse in the operational cost.

Table 13 – Cost analysis for production of nGO and nGO-NH_2-Fe_3O_4

Reactant	Amount (g, mL, h)	Unit price (BRL)	Price/amount used (BRL)	Unit price (USD)	Price/amount used (USD)
nGO					
Graphite (1kg) - Merck/Synth, Brazil	1.0	498.00	0.50	128.68	0.13
Potasse permanganate A.P. (1000 g) - *NEON*, Brazil	3.0	71.36	0.21	18.44	0.06
Sulphuric Acid A.P. 99% (5000 mL) - *NEON*, Brazil	27.0	274.08	1.48	70.82	0.38
Chloridric acid A.P. 99% (5000 mL) - *NEON*, Brazil	2.5	120.00	0.06	31.01	0.02
Ice bath and refrigeration - cooler, 125 W (h, kWh)	0.5	1.72	0.11	0.44	0.03
Energy agitation - Quimis Q621 600 W (6 h)	6.0	1.72	6.19	0.44	1.60
TOTAL (per 600 mL of GO suspension)			14.25		3.68
TOTAL (per 1 kg adsorbent)			**2500.47**		**646.12**
nGO-NH_2-Fe_3O_4					
GO production (175 mL of 500 mL)			4.99		1.29
Diethylenetriamine (DETA) A.P. 99% (18000 mL) - Sigma Aldrich, Germany	32.0	2764.00	4.91	714.21	1.27
Ethyleneglicol A.P. 99% (5000 mL) - *Synth*, Brazil	200.0	160.00	6.40	41.34	1.65
$FeCl_3 \cdot 6H_2O$ - *Dinâmica*, Brazil	3.0	83.25	0.49	21.51	0.12
Sodium Acetate (1 kg) - *Química Moderna*, Brazil	3.0	59.00	0.18	15.25	0.05
Anhydrous ethanol A.P. 98-99% (1000 mL) - Dinâmica, Brazil	150.0	21.50	3.23	5.56	0.83
Energy - heater Quimis Q621 600 W (heating to 190 ºC for 6h = 4.8 kWh)	4.8	1.72	8.26	0.44	2.13
Energy agitation - Quimis Q621 600 W (6 h)	6.0	1.72	6.19	0.44	1.60
Total (per 800 mL of GO-(NH)R suspension)			43.18		11.15
TOTAL (per 1 kg adsorbent)			**7489.52**		**1935.28**

The operational cost of each dye removal took into consideration the adsorption capacity reached in the regeneration experiments (for C_0 = 20.0±1.0 $mg \cdot L^{-1}$). This value was chosen according to the standard concentration of dye after coagulation process, which varies from 10 to

20 $mg \cdot L^{-1}$ (WANG *et al*. 2011). Moreover, density values of each adsorbent solution were very near to 5.70 $g \cdot L^{-1}$; and it was applied the official exchange rate of December, 2018 (BRL 3.87/USD). Operational costs in recycling experiments were not calculated for the adsorption of MB and RB by nGO and nGO-NH_2-Fe_3O_4, once recyclability tests were not conducted for nGO nanosorbent.

Table 14 – Operational costs for the adsorption of MB and RB by nGO and nGO-NH_2-Fe_3O_4; cost savings were calculated when considered the nanosorbent recycling.

Nanosorbent	**q (mg MB·g^{-1})**	**Operational cost (USD/kg of dye adsorbed)**	**Operational cost for each cycle* (USD/kg of dye adsorbed)**	**Saving (%)**
		MB		
nGO	38.0	20404	N/A	N/A
nGO-NH_2-Fe_3O_4	100.2	19875	2076	89.55
		RB		
nGO	3.0	258447	N/A	N/A
nGO-NH_2-Fe_3O_4	41.93	47498	8158	82.82

* calculated after 10 cycles of adsortpion-desorption (C_0 ~ 20 $mg \cdot L^{-1}$).

It is important to mention that the operational cost of an adsorbent decreases considerably when it is possible to reuse it in several cycles (Table 14). This is another advantage of nGO-NH_2-Fe_3O_4, in face of it is possibility to being reused for 10 cycles when it is employed to remove MB from aquous solutions. Moreover, it is necessary an indepth investigation of the nGO-NH_2-Fe_3O_4 recyclability when it is employed as adsorbent of real textile wastewaters, since there are many compounds which interact between them and compet with dyes for the active sites of the adsorbent. In this sense, it is expected that the numbers of cycles might decrese if nGO-NH_2-Fe_3O_4 would be applied to treat raw and coagulated textile effluents.

In order to establish a comparative assessment over the efficiency and cost of some adsorbents reported in works published in the literature was carried out based on the costs of raw materials, reactants, additives, transport, and energy consumption according to their reported

methodology (Table 15). This economical assessment was thoroughly carried out over the synthesis and operation with the materials subject of this thesis (nGO and nGO-NH_2-Fe_3O_4) and showed that the cost of nGO-NH_2-Fe_3O_4 production was nearly USD 1900 per kg. However, nGO-NH_2-Fe_3O_4 high regeneration rate allows its reuse in several removal processes, which lowered its operational cost (in USD/kg of adsorbed dye) in 89.6% and 82.8% for MB and RB, respectively. Additionally, a comparative evaluation in terms of costs and adsorption efficiency showed that, despite its lower production costs in some countries (18.95 USD per kg, in Brazil), commercial activated carbon showed an elevated operational cost (1710 USD per kg of removed dye) in the adsorption of Reactive Blue 2 (AL-DEGS *et al*. 2008). Nevertheless, it is 17% lower in comparison to nGO-NH_2-Fe_3O_4. Otherwise, when considering other engineered materials and their efficiencies regarding the adsorption of each reported adsorbates, it is verified elevated operational costs. This is evidenced by economic analysis carried out for ceria hollow spheres as adsorbent of Acid Black 210 (HU; DENG; CHENG, 2017) and KOH-activated-Yellow Mombin biochar as adsorbent of Dianix Royal Blue (BRITO *et al*. 2018). In this comparison, nGO-NH_2-Fe_3O_4 operational cost of the adsorption of RB is substantially lower, 80.6% and 58.7%, respectively. A complete assessment regarding cost analysis is provided in Table 15.

Table 15 – Comparative assessment of efficient and cost of reported adsorbents in published works

Adsorbent, reactants, methodology	Cost (USD/kg)	Dye evaluated	Adsorption capacity (mg/g)	Reg. cycles	Removal cost (USD/kg dye)	Ref.
Activated Carbon (1 kg), Brazil – BRL 60.90/kg	**18.95**	-	N/A		-	Table 12
Activated Carbon (1 kg), (TCI America), US	**358.00**	Reactive Blue 2	208.84	N/A	**1710.00**	Al-Degs *et al*. (2008)
Ceria Hollow Spheres						
Poly(styrene-co-acrylonitrile) (Aldrich) (2g/100g)	4.41					
Cerium Nitrate (III) (Aldrich) - sol (0.434g/125g)	7.67	Acid Black 210	173.60	N/A	**41950.00**	Hu, Deng and Cheng (2017)
Absolute Ethanol ACS (Fisher Sci.) (0.08L/4L) - 80 mL	5.79					
SUB-TOTAL (2.45 g adsorbent)	17.87					
TOTAL (1kg adsorbent)	**7282.26**					
Magnetic Activated Carbon/Coconut shells						
Coconut shells - transport cost (BRL 0.26/ton/km), Brazil	0.00					
$FeCl_3.6H_2O$ (Danica, 500 g), 1:3 wt ratio	17.27	Sunset Yellow	22.30	N/A	**2125.34**	Cazetta *et al*. (2016)
Energy Drying - (110 ºC/48h 2x)	9.41					
Energy - muffle (500 ºC/2h)	0.48					
Energy - muffle (700 ºC/1,5h)	0.36					
TOTAL (1kg adsorbent)	**47.55**					
KOH activated-Yellow Mombin biochar						
Energy grinding - grinder Anton Paar BM500 200 W (10 min)	200					
KOH 90% reactant grade (solid) - 10 kg - Sigma Aldrich. Brazil	100	Dianix® Royal Blue CC	82.28	N/A	**19754.11**	Brito *et al*. (2018)
Energy drying. Oven 105 ºC 600W (24 h)	500					
Energy carbonization. furnace 9000 W (1 h)						
N_2 gas carbonization 50 mL/min. BRL 935/4 m^3 (4000 L)						
SUB-TOTAL (per 50 g)						
TOTAL (1kg adsorbent)	**1625.37**					
Oil palm shell biochar						
Energy drying. Oven 110 ºC 600W (2h)	0.54					
Energy grinding - grinder Anton Paar BM500 200 W (10 min)	4.48	Methylene Blue	20.00	N/A	**1075.00**	Kong *et al*. (2019)
Energy pirolysis. microwave oven Sharp R213CST 900W (20 min)	0.14					
Energy drying. Oven 110 ºC 600W (2h)	6.45					
TOTAL (1kg adsorbent)	**21.50**					

8 CONCLUSIONS AND PERSPECTIVES

In the present work, the novel multilayered amino-Fe_3O_4-functionalized graphene oxide was synthesized and employed as nanosorbent of Methylene Blue (MB) and Remazol Black B (RB). The adsorption of MB and RB by nGO-NH_2-Fe_3O_4 showed adsorptive capacity values considerably higher than nGO (three times and nearly twice higher, for MB and RB, respectively); substantial enhancement is attributed to an increase in π-electron disposal over graphenic plane surface. pH effect evaluation showed that MB adsorption is strongly influenced by pH variation; RB and DR, on the other hand, did not show changes in its adsorption capacity with pH.

Equilibrium experiments showed a maximum adsorption capacity at monolayer (q_m) of 2319.20 $mg \cdot g^{-1}$ (L-F model, n = 1.27), 264.17 $mg \cdot g^{-1}$ (L-F model, n = 1.35) and 219.75 $mg \cdot g^{-1}$ (BET applied for L-S systems) for the removal of MB, RB and DR by nGO-NH_2-Fe_3O_4. Moreover, the adsorption of MB and RB by pristine nGO exhibited maximum adsorptive capacity of 717.30 $mg \cdot g^{-1}$ (Langmuir) and 69.78 $mg \cdot g^{-1}$ (L-F model, n = 2.89), respectively. The values four times greater for maximum adsorptive capacity of nGO-NH_2-Fe_3O_4 in comparison with its precursor nGO is a strong indicative of the enhancement of the adsorptive power by amino-functionalization. Moreover, increase in the maximum adsorption capacity is related to the increase of sorbent-sorbate interfacial relations, in which the main reported interactions were π–π stacking, electrostatic attraction (mostly for MB dye), dipole-dipole and H-bonds (for the reactive RB and DR).

Kinetic experiments revealed that MB adsorption reached the equilibrium state within 5 min, different from RB, which adsorption capacity stabilized after 90 min. The mathematical modeling showed that PSO and PNO models showed the best fit for the experimental data for MB and RB, while Elovich and PNO showed the best fit for DR. Kinetics parameters for adsorptive capacity at equilibrium for MB, RB and DR were 973.51 $mg \cdot g^{-1}$ (PNO), 177.85 $mg \cdot g^{-1}$ (PSO) and 219.17 $mg \cdot g^{-1}$ (PNO), respectively. Kinetic rate constant were $1.35 \cdot 10^{-1}$ $(g \cdot mg \cdot min^{-1})^{1-n}$ (PNO, n = 1.71), $2.40 \cdot 10^{-3}$ $g \cdot mg^{-1} \cdot min^{-1}$ (PSO) and $7.11 \cdot 10^{-1}$ $(g \cdot mg \cdot min^{-1})^{1-n}$ (PNO, n = 7.46) for MB, RB and DR, respectively.

Thermodynamic studies evidenced that the adsorption of all dyes were spontaneous, in which DG^o were (in 298 K): –37.94 $kJ \cdot mol^{-1}$ (MB) and –23.19 $kJ \cdot mol^{-1}$(RB) and –6.28 $kJ \cdot mol^{-1}$ (DR). Moreover, MB adsorption presented exothermic behavior, while RB and DR showed

endothermic behavior. These data evidenced the physisorption nature of MB removal, while RB and DR adsorption showed chemisorptive behavior. Amino-functionalization of nGO nanosheets is pointed as main responsible to enhance MB and RB maximum adsorption capacity in comparison with precursor graphene oxide; this phenomenon is caused by an increase in π–π interactions between the adsorbent and both dyes.

Studies with real textile effluent from laundromats showed satisfactory results of more than 75% in effluent concentration decrease and 55% of its COD, which highlight the great potential of application of nGO-NH_2-Fe_3O_4 in the treatment of raw textile wastewater. Moreover, the main parameters of wastewater for disposal (apparent color, turbidity, COD, BOD and TSS concentration) in water bodies after the treatment by nGO-NH_2-Fe_3O_4 fit the Brazilian legislation CONAMA 430/2011 and the Guidelines for Water Reuse of US Environmental Protection Agency (2012). In this sense, despite of several works which deal with the use of graphene nanocomposites in the adsorption of textile dyes, there is a lack of literature towards the investigation of the efficiency of graphene and its nanoderivatives in the treatment of real textile wastewaters. This consists nowadays in one of the knowledge gaps in this field.

It was thoroughly discussed about the reasons why to employ some functionalization routes, which aims to facilitate the separation process after pollutant adsorption in aqueous medium. Among them, the grafting of MNPs (Fe_3O_4, α–Fe_3O_4, γ–Fe_3O_4) on graphene; functionalized graphene decorated over polymeric matrices; and functional GO anchored over charcoal and biomass fibers; and graphene-silica-derived composites. Other methods, on the other hand, aim to boost graphene with catalytic properties, as can be seen by the anchoring of TiO_2 nanoparticles over GO and the doping of different graphene nanostructures with Au, Pt and Pd. The high regeneration capacity of these sorbents is another improvement promoted by functionalization; some works have reported outstanding sorbent regeneration rate, even after ten cycles, as observed in the adsorption of MB by nGO-NH_2-Fe_3O_4.

In this work, nGO-NH_2 was supported in charcoal produced from the gasification of wood residues and it was applied in the adsorption of MB and RB. Kinetics experiments showed that the equilibrium state was reached within 10 min for MB, with equilibrium adsorption capacity of 25.81 $mg \cdot g^{-1}$, PNO model was sucessfully fitted to experimental data (R^2 0.9999). Equilibrium studies were carried out and showed that L-F model was the one which best fitted to experimental data, maximum monolayer adsorption capacity was 50.07 $mg \cdot g^{-1}$.

The expensive costs related to materials synthesis is the main drawback to use of graphene-derived nanomaterials as adsorbents of textile wastewaters. Moreover, the scale-up of these processes remain challenging. In this work is reported the production cost of nGO-NH_2-Fe_3O_4 of USD 1935.28/kg, whilst the operational cost in MB adsorption was USD 2076.00/kg of removed MB and USD 8158.00/kg of removed RB, considering the regeneration cycles of these dyes. Moreover, economic evaluation revealed that nGO-NH_2-Fe_3O_4 possesses an elevated cost of production when compared with other classical adsorbents. Nevertheless, the use of nGO-NH_2-Fe_3O_4 consists in a long-term profitable alternative to textile wastewater treatments, due to its high sorption capacity and recyclability, which decrease the operational costs (USD/kg of removed dye). Moreover, these costs tend to be reversed once the technology to produce graphene nanosheets in large scale is fully mastered.

Researchers must drive their efforts to the investigation of non-aggressive and environmentally friend compounds in their synthesis, since most of the current functionalization routes employs chemicals which generate toxic by-products. It can be found in the literature some works which report innovative protocols of functionalization with bio-compounds, such plant extracts, biomass fibers and natural reactants. Synthesis protocols must also be updated in order to avoid great consumption of water and energy. In this sense, novel techniques for conducting reactions in environmental and mild conditions are most welcome.

Despite the aforementioned challenges, great adsorptive capacities of nGO-NH_2-Fe_3O_4 were identified for the three dyes investigated in this thesis, as well as high regeneration rate, with the exception of DR dye. These parameters, as well as facile separation from aqueous medium, have been reached through amino-functionalization of nGO. These achievements point to great prospects for the employment of functionalized graphene as adsorbents; either by optimization of the synthesis processes, or by the possibility of reuse of these adsorbents in multiple cycles.

REFERENCES

1. AHMAD, I.; SHUKRULLAH, S.; AHMAD, M.; AHMED, E.; NAZ, M. Y.; AKHTAR, M. S.; KHALID, N. R.; HUSSAIN, A.; HUSSAIN, I. Effect of Al doping on the photocatalytic activity of ZnO nanoparticles decorated on CNTs and graphene: Solvothermal synthesis and study of experimental parameters. **Materials Science in Semiconductor Processing**, v. 123, n. 105584, 2021.

2. AI, L. H.; ZHANG, C. Y.; CHEN, Z. Y. Removal of methylene blue from aqueous solution by a solvothermal-synthesized graphene/magnetite composite. **Journal of Harzardous Materials,** v. 192, p. 1515–1524, 2011.

3. ALAYANDE, A. B.; PARK, H.-D.; VROUWENVELDER, J. S.; KIM, I. S. Implications of chemical reduction using hydriodic acid on the antimicrobial properties of graphene oxide and reduced graphene oxide membranes. **Small**, v. 15 (28), n. 1901023, 2019.

4. AL-DEGS, Y. S.; EL-BARGHOUTHI, M. I.; EL-SHEIKH, A. H.; WALKER, G. M. Effect of solution pH, ionic strength, and temperature on adsorption behavior of reactive dyes on activated carbon. **Dyes and Pigments**, v. 77, p. 16–23, 2008.

5. ALLEN, S. J.; MCKAY, G.; PORTER, J. F. Adsorption isotherm models for basic dye adsorption by peat in single and binary component systems. **Journal of Colloid and Interface Sciences**, v. 280, p. 322–333, 2004.

6. APHA – American Public Health Association. **Standard Methods for the Examination of Water and Wastewater (Part 1000-3000).** Washington, DC: APHA, 1999.

7. ARAÚJO, C. M. B.; ASSIS FILHO R. B.; BAPTISTTELLA, A. M. S.; NASCIMENTO, G. F. O.; DA COSTA, G. R. B.; CARVALHO, M. N.; GHISLANDI, M.; DA MOTTA SOBRINHO, M. A. Systematic study of graphene oxide production using factorial design techniques and its application to the adsorptive removal of methylene blue dye in aqueous medium. **Materials Research Express**, v. 5(6), p. 65042, 2018.

8. ARAÚJO, C. M. B.; NASCIMENTO, G. F. O.; DA COSTA, G. R. B.; DA SILVA, K. S.; BAPTISTTELLA, A. M. S.; GHISLANDI, M. G.; DA MOTTA SOBRINHO, M. A. Adsorptive removal of dye from real textile wastewater using graphene oxide produced via modifications of hummers method. **Chemical Engineering Communications**, v. 206 (11), p. 1375–1387, 2019.

9. ARAÚJO, C.M.B.; NASCIMENTO, G.F.O.; COSTA, G.R.B.; BAPTISTTELLA, A.M.S.; FRAGA, T.J.M.; ASSIS FILHO, R.B.; GHISLANDI, M.G.; DA MOTTA SOBRINHO, M.A. Real textile wastewater treatment using nano graphene-based materials: Optimum pH, dosage, and kinetics for colour and turbidity removal. **Canadian Journal of Chemical Engineering**, v. 98(7), p. 1429–1440, 2020.

10. ARAUJO, P. T.; TERRONES, M.; DRESSELHAUS, M. S. Defects and impurities in graphene-like materials. **Materials Today**, v. 15 (3), p. 98–109, 2012.

11. ASSIS FILHO, R. B.; ARAÚJO, C. M. B.; BAPTISTTELLA, A. M. S.; BATISTA, E. B.; BARATA, R. A.; GHISLANDI, M. G.; DA MOTTA SOBRINHO, M. A. Environmentally friendly route for graphene oxide production via electrochemical synthesis focused on the adsorptive removal of dyes from water. **Environmental Technology**, v. 41 (21), p. 2771–2782, 2020.

12. AZIZI, N.; SAIDI, M. S. Highly Chemoselective Addition of Amines to Epoxides in Water. **Organic Letters**, v. 7 (17), p. 3649–3651, 2005.

13. BAGUR-GONZÁLEZ, M. G.; ESTEPA-MOLINA, C.; MARTÍN-PEINADO, F.; MORALES-RUANO, S. Toxicity assessment using *Lactuca sativa L*. bioassay of the metal(loid)s As, Cu, Mn, Pb and Zn in soluble-in-water saturated soil extracts from an abandoned mining site. **Journal of Soils and Sediments**, v. 11, p. 281–289, 2011.

14. BANERJEE, P.; SAU, S.; DAS, P.; MUKHOPADHAYAY, A. Optimization and modelling of synthetic azo dye wastewater treatment using graphene oxide nanoplatelets: characterization toxicity evaluation and optimization usingartificial neural network. **Ecotoxicology and Environmental Safety**, v. 119, p. 47–57, 2015.

15. BAPTISTTELLA, A. M. S.; ARAÚJO, C. M. B.; DA SILVA, M. P.; DO NASCIMENTO, G. F. O.; DA COSTA, G. R. B.; DO NASCIMENTO, B. F.; GHISLANDI, M. G.; DA MOTTA SOBRINHO, M. A. Magnetic Fe_3O_4-graphene oxide nanocomposite – synthesis and practical application for the heterogeneous photo-Fenton degradation of different dyes in water. **Separation Science and Technology**, v. 56 (2), p. 425–438, 2021.

16. BARIŞÇI, S.; TURKAY, O.; DIMOGLO, A. **Review on Greywater Treatment and Dye Removal from Aqueous Solution by Ferrate (VI)**. In: Ferrites and Ferrates: Chemistry and Applications in Sustainable Energy and Environmental Remediation. Cap. 14, pp. 349–409. ACS Symposium Series, v. 1238, Washington-DC: ACS, 2016.

17. BAYANTONG, A. R. B.; SHIH, Y.-J.; ONG, D. C.; ABARCA, R. R. M.; DONG, C.-D.; DE LUNA, M. D. G. Adsorptive removal of dye in wastewater by metal ferrite-enabled graphene oxide nanocomposites. **Chemosphere**, v. 274, n. 129518, 2021.

18. BHUNIA, P.; HWANG, E.; MIN, M.; LEE, J.; SEO, S.; SOME, S.; LEE, H. A non-volatile memory device consisting of graphene oxide covalently functionalized with ionic liquid. **Chemical Communications**, v. 48, p. 913–915, 2012.

19. BILAL, M.; RASHEED, T.; IQBAL, H.M.N.; HU, H.; WANG, W.; ZHANG, X. Toxicological Assessment and UV/TiO_2-Based Induced Degradation Profile of Reactive Black 5 Dye. **Environmental Management**, v. 61, p. 171–180, 2018.

20. BLAKE, P.; HILL, E. W.; CASTRO NETO, A. H.; NOVOSELOV, K. S.; JIANG, D.; YANG, R.; BOOTH, T. J.; GEIM, A. K. Making graphene visible. **Applied Physics Letters**, v. 91, n. 063124, 2007.

21. BRAZIL: Ministério do Meio Ambiente, "**Ministry of Environment"** (*in Portuguese*). **Resolução n. 430, Resolution 430** (*in Portuguese*). Brasília, 2011.

22. BRITO, M. J. P.; VELOSO, C. M.; SANTOS, L. S.; BONOMO, R. C. F.; FONTAN, R. C. I. Adsorption of the textile dye Dianix® royal blue CC onto carbons obtained from yellow mombin fruit stones and activated with KOH and H_3PO_4: kinetics, adsorption equilibrium and thermodynamic studies. **Powder Technology**, v. 339, p. 334–343, 2018.

23. BRODIE, B.C. Hydration behavior and dynamics of water molecules in graphite oxide. **Annalen Chimie Physics**, v. 59, p. 466–472, 1860.

24. BRUNAUER, S.; EMMETT, P. H.; TELLER, E. Adsorption of gases in multimolecular layers. **Journal of the American Chemical Society**, v. 60 (2), p. 309–319, 1938.

25. BUENO, R. A.; MARTÍNEZ, J. I.; LUCCAS, R. F.; DEL ÁRBOL, N. R.; MUNUERA, C.; PALACIO, I.; PALOMARES, F. J.; LAUWAET, K.; THAKUR, S.; BARANOWSKI, J. M.; STRUPINSKI, W.; LÓPEZ, M. F.; MOMPEAN, F.; GARCÍA-HERNÁNDEZ, M.; MARTÍN-GAGO, J. A. Highly selective covalent organic functionalization of epitaxial graphene. **Nature Communications**, v.8, n. 15306, 2017.

26. CAI, N.; CASANOVA, L. Application of positive-charged ethylenediamine-functionalized graphene for the sorption of anionic organic contaminants for water. **Journal of Environmental Chemical Engineering**, v. 4, p. 2941–2951, 2016.

27. CALIMAN, C. C.; MESQUITA, A. F.; CIPRIANO, D. F.; FREITAS, J. C. C.; COTTA, A. A. C.; MACEDO, W. A. A.; PORTO, A. O. One-pot synthesis of amine-functionalized graphene oxide by microwave-assisted reactions: an outstanding alternative for supporting materials in supercapacitors. **RSC Advances**, v. 8, p. 6136–6145, 2018.

28. CARVALHO, M. N.; ABREU, C. A. M.; BENACHOUR, M.; SALES, D. C. S.; BARAÚNA, O. S.; DA MOTTA SOBRINHO, M. A. Applying combined Langmuir–Freundlich model to the multi-component adsorption of BTEX and phenol on smectite clay. **Adsorption Science and Technology**, v. 30 (8-9), p. 691-699, 2012.

29. CARVALHO, M. N.; DA SILVA, K. S.; SALES, D. C. S.; FREIRE, E. M.; SOBRINHO, M. A. M.; GHISLANDI, M. G. Dye removal from textile industrial effluents by adsorption on exfoliated graphite nanoplatelets: kinetic and equilibrium studies. **Water Science and Technology**, v. 73 (9), p.2189–2198, 2016.

30. CASIRAGHI, C.; HARTSCHUH, A.; QIAN, H.; PISCANEC, S.; GEORGI, C.; FASOLI, A.; NOVOSELOV, K. S.; BASKO, D. M.; FERRARI, A. C. Raman Spectroscopy of Graphene Edges. **Nano Letters**, v. 9(4), p. 1433–1441, 2009.

31. CASIRAGHI, C.; HARTSCHUH, A.; LIDORIKIS, E.; QIAN, H.; HARUTYUNYAN, H.; GOKUS, T.; NOVOSELOV, K. S.; FERRARI, A. C. Rayleigh Imaging of Graphene and Graphene Layers. **Nano Letters**, v. 7(9), p. 2711–2717, 2007.

32. CAZETTA A. L., PEZOTI O., BEDIN K. C., SILVA T. L., PAESANO JUNIOR A., ASEFA T., ALMEIDA V. C. Magnetic activated carbon derived from biomass waste by concurrent synthesis: efficient adsorbent for toxic dyes. **ACS Sustainable Chemistry and Engineering**, v. 4 (3), p. 1058 – 1068, 2016.

33. CAVALCANTE, Paula. **Indústrias de beneficiamento de peças em jeans investem em reuso da água.** Reportagem de 22 Mai. 2015 para o G1 Caruaru e Toritama. "Industries for the processing of garments in jeans invest in the reuse of water. Report of May 22nd, 2015 to G1 Caruaru and Toritama" (in Portuguese). Available in: <http://g1.globo.com/pe/caruaru-regiao/noticia/2015/05/industrias-de-beneficiamento-de-pecas-em-jeans-investem-em-reuso-da-agua.html>. Accessed on Feb. 27th, 2018.

34. CHAILEK, N.; DARANARONG, D.; PUNYODOM, W.; MOLLOY, R.; WORAJITTIPHON, P. Crosslinking assisted fabrication of ultrafine poly(vinyl alcohol)/functionalized graphene electrospun nanofibers for crystal violet adsorption. **Journal of Applied Polymer Science**, v. 135 p. 46318–46331, 2018.

35. CHANG, Raymond; THOMAN JR., John W. **Physical Chemistry for the Chemical Sciences**, South Orange: University Science Books, 2014, 698p.

36. CHEN, L.; HAN, Q.; LI, W.; ZHOU, Z.; FANG, Z.; XU, Z.; WANG, Z.; QIAN, X. Three-dimensional graphene-based adsorbents in sewage disposal: a review. **Environmental Science and Pollution Research**, v. 25 (26), p. 25840–25861, 2018.

37. CHEN, L.; LI, Y.; HU, S.; SUN, J.; DU, Q.; YANG, X.; JI, Q.; WANG, Z.; WANG, D.; XIA, Y. Removal of methylene blue from water by cellulose/graphene oxide fibres. **Journal of Experimental Nanoscience**, v. 11 (14), p. 1156–1170, 2016.

38. CHEN, X.; ZHU, Y.-B.; YU, H.; LIU, J. Z.; EASTON, C. D.; WANG, Z.; HU, Y.; XIE, Z.; WU, H.-A.; ZHANG, X.; LI, D.; WANG, H. Ultrafast water evaporation through graphene membranes with subnanometer pores for desalination. **Journal of Membrane Science**, v. 621, n. 118934, 2021.

39. CHEN, Y.; WANG, Z.; LI, X.; YAO, X.; WANG, C.; LI, Y.; XUE, W.; YU, D.; KIM, S. Y.; YANG, F.; KUSHIMA, A.; ZHANG, G.; HUANG, H.; WU, N.; MAI, Y.-W.; GOODENOUGH, J. B.; LI, J. Li metal deposition and stripping in a solid-state battery via Coble creep. **Nature**, v. 578, p. 251–255, 2020.

40. CHO, C.-W.; PREISS, U.; JUNGNICKEL, C.; STOLTE, S.; ARNING, J.; RANKE, J.; KLAMT, A.; KROSSING, I.; THÖMING, J. Ionic Liquids: Predictions of physicochemical properties with experimental and/or DFT-Calculated LFER parameters to understand molecular interactions in solution. **The Journal of Physical Chemistry B**, v. 115, p. 6040–6050, 2011.

41. CHOI, Y. S.; YEO, C.-S.; KIM, S. J.; LEE, J.-Y.; KIM, Y.; CHO, K. R.; JU, S.; HONG, B. H.; PARK, S. Y. Multifunctional reduced graphene oxide-CVD graphene core–shell fibers. **Nanoscale**, v. 11, p. 12637-12642, 2019.

42. CHUA, C. K.; PUMERA, M. Chemical reduction of graphene oxide: a synthetic chemistry viewpoint. **Chemical Society Reviews**, v. 43, p. 291–312, 2014.

43. CHUA, C. K.; PUMERA, M. Covalent chemistry on graphene. **Chemical Society Reviews**, v. 42, p. 3222–3234, 2013.

44. COHEN-TANUGI, D.; LIN, L.-C.; GROSSMAN, J. C. Multilayer nanoporous graphene membranes for water desalination, **Nano Letters**, v. 16, p. 1027–1033, 2016.

45. CZEPA, W.; PAKULSKI, D.; WITOMSKA, S.; PATRONIAK, V.; CIESIELSKI, A.; SAMORÌ, P. Graphene oxide-mesoporous SiO_2 hybrid composite for fast andefficient removal of organic cationic contaminants. **Carbon**, v. 158, p. 193–201, 2020.

46. DA SILVA, M. P.; DE SOUZA, Z. S. B.; CAVALCANTI, J. V. F. L.; FRAGA, T. J. M.; DA MOTTA SOBRINHO, M. A.; GHISLANDI, M. G. Adsorptive and photocatalytic activity of Fe_3O_4-functionalized multilayer graphene oxide in the treatment of industrial textile wastewater. **Environmental Science and Pollution Research** (*in press*), 2021. https://doi.org/10.1007/s11356-020-10926-6

47. DAI, L.; CHANG, D. W.; BAEK, J. B.; LU, W. Carbon nanomaterials for advanced energy conversion and storage. **Small**, v. 8, p. 1130–1166, 2012.

48. DANILOV, M. O.; RUSETSKII1, I. A.; SLOBODYANYUK, I. A.; DOVBESHKO, G. I.; KHYZHUN, O. Y.; STRELCHUK, V. V.; KOLBASOV, G. Y. A Facile Electrochemical Method for Graphene Nanoplatelets Preparation Using Multi-walled Carbon Nanotubes. **Fuel Cells**, v. 19 (3), p. 202-210, 2019.

49. DAS, T.R.; PATRA, S.; MADHURI, R.; SHARMA, P.K. Bismuth oxide decorated graphene oxide nanocomposites synthesized via sonochemical assisted hydrothermal method for adsorption of cationic organic dyes. **Journal of Colloid and Interface Science**, v. 509, p. 82–93, 2018.

50. DAS, P.; MAI, V. C.; DUAN H. Flexible Bioinspired Ternary Nanocomposites Based on Carboxymethyl Cellulose/Nanoclay/Graphene Oxide. **ACS Applied Polymer Materials**, v. 1, p. 1505–1513, 2019.

51. DAWOOD, S.; SEN, T.K.; PHAN, C. Performance and dynamic modelling of biochar and kaolin packed bed adsorption column for aqueous phase methylene blue (MB) dye removal. **Environmental Technology**, v. 40(28), p. 3762–3772, 2019.

52. DE OLIVEIRA, E. H. C.; MARQUES FRAGA, D. M. S.; DA SILVA, M. P.; FRAGA, T. J. M.; CARVALHO, M. N.; FREIRE, E. M. P. L.; GHISLANDI, M. G.; DA MOTTA SOBRINHO, M. A. Removal of toxic dyes from aqueous solution by adsorption onto

highly recyclable xGnP® graphite nanoplatelets. **Journal of Environmental Chemical Engineering**, v. 7, n. 103001, 2019.

53. DE SILVA, K. K. H.; HUANG, H.-H.; JOSHI, R. K.; YOSHIMURA, M. Chemical reduction of graphene oxide using green reductants. **Carbon**, v. 119, p. 190–199, 2017.

54. DHAR, L.; HOSSAIN, S.; RAHMAN, M. S.; QURAISHI, S. B.; SAHA, K.; RAHMAN, F.; RAHMAN, M. T. Adsorption Mechanism of Methylene Blue by Graphene Oxide-Shielded Mg–Al-Layered Double Hydroxide from Synthetic Wastewater. **The Journal of Physical Chemistry A**, v. 125 (4), p. 954–965, 2021.

55. DIRAKI, A.; MACKEY, H.; McKAY, G.; ABDALA, A. Removal of oil from oil–water emulsions using thermally reduced graphene and graphene nanoplatelets. **Chemical Engineering Research and Design**, v. 137, p. 47–59, 2018.

56. DOTTO, G. L.; MCKAY, G. Current scenario and challenges in adsorption for water treatment. **Journal of Environmental Chemical Engineering**, v. 8, n. 103988, 2020.

57. EBADI, A.; MOHAMMADZADEH, J.S.S.; KHUDIEV, A. What is the correct form of bet isotherm for modeling liquid phase adsorption? **Adsorption**, v. 15, p. 65–73, 2009.

58. EIGLER, S.; HIRSCH, A. Chemistry with graphene and graphene oxide – challenges for synthetic chemists, **Angewandte Chemie International Edition**, v. 53, p. 2–21, 2014.

59. EIGLER, S.; HOF, F.; ENZELBERGER-HEIM, M.; GRIMM, S.; MÜLLER, P.; HIRSCH, A. Statistical Raman Microscopy and Atomic Force Microscopy on Heterogeneous Graphene Obtained after Reduction of Graphene Oxide. **Journal of Physical Chemistry C**, v. 118, p. 7698−7704, 2014.

60. EL FARISSI, H.; LAKHMIRI, R.; ALBOURINE, A.; SAFI, M.; CHERKAOUI, O. Adsorption study of charcoal of cistus ladaniferus shell modified by H_3PO_4 and NaOH used as a low-cost adsorbent for the removal of toxic reactive red 23 dye: Kinetics and thermodynamics. **Materials Today:** Proceedings (*in press*), 2020. https://doi.org/10.1016/j.matpr.2020.10.438

61. ENGLERT, J. M.; DOTZER, C.; YANG, G.; SCHMID, M.; PAPP, C.; J. GOTTFRIED, M.; HANS-PETER STEINRÜCK, H.-P.; SPIECKER, E.; HAUKE, F.; HIRSCH, A. Covalent bulk functionalization of graphene. **Nature Chemistry**, v. 3, p. 279–286, 2011.

62. ERSAN, G.; APUL, O. G.; PERREAULT, F.; KARANFIL, T. Adsorption of organic contaminants by graphene nanosheets: A review. **Water Research**, v. 126, p. 385–398, 2017.

63. FAN, Y.; WANG, B.; YUAN, S.; WU, X.; CHEN, J.; WANG, L. Adsorptive removal of chloramphenicol from wastewater by NaOH modified bamboo charcoal. **Bioresource Technology**, v. 101 (19), p. 7661–7664, 2010.

64. FANG, M.; WANG, K.; LU, H.; YANG, Y.; NUTT, S. Covalent polymer functionalization of graphene nanosheets and mechanical properties of composites. **Journal of Materials Chemistry**, v. 19, p. 7098–7105, 2009.

65. FARIAS, Maria Mariah M. W. E. C. **Aproveitamento de águas de chuva por telhados: aspectos quantitativos e qualitativos, "Roof rainwater utilization: quantitative and qualitative aspects"** (*in Portuguese*)**.** Master Dissertation. Caruaru, PE: UFPE, 2012.

66. FENG, Y.; LIU, H.; LUO, W.; LIU, E.; ZHAO, N.; YOSHINO, K.; FENG, W. Covalent functionalization of graphene by azobenzene with molecular hydrogen bonds for long-term solar thermal storage. **Scientific Reports**, v. 3, p. 1–8, 2013.

67. FERRARI, A. C.; BASKO, D. M. Raman spectroscopy as a versatile tool for studying the properties of graphene. **Nature Nanotechnology**, v. 8, p. 235–246, 2013.

68. FERRARI, A.C.; MEYER, J.; SCARDACI, V.; CASIRAGHI, C.; LAZZERI, M.; MAURI, F.; PISCANEC, S.; JIANG, D.; NOVOSELOV, K.S.; ROTH, S.; GEIM, A.K. Raman spectrum of graphene and graphene layers. **Physical Review Letters**, v. 97 (18), p.187401, 2006.

69. FOO, K.Y.; HAMEED, B.H. Insights into the modeling of adsorption isotherm systems. **Chemical Engineering Journal**, v. 156 (1), p. 2–10, 2010.

70. FRAGA, T. J. M.; DE LIMA, L. E. M.; SOUZA, Z. S. B.; CARVALHO, M. N.; FREIRE, E. M. P. L.; GHISLANDI, M. G.; DA MOTTA, M. A. Amino-Fe_3O_4-functionalized graphene oxide as a novel adsorbent of Methylene Blue: kinetics, equilibrium, and recyclability aspects. **Environmental Science and Pollution Research**, v. 26, p. 28593–28602, 2018.

71. FRAGA, T. J. M.; CARVALHO, M. N.; GHISLANDI, M. G.; DA MOTTA SOBRINHO, M. A. Functionalized graphene-based materials as innovative adsorbents of organic pollutants: a concise overview. **Brazilian Journal of Chemical Engineering**, v. 36, p. 1 – 31, 2019a.

72. FRAGA, T. J. M.; SOUZA, Z. S. B.; FRAGA, D. M. S. M.; CARVALHO, M. N.; FREIRE, E. M. P. L.; GHISLANDI, M. G.; DA MOTTA SOBRINHO, M. A. Comparative approach towards the adsorption of Reactive Black 5 and Methylene Blue by n-layer graphene oxide and its amino-functionalized derivative. **Adsorption**, v. 26, p. 283–301, 2019b.

73. FRAGA, T. J. M.; GHISLANDI, M. G.; CARVALHO, M. N.; DA MOTTA SOBRINHO, M. A. One step forward: How can functionalization enhance the adsorptive properties of graphene towards metallic ions and dyes? **Environmental Research**, v. 184, n. 109362, 2020a.

74. FRAGA, T. J. M.; CARVALHO, M. N.; MARQUES FRAGA, D. M. S.; DA SILVA, M. C. L.; FERREIRA, J. M.; DA MOTTA SOBRINHO, M. A. Treated residue from

aluminium lamination as adsorbent of toxic reactive dyes – a kinetic, equilibrium and thermodynamic study. **Environmental Technology**, v. 41 (6), p. 669–681, 2020b.

75. FRAGA, T. J. M.; DA SILVA, L. F. F.; DE LIMA FERREIRA, L. E. M.; DA SILVA, M. P.; MARQUES FRAGA, D. M. S.; ARAÚJO, C. M. B.; CARVALHO, M. N.; CAVALCANTI, J. V. F. L.; GHISLANDI, M. G.; DA MOTTA SOBRINHO, M. A. Amino-Fe_3O_4-functionalized multi-layered graphene oxide as an ecofriendly and highly effective nanoscavenger of the reactive drimaren red. **Environmental Science and Pollution Research**, v. 27, p. 9718–9732, 2020c.

76. GANESAN, V.; LOUIS, C.; DAMODARAN, S. P. Graphene oxide-wrapped magnetite nanoclusters: a recyclable functional hybrid for fast and highly efficient removal of organic dyes from wastewater. **Journal of Environmental Chemical Engineering**, v. 6 (2), p. 2176–2190, 2018.

77. GAO, B.; HU, C.; FU, H.; SUN, Y.; LI, K.; HU, L. Preparation of single-layer graphene based on a wet chemical synthesis route and the effect on electrochemical properties by double layering surface functional groups to modify graphene oxide. **Electrochimica Acta**, v. 361, n. 137053, 2020.

78. GAO, T.; YU, J.; ZHOU, Y.; JIANG, X. The synthesis of graphene oxide functionalized with dithiocarbamate group and its prominent performance on adsorption of lead ions. **Journal of Taiwan Institute of Chemical Engineers**, v. 71, p. 426–432, 2017.

79. GAO, Z.; ZHU, J.; RAJABPOUR, S.; JOSHI, K.; KOWALIK, M.; CROOM, B.; SCHWAB, Y.; ZHANG, L.; BUMGARDNER, C.; BROWN, K. R.; BURDEN, D.; KLETT, J. W.; VAN DUIN, A. C. T.; ZHIGILEI, L. V.; LI, X. Graphene reinforced carbon fibers. **Science Advances**, vol. 6, n. 17, p. eaaz4191, 2020.

80. GE, H.; WANG, C.; LIU, S.; HUANG, Z. Synthesis of citric acid functionalized magnetic graphene oxidized coated corn straw for Methylene Blue adsorption. **Bioresource Technology**, v. 221, p. 419–429, 2016.

81. GEORGAKILAS, V.; TIWARI, J. N.; KEMP, K. C.; PERMAN, J. A.; BOURLINOS, A. B.; KIM, K. S.; ZBORIL, R. Noncovalent functionalization of graphene and graphene oxide for energy materials, biosensing, catalytic, and biomedical applications. **Chemical Reviews**, v. 116 (9), p.5464−5519, 2016.

82. GEVAERD, A.; WATANABE, E. Y.; FERNANDES, K.; PAPI, M. A. P.; BANKS, C. E.; BERGAMINI, M. F.; MARCOLINO-JUNIOR, L. H. Electrochemically reduced graphene oxide as screen-printed electrode modifier for fenamiphos determination. **Electroanalysis**, v. 32 (8), p. 1689–1695, 2020.

83. GHISLANDI, M.; TKALYA, E.; ALEKSEEV, A.; KONING, C.; DE WITH, G. Electrical conductive behavior of polymer composites prepared with aqueous graphene dispersions. **Applied Materials Today**, v. 1, p. 88-94, 2015.

84. GILES, C.H.; SMITH, D.; HUITSON, A.A. General treatment and classification of the solute adsorption isotherm. **I. Theoretical Journal of Colloid and Interface Science**, v. 47, p. 755–765, 1974.

85. GOHARIBAJESTANI, Z.; YÜRÜM, A.; YÜRÜM, Y. Effect of transition metal oxide nanoparticles on gas adsorption properties of graphene nanocomposites. **Applied Surface Science**, v. 475, p. 1070–1076, 2019.

86. GONÇALVES, M.; CASTRO, C.S.; OLIVEIRA, L.C.A.; GUERREIRO, M.C. Sintese e caracterização de nanopartículas de óxido de ferro suportadas em matriz carbonácea: remoção do corante orgânico Azul de Metileno em água, "Synthesis and characterization of iron oxide nanoparticles supported on carbonaceous matrix: removal of organic dye Methylene Blue in water" (*in Portuguese*). **Química Nova**, v. 32, p. 1723–1726, 2009.

87. GONZÁLEZ, J.A.; VILLANUEVA, M.E.; PIEHL, L.L.; COPELLO, G.J. Development of a chitin/graphene oxide hybrid composite for the removal of pollutant dyes: adsorption and desorption study. **Chemical Engineering Journal**, v. 280, p. 41–48, 2015.

88. GOSCIANSKA, J.; FATHY, N. A.; ABOELENIN, R. M. M. Adsorption of solophenyl red 3BL polyazo dye onto amine-functionalized mesoporous carbons. **Journal of Colloid and Interface Science**, v. 505, p. 593–604, 2017.

89. GRAJEK, H. Regeneration of Adsorbents by the Use of Liquid, Subcritical and Supercritical Carbon Dioxide. **Adsorption Science and Technology**, v. 18 (4), p. 347–371, 2000.

90. GREGORY, Peter. **Classification of Dyes by Chemical Structures**, in: The Chemical and Application of Dyes, edited by David R. Waring and Geoffrey Hallas. New York: Springer, 1990. 414p.

91. GU, X.; ZHAO, Y.; SUN, K.; VIEIRA, C. L. Z.; JIA, Z.; CUI, C.; WANG, Z.; WALSH, A.; HUANG, S. Method of ultrasound-assisted liquid-phase exfoliation to prepare graphene. **Ultrasonics Sonochemistry**, v. 58, n. 104630, 2019.

92. GUARATINI, C.C.I.; ZANONI, M.V.B. Corantes têxteis, "Textile dyes" (*in Portuguese*). **Química Nova**, v. 23 (1), p. 71–78, 2000.

93. GUO, Z.; XIE, C.; ZHANG, P.; ZHANG, J.; WANG, G.; HE, X.; MA, Y.; ZHAO, B.; ZHANG, Z. Toxicity and transformation of graphene oxide and reduced graphene oxide in bacteria biofilm. **Science of The Total Environment**, v. 580, p. 1300–1308, 2017.

94. GUO, L.Q.; YE, P.R.; WANG, J.; FU, F.F.; WU, Z.J. Three-dimensional Fe3O4-graphene macroscopic composites for arsenic and arsenate removal. **Journal of Hazardous Materials**, v. 298, p. 28–35, 2015.

95. HABIBI, N. Preparation of biocompatible magnetite-carboxymethyl cellulose nanocomposite: Characterization of nanocomposite by FTIR, XRD, FESEM and TEM.

Spectrochimica Acta Part A: Molecular and Biomolecular Spectroscopy, v. 131, p. 55–58, 2014.

96. HAN, S.; LIU, K.; HU, L.; TENG, F.; YU, P.; ZHU, Y. Superior Adsorption and Regenerable Dye Adsorbent Based on Flower-Like Molybdenum Disulfide Nanostructure. **Scientific Reports**, v. 7, n. 43599, 2017.

97. HASHEMI, S. A.; RAMAKRISHNA, S.; ABERLE, A. G. Recent progress in flexible–wearable solar cells for self-powered electronic devices. **Energy and Environmental Sciences**, v. 13, p. 685–743, 2020.

98. HO, Y. S.; McKAY, G. Pseudo-second order model for sorption processes. **Process Biochemistry**, v. 34 (5), p. 451-465, 1999.

99. HO, Y. S.; CHIU, W.-T.; WANG, C.-C. Regression analysis for the sorption isotherms of basic dyes on sugarcane dust. **Bioresource Technology**, v. 96, p. 1285–1291, 2005.

100. HORROCKS, A. Richards; ANAND, Subhash C. **Handbook of Technical Textiles**. Cambridge: Woodhead Publishing, 2000. 677p.

101. HU, J.; DENG, W.; CHEN, D. Ceria Hollow spheres as an adsorbent for efficient removal of acid dye. **ACS Sustainable Chemistry and Engineering**, v. 5 (4), p. 3570-3582, 2017.

102. HU, W.; PENG, C.; LUO, W.; LV, M; LI, X.; LI, D.; HUANG, Q.; FAN, C. Graphene-Based Antibacterial Paper. **ACS Nano**, v. 4 (7), p 4317–4323, 2010.

103. HU, X.; ZHOU, Q. Health and Ecosystem Risks of Graphene. **Chemical Reviews**, v. 113 (5), p. 3815–3835, 2013.

104. HUANG, J.; YAN, Z. Adsorption mechanism of oil by resilient graphene aerogels from oil-water emulsion. **Langmuir**, v. 34 (5), pp 1890-1898, 2018.

105. HUANG, L.; JIN, Y.; SUN, L.; CHEN, F.; FAN, P.; ZHONG, M.; YANG, J. Graphene oxide functionalized by poly(ionic liquid)s for carbon dioxide capture. **Journal of Applied Polymer Sciences**, v. 134 (11), n. 44592, 2016,

106. HUANG, W.; CHEN, J.; ZHANG, J. Adsorption characteristics of methylene blue by biochar prepared using sheep, rabbit and pig manure. **Environmental Science and Pollution Research**, v. 25 (29), p. 29256–29266, 2018.

107. HUANG, Y.; TANG, J.; GAI, L.; GONG, Y.; GUAN, H.; HE, R.; LYU, H. Different approaches for preparing a novel thiol-functionalized graphene oxide/Fe-Mn and its application for aqueous methylmercury removal. **Chemical Engineering Journal**, v. 319, p. 229–239, 2017.

108. HUBER, F.; BERWANGER, J.; POLESYA, S.; MANKOVSKY, S.; EBERT, H.; GIESSIBL, F. J. Chemical bond formation showing a transition from physisorption to chemisorption. **Science**, v. 366, p. 235–238, 2019.

109. HUMMERS, W. S.; OFFEMAN, R. E. Preparation of Graphitic Oxide. **Journal of the American Chemical Society**, v. 80 (6), p. 1339–1339, 1958.

110. IM, K.; NGUYEN, D. N.; KIM, S.; KONG, H. J.; KIM, Y.; PARK, C. S.; KWON, O. S.; YOON, H. Graphene-embedded hydrogel nanofibers for detection and removal of aqueous-phase dyes. **ACS Applied Materials and Interfaces**, v. 9 (12), p. 10768-10776, 2017.

111. INTERNATIONAL ORGANIZATION FOR STANDARDIZATION - ISO. **ISO TS 80004/2017**: Nanotechnologies – Vocabulary – Part 13: Graphene and related two-dimensional (2D) materials. Geneve, 2017. 21p. Available in <https://www.iso.org/obp/ui/#iso:std:iso:ts:80004:-13:ed-1:v1:en>

112. ISLAM, M. A.; AHMED, M. J.; KHANDAY, W. A.; ASIF, M.; HAMEED, B.H. Mesoporous activated carbon prepared from NaOH activation of rattan (*Lacosperma secundiflorum*) hydrochar for methylene blue removal. **Ecotoxicology and Environmental Safety**, v. 138, p. 279–285, 2017.

113. IVANOVA, R.; KOTSILKOVA, R.; IVANOV, E.; DONATO, R. K.; FECHINE, G. J. M.; ANDRADE, R. J. E.; DI MAIO, R.; SILVESTRE, C. Composition dependence in surface properties of poly(lactic acid)/graphene/carbon nanotube composites. **Materials Chemistry and Physics**, v. 249, n. 122702, 2020.

114. JI, B.; WANG, J.; SONG, H.; CHEN, W. Removal of methylene blue from aqueous solutions using biochar derived from a fallen leaf by slow pyrolysis: Behavior and mechanism. **Journal of Environmental Chemical Engineering**, v. 7, n. 103036, 2019.

115. JIANG, L.; LIU, Y.; LIU, S.; HU, X.; ZENG, G.; HUE, X.; LIU, S.; LIU, S.; HUANG, B.; LI, M. Fabrication of β-cyclodextrin/poly (L-glutamic acid) supported magnetic graphene oxide and its adsorption behavior for 17β-estradiol. **Chemical Engineering Journal**, v. 308, p. 597–605, 2017.

116. KELM, M. A. P.; SILVA JÚNIOR, M. J.; BARROS HOLANDA, S. H.; ARAÚJO, C. M. B.; ASSIS FILHO, R. B.; JAGUARIBE E. F.; DOS SANTOS, D. R.; DA MOTTA SOBRINHO, M. A. Removal of azo dye from water via adsorption on biochar produced by the gasification of wood wastes. **Environmental Science and Pollution Research**, v. 26, p. 28558–28573, 2019.

117. KHURANA, I.; SHAW, A.K.; BHARTIA; KHURANA, J.M.; RAI, P.K. Batch and dynamic adsorption of Eriochrome Black T from water on magnetic graphene oxide: Experimental and theoretical studies. **Journal of Environmental Chemical Engineering**, v. 6, p. 468–477, 2018.

118. KIM, Y.; KIM, T.; LEE, J.; CHOI, Y. S.; MOON, J.; PARK, S. Y.; LEE, T. H.; PARK, H. K.; LEE, S. A.; KWON, M. S.; BYUN, H.-G.; LEE, J.-H.; LEE, M.-G.; HONG, B. H.; JANG, H. W. Tailored graphene micropatterns by wafer-scale direct transfer for flexible chemical sensor platform. **Advanced Materials**, v. 33 (2), n. 2004827, 2020.

119. KLIMOV, N. N.; JUNG, S.; ZHU, S.; LI, T.; WRIGHT, C. A.; SOLARES, S. D.; NEWELL, D. B.; ZHITENEV, N. B.; STROSCIO, J. A. Electromechanical Properties of Graphene Drumheads. **Science**, v. 336 (6088), p. 1557-1561, 2012.

120. KONG, S.; LAM, S. S.; YEK, P. N. Y.; LIEW, R. K.; MA, N. L.; OSMAN, M. S.; WONG, C. C. Self-purging microwave pyrolysis: an innovative approach to convert oil palm shell into carbon-rich biochar for methylene blue adsorption. **Journal of Chemical Technology and Biotechnology**, v. 59(5), p. 1397–1405, 2019.

121. KOOPAL, L. K.; RIEMSDIJK, J. C. M.; DE WIT, J. C. M.; BENEDETTI, M. F. Analytical isotherm equations for multicomponent adsorption to heterogeneous surfaces. **Journal of Colloid and Interface Sciences**, v. 166, p. 51–60, 1994.

122. KUO, C. Y.; WU, C. H.; WU, J. Y. Adsorption of direct dyes from aqueous solutions by carbon nanotubes: Determination of equilibrium, kinetics and thermodynamics parameters. **Journal of Colloid and Interface Science**, v. 327(2), p. 308–315, 2008.

123. KYZAS, G. Z.; DELIYANNI, E. A.; BIKIARIS, D. N.; MITROPOULOS, A. C. Graphene composites as dye adsorbents: Review. **Chemical Engineering Research and Design**, v. 129, p. 75–88, 2018.

124. KYZAS, G. Z.; SIAFAKA, P. I.; BIKIARIS, D. N.; KOUKARAS, E. N.; FROUDAKIS, G. E. Alternative use of cross-linked polyallylamine (known as Sevelamerpharmaceutical compound) as biosorbent. **Journal of Colloid and Interface Science**, v. 442, p. 49–59, 2015.

125. KONICKI, W.; ALEKSANDRZAK, M.; MOSZYNSKI, D.; MIJOWSKA, E. Adsorption of anionic azo-dyes from aqueous solutions onto graphene oxide: Equilibrium, kinetic and thermodynamic studies. **Journal of Colloid and Interface Science**, v. 496, p. 188–200, 2017.

126. LAGERGREN, S. **About the theory of so-called adsorption of soluble substances**. Kungliga Svenska Vetenskapsakademiens Handlingar, 1898.

127. LAI, K. C.; LEE, L. Y.; HIEW, B. Y. Z.; THANGALAZHY-GOPAKUMAR, S.; GAN, S. Environmental application of three-dimensional graphene materials as adsorbents for dyes and heavy metals: Review on ice-templating method and adsorption mechanisms. **Journal of Environmental Sciences**, v. 79, p. 174–199, 2019.

128. LEE, W.-C.; BONDAZ, L.; HUANG, S.; HE, G.; DAKHCHOUNE, M.; AGRAWAL, K. V. Centimeter-scale gas-sieving nanoporous single-layer graphene membrane. **Journal of Membrane Science**, v. 618, n. 118745, 2021.

129. LEVCHENKO, I.; OSTRIKOV, K.; ZHENG, J.; LI, X.; KEIDARD, M.; TEO, K. Scalable graphene production: perspectives and challenges of plasma applications. **Nanoscale**, v. 8, p. 10511–10527, 2016.

130. LI, X.; ZHU, B.; ZHU, J. Graphene oxide based materials for desalination. **Carbon**, v. 146, p. 320–328, 2019.

131. LIMA, E. C.; HOSSEINI-BANDEGHARAEI, A.; MORENO-PIRAJÁN, J. C.; ANASTOPOULOS, I. A critical review of the estimation of the thermodynamic parameters on adsorption equilibria. Wrong use of equilibrium constant in the Van't Hoof equation for calculation of thermodynamic parameters of adsorption. **Journal of Molecular Liquids**, v. 273, p. 425–434, 2019.

132. LINGAMDINNE, L.P.; KODURU, J.R.; CHANG, Y.-Y.; KARRI, R.R. Process optimization and adsorption modeling of Pb(II) on nickel ferrite-reduced graphene oxide nano-composite. **Journal of Molecular Liquids**, v. 250, p. 202–211, 2018.

133. LIU, N.; CHORTOS, A.; LEI, T.; JIN, L.; KIM, T. R.; BAE, W.-G.; ZHU, C.; WANG, S.; PFATTNER, R.; CHEN, X.; SINCLAIR, R.; BAO, Z. Ultratransparent and stretchable graphene electrodes. **Science Advances**, v. 3, n. 9, e. 1700159, 2017.

134. LORYUENYONG, V.; TOTEPVIMARN, K.; EIMBURANAPRAVAT, P.; BOONCHOMPOO, W.; BUASRI, A. Preparation and Characterization of Reduced Graphene Oxide Sheets via Water-Based Exfoliation and Reduction Methods. **Advances in Materials Science and Engineering**, v. 2013, n. 923403, p. 5, 2013.

135. LUPUL, I.; YPERMAN, J.; CARLEER, R.; GRYGLEWICZ, G. Adsorption of atrazine on hemp stem-based activated carbons with different surface chemistry. **Adsorption**, v. 21, p. 489–498, 2015.

136. LUZ-ASUNCIÓN, M.; PÉREZ-RAMÍREZ, E. E.; MARTÍNEZ-HERNÁNDEZ, A. L.; GARCÍA-CASILLAS, P. E.; LUNA-BÁRCENAS, J. G.; VELASCO-SANTOS, C. Adsorption and kinetic study of Reactive Red 2 dye onto graphene oxides and graphene quantum dots. **Diamond and Related Materials**, v. 109, n. 108002, 2020.

137. LV, Q.; LI, G.; SUN, H.; KONG, L.; LU, H.; GAO X. Preparation of magnetic core/shell structured γ-Fe_2O_3@Ti-tmSiO_2 and its application for the adsorption and degradation of dyes. **Microporous and Mesoporous Materials**, v. 186, p. 7-13, 2014.

138. MA, F. F.; ZHANG, D.; HUANG, T.; ZHANG, N.; WANG, Y. Ultrasonication-assisted deposition of graphene oxide on electrospun poly(vinylidene fluoride) membrane and the adsorption behavior. **Chemical Engineering Journal**, v. 358, p. 1065–1073, 2019.

139. MAHMOOD, T.; SADDIQUE, M. T.; NAEEM, A.; WESTERHOFF, P.; MUSTAFA, S.; ALUM, A. Comparison of different methods for the point of zero charge determination of NiO. **Industrial and Engineering Chemistry Research**, v. 50, p. 10017–10023, 2011.

140. MAHMOODI, N. M.; GHEZELBASH, M.; SHABANIAN, M.; ARYANASAB, F.; SAEB, M R. Efficient removal of cationic dyes from colored wastewaters by dithiocarbamate-functionalized graphene oxide nanosheets: From synthesis to detailed kinetics studies. **Journal of Taiwan Institute of Chemical Engineers**, v. 81, p. 239–246, 2017.

141. MAHMOUD, A. E. D.; STOLLE, A.; STELTER, M. Sustainable Synthesis of High-Surface-Area Graphite Oxide via Dry Ball Milling. **ACS Sustainable Chemistry and Engineering**, v. 6, p. 6358−6369, 2018.

142. MAHMOUDI, E.; ANG, W. L.; NG, C. Y.; NG, L. Y.; MOHAMMAD, A. W.; BENAMOR, A. Distinguishing characteristics and usability of graphene oxide based on different sources of graphite feedstock. **Journal of Colloid and Interfaces Science**, v. 542, p. 429–440, 2019.

143. MANOJ, B. A comprehensive analysis of various structural parameters of Indian coals with the aid of advanced analytical tools. **International Journal of Coal Science and Technology**, v. 3, n. 2, p. 123–132, 2016.

144. McCABE, Warren, SMITH, Julian, HARRIOTT, Peter. **Unit operations of chemical engineering.** 7th edition. New York: McGraw-Hill, 2004. 1168p.

145. McKAY, G.; MESDAGHINIA, A.; NASSERI, S.; HADI, M.; AMINABAD, M.S. Optimum Isotherms of Dyes Sorption by Activated Carbon: Fractional Theoretical Capacity & Error Analysis. **Chemical Engineering Journal**, v. 251, p. 236–247, 2014.

146. MEDEIROS, G. S.; MUÑOZ, P. A. R.; DE OLIVEIRA, C. F. P.; LAURA C. E. DA SILVA, L. C. E.; MALHOTRA, R.; GONÇALVES, M. C.; ROSA, V.; FECHINE, G. J. M. Polymer nanocomposites based on poly(ε-caprolactone), hydroxyapatite and graphene oxide. **Journal of Polymers and the Environment**, v. 28, p. 331–342, 2020.

147. MEILI, L.; LINS, P. V.; ZANTA, C. L. P. S.; SOLETTI, J. I.; RIBEIRO, L. M. O.; DORNELAS, C. B.; SILVA, T. L.; VIEIRA, M. G. A. MgAl-LDH/Biochar composites for methylene blue removal by adsorption. **Applied Clay Science**, v. 168, p. 11–20, 2019.

148. MINITHA, C. R.; LALITHA, M.; JEYACHANDRAN, Y. L.; SENTHILKUMAR, L.; RAJENDRA KUMAR, R. T. Adsorption behaviour of reduced graphene oxide towards cationic and anionic dyes: Co-action of electrostatic and π–π interactions. **Materials Chemistry and Physics**, v. 194, p. 243–252, 2017.

149. MOREIRA, R. C. L.; OLIVEIRA, J. H.; LIBEL, G. P.; AMARAL, P. E. R.; PEREIRA, E. C. A.; SIQUEIRA, V. L. D.; GRASSI, M. F. N. N.; RADOVANOVIC, E. Modified polystyrene spheres/graphene oxide decorated with silver nanoparticles as bactericidal material. **Journal of Molecular Structure**, v. 1233, n. 130091, 2021.

150. MOZTAHIDA, M.; LEE, D. S. Photocatalytic degradation of methylene blue with P25/graphene/polyacrylamide hydrogels: Optimization using response surface methodology. **Journal of Hazardous Materials**, v. 400, p. 123314, 2020.

151. MU, S.-J.; SU, Y.-C.; XIAO, L.-H.; LIU, S.-D.; HU, T.; TANG, H.-B. X-Ray Diffraction Pattern of Graphite Oxide. **Chinese Physics Letters**, v. 30, n. 9, p. 096101, 2013.

152. MUKHERJEE, S.; KAVALSKY, L.; CHATTOPADHYAY, K.; SINGH, C. V. Dramatic improvement in the performance of graphene as Li/Na battery anodes with suitable electrolytic solvents. **Carbon**, v. 161, p. 570–576, 2020.

153. MUÑOZ, P.A.R.; DE OLIVEIRA, C.F.P.; AMURIN, L.G.; RODRIGUEZ, C.L.C.; NAGAOKA, D.A.; TAVARES, M.I.B.; DOMINGUES, S.H.; ANDRADE, R.J.E.; FECHINE, G.J.M. Novel improvement in processing of polymer nanocomposite based on 2D materials as fillers. **Express Polymer Letters**, v. 12, p. 930–945, 2018.

154. NAVIK, R.; GAI, Y.; WANG, W.; ZHAO, Y. Curcumin-assisted ultrasound exfoliation of graphite to graphene in ethanol. **Ultrasonics Sonochemistry**, v. 48, p. 96–102, 2018.

155. NAZARI, Y.; SALEM, S. Efficient photocatalytic methylene blue degradation by Fe_3O_4@TiO_2 core/shell linked to graphene by aminopropyltrimethoxysilane. **Environmental Science and Pollution Research**, v. 26 (4), p. 25359–25371, 2019.

156. NEOH, C.H.; LAM, C.Y.; LIM, C.K.; YAHYA, A.; BAY, H.H.; IBRAHIM, Z.; NOOR, Z.Z. Biodecolorization of recalcitrant dye as the sole source of nutrition using Curvularia clavata NZ2 and decolorization ability of its crude enzymes. **Environmental Science and Pollution Research**, v. 22, p. 11669–11678, 2015.

157. NGUYEN, H. N.; CASTRO-WALLACE, S. L.; RODRIGUES, D. F. Acute toxicity of graphene nanoplatelets on biological wastewater treatment process. **Environmental Sciences: Nano**, v. 4, p. 160–169, 2017.

158. NOVOSELOV, H. S.; GEIM, A. K.; MOROZOV, S. V.; JIANG, D.; ZHANG, Y.; DUBONOS, S. V.; GRIGORIEVA, I. V.; FIRSOV, A. A. Electric field effect in atomically thin carbon films. **Science**, v. 306, p. 666–669, 2004.

159. OTHMAN, N. H.; ALIAS, N. H.; SHAHRUDDIN, M. Z.; BAKAR, N. F. A. HIM, N. R. N.; LAU, W. J. Adsorption kinetics of methylene blue dyes onto magnetic graphene oxide. **Journal of Environmental Chemical Engineering**, v. 6 (2), p. 2803–2811, 2018.

160. PARK, S.; RUOFF, R. S. Chemical methods for the production of graphenes. **Nature Nanotechnology**, v. 4, p. 217–224, 2009.

161. PARVIZ, D.; DAS, S.; AHMED, H. S.; IRIN, F.; BHATTACHARIA, S.; GREEN, M. J. Dispersions of non-covalently functionalized graphene with minimal stabilizer. **ACS Nano**, v. 6, p. 8857–8867, 2012.

162. PATTAMMATTEL, A.; PANDE, P.; KUTTAPPAN, D.; PUGLIA, M.; BASU, A. K.; AMALARADJOU, M. A.; KUMAR, C. V. Controlling the Graphene−Bio Interface: Dispersions in Animal Sera for Enhanced Stability and Reduced Toxicity. **Langmuir**, v. 33 (49), p. 14184–14194, 2017.

163. PERREAULT, F.; DE FARIA, A. F.; ELIMELECH, M. Environmental applications of graphene-based nanomaterials. **Chemical Society Reviews**, v. 44, p. 5861–5896, 2015.

164. PERRY, Robert H., GREEN, Don W., MALONEY, James O. **Perry's Chemical Engineer's Handbook**, 7ª Ed. Sec.: Adsorption and Ion Exchange – p. 1497–1562, New York: McGraw-Hill, 1999. 1709p.

165. PESSÔA, T. S.; LIMA FERREIRA, L. E. M.; DA SILVA, M. P.; PEREIRA NETO, L. M.; NASCIMENTO, B. F.; FRAGA, T. J. M.; JAGUARIBE, E. F.; CAVALCANTI, J. V.; DA MOTTA SOBRINHO, M. A. Açaí waste beneficing by gasification process and its employment in the treatment of synthetic and raw textile wastewater. **Journal of Cleaner Production**, v. 240, n. 118047, 2019.

166. PICCIN, Jefferson S.; CADAVAL JR, Tito Roberto S.; PINTO, Luiz Antonio A.; DOTTO, Guilherme L. **Adsorption Isotherms in Liquid Phase: Experimental, Modeling, and Interpretations**. In: Bonilla-Petriciolet A., Mendoza-Castillo D., Reynel-Ávila H. (eds), Adsorption Processes for Water Treatment and Purification, p. 19–51. New York: Springer, 2017.

167. PIRAS, A.; EHLERT, C.; GRYN'OVA, G. Sensing and sensitivity: Computational chemistry of graphene-based sensors. **WIREs Computational Molecular Science** (in press), 2021. https://doi.org/10.1002/wcms.1526

168. POTHAYA, S.; REGALBUTO, J. R.; MONNIER, J. R.; PUNYAWUDHO, K. Preparation of Pt/graphene catalysts for polymer electrolyte membrane fuel cells by strong electrostatic adsorption technique, **International Journal of Hydrogen Energy**, v. 44, p. 26361–26372, 2019.

169. PUNETHA, V. D.; RANA, S.; YOO, H. J.; CHAURASIA, A.; MCLESKEY JR., J. T.; RAMASAMY, M. S.; SAHOO, N. G.; CHO, J. W. Functionalization of carbon nanomaterials for advanced polymer nanocomposites: A comparison study between CNT and graphene. **Progess in Polymer Science**, v. 67, p. 1–47, 2017.

170. PURBIA, R.; KWON, Y. M.; KIM, H.-D.; LEE, Y. S.; SHIN, H.; BAIK, J. M. Zero-dimensional heterostructures: N-doped graphene dots/SnO_2 for ultrasensitive and selective NO_2 gas sensing at low temperatures. **Journal of Materials Chemistry A**, v. 8, 11734–11742, 2020.

171. RAFIEE, J.; MI, X.; GULLAPALLI, H.; THOMAS, A. V.; YAVARI, F.; SHI, Y.; AJAYAN, P. M.; KORATKAR, N. A. Wetting transparency of graphene. **Nature Materials**, v. 11, p. 217–222, 2012.

172. RAMALINGAM, B.; PARANDHAMAN, T.; CHOUDHARY, P.; DAS, S. K. Biomaterial functionalized graphene-magnetite nanocomposite: a novel approach for simultaneous removal of anionic dyes and heavy-metal ions. **ACS Sustainable Chemistry and Engineering**, v. 8 (5), p. 6328–6341, 2018.

173. REYNOSA-MARTÍNEZ, A. C.; NAVARRO TOVAR, G.; GALLEGOS, W. R.; RODRÍGUEZ-MELÉNDEZ, H.; TORRES-CADENA, R.; MONDRAGÓN-SOLÓRZANO, G.; BARROSO-FLORES, J.; ALVAREZ-LEMUS, M. A.; GARCÍA MONTALVO, V.; LÓPEZ-HONORATO, E. Effect of the degree of oxidation of

graphene oxide on As(III) adsorption. **Journal of Hazardous Materials**, v. 384, n. 121440, 2020.

174. RODRIGUEZ, J. R.; KIM, P. J.; KIM, K.; QI, Z.; WANG, H.; POL, V. G. Engineered heat dissipation and current distribution boron nitride-graphene layer coated on polypropylene separatorfor high performance lithium metal battery. **Journal of Colloid and Interface Science**, v. 583, p. 362–370, 2021.

175. ROHAIZAD, A.; SHAHABUDDIN, S.; SHAHID, M.M.; RASHID, N.M.; HIR, Z.A.M.; RAMLY, M.M.; AWANG, K.; SIONG, C.W.; ASPANUT, Z. Green synthesis of silver nanoparticles from Catharanthus roseus dried bark extract deposited on graphene oxide for effective adsorption of methylene blue dye. **Journal of Environmental Chemical Engineering**, v. 8, n. 103955, 2020.

176. ROUQUEROL, Françoise; ROUQUEROL, Jean; SING, Kenneth. **Adsorption by powders and porous solids – principles, methodology and applications.** London: Academic Press, 1999. 467p.

177. RUIZ, A.; LUCHERELLI, M. A.; MURERA, D.; LAMON, D.; MÉNARD-MOYON, C.; BIANCO, A. Toxicological evaluation of highly water dispersible few-layer graphene in vivo. **Carbon**, v. 170, p. 347–360, 2020.

178. RUTHVEN, Douglas M. **Principles of adsorption and adsorption processes**. New York: Jhon Wiley and Sons, 1984. 433p.

179. SABESP – Companhia de Saneamento Básico do Estado de São Paulo, "Basic Sanitation Company of the State of São Paulo" (*in Portuguese*). **Norma Técnica Interna SABESP NTS 013, "Internal Technical Standard NTS 013"** (*in Portuguese*). São Paulo: SABESP, 1999. 8p.

180. SAINSBURY, T.; PASSARELLI, M.; NAFTALY, M.; GNANIAH, S.; SPENCER, S. J.; POLLARD, A. J. Covalent carbene functionalization of graphene: toward chemical bandgap manipulation. **ACS Applied Materials and Interfaces**, v. 8 (7), p. 4870–4877, 2016.

181. SAHA, Papita; CHOWDHURY, Shamik. **Insight into adsorption thermodynamics.** In: Thermodynamics, Prof. Mizutani Tadashi (Ed.), Shangai: Intech Open, 2011, p. 349–364.

182. SAMSAMI, S.; MOHAMADI, M.; SARRAFZADEH, M.-H.; RENE, E. R.; FIROOZBAHR, M. Recent advances in the treatment of dye-containing wastewater from textile industries: Overview and perspectives. **Process Safety and Environmental Protection**, v. 143, p. 138-163, 2020.

183. SARKAR, C.; BORA, C.; DOLUI, S. K. Selective Dye Adsorption by pH Modulation on Amine-Functionalized Reduced Graphene Oxide−Carbon Nanotube Hybrid. **Industrial and Engineering Chemistry Research**, v. 53 (42), p. 16148–16156, 2014.

184. SCHEUFELE, F.B.; MÓDENES, A.N.; BORBA, C.E.; RIBEIRO, C.; ESPINOZA-QUIÑONES, F.R.; BERGAMASCO, R.; PEREIRA, N.C. Monolayer–multilayer adsorption phenomenological model: Kinetics, equilibrium and thermodynamics, **Chemical Engineering Journal**, v. 284, p. 1328–1341, 2016.

185. SENTHILNATHAN, J.; SELVARAJ, A.; YOUNIS, S. A.; KIM, K.-H.; YOSHIMURA, M. An upgraded electro-Fenton treatment of wastewater using nanoclay-embedded graphene composite prepared via exfoliation of pencil rods bysubmerged liquid plasma. **Journal of Hazardous Materials**, v. 397, n. 122788, 2020.

186. SHANG, J.; GAO, J.; XI, J.; WANG, Y.; JI, F.; LI, R. Immobilization of Cr(VI) from solution by a graphene oxide-nZVI/biochar composite. **Water Environment Research**, v. 91 (7), p. 565–572, 2019.

187. SHANG, M.-R.; LIU, Y.-G.; LIU, S.-B.; ZENG, G.-M.; TAN, X.-F.; JIANG, L.-H.; HUANG, X.-X.; DING, Y.; GUO, Y.-M.; WANG, S.-F. A novel graphene oxide coated biochar composite: synthesis, characterization and application for Cr(VI) removal. **RSC Advances**, v. 6, p. 85202–85212, 2016.

188. SHEARER, C. J.; SLATTERY, A. D.; STAPLETON, A. J.; SHAPTER, J. G.; GIBSON, C. T. Accurate thickness measurement of graphene. **Nanotechnology**, v. 27, n. 125704, 2016.

189. SHEN, J.; SHI, M.; LI, N.; YAN, B.; MA, H.; HU, Y.; YE, M. Facile synthesis and application of Ag-chemically converted graphene nanocomposite. **Nano Research**, v. 3, p. 339–349, 2010.

190. SHEN, J.; HU, Y.; SHI, M.; LU, X.; QIN, C.; LI, C.; YE, M. Fast and facile preparation of graphene oxide and reduced graphene oxide nanoplatelets. **Chemistry of Materials**, v. 21, p. 3514–3520, 2009.

191. SHU, D.; FENG, F.; HAN, H.; MA, Z. Prominent adsorption performance of amino-functionalized ultra-light graphene aerogel for methyl orange and amaranth. **Chemical Engineering Journal**, v. 324, p. 1–9, 2017.

192. SIMONIN, J.-P. On the comparison of pseudo-first-order and pseudo-second-order rate laws in the modeling of adsorption kinetics. **Chemical Engineering Journal**, v. 300, p. 254–263, 2016.

193. SITEK, J.; PLOCHARSKI, J.; PASTERNAK, I.; GERTYCH, A. P.; MCALEESE, C.; CONRAN, B. R.; ZDROJEK, M.; STRUPINSKI, W. Substrate-Induced Variances in Morphological and Structural Properties of MoS_2 Grown by Chemical Vapor Deposition on Epitaxial Graphene and SiO_2. **ACS Applied Materials and Interfaces**, v. 12, p. 45101–45110, 2020.

194. SOBRERO, Maria Cecília; RONCO, Alícia. **Ensayo de toxicidad aguda con semillas de lechuga (*Lactuca sativa L*)**, In: Ensayos toxicológicos y métodos de evaluación de cualidad de aguas – estandarización, intercalibración, resultados y aplicaciones, "**Assay of**

acute toxicicity with lettuce seeds (*Lactuca sativa L*), In: Toxicological assays and methods of water quality evaluation – standardization, intercalibration, results and applications" (*In Spanish*). Mexico City: Centro Internacional de Investigaciones para el Desarollo, 2004. 118p.

195. SONG, Y.; CAO, L.; YU, J.; ZHANG, S.; CHEN, S.; JIANG, Y. Amino-functionalized graphene oxide blend with monoethanolamine for efficient carbon dioxide capture. **Journal of Alloys Compounds**, v. 704, p. 245–253, 2017.

196. SPYROU, Konstantinos; RUDOLF, Petra. **An Introduction to Graphene**. In: Functionalization of Graphene, 1st Ed. Edited by Vasilios Georgakilas. Weinheim: Wiley-VCH Verlag GmbH & Co., 2014. 20p.

197. STAUDENMAIER, L. Verfahren zur darstellung der graphitsäure, "process for the preparation of graphite acid" (*in german*). **Berichte der deutschen chemischen gesellschaft**, v. 31(2), p. 1481–1487, 1898.

198. STEPHAN, O.; AJAYAN, P.; COLLIEX, C.; REDLICH, P.; LAMBERT, J.M.; BERNIER, P.; LEFIN, P. Doping graphitic and carbon nanotube structures with boron and nitrogen. **Science**, v. 266(5191), p. 1683–1685, 1994.

199. SUTER, J. L.; SINCLAIR, R. C.; COVENEY, P. V. Principles governing control of aggregation and dispersion of Graphene and Graphene Oxide in polymer melts. **Advanced Materials**, v. 32 (36), n. 2003213, 2020.

200. SZCZESNIAK, B.; CHOMA, J.; JARONIEC, M. Gas adsorption properties of hybrid graphene-MOF materials. **Journal of Colloid and Interface Sciences**, v. 514, p. 801–813, 2018.

201. TAHIR, M. A.; BHATTI, H. N.; IQBAL, M. Solar Red and Brittle Blue direct dyes adsorption onto Eucalyptus angophoroides bark: Equilibrium, kinetics and thermodynamic studies. **Journal of Environmental Chemical Engineering**, v. 4, p. 2431–2439, 2016.

202. TAMILARASAN, P.; RAMAPRABHU, S. Integration of polymerized ionic liquid with graphene for enhanced CO_2 adsorption. **Journal of Materials Chemistry A**, v. 3, p. 101 – 108, 2015.

203. TAN, P.; HU, Y. Improved synthesis of graphene/β-cyclodextrin composite for highly efficient dye adsorption and removal. **Journal of Molecular Liquids**, v. 242, p. 181-189, 2017.

204. TANG, S.; XIA, D.; YAO, Y.; CHEN, T.; SUN, J.; YIN, Y.; SHEN, W.; PENG, Y. Dye adsorption by self-recoverable, adjustable amphiphilic graphene aerogel. **Journal of Colloid and Interface Science,** v. 554, p. 682–691, 2019.

205. THOMAS, G.; SPITZER, D. Double-side microcantilevers as a key to understand the adsorption mechanisms and kinetics of chemical warfare agents on vertically-aligned TiO2 nanotubes. **Journal of Hazardous Materials**, v. 406, n. 124672, 2021.

206. THOMAS, H. R.; MARSDEN, A. J.; WALKER, M.; WILSON, N. R.; ROURKE, J. P. Sulfur-Functionalized Graphene Oxide by Epoxide Ring-Opening. **Angewandte Chemie International Edition**, v. 53, p. 1–7, 2014.

207. THOMMES, M.; KANEKO, K.; NEIMARK, A. V.; OLIVIER, J. P.; RODRIGUEZ-REINOSO, F.; ROUQUEROL, J.; SING, K. S. W. Physisorption of gases, with special reference to the evaluation of surface area and pore size distribution (IUPAC Technical Report). **Pure and Applied Chemistry**, v. 87 (9–10), p. 1051–1069, 2015.

208. TSENG, R. L.; WU, P. H.; WU, F. C.; JUANG, R. S. A convenient method to determine kinetic parameters of adsorption processes by nonlinear regression of pseudo-n^{th}-order equation. **Chemical Engineering Journal**, v. 237, p. 153–161, 2014.

209. TU, T. H.; CAM, P. T. N.; HUY, L. V. T.; PHONG, M. T.; NAM, H. M.; HIEU, N. H. Synthesis and application of graphene oxide aerogel as an adsorbent for removal of dyes from water. **Materials Letters**, v. 238, p. 134–137, 2019.

210. TURIEL, E.; PEREZ-CONDE, C.; MARTIN-ESTEBAN, A. Assessment of the cross-reactivity and binding sites characterisation of a propazine-imprinted polymer using the Langmuir-Freundlich isotherm. **Analyst**, v. 128, p. 137–141, 2003.

211. USEPA, United State Environmental Protection Agency. **2012 Guidelines for Water Reuse**. Washington-DC: EPA, 2012. 643p.

212. VALENZUELA, L.; IGLESIAS-JUEZ, A.; BACHILLER-BAEZA, B.; FARALDOS, M.; BAHAMONDE, A.; ROSAL, R. Biocide mechanism of highly efficient and stable antimicrobial surfaces based on zinc oxide–reduced graphene oxide photocatalytic coatings. **Journal of Materials Chemistry B**, v. 8, p. 8294–8304, 2020.

213. VELUSAMY, S.; ROY, A.; SUNDARAM, S.; MALLICK, T. K. A review on heavy metal ions and containing dyes removal through graphene oxide-based adsorption strategies for textile wastewater treatment. **The Chemical Record**, v. 21, p. 1–42, 2021.

214. WANG, G.; SHEN, X.; WANG, B.; YAO, J.; PARK, J. Synthesis and characterisation of hydrophilic and organophilic graphene nanosheets. **Carbon**, v. 47, p. 1359–1364, 2009.

215. WANG, S.; XU, M.; PENG, T.; ZHANG, C.; LI, T.; HUSSAIN, I.; WANG, J.; TAN, B. Porous hypercrosslinked polymer-TiO_2-graphene composite photocatalysts for visible-light-driven CO_2 conversion. **Nature Communications**, v. 10, n. 676, 2019a.

216. WANG, J.; ZHANG, W.; ZHENG, Y.; ZHANG, N.; ZHANG, C. Multi-functionalization of magnetic graphene by surface-initiated ICAR ATRP mediated by polydopamine chemistry for adsorption and speciation of arsenic. **Applied Surface Science**, v. 478, p. 15–25, 2019b.

217. WANG, F.; YU, X.; GE, M.; WU, S.; GUAN, J.; TANG, J.; WU, X.; RITCHIE, R. O. Facile self-assembly synthesis of γ-Fe_2O_3/graphene oxide for enhanced photo-Fenton reaction. **Environmental Pollution**, v. 248, p. 229–237, 2019c.

218. WANG, S.; LI, X.; LIU, Y.; ZHANG, C.; TAN, X.; ZENG, G.; SONG, B.; JIANG, L. Nitrogen-containing amino compounds functionalized graphene oxide: Synthesis, characterization and application for the removal of pollutants from wastewater: A review. **Journal of Hazardous Materials**, v. 342, p. 177–191, 2018a.

219. WANG, X.; LIU, Z.; YE, X.; HU, K.; ZHONG, H.; YU, J.; JIN, M.; GUO, Z. A facile one-step approach to functionalized graphene oxide-based hydrogels used as effective adsorbents toward anionic dyes. **Applied Surface Science**, v. 308, p. 82–90, 2014.

220. WANG, Z.; SHEN, D.; WU, C.; GU, S. State-of-the-art on the production and application of carbon nanomaterials from biomass. **Green Chemistry**, v. 20, p. 5031–5057, 2018b.

221. WANG, Z.; LIU, H.; CHEN, F.; ZHANG, Q. A three-dimensional printed biomimetic hierarchical graphene architecture for high-efficiency solar steam-generation. **Journal of Materials Chemistry A**, v. 8, p. 19387–19395, 2020.

222. WANG, Zongping; XUE, Miaomiao; HUANG, Kai; LIU, Zizheng. **Textile Dyeing Wastewater Treatment**, In: Advances in Treating Textile Effluent, Prof. Peter Hauser (Ed.). Shangai: Intech Open, 2011. pp. 91–116

223. WANJERI, V.W.O.; SHEPPARD, C.J.; PRINSLOO, A.R.E.; NGILA, J.C.; NDUNGU, P.G. Isotherm and kinetic investigations on the adsorption of organophosphorus pesticides on graphene oxide based silica coated magnetic nanoparticles functionalized with 2-phenylethylamine. **Journal of Environmental Chemical Engineering**, v. 6, p. 1333–1346, 2018.

224. WEBER, W. J.; MORRIS, J. C. Kinetics of Adsorption on Carbon from Solution. **Journal of the Sanitary Engineering Division**, v. 89 (2), p. 31–60, 1963.

225. WERBER, J. R.; OSUJI, C. O.; ELIMELECH, M. Materials for next-generation desalination and water purification membranes. **Nature Reviews Materials**, v. 1, n. 16018, 2016.

226. WU, Y.; HAO, Y.; JEONG , H. Y.; LEE, Z.; CHEN, S.; JIANG, W.; WU, Q.; PINER, R. D.; KANG, J.; RUOFF, R. S. Crystal structure evolution of individual graphene islands during CVD growth on copper foil. **Advanced Materials**, v. 25 (46), p. 6744–6751, 2013.

227. VALIZADEH, S.; RASOULIFARD, M. H.; SEYED DORRAJI, M. S. Modified Fe_3O_4-hydroxyapatite nanocomposites as heterogeneouscatalysts in three UV, Vis and Fenton like degradation system. **Applied Surface Science**, v. 319, p. 358-366, 2014.

228. VECERA, P.; CHACÓN-TORRES, J. C.; PICHLER, T.; REICH, S.; SONI, H. R.; GÖRLING, A.; EDELTHALHAMMER, K.; PETERLIK, H.; HAUKE, F.; HIRSCH, A.

Precise determination of graphene functionalization by in situ Raman spectroscopy. **Scientific Reports**, v. 8, p. 15192, 2017.

229. XIONG, Y.; CUI, X.; ZHANG, P.; WANG, Y.; LOU, Z.; SHAN, W. Improving Re(VII) adsorption on diisobutylamine functionalized graphene oxide. **ACS Sustainable Chemistry and Engineering**, v. 5 (1), p. 1010–1018, 2017.

230. YANG, H.; BAI, L.; WEI, D.; YANG, L.; WANG, W.; CHEN, H.; NIU, Y.; XUE, Z. Ionic self-assembly of poly(ionic liquid)-polyoxometalate hybrids for selective adsorption of anionic dyes. **Chemical Engineering Journal**, v. 358, p. 850–859, 2019.

231. YANG, H.; LI, F.; SHAN, C.; HAN, D.; ZHANG, Q.; NIU, L.; IVASKA, A. Covallent functionalization of chemically converted graphene sheets via silane and its reinforcement. **Journal of Materials Chemistry**, v. 19, p. 4632–4638, 2009.

232. YANG, K.; LI, Y.; TAN, X.; PENG, R.; LIU, Z. Behavior and toxicity of graphene and its functionalized derivatives in biological systems. **Small**, v. 9 (9-10), p. 1492–1503, 2013.

233. YAO, T.; JIA, W.; FENG, Y.; ZHANG, J.; LIAN, Y.; WU, J.; ZHANG, X. Preparation of reduced graphene oxide nanosheet/fe_xo_y/nitrogen-doped carbon layer aerogel as photo-Fenton catalyst with enhanced degradation activity and reusability. **Journal of Hazardous Materials**, v. 362, p. 62–71, 2019.

234. YAP, P. L.; HASSAN, K.; AUYOONG, Y. L.; MANSOURI, N.; FARIVAR, F.; TRAN, D. N. H.; LOSIC, D. All-in-one bioinspired multifunctional graphene biopolymer foam for simultaneous removal of multiple water pollutants. **Advanced Materials Interfaces**, v. 7 (18), n. 2000664, 2020.

235. YASEEN, D. A.; SCHOLZ, M. Textile dye wastewater characteristics and constituents of synthetic effluents: a critical review. **International Journal of Environmental Science and Technology**, v. 16, p. 1193–1226, 2019.

236. YOUSEFI, N.; LU, X.; ELIMELECH, M.; TUFENKJI, N. Environmental performance of graphene-based 3D macrostructures. **Nature Nanotechnology**, v. 14, p. 107–119, 2019.

237. YOU, Y.; NI, Z.; YU, T.; SHEN, Z. Edge chirality determination of graphene by Raman spectroscopy. **Applied Physics Letters**, v. 93, p. 163112, 2008.

238. ZAMBARE, R.; SONG, X.; BHUVANA, S.; PRINCE, J. S. A.; NEMADE, P. Ultrafast Dye Removal Using Ionic Liquid–Graphene Oxide Sponge. **ACS Sustainable Chemistry and Engineering**, v. 5(7), p. 6026–6035, 2017.

239. ZEESHAN, M.; YALCIN, K.; OZTUNA, F. E. S.; UNAL, U.; KESKIN, S.; UZUN, A. A new class of porous materials for efficient CO_2 separation: Ionic liquid/graphene aerogel composites. **Carbon**, v. 171, p. 79–87, 2021.

240. ZHANG, F. R.; SONG, Y. W.; SONG, S.; ZHANG, R. J.; HOU, W. G. Synthesis of magnetite-graphene oxide-layered double hydroxide composites and applications for the removal of Pb(II) and 2,4-dichlorophenoxyacetic acid from aqueous solutions. **ACS Applied Materials and Interfaces**, v. 7, p. 7251-7263, 2015.

241. ZHANG, Q.; GAO, Y.; ZHAI, Y. A.; LIU, F. Q.; GAO, G. Synthesis of sesbania gum supported dithiocarbamate chelating resin and studies on its adsorption performance for metal ions. **Carbohydrate Polymers**, v. 73(2), p. 359–363, 2008.

242. ZHANG, X.; YANG, S.; YANG, Z.; XU, X. Kinetics and intermediate phases in epitaxial growth of Fe_3O_4 films from deposition and thermal reduction. **Journal of Applied Physics**, v. 120, n. 085313, 2016.

243. ZHANG, Y.; MA, H. L.; PENG, J.; ZHAI, M.; YU, Z. Z. Cr(VI) removal from aqueous solution using chemically reduced and functionalized graphene oxide. **Journal of Materials Science**, v. 48, p. 1883–1889, 2013.

244. ZHAO, W.; TANG, Y.; XI, J.; KONG, J. Functionalized graphene sheets with poly(ionic liquide)s and high adsorption capacity of anionic dyes. **Applied Surface Science**, v. 326, p. 276–284, 2015.

245. ZHAO, D.; GAO, X.; WU, C.; XIE, R.; FENG, S.; CHEN, C. Facile preparation of amino functionalized graphene oxide decorated with Fe_3O_4 nanoparticles for the adsorption of Cr (VI). **Applied Surface Science**, v. 384, p. 1–9, 2016.

246. ZHAO, Y.; LIU, C.; HUANG, Q. Ultrafine Pt stabilized on $Ti_3C_2T_x$/reduced graphene oxide nanocomposites for alcohol oxidation reaction (AOR). **Materials Letters**, v. 285, n. 129082, 2021.

247. ZHAO, Y.; ZHANG, Y.; LIU, A.; WEI, Z.; LIU, S. Construction of three-dimensional Hemin-functionalized graphene hydrogel with high mechanical stability and adsorption capacity for enhancing photodegradation of Methylene Blue. **ACS Applied Materials and Interfaces**, v. 9 (4), p. 4006–4014, 2017.

248. ZHOU, Y.; APUL, O. G.; KARANFIL, T. Adsorption of halogenated aliphatic contaminants by graphene nanomaterials. **Water Research**, v. 79, p. 57-67, 2015.

249. ZHU, Y.; MURALI, S.; CAI, W.; LI, X.; SUK, J. W.; POTTS, J. R.; RUOFF, R. S. Graphene and Graphene Oxide: Synthesis, Properties, and Applications. **Advanced Materials**, v. 22, p. 3906–3924, 2010a.

250. ZHU, Y.; MURALI, S.; STOLLER, M. D.; VELAMAKANNI, A.; PINER, R. D.; RUOFF, R. S. Microwave assisted exfoliation and reduction of graphite oxide for ultracapacitors. **Carbon**, v. 48 (7), p. 2118–2122, 2010b.

APPENDIX A - Photodegradation of dyes in textile wastewater by uv-light assisted Fenton-like process using NH_2-Fe_3O_4-functionalized multilayer graphene oxide

Maryne Patrícia da Silva[1], Lettícia Emely de Lima Farreira[1,2], Luiz Martins Pereira Neto[3], Tiago José Marques Fraga[1]*, Caroline Maria Bezerra de Araújo[1], Maurício Alves da Motta Sobrinho[1†], Marcos Gomes Ghislandi[1,4]

[1] *Department of Chemical Engineering, Universidade Federal de Pernambuco (UFPE), 1235 Prof. Moraes Rego Av, Cidade Universitária, zip code: 50670-901, Recife/PE, Brazil*

[2] *Center of Biosciences, Universidade Federal de Pernambuco (UFPE), Engineering Av. Cidade Universitária, zip code: 50740-570, Recife/PE, Brazil*

[3]*Environmental Engineering Post-Graduation Program, Universidade Federal Rural de Pernambuco (UFRPE), Dom Manuel de Medeiros St. W/N, Dois Irmãos, zip code: 521171-900, Recife/PE, Brazil*

[3] *Engineering Campus – UACSA, Federal Rural University of Pernambuco (UFRPE), 300 Cento e sessenta e Três Av., Cabo de Santo Agostinho/PE, Brazil*

ABSTRACT

The presence of dyes in textile effluents is a huge problem, due to the difficulty of degrading these substances. Advanced oxidation processes (AOPs) emerge as an alternative for the degradation of dyes and other organic components. In this context, this project evaluated the activity of iron ions present on the surface of Graphene Oxide (GO) in the degradation of Reactive Black 5 (RB5) dye. GO was synthesized via modified Hummers method and functionalized with diethylenetriamine (DETA) and $FeCl_3$ to obtain the NH_2-Fe_3O_4 functionalized graphene oxide (AmGO). A preliminary study was carried out in which it was observed that the volume of AmGO played a significant role in the process, whereas H_2O_2 volume had no effect. Tests with sun light presented lower results than those with UV radiation. Thereafter, 2^3 factorial design was carried out using the variables: AmGO dosage, pH and H_2O_2 concentration. Factorial design results demonstrated that the most significant effect was the AmGO dosage, followed by the pH and H_2O_2 concentration. Furthermore, kinetics of the photo-Fenton-*like* reaction was performed, showing that in RB5 degradation, the experimental data fitted pseudo-first order model. In overall, AmGO application in the photodegradation of RB5

dye exhibited significant results, with color degradation over 75% in less than 2h for the initial concentration of the dye of 100 $mg \cdot L^{-1}$.

Keywords: textile wastewater; advanced oxidation processes; 2D nanomaterials; graphene oxide; photo-Fenton-like; Reactive Black 5

A.1 INTRODUCTION

Textile wastewaters are characterized by the content of several chemical species with various negative effects in the environment and human health. Among the substances, textiles effluents contain soaps, metallic ions, salts, surfactants and dyes, which are classified as toxic and carcinogenic species. In addition to the high toxicity, the presence of dyes may even be visible to the naked eye, causing the depletion of dissolved oxygen and poor penetration of sunlight into the water, damaging the photosynthetic activity of aquatic plants (INCE; TEZCANLI, 1999; KANG *et al*., 2000; RAMIREZ; COSTA; MADEIRA, 2005). The treatment of effluent in the textile industry, in general, is based on physical-chemical processes of precipitation-coagulation, followed by biological treatment through activated sludge system, which allows a removal of approximately 80% of the dye load. However, the large amount of adsorbed dye prevents any practice of reuse of the sludge (KUNZ *et al*., 2002). In this scenario, the investment in new effluent treatment technologies, and more precisely of dye degradation, can help to optimize existing treatment processes and to stop problems such as the reutilization of sludge.

The use of Advanced Oxidative Processes (AOP), and more specifically the Fenton and photo-Fenton process, in the treatment of textile effluents has been widely studied because the textile industry produces large amounts of effluents with high concentrations of organic matter, beyond the carcinogenic dyes. The photo-Fenton reaction is a ferric to ferric ion oxidation reaction to decompose hydrogen peroxide into hydroxyl radicals in the presence of ultraviolet light or sunlight (BABUPONNUSAMI; MUTHUKUMAR, 2014). This generation of free radicals causes an attack on the dye molecular, promoting their breakdown in by-products that are characterized as having less toxic potential. Finally, when Fe^{3+} ions are provided by a heterogeneous source, the process is named by photo-Fenton-*like* reaction.

Among the dyes used in the textile industry, it is worth mentioning those classified as reactive, due to the presence of chromophore groups (such as azo, with N=N bonds), responsible for color; auxhochromes, wich give the color intensity in the fiber; and the fixing groups, such as

sulfonic (SO^{3-}). Among them, it merits to be cited the Reactive Black 5 [RB5] (AKSU; AKIN, 2010; VINODGOPAL *et al*., 1998; WANG *et al*., 2013). The choice of RB5 was due to the fact that this dye is in the class of azo-reactive dyes and used in a variety of industries, from textiles to the paper industry. In addition, RB5 presents in its structure complex groups that are difficult to degrade, constituting a high polluting potential of water resources (ARAÚJO *et al*., 2018; VINODGOPAL *et al*., 1998).

Although reports of graphite oxide exfoliation have been portrayed since 1840, when the German scientist Schafhaeutl cited graphite exfoliation with sulfuric and nitric acid, the term "graphene" was only used for the first time in 1987. Researches using Graphene became possible only in 2004, when Geim and Novolosev, from the University of Manchester, were able to isolate it using a method known as the "Scotch tape method". Through the incidence of an electromagnetic field and with the support of a Scotch adhesive tape, the authors were able to exfoliate graphene nanosheets from graphite with a high degree of purity (NOVOSELOV *et al*., 2014). This finding led Geim and Novoselov to win the Nobel Prize in Physics in 2010. Graphene is then defined as a two-dimensional sheet of sp^2 hybridized carbon atoms arranged in six-membered rings (LAI *et al*., 2019; ERSAN *et al*., 2017; RANDVIIR; BROWNSON; BANKS, 2014; DREYER *et al*., 2010). Due to its extensive properties, graphene has made it possible to develop new technologies in different areas. Thus, one can cite the construction of a graphene membrane capable of separating organic solvent from water and removing it from a gas mixture (YUSUF *et al*., 2015; HUANG *et al*., 2018; VANE *et al*., 2019); additionally, the production of composites combined graphene with ink and formed a unique coating of graphene capable of combating rust in ships and cars (MANCHESTER, 2018). In addition, other possible applications of products obtained from graphene-based composites are: development of more efficient solar cells, batteries with longer duration, production of flexible and resistant plastics, medical technologies, between many others (LI *et al*., 2019; WANG *et al*., 2013). Within the environmental science and technology, one of the applications of graphene derived nanomaterials is the removal of dyes and other organic compounds through processes such as Fenton's reaction (ARSHAD *et al*., 2018; YU *et al*., 2016).

Therefore, the present article aimed to evaluate the degradation of RB5 dye through the UV assisted Fenton-like process using Fe^{3+} ions present in AmGO as a photocatalyst. Also having specific objectives to synthesize graphene oxide by the modified Hummers method;

functionalize the graphene oxide to obtain AmGO; perform a preliminary study of the photo-Fenton reaction. Another objective is to evaluate, by means of a 2^3 factorial design with central point, the variables that influence the advanced oxidation process (dosage of AmGO, H_2O_2 concentration and pH of the dye solution) and to study the kinetics of the reaction.

A.2 METHODOLOGY

A.2.1 SYNTHESIS OF GRAPHENE OXIDE AND ITS FUNCTIONALIZATION

The synthesis of graphene oxide was realized following the modified Hummers' method. An aliquot of 1.0 g of powdered graphite (99% A.P., *Merck, Brazil*) was added along with 27.0 mL of sulfuric acid (H_2SO_4 97% A.P., *Fluka, Germany*) under stirring and controlled temperature between 0–6 °C until homogenization of the mixture. Then, 3.0 g of potassium permanganate ($KMnO_4$ 99% A.P., *Dinâmica Química, Brazil*) was gradually added to the flask and the temperature was controlled between 30–40 °C under stirring for 6 hours. After the reaction, 200.0 mL of distilled water and 10.0 mL of hydrogen peroxide (H_2O_2 30%, *Dinâmica Química, Brazil*) was added to complete the oxidation. The sample was washed with 25 mL of hydrogen chloride (HCl, 97% a.p., *Dinâmica Química, Brazil*) and 50.0 mL of distilled water until the pH of the suspension was stabilized. The result of the process described above is the graphite oxide. To obtain GO, the graphite oxide was submitted to sonication of 65 W for 4 hours in an ultrasound bath Elma, model E30H. The final material obtained was graphene oxide.

Covalent amino-functionalization of GO was carried out at the same time as the solvothermal method of anchoring of Fe_3O_4 nanoparticles in the graphene plane. For this, 360.0 mL of graphene oxide was used with 3.0 g of sodium acetate (99% A.P., *Sigma-Aldrich, Brazil*) and 0.5 g of iron chloride ($FeCl_3{\cdot}6H_2O$, *Dinâmica Química, Brazil*), and 200 mL of monoethylene glycol. The material was put under temperature and diethylenetriamine (DETA 99% A.P., *Sigma-Aldrich, Germany*) was added when the temperature reached ~ 170 ºC. The functionalization synthesis occurred in vigorous stirring speed for 6 hours and temperature strictly controlled at 180 ºC. After the 6 hours, the material had to be washed. For the first wash, was used 200.0 mL of ethanol to remove the polar organic compounds, then, the material with the ethanol was placed in a centrifuge (Quimis, model Q222T), 6500 rpm for 7 minutes. For the rest

of the washes, was added in the system distilled water into complete 500.0 mL and then repeat the process until the suspension ph stabilized (~ 9.0–9.5). Averages of 6 washes were completed.

A.2.2 CHARACTERIZATION OF GO AND AmGO

The characterization of graphene oxide (GO) and amino-Fe_3O_4-functionalized-GO (AmGO) samples were conducted by fourier transformed infrared spectroscopy (FTIR) in an IR spectrometer with attenuated total reflectance (ATR) crystal, model Shimadzu IRAffinity-1S. X-ray diffraction (XRD) was performed in a diffractometer Rigaku Ultima IV equipped with a copper radiation source. Raman spectra of all samples were acquired by a confocal raman spectrometer with laser excitation source of 532 nm, model WITEC Alpha 300R. For each sample, 10 individual spectra were measured at random points and the average intensity of each peak was used to plot the raman spectra. Finally, uv-vis spectra of AmGO was obtained by a UV-Vis spectrophotometer model ThermoFisher, model Genius 10S.

A.2.3 PRELIMINARY STUDY AND PHOTO-FENTON-*LIKE* REACTION

Preliminary experiments were carried out in duplicate and had the objective of evaluating the influence of the dosage of AmGO, hydrogen peroxide volume and the source of radiation. For this study it was chosen to perform the experiments using sunlight and UV-A radiation lamp, AmGO suspension dosage ranged between 0.5 mL and 1.0 mL (~ 6.0 $mg \cdot mL^{-1}$ of concentration) and hydrogen peroxide volume (0.5 mL and 1.0 mL). For do these tests, 25 mL of RB5 were placed in a Petri dish and combined with the variables in a way that all combinations were tested. The experiments were realized under UV-A radiation and sun radiation for 90 minutes. Then, the final concentration of the dye was determined in order to calculate the percentage of degradation of the dye. The experiments were performed on petri dishes, where 25 mL of a solution of RB5 with 106.08 $mg \cdot L^{-1}$ and 53.66 $mg \cdot L^{-1}$ of initial concentration, and one of the values of the variable in study. The final concentration of the synthetic RB5 effluent was measured in the UV-Vis spectrophotometer.

Photo-Fenton reaction occurs according to a chain reaction of a series of radical chemical reactions, so that free radicals $\bullet O_2$ and $\bullet OH$ are generated and allow the degradation of the dye

molecules (ARAÚJO *et al*., 2011). The mechanism of photo-Fenton reaction is demonstrated by Equations A1 to A4.

$$Fe^{3+} + H_2O_2 \rightarrow Fe^{2+} + HO_2^{\bullet} + H^+ \quad \text{(A1)}$$

$$Fe^{2+} + H_2O_2 \rightarrow Fe^{3+} + OH^- + OH^{\bullet} \quad \text{(A2)}$$

$$HO_2^{\bullet} \leftrightarrow H^+ + O_2^{\bullet -} \quad \text{(A3)}$$

$$Fe^{3+} + HO_2 \rightarrow Fe^{2+} + H^+ + O_2 \quad \text{(A4)}$$

According to verified by Perreault, de Faria and Elemelech (2015), the photocatalytic process of degradation of dyes takes place in three steps: adsorption of the pollutant in the active sites of catalyst, when it regards to heterogeneous process (Figure A1) (WANG *et al*., 2019c); photoactivation, through the light, provoking the photoelectric effect and consequently the *in situ* generation of free radicals •OH (DEVI *et al*., 2010); and, finally, the attack of free radicals, provoking breaks in the dye molecules. The steps of photodegradation of Methylene Blue were described by the authors in the scheme depicted in Figure A1 and might be used to ilustrate the photo-Fenton-*like* degradation of the RB5, reported in this work.

Figure A1 – scheme describing the step of a heterogeneous photo-Fenton degradation of MB by metallic nanoparticles anchored in graphene.

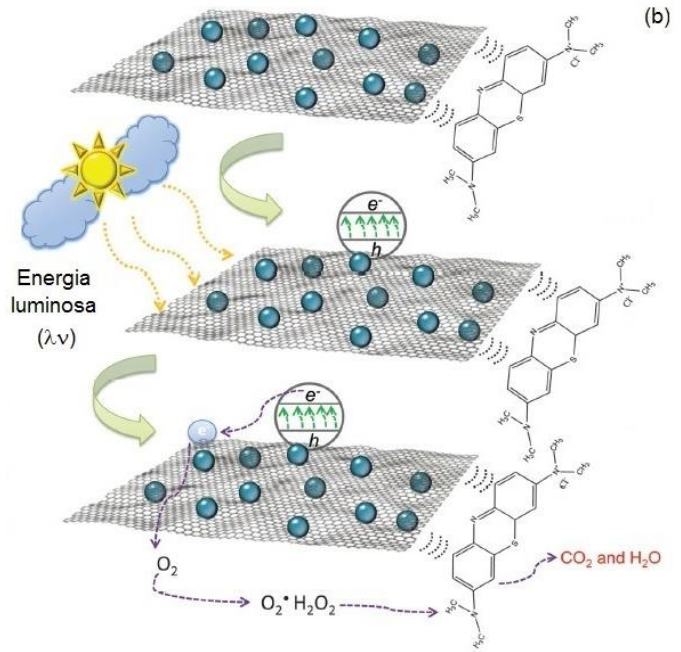

Source: adapted from Perreault, de Faria e Elemelech (2015), with permission from the Royal Society of Chemistry, Copyright 2019

A.2.4 FACTORIAL DESIGN 2^3

Following the results of preliminary study, the 2^3 factorial design was made using as variables the ph of the reaction, hydrogen peroxide concentration and volume of AmGO. Thus, were used the following values of variables: volume of AmGO, 0.0057 $g \cdot mL^{-1}$ - $V_{(AmGO)}$: 1.0 mL (-); 3.0 mL; [H_2O_2]: 0.1 $mol \cdot L^{-1}$ (-); 1.0 $mol \cdot L^{-1}$ (+); pH of RB5 solution: 4.0 (-); 8.0 (+), where the data of the central point was: $V_{(AmGO)}$: 2.0 mL; [H_2O_2]: 0.55 $mol \cdot L^{-1}$; pH 6.0. Thus, it was realized the tests with all possible combinations of the variables, following the factorial design matrix (Table A1). All acquired data were then treated in statistical analyzer software. The systems were placed in the uv light reaction under the same conditions of the preliminary study.

A.2.5 KINETIC OF PHOTODEGRADATION

The reaction kinetic was conducted using the best conditions following the results of 2^3 factorial design. Thereafter, the samples were placed in the reactor equipped with A-type UV light for times of 1, 5, 10, 15, 30, 60, 120, 180, 240, 300, 360, 420, 480 minutes. Then, the final concentration was measured on a spectrophotometer. The same experiment was carried out without the addition of H_2O_2 and uv radiation in order to evaluate the influence of adsorptive process on the overall removal of RB5. Experimental data were modeled by both linear regression and non-linear fitting of the chan and chu model, with the help of mathematical software.

A.2.6 PHOTO-FENTON-*LIKE* OF REAL TEXTILE WASTEWATER

The raw textile wastewater was collected in the Laundromat *Lavanderia Nossa Senhora do Carmo Ltd.*, located in the district of Caruaru, Pernambuco, Brazil. Experiments were performed after a previous coagulation process, and the parameters of chemical oxygen demand (COD), biochemical oxygen demand (BOD), turbidity, apparent color and total solid in aqueous medium were evaluated before and after the UV-assisted heterogeneous photo-Fenton degradation. Photo-Fenton-*like* experiments were carried out with 1.0 mL of AmGO (6.0 $mg \cdot mL^{-1}$), with 25 mL of real textile effluent, under UV-A light radiation during 120 min.

A.3 RESULTS AND DISCUSSION

A.3.1 CHARACTERIZATION

FTIR spectra for GO and AmGO are depicted in Figure A2a it is possible see the characteristic peaks at 1632.5 cm^{-1}, attributed to the carbonyl (–C=C) stretching vibration of GO. The band at 1064 cm^{-1} is referent to stretching vibrations of C–O presents in several groups containing oxygen (LI *et al*., 2013). The band between 3427–3250 cm^{-1} might be attributed to the $\delta_{(O–H)}$ vibrations, referent to moisture content in the sample, as well as the stretching vibrations of the hydroxyl and carboxyl groups of GO and amino-Fe_3O_4-functionalized-GO (ZHANG *et al*., 2015). Bands with medium intensity at 3300-3500 cm^{-1} is finding in AmGO spectrum and is attribute to the presence of –NH stretching vibration; the peak at 1168 cm^{-1} presents in GO spectrum can be attributed to the elongation of the C–O–C bonds from epoxide rings (ARAÚJO *et al*., 2018). The peak at 580.0 cm^{-1} is referent to the vibrations of the Fe–O bonds presents in magnetite (Fe_3O_4) (GUO *et al*., 2015).

XRD patterns of GO (Figure A2b) show a small peak at 2θ 26.5º (002 diffraction plane), evidencing a presence of graphitic crystalline structure, which evidences that graphite was not entirely oxidized by modified Hummers' method. Moreover, small characteristic peaks for graphene nanostructures are observed at 2θ 11º, which is related to the diffraction plane (001). Moreover, all peaks (2θ 26.5º, 44.5º and 54.6º), which indicate the presence of tridimensional crystalline structures, in standard graphite pattern (JCPDS 75-2078, 3347 Å), are not exhibited in XRD patterns of GO and AmGO.

At the Figure A2c it is possible to see in all Raman spectra the presence of the characteristic set of bands for the carbonaceous materials that are the D-band (1360 cm^{-1}) and the G-band (1560 cm^{-1}). The G-band presents the stretching movement of the sp^2 bonds between carbon atoms of the basal plane. Band D is due to Raman scattering in the discontinuity zone, which reflects disordered structures such as defects, crystal boundaries, impurities and symmetry breaking. The 2D band reflects the stacking structure of the graphene sheets along the "c" axis (FERRARI *et al*., 2006). However, this peak is not observed in the GO and AmGO spectra, it concluded that these materials might not have a perfect 2D structure, as monolayer or few-layer graphene. The intensity ratio of D to G band (I_D/I_G) is usually used to evaluate the lattice disorder of graphite derivatives (PENG *et al*., 2016). Thus, analyzing the ratio I_D/I_G in the Figure A2c, it is possible

see the AmGO presents a higher degree of characteristic disorder that can be attributed to functionalization process, since it increased from 1.02 to 1.17 after NH_2 functionalization and Fe_3O_4 anchoring on GO frameworks.

By UV-Vis spectra for GO and AmGO (Figure A2d) it is possible to see in both spectra a peak at 230 nm that is referent to $\pi \rightarrow \pi^*$ transition, attributed to the C=C bonds of aromatic rings. It is also possible see a shoulder at 300 nm in the GO spectrum, which is attributed to the C=O groups (LI *et al*., 2008).

Figure A2 – a) FTIR spectra of GO and AmGO; b) XRD patterns of GO and AmGO; c) Raman spectra for GO and AmGO; and d) UV-Vis spectra for GO and AmGO.

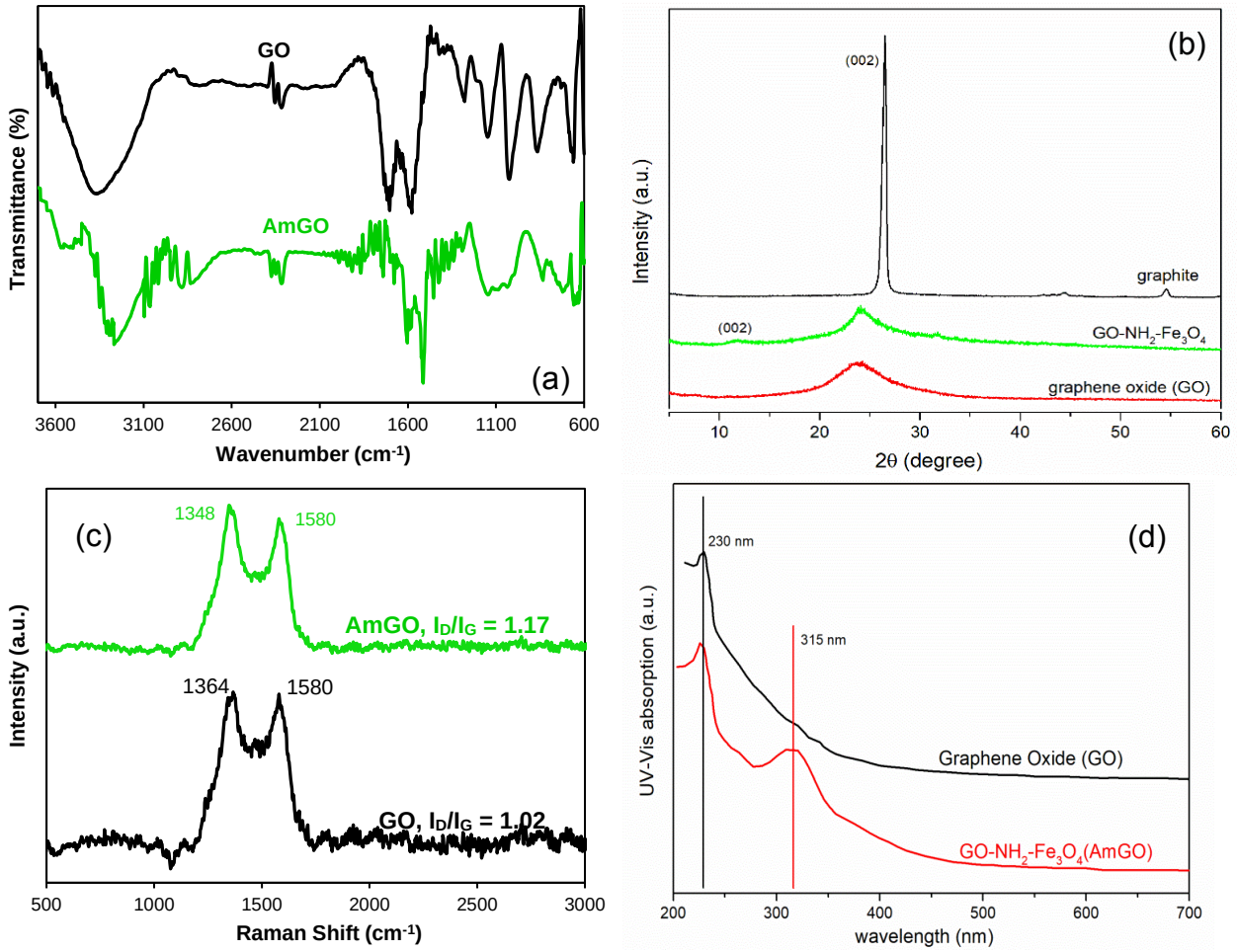

Source: the author (2019).

A.3.2 PRELIMINARY ASSESSMENTS

Preliminary studies were carried out to evaluate the range and influences of the main variables to be investigated in 2^3 factorial design. Figure A3a shows that the heterogeneous photodegradation of RB5 realized under UV-A radiation were more efficient than those realized under solar radiation. The large discrepancy of percentage yield results would not justify the use of sunlight radiation, even though its costs in terms of energy is lower than UV-assisted Fenton-like. Then, it was analyzed the influence of the functionalized graphene oxide volume and hydrogen peroxide volume under UV-A radiation (Figure A3b and Figure A3c). Analyzing the graphs in Figure A3, it is possible observed that the systems containing 1.0 mL of AmGO presented a higher percentage of RB5 when compared to the systems formed with 0.5 mL of AmGO and the same volume of H_2O_2. These results were already expected because the higher amount of AmGO corresponds to a higher adsorption capacity, besides being source of Fe^{3+} ions to act in the Fenton's reaction. From Figure A3b, it is possible conclude that the increase in the volume of hydrogen peroxide did not cause a significant difference in the percentage of degradation of RB5. In addition, it can be concluded that the hydrogen peroxide acting alone is not sufficient to degrade the RB5.

Figure A3 – a) Influence of UV and solar light irradiation on photo-Fenton-*like* degradation of RB5; b) Effect of AmGO dosage (in mL of AmGO suspension of 6.0 mg·mL^{-1}) in the photodegradation of RB5; c) effect of hydrogen peroxide (H_2O_2, 30%) volume in the photodegradation of RB5

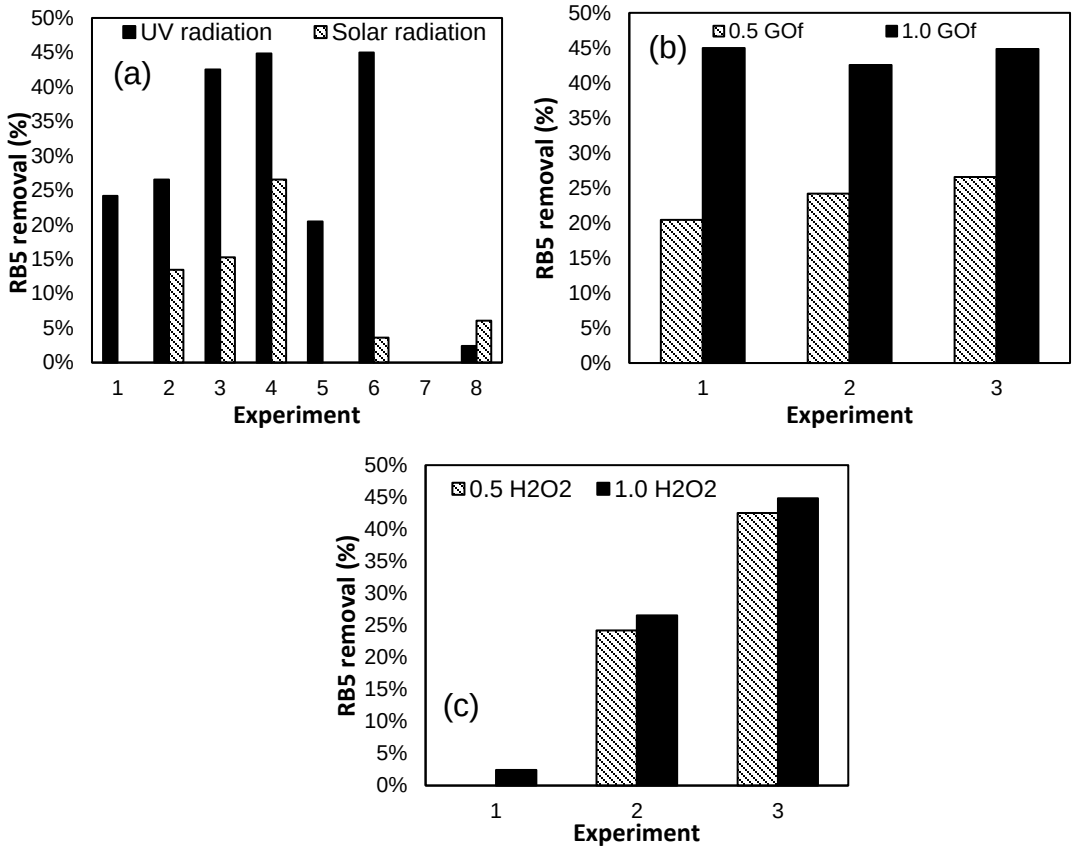

Source: the author (2018).

A.3.3 FACTORIAL DESIGN 2^3

According to the results obtained in the preliminary study, it was decided to carry out the factorial design 2^3 under UV-A reaction, with variation of AmGO volume (1.0 mL (-); 3.0 mL (+)); and, as the variation of the volume of hydrogen peroxide did not present relevant results, it was chosen to work with the variation of peroxide concentration (0.1 $mol \cdot L^{-1}$ (-); 1.0 $mol \cdot L^{-1}$ (+)). The other variable chosen to complete the 2^3 factorial design was the pH (4.0 (-); 8.0 (+)) since this is an important parameter for the photo-Fenton-*like* reaction. The experiments of factorial design were realized in petri dishes with 25 mL of RB5 dye, with an initial concentration equal to 103.68 $mg \cdot L^{-1}$, at room temperature. The results are shown in Table A1 and were analyzed in statistical software and it was possible to make a Pareto graph (Figure A5a) to analyze the most efficient combination of values for the process.

The analysis of the Pareto diagram evidenced that all effects of the variables evaluated were statistically significant, however, only the AmGO dosage had a major influence, followed by the pH of the reaction. It can also be analyzed that all interactions were significant for the reaction. The dosage of AmGO (in mL of suspension of 6.0 $mg \cdot mL^{-1}$) was the most significant variable of the 2^3 factorial design. This can be explained because the larger volume/dosage represents a greater availability of active sites from the catalyst in the reaction and with this, the efficiency of the reaction increases, once the value of Pareto graph was positive. From the Pareto diagram, it is also possible to observe that the concentration of hydrogen peroxide contributed positively; therefore, higher concentrations of H_2O_2 lead to more efficient process. This is already expected due to the efficiency of the degradation increases with increasing of peroxide concentration until reaching a maximum value where any concentration value above this maximum value will contribute to the recombination of the hydroxyl radicals (TROVÓ *et al*., 2013). Pareto diagram of Figure A4a shows that the increase of the percentage of degradation was observed with increase of the AmGO. It was also possible to observe that the optimum value of peroxide concentration was close to the central point.

Analyzing the changing of the ph of the solution of RB5 according to the surface respond graph, it is possible to observe its importance in increasing the percentage of degradation (%Rem), since the surface of response (Figure A4b) shows an increase in intensity as the level of pH increases (- for +). In the literature, it is possible see that the ideal pH for the photo-Fenton reaction is 3. However, the result obtained in the 2^3 factorial design was that the ph influences the process positively. These results can be justified by the fact that the reaction studied in this paper is of the heterogeneous type that means the iron ions would be impregnated in the catalyst and, therefore, do not coagulate or form complexes at high pH. The confirmation of this result, however, is only confirmed after performing a FTIR analysis in the sample after the photo-Fenton process. This result has an advantage since one of the possible application of this catalyst is in the photo-Fenton-*like* reaction for the treatment of effluents of the textile industry and this type of effluent presents high pH and, therefore, it would not be necessary to make the correction of the pH, which can be characterized as cost saving.

Table A1 – Factorial design 2^3 matrix and final concentration of RB5 after UV-assisted photo-Fenton like degradation

pH	**AmGO** ($mg \cdot mL^{-1}$)	**[H_2O_2]** ($mol \cdot L^{-1}$)	**Final RB5 concentration** ($mg \cdot L^{-1}$)		**C MED** ($mg \cdot L^{-1}$)
+	+	+	0.48	0.47	0.48
+	+	-	0.54	0.62	0.58
+	-	+	18.32	18.11	18.22
+	-	-	21.18	21.36	21.27
-	+	+	2.21	1.93	2.07
-	+	-	2.24	2.32	2.28
-	-	+	34.41	36.82	35.61
-	-	-	40.31	41.83	41.07
0	0	0	7.43		
0	0	0	6.30		6.58
0	0	0	6.01		

Figure A4 – a) Pareto graph for the photodegradation process of the RB5, evaluated variables: OG-NH_2-Fe_3O_4 (AmGO) dosage; pH of the RB5 solution (pH); and H_2O_2 concentration (H_2O_2); b) Surface respond graph AmGO versus H_2O_2 versus %Rem; c) Surface respond graph AmGO versus pH versus %Rem; Experiments performed at 25°C, with 25 mL of solution.

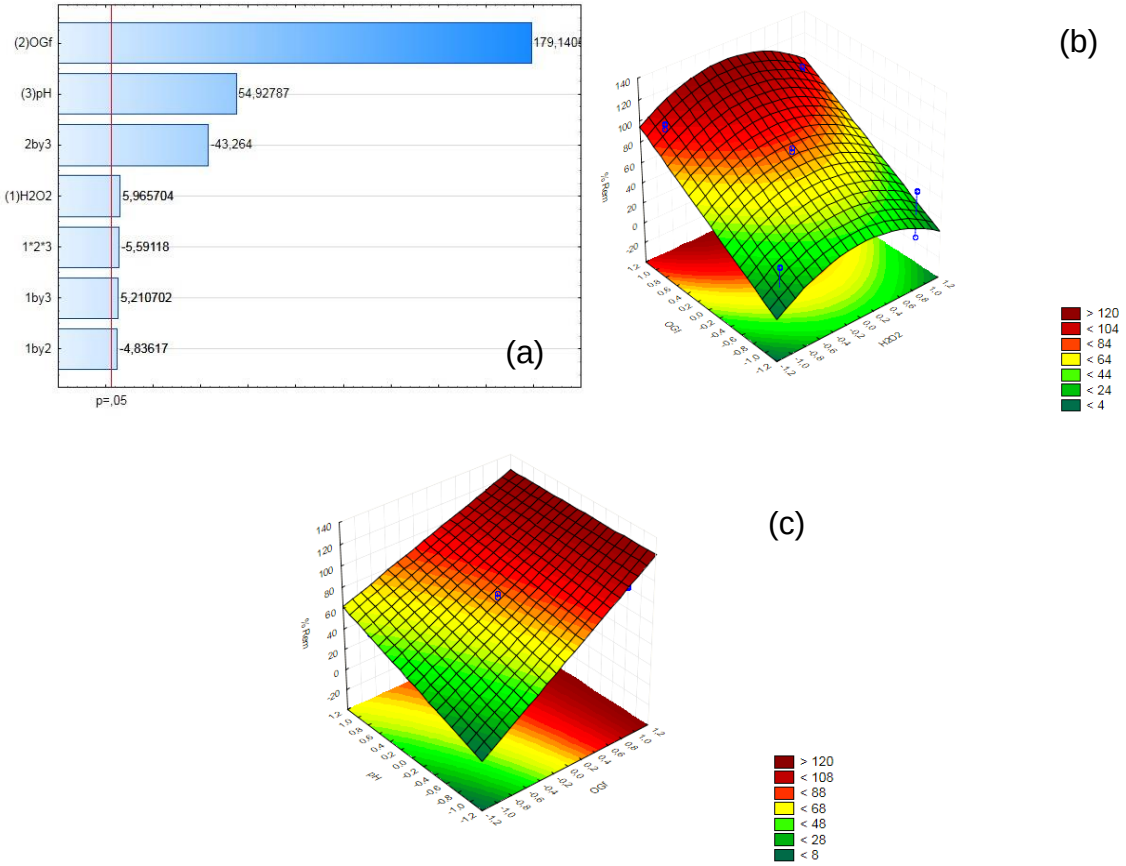

Source: the author (2018).

A.3.4 KINETIC AND MATHEMATICAL MODELING

To evaluate the kinetic of degradation, it was evaluated the change in dye concentration over time in systems with an initial concentration of 100 mg·L^{-1} and 50 mg·L^{-1}, and with a pH value, H_2O_2 concentration and AmGO dosage optimized according to the results found in 2^3 factorial design. Kinetic behavior of UV-assisted Fenton-like degradation of RB5 is depicted in the curve of removal percentage (%Rem) *versus* t (Figure A5a and Figure A5b) for the photo-Fenton process and adsorption process. Although the object of this investigation was photo-Fenton-*like* process, it was necessary to analyze the adsorption influence of amgo. According to Perreault, de Faria and Elimelech (2015), the adsorption of the pollutant by Fe_3O_4-graphene surface is the first step, prior to the generation of hydroxyl free radicals (•OH) and the attack/degradation of dye

molecules by •OH radicals. The Fe(III) ions, the photo-Fenton catalyst, were attached on the surface of the amino-graphene oxide by van der Waals forces, electron donor-receptor interactions, and other weak interactive forces (TAVASSOLI LARIJANI *et al*., 2015). On the other hand, amino-graphene oxide (NH-GO), a material of high adsorptive power (FRAGA *et al*., 2018), has shown strong capacity to retain RB5 molecules. Then, degradation of RB5 occurred by adsorption and photo-Fenton-*like* process, which is depicted in the Figure A5. Therefore, to unravel how adsorption of RB5 by AmGO influenced the whole RB5 degradation, it was necessary to realize adsorption tests in the same conditions previously described, without the addition of H_2O_2 and UV radiation, though. Analyzing the graphs of Figure A5a and Figure A5b, it can be seen that for the system with concentration of RB5 equal to 106.08 $mg \cdot L^{-1}$ the equilibrium state is reached after 120 minutes, whereas for the system with RB5 concentration of 53.66 $mg \cdot L^{-1}$ the equilibration time is only reached in 240 minutes.

Figure A5 – a) % Rem *versus* t (min) graph for systems with initial concentration of RB5 equal to 106.08 $mg.L^{-1}$; b) % Rem versus t (min) graph for systems w ith initial concentration of RB5 equal to 53.66 $mg.L^{-1}$

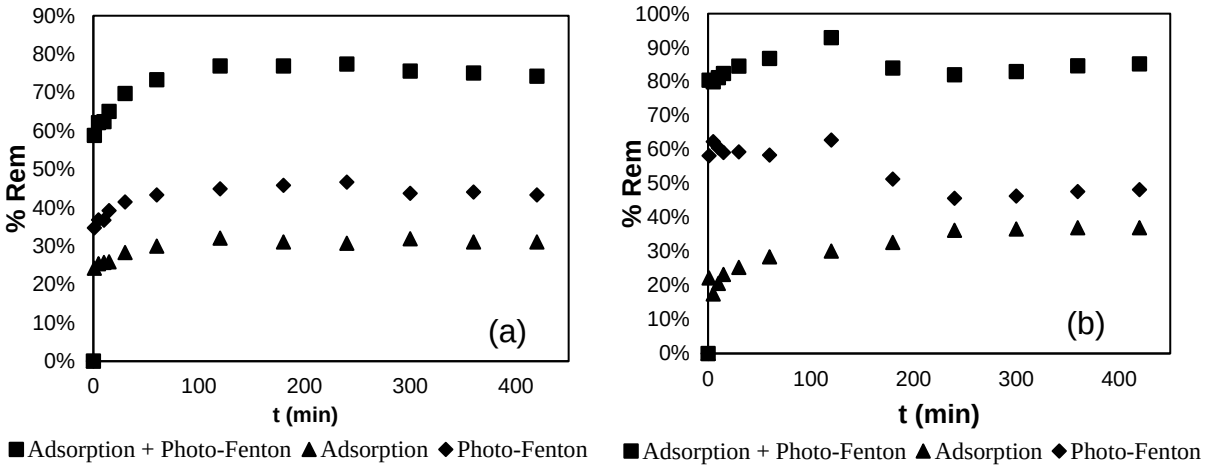

Source: the author (2018).

After kinetic experiments, it was applied the nonlinear fitting for the kinetic pseudo-first-order proposed by (CHAN; CHU, 2003), mathematically represented by Equation A5.

$$C/C_0=1 - t/(\rho+\sigma t) \quad (A5)$$

Through the linearization of Equation A5, the values of ρ and σ were found and the graph of $t/(1 - c/c_0)$ *versus* t where the angular coefficient and the slope of the generated line represents, respectively, ρ and σ. The linear fit of chan and chu model for the kinetic data acquired for initial RB5 concentration 53.66 and 106.08 $mg \cdot L^{-1}$ are shown in Figure A6a and Figure A6b, respectively. According to Chan and Chu (2003), the constants $1/\rho$ (min^{-1}) and $1/\sigma$ represent the initial removal rate of RB5 and the maximum oxidative capacity in the process. Analyzing the data in Table A2, it is possible conclude that the system with a highest concentration of RB5 presents a higher initial rate of degradation, whereas the system with lower concentration of the dye presents a greater oxidative capacity. This means that, at the beginning of the reaction, the system with a highest concentration of dye will degrade faster, but for a long enough time, to the point that the entire degradation reaction has been completed; the lower concentration system will present a larger degradation. In addition, it can be stated that the proposed model was fitted efficiently to the experimental data, with linear regression values greater than 0.99. Then, the values obtained experimentally and those obtained from the kinetic model were evaluated. Non-linear fitting of chan and chu model for kinetic data for 53.66 and 106.08 $mg \cdot L^{-1}$ are shown in Figure A6c and Figure A6d, respectively.

Analyzing the graph of Figure A6c it is possible seen that the reaction occurs faster in the first 60 minutes and the process stabilizes after 180 minutes. In Figure A6d it can be seen that the reaction occurs most rapidly in the first 60 minutes and stabilizes at 120 minutes. This is explained by the fact that in the first few minutes hydrogen peroxide is consumed instantly for the formation of hydroxyl radicals. As the H_2O_2 concentration decreases, the formation of hydroxyl radicals is impaired, initiating the slow reaction step. Through the equation of the trend line generated for both graphs of Figure A6 (a and b), it was possible to determine the value of the constants (ρ) and (σ). The results are shown in Table A2.

Figure A6 – Linear regression of the kinetic model of pseudo-first order proposed by Chan and Chu (2003) for system with an initial concentration of RB5 equal to 53.66 mg.L^{-1} (a) and 106.08 mg.L^{-1} (b); Non-linear fitting of experimental data by Chan and Chun model for systems with initial concentration of RB5 equal to 53.66 mg.L^{-1} (c) and 106.08 mg.L^{-1} (d)

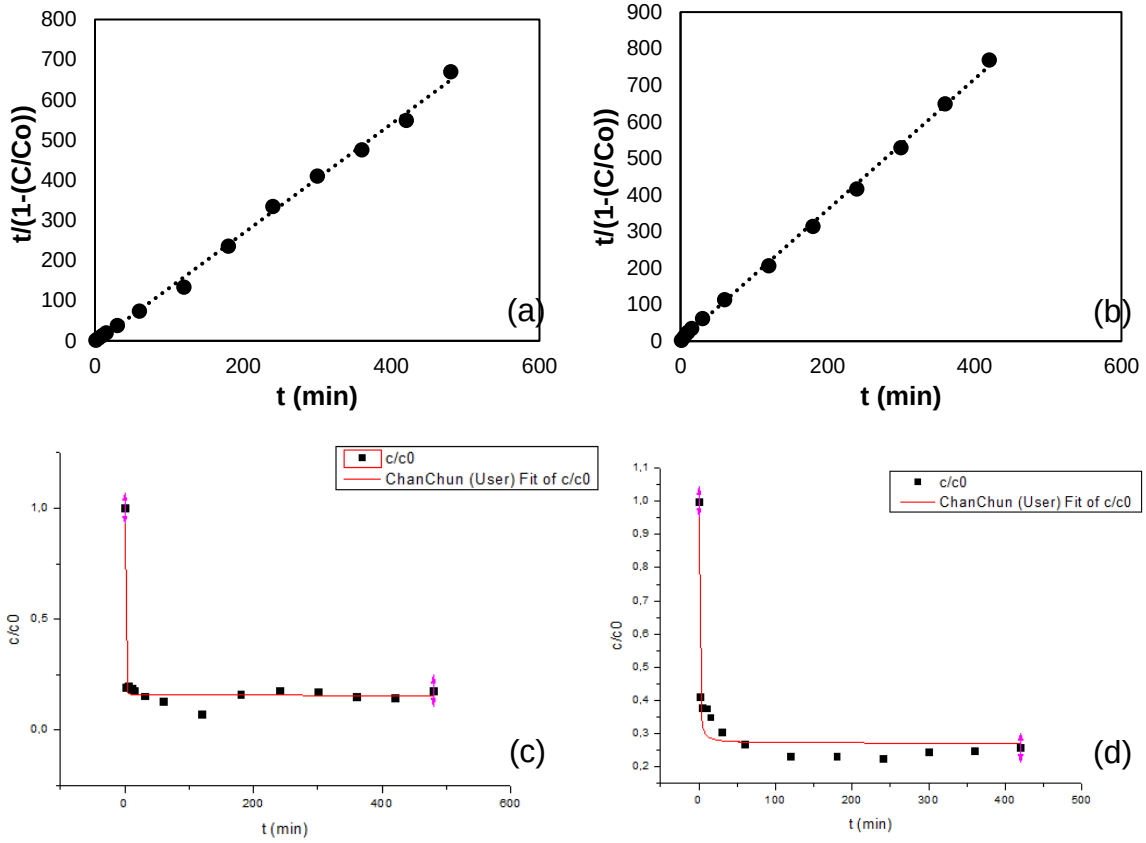

Source: the author (2018).

Table A2 – Values of ρ and σ found by linearization of the kinetic equation of pseudo-first order.

Initial concentration (mg.L^{-1})	**ρ (min)**	**σ**	**1/ρ (min^{-1})**	**1/σ**	**R²**
53.66	-1.52	1.20	-0.66	0.83	0.9992
106.08	0.41	1.33	2.41	0.75	0.9996

A.3.5 PHOTODEGRADATION OF REAL TEXTILE WASTEWATER

Experiments carried out with raw textile wastewater showed that after the photodegradation by AmGO, the main paramenters of the effluent was in agreement with Brazilian legislative quality standards for water bodies (Brazil, 2005). The exception was the color measurement (Hazen), which remained 164 Hazen after the photodegration, above the limit established in legislation, 75 Hazen (Table A3). Such result happened since the degradation of dyes was influenced by the presence of other compounds of the raw wastewater. Similarly as the adsorptive processes, the presence of surfactants, salts, metallic ions and other chemical species in the raw wastewater, established a competitive adsorption for AmGO active sites, and consequently, it lowered the photodegradation of dyes, the main responsible for colorimetry parameters.

Table A3 - Parameters of raw textile wastewater before and after the photodegradation. Experiments carried out under the following conditions: AmGO dosage 6.0 $mg \cdot mL^{-1}$; room temperature, 25 ºC; 25 mL of wastewater; UV-light radiation

	Before photo-Fenton-*like*		**After photo-Fenton-*like***		
	Raw wastewater	**Coagulated wastewater**	**Raw wastewater**	**Coagulated wastewater**	**Maximum limit***
Turbidity (NTU)	91.4	54.2	32.4	24.9	100.0
pH	7.86	7.51	9.18	9.01	6.00–9.00
Color (Hazen)	585	266	180	164	75
COD (mg $O_2 \cdot L^{-1}$)	131.99	31.53	115.73	75.68	N/A
BOD (mg $O_2 \cdot L^{-1}$)	555	471	N/A	N/A	10.0

* Classification of “fresh water type 3”, destined to human consumption after conventional and specialized treatments, according to the resolution 357 of CONAMA (Brazil, 2005).

A.4 CONCLUSIONS

Analyzing the degradation of the RB5, it was seen that the Fe^{3+} ions present on the surface of the amgo acted as a catalyst in the photo-Fenton-*like* reaction. Characterization analysis of graphene oxide showed the success of the GO synthesis by modified hummers method and its functionalization and anchoring of Fe_3O_4¬ nanoparticles in the graphene plane. Results of XRD and Raman spectroscopy confirmed the GO synthesis, showing the characteristic peaks of three-dimensional crystalline graphite were found, and peaks indicating an increase in the degree of disorder of the material. The functionalization of graphene oxide and the solvothermic method of anchoring Fe_3O_4 nanoparticles in the solvothermic method of anchoring Fe_3O_4 nanoparticles in the graphene plane were confirmed by FTIR and sem analyzes where the images show the presence of iron at various points on go surface.

The preliminary study showed that the best working variables for 2^3 factorial design with center point would be the volume of AmGO, and ph, it was also seen that the volume of H_2O_2 had no effect under the reaction. As the results of the 2^3 factorial design exhibited that the most influential variable in the process was the volume of AmGO, a result that is justified by the fact that the higher volume of amgo represents more ions Fe^{3+} in the system to act on the degradation of hydrogen peroxide and formation of the hydroxyl radicals. It was also observed that the reaction does not need to occur at acid ph to obtain a higher efficiency. Finally, the kinetic study showed that the degradation of the RB5 best suited the kinetic model of pseudo-first order proposed by chan and chun (2003) for photodegradation.

REFERENCES

1. AKSU, Z.; AKIN, A. B. Comparison of remazol black b biosorptive properties of live and treated activated sludge. **Chemical Engineering Journal**, v. 165, p. 184–193, 2010.

2. ARAÚJO, C. M. B.; ASSIS FILHO, R. B.; BAPTISTTELLA, A.M.S.; NASCIMENTO, G. F. O.; COSTA, G. R. B.; CARVALHO, M. N.; GHISLANDI, M. G.; DA MOTTA SOBRINHO, M. A. Systematic study of graphene oxide production using factorial design techniques and its application to the adsorptive removal of methylene blue dye in aqueous medium. **Materials Research Express**, v. 5, n. 65042, 2018.

3. ARSHAD, A.; IQBAL, J.; AHMAD, I.; ISRAR, M. Graphene/Fe_3O_4 nanocomposite: Interplay between photo-Fenton type reaction, and carbon purity for the removal of methyl orange. **Ceramics International**, v. 44, p. 2643–2648, 2018.

4. BABUPONNUSAMI, A.; MUTHUKUMAR, K. A review on Fenton and improvements to the Fenton process for wastewater treatment. **Journal of Environmental Chemical Engineering**, v. 2, p. 557–572, 2014.

5. Brazil., 2005. **Ministério do Meio Ambiente. Resolução n. 357**, "**Ministry of Environment, Resolution # 357**" (*in Portuguese*). Brasília.

6. CHAN, K. H.; CHU, W. Modeling the reaction kinetics of Fenton's process on the removal of atrazine. **Chemosphere**, v. 51, p. 305–311, 2003.

7. DEVI, L. G.; KUMAR, S. G.; RAJU, K. S. A.; RAJASHEKHAR, K. E. Photo-Fenton and photo-Fenton-like processes for the degradation of methyl orange in aqueous medium: Influence of oxidation states of iron. **Chemical Papers**, v. 64 (3), p. 378–385, 2010.

8. DREYER, D. R.; RUOFF, R. S.; BIELAWSKI, C. W. From Conception to Realization: An Historial Account of Graphene and Some Perspectives for Its Future. **Angewandte Chemie International Edition**, v. 49, p. 9336–9344, 2010.

9. ERSAN, G.; APUL, O. G.; PERREAULT, F.; KARANFIL, T. Adsorption of organic contaminants by graphene nanosheets: A review. **Water Research**, v. 126, p. 385–398, 2017.

10. FERRARI, A. C.; MEYER, J. C.; SCARDACI, V.; CASIRAGHI, C.; LAZZERI, M.; MAURI, F.; PISCANEC, S.; JIANG, D.; NOVOSELOV, K. S.; ROTH, S.; GEIM, A. K. Raman spectrum of graphene and graphene layers. **Physical Review Letters**, v. 97, p. 1–4, 2006.

11. FRAGA, T. J. M.; DE LIMA, L. E. M.; DE SOUZA, Z. S. B.; CARVALHO, M. N.; FREIRE, E. M. P. L.; GHISLANDI, M. G.; DA MOTTA, M. A. Amino-Fe_3O_4-functionalized graphene oxide as a novel adsorbent of Methylene Blue: kinetics, equilibrium, and recyclability aspects. **Environmental Science and Pollution Research**, v. 26, p. 28593–28602, 2018.

12. GUO, L.; YE, P.; WANG, J.; FU, F.; WU, Z. Three-dimensional Fe_3O_4-graphene macroscopic composites for arsenic and arsenate removal. **Journal of Hazardous Materials**, v. 298, p. 28–35, 2015.

13. HUANG, S.; DAKHCHOUNE, M.; LUO, W.; OVEISI, E.; HE, G.; REZAEI, M.; ZHAO, J.; ALEXANDER, D. T. L.; ZÜTTEL, A.; STRANO, M. S.; AGRAWAL, K.V. Single-layer graphene membranes by crack-free transfer for gas mixture separation. **Nature Communications**, v. 9, p. 1–11, 2018.

14. INCE, N. H.; TEZCANLI, G. Treatability of textile dye-bath effluents by advanced oxidation: preparation for reuse. **Water Science Technology**, v. 40, p. 183–190, 1999.

15. KANG, S.-F.; LIAO, C.-H.; PO, S.-T. Decolorization of textile wastewater by photo-fenton oxidation technology. **Chemosphere**, v. 41, p. 1287–1294, 2000.

16. KUNZ, A.; PERALTA-ZAMORA, P.; MORAES, S.G.; DURÁN, N. Novas tendências no tratamento de efluentes têxteis, "New trends in the treatment of textile effluents" (*in Portuguese*). **Química Nova**, v. 25, p. 78–82, 2002.

17. LI, D.; MÜLLER, M. B.; GILJE, S.; KANER, R. B.; WALLACE, G. G. Processable aqueous dispersions of graphene nanosheets. **Nature Nanotechnology**, v. 3, p. 101–105, 2008.

18. LI, G.; HUANG, B.; PAN, Z.; SU, X.; SHAO, Z.; AN, L. Advances in three-dimensional graphene-based materials: configurations, preparation and application in secondary metal (Li, Na, K, Mg, Al)-ion batteries. **Energy and Environment Science**, v. 12, p. 2030–2053, 2019.

19. LI, Y., DU, Q., LIU, T., PENG, X., WANG, J., SUN, J., WANG, Y., WU, S., WANG, Z., XIA, Y., XIA, L. Comparative study of methylene blue dye adsorption onto activated carbon, graphene oxide, and carbon nanotubes. **Chemical Engineering Research and Design**, v. 91, p. 361–368, 2013.

20. MANCHESTER, University of, Graphene-based composite materials [WWW Document]. Graphene, 2018. <https://www.graphene.manchester.ac.uk/learn/applications/composites-and-coatings/> (accessed in 5.19.19).

21. NOVOSELOV, H. S.; GEIM, A. K.; MOROZOV, S. V.; JIANG, D.; ZHANG, Y.; DUBONOS, S. V.; GRIGORIEVA, I. V.; FIRSOV, A. A. Electric field effect in atomically thin carbon films. **Science**, v. 306, p. 666–669, 2004.

22. PENG, W.; LI, H.; LIU, Y.; SONG, S. Comparison of Pb(II) adsorption onto graphene oxide prepared from natural graphites: Diagramming the Pb(II) adsorption sites. **Applied Surface Science**, v. 364, p. 620–627, 2016.

23. PERREAULT, F.; DE FARIA, A. F.; ELIMELECH, M. Environmental applications of graphene-based nanomaterials. **Chemical Society Reviews**, v. 44, p. 5861–5896, 2015.

24. RAMIREZ, J. H.; COSTA, C. A.; MADEIRA, L. M. Experimental design to optimize the degradation of the synthetic dye Orange II using Fenton's reagent. **Catalysis Today**, v. 107–108, p. 68–76, 2005.

25. RANDVIIR, E. P.; BROWNSON, D. A. C.; BANKS, C. E. A decade of graphene research : production , applications and outlook. **Biochemical Pharmacology**, v. 17, p. 426–432, 2014.

26. TAVASSOLI LARIJANI, H.; DARVISH GANJI, M.; JAHANSHAHI, M. Trends of amino acid adsorption onto graphene and graphene oxide surfaces: a dispersion corrected DFT study. **RSC Advances**, v. 5, p. 92843–92857, 2015.

27. TROVÓ, A. G.; GOMES JUNIOR, O.; MACHADO, A. E. H.; BORGES NETO, W.; SILVA, J.O. Degradation of the herbicide paraquat by photo-fenton process: optimization by experimental design and toxicity assessment. **Journal of the Brazilian Chemical Society**, v. 24, p. 76–84, 2013.

28. VANE, L. M. Review: membrane materials for the removal of water from industrial solvents by pervaporation and vapor permeation. **Journal of Chemical Technology and Biotechnology**, v. 94, p. 343–365, 2019.

29. VINODGOPAL, K.; PELLER, J.; MAKOGON, O.; KAMAT, P. V. Ultrasonic mineralization of a reactive textile azo dye, Remazol Black B. **Water Research**, v. 32, p. 3646–3650, 1998.

30. WANG, H.; SUN, K.; TAO, F.; STACCHIOLA, D. J.; HU, Y. H. 3D Honeycomb-Like Structured Graphene and Its High Efficiency as a Counter-Electrode Catalyst for Dye-Sensitized Solar Cells. **Angewantde Chemie International Edition**, v. 52, p. 9210–9214, 2013.

31. YU, L.; CHEN, J.; LIANG, Z.; XU, W.; CHEN, L.; YE, D. Degradation of phenol using Fe_3O_4-GO nanocomposite as a heterogeneous photo-Fenton catalyst. **Separation and Purification Technology**, v. 171, p. 80–87, 2016.

32. YUSUF, M.; ELFGHI, F.M.; ZAIDI, S.A.; ABDULLAH, E.C.; KHAN, M.A. Applications of graphene and its derivatives as an adsorbent for heavy metal and dye removal: A systematic and comprehensive overview. **RSC Advances**, v. 5, p. 50392–50420, 2015.

33. ZHANG, F.; SONG, Y.; SONG, S.; ZHANG, R.; HOU, W. Synthesis of Magnetite–Graphene Oxide-Layered Double Hydroxide Composites and Applications for the Removal of Pb(II) and 2,4-Dichlorophenoxyacetic Acid from Aqueous Solutions. **ACS Applied Materials and Interfaces**, v. 7, p. 7251–7263, 2015.

APPENDIX B – Phytotoxicity assessment data of carbonaceous frameworks: xGNP, nGO and nGO-NH_2-Fe_3O_4

Table B1 – data of the measurements of seed germination, root elongation, SG and SE of *Lactuca sativa L* after the exposition to commercial GNP samples.

xGNP®										
Sample	100%		30%		10%		3%		1%	
Duplicity	A	B	A	B	A	B	A	B	A	B
% germ	30%	70%	80%	50%	70%	100%	100%	90%	100%	80%
Av. % germ	50%		65%		85%		95%		90%	
SG	**-0.67**	**-0.22**	**-0.11**	**-0.44**	**-0.22**	**0.11**	**0.11**	**0.00**	**0.11**	**-0.11**
Root length (cm)	2	1.3	1.9	1.1	1	0.9	1.2	1.1	1.1	2.2
	1.1	1.9	2.8	1.9	0.9	1.5	2.3	0.9	0.3	1
	1	1.2	0.7	2.3	1.6	0.6	0.9	1	0.9	1
		1.2	1.4	0.9	1.3	1	1.1	1.5	1	0.6
		0.7	1.4	1.9	0.5	0.9	1.8	0.9	1.5	0.6
		1.4	0.9		0.5	1.3	1.2	0.8	1.3	1.1
		0.6	0.5		0.5	1	1.8	2.4	1.9	0.9
			1		0.6	1.2	0.9	2.1	1	1.5
						0.2	0.9	2	0.8	
						2.2	1.5		0.9	
Elong. (cm)	1.37	1.19	1.33	1.62	0.86	1.08	1.36	1.41	1.07	1.11
Av. Elong. (cm)	1.28		1.47		0.97		1.39		1.09	
SE	**0.25**	**0.09**	**0.22**	**0.49**	**-0.21**	**-0.01**	**0.25**	**0.29**	**-0.02**	**0.02**

Source: reproduced from the Supplementary Material of de Oliveira *et al*., (2019), with permission from Elsevier, Copyright, 2019.

Table B2 – data of the measurements of seed germination, root elongation, SG and SE of *Lactuca sativa L* after the exposition to nGO samples.

nGO										
Sample	100%		30%		10%		3%		1%	
Duplicity	A	B	A	B	A	B	A	B	A	B
% germ	30%	20%	40%	30%	50%	40%	60%	40%	70%	90%
Av. % germ	25%		35%		45%		50%		80%	
SG	**-0.67**	**-0.78**	**-0.56**	**-0.67**	**-0.44**	**-0.56**	**-0.33**	**-0.56**	**-0.22**	**0.00**
Root length (cm)	1.5	0.4	1.2	0.2	1.7	0.3	2.1	0.5	0.2	2.4
	1	0.3	0.3	0.2	0.2	0.2	0.9	0.2	0.4	1.8
	0.9		0.1	1.1	0.3	0.4	0.9	0.1	0.6	1.5
			0.5		0.3	0.1	0.5	0.3	0.5	0.4
					0.2		0.4		0.4	0.4
							0.2		2.1	0.3
									1.8	0.2
										0.5
										1.1
Elong. (cm)	1.13	0.35	0.53	0.50	0.54	0.25	0.83	0.28	0.86	0.96
Av. Elong. (cm)	0.74		0.51		0.40		0.55		0.91	
SE	**0.04**	**-0.68**	**-0.52**	**-0.54**	**-0.50**	**-0.77**	**-0.24**	**-0.75**	**-0.21**	**-0.12**

Table B3 – data of the measurements of seed germination, root elongation, SG and SE of *Lactuca sativa L* after the exposition to nGO-NH_2-Fe_3O_4 samples.

nGO-NH-Fe_3O_4										
Sample	100%		30%		10%		3%		1%	
Duplicity	A	B	A	B	A	B	A	B	A	B
% germ	40%	70%	70%	60%	90%	100%	80%	100%	100%	100%
Av. % germ	55%		65%		95%		90%		100%	
SG	**-0.56**	**-0.22**	**-0.22**	**-0.33**	**0.00**	**0.11**	**-0.11**	**0.11**	**0.11**	**0.11**
Root length (cm)	3.5	2.1	1.2	2.4	3.5	0.6	0.4	0.2	1.1	2.2
	2	0.9	0.8	2.8	4.2	0.5	0.2	0.9	2.1	0.3
	1.5	0.4	0.5	1.5	1.1	0.1	1.2	0.4	2.1	0.4
	0.9	1.5	0.4	1.5	0.2	2.1	1.1	1.1	0.4	0.3
		1.7	2.1	1.2	0.1	2.5	1	3.1	3.2	1.8
		2.1	1.3	0.9	0.5	0.9	2.5	0.9	0.9	1.1
		0.5	0.5		0.4	1.1	1.4	0.4	0.9	0.6
					1.3	0.4	1.5	0.4	0.5	2.2
					0.9	0.4		1	0.4	2.5
						0.1		0.3	0.3	0.9
Elong. (cm)	1.98	1.31	0.97	1.72	1.36	0,87	1,16	0,87	1,19	1,23
Av. Elong. (cm)	1.64		1.34		1.11		1.02		1.21	
SE	**0.81**	**0.21**	**-0.11**	**0.57**	**0.24**	**-0.20**	**0.07**	**-0.20**	**0.09**	**0.13**

APPENDIX C – Magnetization assessment

Magnetization measurements were carried out at room temperature, using a vibrating sample magnetometer (VSM), model Av 7 (*Microsense*), ame methodology reported by Da Silva *et al*. (2021). Differently from Fe_3O_4 magnetization, the coercivity field and remnant magnetization cannot be detected from the curve, indicating that nGO-NH_2-Fe_3O_4 has superparamagnetic properties.

Figure C1 – magnetization analysis of nGO-NH_2-Fe_3O_4 in a comparative basis with nGO-Fe_3O_4 and pure Fe_3O_4.

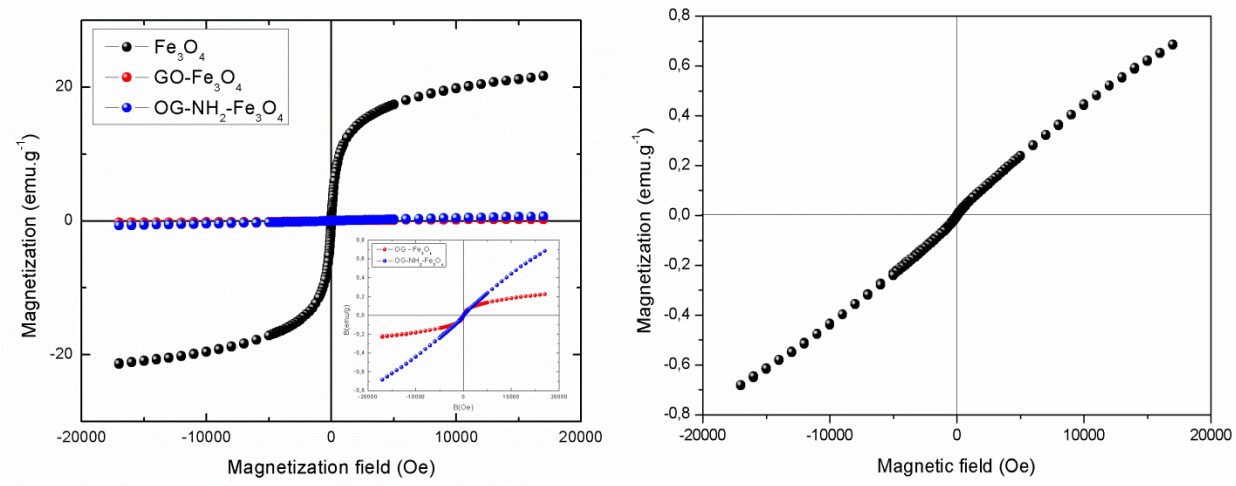

Source: the author (2020).

APPENDIX D – Study of sedimentation of nGO and nGO(NH)R/C

Decantation assays were carried out with the objective of determine the time in which the samples of nGO and nGO(NH)R/C (1:1 w/w) fully sedimentate. For that, 1.0 g of each sample was weighted and deposited in graduated beaker of 100 mL with 100 mL of distilled water. The suspension was then agitated until fully homogenization. Finally, both beakers were placed in a plane surface (Figure D1) and the time began to set.

Figure D1 – Decantation assays with nGO and nGO(NH)R/C (1:1) in aqueous suspension.

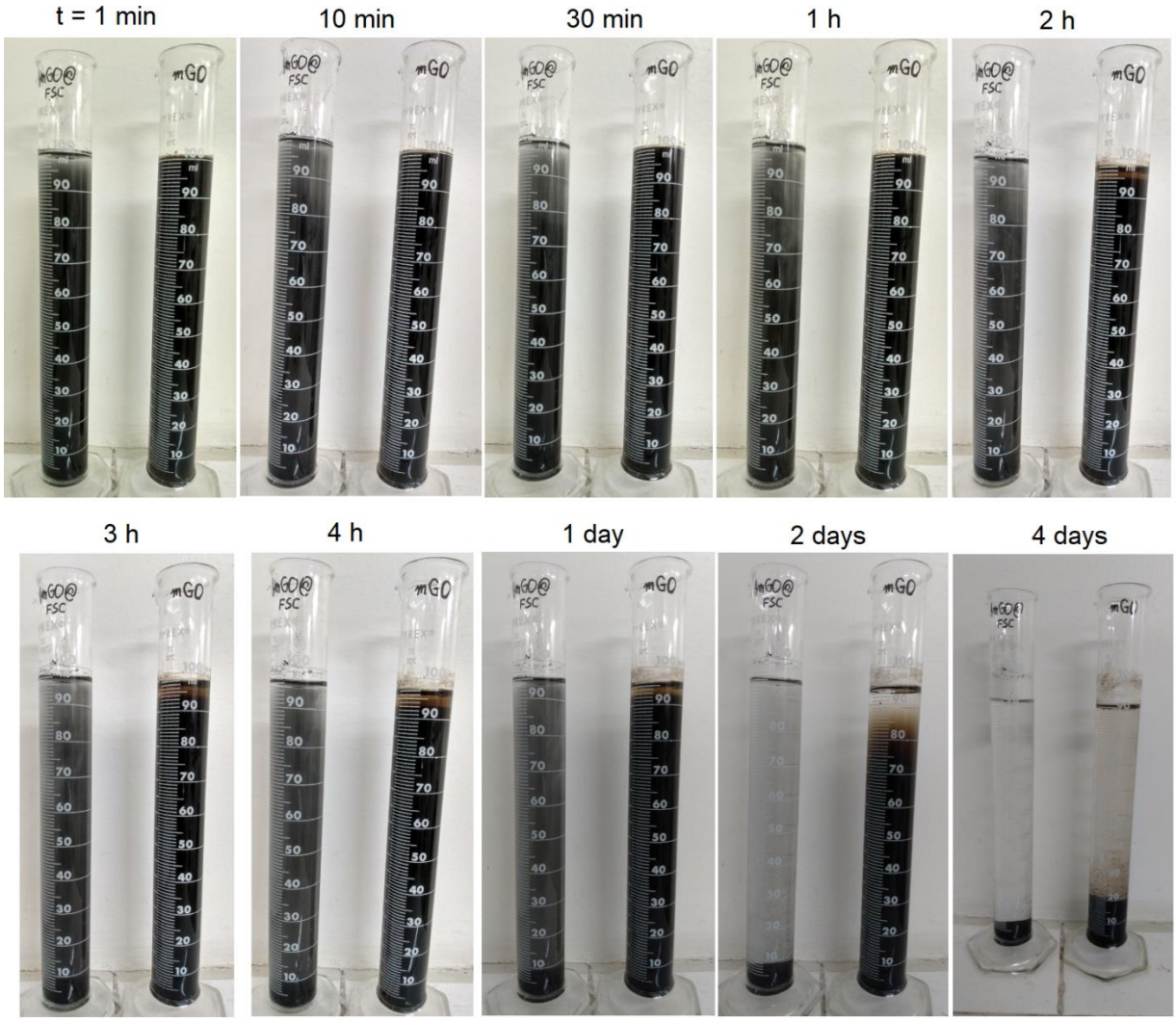

Source: the author (2020).

The concentration of solids (nGO and/or nGO(NH)R/C) in water was measured from aliquots of 1.0 mL collected in the top of the beakers. The measurements were performed by gravimetry, in Petri dishes previously dried in a stove at 100 ºC and weighted. Figure D2 shows the evolution of concentration of solids in the top of beakers with the time.

Figure D2 – study of the decantation of nGO and nGO(NH)R/C over the time. Conditions: 1.0 g of solid [nGO, nOG(NH)R/C] suspended in 100 mL of distilled water.

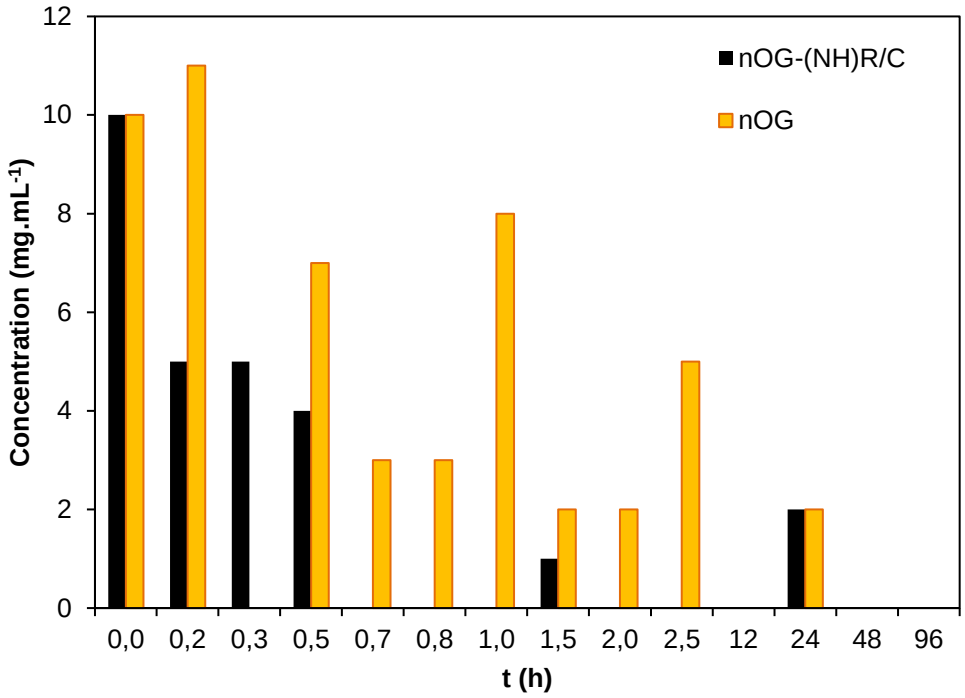

Source: the author (2020).

APPENDIX E – Published papers relative to the research reported in the thesis

E.1. One step forward: How can functionalization enhance the adsorptive properties of graphene towards metallic ions and dyes?

Environmental Research 184 (2020) 109362

Contents lists available at ScienceDirect

Environmental Research

journal homepage: www.elsevier.com/locate/envres

Review article

One step forward: How can functionalization enhance the adsorptive properties of graphene towards metallic ions and dyes?

Tiago José Marques Fraga[a,*], Marcos Gomes Ghislandi[a,b], Marilda Nascimento Carvalho[a], Maurício Alves da Motta Sobrinho[a]

[a] Department of Chemical Engineering, Federal University of Pernambuco (UFPE), 1235 Prof. Moraes Rego Av, Cidade Universitária, 50670-901, Recife, PE, Brazil
[b] Engineering Campus – UACSA, Federal Rural University of Pernambuco (UFRPE), 300 Cento e sessenta e Três Av., Cabo de Santo Agostinho, PE, Brazil

https://doi.org/10.1016/j.envres.2020.109362

Environmental Research, Impact factor **5.715** (2019)

This review article is the second published by me and my advisors which deals with the use of functionalized graphene nanomaterials in adsorptive processes. Differently from the first one (E.6), this work investigated the influence of different types of functionalization over the adsorption of metallic ions and dyes. The discussion focuses on the methods of synthesis, characterization and the role of functional groups in the different interface interactions between sorbent and sorbate. The surveyed data is thoroughly criticized and the nanosorbent performance is compared. Perspectives and future research needs are also remarked, especially regarding the employment of ecofriendly reactants to functionalize graphene, GO and their derivated.

E.2. Amino-Fe_3O_4-functionalized multi-layered graphene oxide as an ecofriendly and highly effective nanoscavenger of the reactive drimaren red

Environmental Science and Pollution Research
https://doi.org/10.1007/s11356-019-07539-z

RESEARCH ARTICLE

Amino-Fe_3O_4-functionalized multi-layered graphene oxide as an ecofriendly and highly effective nanoscavenger of the reactive drimaren red

Tiago José Marques Fraga [1] · Luiz Filipe Félix da Silva [1] · Letticia Emely Maria de Lima Ferreira [1,2] · Maryne Patrícia da Silva [1] · Daysianne Mikaella dos Santos Marques Fraga [1] · Caroline Maria Bezerra de Araújo [1] · Marilda Nascimento Carvalho [1] · Jorge Vinicius Fernandes de Lima Cavalcanti [1] · Marcos Gomes Ghislandi [1,3] · Maurício Alves da Motta Sobrinho [1]

Received: 28 October 2019 / Accepted: 25 December 2019

https://doi.org/10.1007/s11356-019-07539-z

Environmental Science & Pollution Research, Impact factor **3.056** (2019)

This article is a continuation of the research regarding the use of amino-Fe_3O_4-functionalized graphene oxide in the removal of dyes of different types from aqueous media. In this paper, the adsorption of the reactive Drimaren Red by nGO-NH-Fe_3O_4 is reported. The adsorption mechanisms were also analyzed based on the parameters obtained from the kinetic modeling and the thermodynamic parameters. This work also discusses the results of equilibrium, kinetics and thermodynamics of adsorption. In addition, a special focus was given to toxicity assays, used for the adsorbent and its precursor material. This paper is recommended to be read together with the ones listed in E.4 and E.5, since all papers consist in a compendium that reports the results and main findings of the research subject of this thesis.

E.3. Real textile wastewater treatment using nano graphene-based materials: Optimum pH, dosage, and kinetics for colour and turbidity removal

Received: 27 June 2019 | Revised: 15 October 2019 | Accepted: 17 October 2019

DOI: 10.1002/cjce.23712

ARTICLE

Real textile wastewater treatment using nano graphene-based materials: Optimum pH, dosage, and kinetics for colour and turbidity removal

Caroline M. B. de Araújo[1] | **Gabriel F. Oliveira do Nascimento**[1] | **Gabriel R. Bezerra da Costa**[2] | **Ana M. S. Baptisttella**[1] | **Tiago J. M. Fraga**[1] | **Romero B. de Assis Filho**[1,3] | **Marcos G. Ghislandi**[4] | **Mauricio A. da Motta Sobrinho**[1]

https://doi.org/10.1002/cjce.23712

Canadian Journal of Chemical Engineering, Impact factor **1.687** (2019)

This paper is the first of our research group which dealth with a systematic treatment of raw textile wastewaters with graphene oxide (GO). I was invited by my colleague Caroline M. B. Araújo to revise the text and validate some results, especially regarding the material characterization. Textile wastewater samples were collected in a laundromat and were then characterized. From that, significant information could be taken and the main parameters of wastewater were monitored before and after the adsorption by GO. Kinetics experiments were carried out by monitoring color and turbidity removal. Moreover, the salting out effect were assessed and its influence on GO aggregation was discussed.

E.4. Comparative approach towards the adsorption of Reactive Black 5 and methylene blue by n-layer graphene oxide and its amino-functionalized derivative

Adsorption
https://doi.org/10.1007/s10450-019-00156-9

Comparative approach towards the adsorption of Reactive Black 5 and methylene blue by n-layer graphene oxide and its amino-functionalized derivative

Tiago José Marques Fraga[1] · Ziani Santana Bandeira de Souza[1] · Daysianne Mikaella dos Santos Marques Fraga[1] · Marilda Nascimento Carvalho[1] · Eleonora Maria Pereira de Luna Freire[1] · Marcos Gomes Ghislandi[2] · Maurício Alves da Motta Sobrinho[1]

Received: 18 January 2019 / Revised: 19 July 2019 / Accepted: 23 July 2019

https://doi.org/10.1007/s10450-019-00156-9
Adsorption, Impact factor **1.949** (2019)

This article deals with the comparative study of the adsorption of the dyes of Methylene Blue and Reactive Black 5 onto amino-functionalized multilayer graphene oxide (nGO-NH). It contains data of equilibrium, kinetics and thermodynamics of adsorption. It is highlighted the section that deals with two-component adsorption in which the mixture of MB and RB5 was submitted to adsorption by nGO-NH and the nature of the adsorption was verified. This article also discusses the adsorption mechanisms provided for each dye. It is reported that each dye interacts with nGO-NH differently, given that the nature of MB adsorption is physical, while RB5 is linked to the active sites of nGO-NH through chemosorption. Finally, the cost analysis of preparing the nanosorbent is reported based on the reagent prices and the 2019 exchange rate.

E.5. Açaí waste beneficing by gasification process and its employment in the treatment of synthetic and raw textile wastewater

Journal of Cleaner Production 240 (2019) 118047

Contents lists available at ScienceDirect

Journal of Cleaner Production

journal homepage: www.elsevier.com/locate/jclepro

Açaí waste beneficing by gasification process and its employment in the treatment of synthetic and raw textile wastewater

Thiago Sabino Pessôa [a], Letticia Emely de Lima Ferreira [b], Maryne Patrícia da Silva [b], Luiz Martins Pereira Neto [c], Bruna Figueiredo do Nascimento [b], Tiago José Marques Fraga [b, *], Emerson Freitas Jaguaribe [d], Jorge Vinicius Cavalcanti [b], Maurício Alves da Motta Sobrinho [b]

[a] Pernambuco Federal Institute of Technology (IFPE), PE 60 Highway, Km 14, California, 55590-000, Ipojuca, PE, Brazil
[b] Department of Chemical Engineering, Universidade Federal de Pernambuco (UFPE), 1235 Prof. Moraes Rego Av, Cidade Universitária, 50670-901, Recife, PE, Brazil
[c] Environmental Engineering Post-Graduation Program, Universidade Federal Rural de Pernambuco (UFRPE), Dom Manuel de Medeiros St. W/N, Dois Irmãos, 521171-900, Recife, PE, Brazil
[d] Department of Mechanical Engineering, Universidade Federal da Paraíba (UFPB), Campus Universitário I, W/N, 58051-900, João Pessoa, PB, Brazil

https://doi.org/10.1016/j.jclepro.2019.118047

Journal of Cleaner Production, Impact factor **7.246** (2019)

This paper was published from the results of the Master Dissertation of my colleague Thiago S. Pessoa, who investigated the adsorptive properties of activated and pure biochar obtained from the gasification of açaí wastes. This was the first step in the investigation of the adsorption of dyes from biochars obtained from the gasifier installed in the Laboratory of Innovation, Federal University of Paraíba. Another dye adsorption onto a biochar acquired from the same method was investigated by Kelm *et al*. (2019) and also supplied information for the studies reported in this thesis. However the authors used wood wastes as biomass. In this paper, it was assessed the energy generation and monetary gains from this activity. Moreover, it was studied the enhancement in adsorptive power promoted by NaOH activation of açaí biochar. These reports embodied the curiosity and aims to use an alternative support for amino-graphene oxide in further investigations.

E.6. Functionalized graphene-based materials as innovative adsorbents of organic pollutants: a concise overview

Brazilian Journal
of Chemical
Engineering

ISSN 0104-6632
Printed in Brazil
www.abeq.org.br/bjche

Vol. 36, No. 01, pp. 1 - 31, January - March, 2019
dx.doi.org/10.1590/0104-6632.20190361s20180283

FUNCTIONALIZED GRAPHENE-BASED MATERIALS AS INNOVATIVE ADSORBENTS OF ORGANIC POLLUTANTS: A CONCISE OVERVIEW

Tiago J. M. Fraga[1*], Marilda N. Carvalho[1], Marcos G. Ghislandi[2] and Maurício A. da Motta Sobrinho[1]

[1] Universidade Federal de Pernambuco, Departamento de Engenharia Química, Recife/PE, Brasil. E-mail: tiago.fraga2012@gmail.com, ORCID: 0000-0002-5683-7307; marildacarv@gmail.com, ORCID: 0000-0001-7872-6432; mottas@ufpe.br, ORCID: 0000-0003-2638-9096
[2] Universidade Federal Rural de Pernambuco, Unidade Acadêmica do Cabo de Santo Agostinho, Cabo de Santo Agostinho/PE, Brasil. E-mail: ghislandi@gmail.com, ORCID: 0000-0001-7415-7260

(Submitted: June 25, 2018 ; Revised: August 5, 2018 ; Accepted: August 28, 2018)

https://doi.org/10.1590/0104-6632.20190361s20180283

Brazilian Journal of Chemical Engineering, Impact factor **1.027** (2019)

This is the first review article which dealth with the employment of graphene-derived nanocomposites in the adsorption of pollutants. However, the main focus here is the removal of organic pollutants (pesticides, pharmaceuticals, volatile organic compounds and atmospheric pollutants). Despite these chemicals are not subject of this research, this work is considered as a "first step" in the summarizing of the outstanding adsorptive capacity of several types of functionalized graphene. In this sense, it is highlighted the boost in adsorptive power and regeneration after functionalization of pristine graphene/GO towards several toxic compounds.

E.7. Amino-Fe_3O_4-functionalized graphene oxide as a novel adsorbent of Methylene Blue: kinetics, equilibrium, and recyclability aspects

Environmental Science and Pollution Research
https://doi.org/10.1007/s11356-018-3139-z

ALTERNATIVE ADSORBENT MATERIALS FOR APPLICATION IN PROCESSES INDUSTRIAL

Amino-Fe_3O_4-functionalized graphene oxide as a novel adsorbent of Methylene Blue: kinetics, equilibrium, and recyclability aspects

Tiago José Marques Fraga [1] · Letticia Emely Maria de Lima [2] · Ziani Santana Bandeira de Souza [1] · Marilda Nascimento Carvalho [1] · Eleonora Maria Pereira de Luna Freire [1] · Marcos Gomes Ghislandi [3] · Maurício Alves da Motta [1]

Received: 4 July 2018 / Accepted: 3 September 2018

https://doi.org/10.1007/s11356-018-3139-z

Environmental Science & Pollution Research, Impact factor **3.056** (2019)

This is the first paper referent to the research reported in this thesis. The adsorption of Methylene Blue by the amino-Fe_3O_4-fucntionalized graphene oxide was investigated with depth. However, this paper does not report the thermodynamic parameters of MB adsorption and therefore it does not bring a thoroughly discussion regarding the interaction between MB and the functionalized amino-graphene oxide. Such in-depth investigation is reported in the paper published in *Adsorption* (E.4, https://doi.org/10.1007/s10450-019-00156-9), in which further data were acquired with the advance of the research.

From the results published in this paper, it is possible to establish comparisons with other carbonaceous adsorbents (nano, micro) and it is evidenced the outstanding adsorptive capacity of GO-NH_2-Fe_3O_4 towards MB. The great efficiency of GO-NH_2-Fe_3O_4 exceeds much times the ones reported for charcoals and pristine graphene oxide. However, it is necessary to note that the adsorption of MB by GO reported at the comparative section is regarding published results by other papers. Again, the comparative assessment of the adsorptive power between nGO and nGO-NH_2 could be only reported in the article published in *Adsorption*.

E.8. State of the art: synthesis and characterization of functionalized graphene nanomaterials

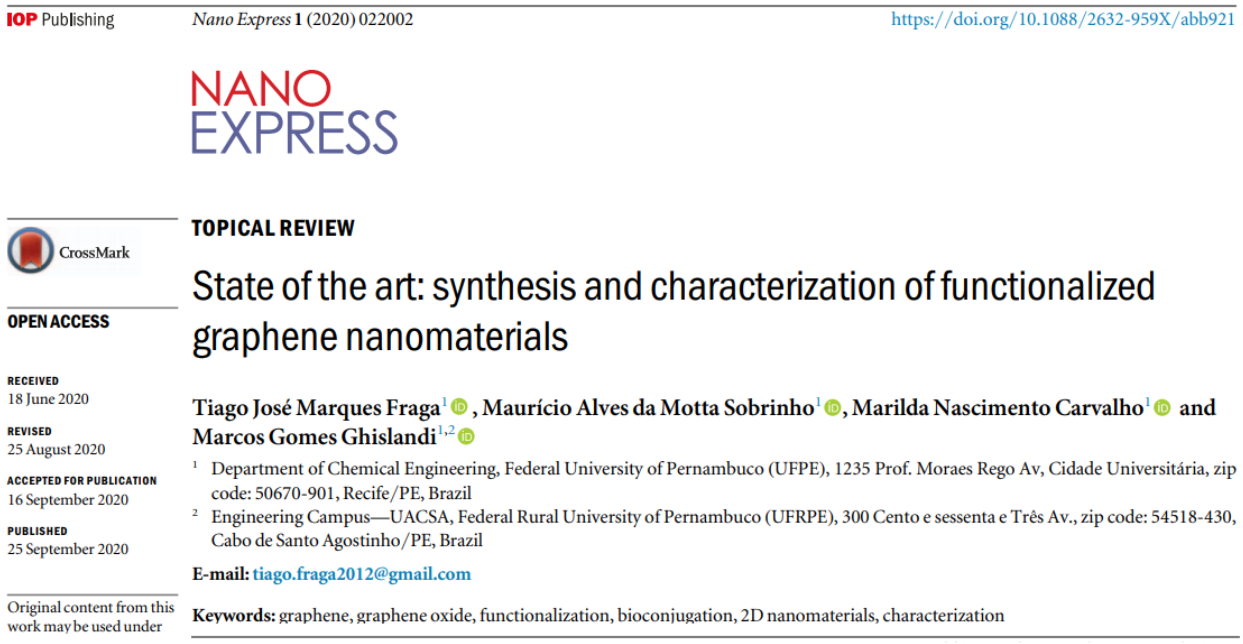

IOP Publishing Nano Express 1 (2020) 022002 https://doi.org/10.1088/2632-959X/abb921

NANO EXPRESS

TOPICAL REVIEW

State of the art: synthesis and characterization of functionalized graphene nanomaterials

Tiago José Marques Fraga[1], Maurício Alves da Motta Sobrinho[1], Marilda Nascimento Carvalho[1] and Marcos Gomes Ghislandi[1,2]

[1] Department of Chemical Engineering, Federal University of Pernambuco (UFPE), 1235 Prof. Moraes Rego Av, Cidade Universitária, zip code: 50670-901, Recife/PE, Brazil

[2] Engineering Campus—UACSA, Federal Rural University of Pernambuco (UFRPE), 300 Cento e sessenta e Três Av., zip code: 54518-430, Cabo de Santo Agostinho/PE, Brazil

E-mail: tiago.fraga2012@gmail.com

Keywords: graphene, graphene oxide, functionalization, bioconjugation, 2D nanomaterials, characterization

OPEN ACCESS

RECEIVED 18 June 2020

REVISED 25 August 2020

ACCEPTED FOR PUBLICATION 16 September 2020

PUBLISHED 25 September 2020

https://doi.org/10.1088/2632-959X/abb921

Nano Express, Impact factor: **not available** (2019)

This topical review is part of my first literature survey, in which it was necessary to research different protocols of graphene and GO functionalization, as well as their characterization techniques. However, differently from the first review papers (D.1 and D.6), which focus on the application of functionalized-graphene nanocomposites, this one focuses on their different methodologies of synthesis and characterization. The topics are presented in a didactic way and are mainly addressed to researchers who are initiating their research in this subject.

E.9. Nanocomposites and their employment as scavengers of water pollutants

Nanocomposites and their employment as scavengers of water pollutants
JCA: Volume 1: Issue 1, March-2019: Page No: 18-31

Journal of Chemistry and Applications
Review Article Open Access

Nanocomposites and their employment as scavengers of water pollutants

Carolina Maria Bezerra de Araújo[1], Ziani Santana Bandeira de Souza[1], Maurício Alves da Motta Sobrinho[1], Marcos Gomes Ghislandi[2] and Tiago José Marques Fraga[1*]

https://doi.org/10.36811/jca.2019.110003

Journal of Chemistry & Applications (RAFT Pubs, USA), Impact factor: **not available** (2019).

This work consists of a broad min-review on the use of different types of nanomaterials in the treatment of effluents in general. In this work, it was investigated in which processes a series of nanomaterials (ceramic, nano-clays and carbonaceous nanomaterials – CNT, quantum dots, graphene, among others) have been applied. Since this is not a review with a focus on adsorptive processes, it is recommended that the reader seek information on this topic in the two review articles published in the *Brazilian Journal of Chemical Engineering* (E.6) and *Environmental Research* (E.1).